

Multifunctional Laminated Composites for Morphing Structures

Dissertation

Presented in Partial Fulfillment of the Requirements for the Degree
Doctor of Philosophy in the Graduate School of The Ohio State
University

By

Venkata Siva Chaithanya Chillara, B.S.

Graduate Program in Mechanical Engineering

The Ohio State University

2018

Dissertation Committee:

Professor Marcelo Dapino, Advisor

Professor Haijun Su

Professor Rebecca Dupaix

Professor Ryan Harne

© Copyright by
Venkata Siva Chaithanya Chillara
2018

Abstract

Morphing panels offer opportunities as adaptive control surfaces for optimal system performance over a broad range of operating conditions. This work presents a design framework for multifunctional composites based on three types of laminae, *viz.*, constraining, adaptive, and prestressed. Based on this framework, laminate configurations are designed to achieve multiple morphing modes such as stretching, flexure, and folding in a given composite structure. Multiple functions such as structural integrity, bistability, and self-actuation are developed. The composites are developed through a concurrent focus on mathematical modeling and experiments.

This research shows that curvature can be created in a composite structure by applying mechanical prestress to one or more of its laminae. Cylindrical curvature can be tailored using a prestressed lamina with zero in-plane Poisson's ratio. Analytical laminated-plate models, based on strain energy minimization, are presented in multiple laminate configurations to characterize composites with curvature, bistability, folding, and embedded smart material-driven actuation. Fabrication methods are also presented for these composite configurations. The mathematical models are validated experimentally using tensile tests and 3D motion capture.

The mechanics of an n -layered composite is explained through modeling of all the stacking sequences of the three generic laminae. Actuation energy requirement is found to be minimal in the constraining-prestressed-adaptive layer configuration. Bistable curved composites are developed using asymmetric prestressed laminae on

either face of a core layer; these composites address the drawbacks of thermally-cured bistable fiber-reinforced polymeric composites. When the prestressed directions are orthogonal, the stable curvatures are weakly-coupled. The composite's domain of bistability and actuation requirements are quantified using a non-dimensional high-order strain model.

Active bistable composites are modeled and demonstrated using shape memory alloy (SMA) actuators in a push-pull configuration. Experiments show that the unactuated SMA dampens the composite's post-transition vibrations. Folds are created by laminating a prestressed layer across a crease. Fold angle is modeled using piecewise displacement functions to account for the low stiffness of a crease relative to its faces. Extensive model-based parametric studies are conducted in various laminate configurations to study the effect of laminae properties, dimensions, and prestress magnitude and orientation, on the composite's shape, stiffness, and actuation energy.

A thorough literature survey is conducted on the effect of various aerodynamic treatments on effective vehicle drag. A morphing fender skirt is demonstrated since it provides a good trade-off between drag reduction (0.038 points) and practical implementation. Through design, manufacturing, and testing, a lightweight, self-supported, and self-actuated morphing fender skirt is developed based on the multifunctional composites characterized at the coupon scale.

Intellectual Merit: Innovative stress-biased curved composites with an irreversible non-zero stress state are presented through this work. A framework for multifunctional composites, backed by analytical modeling tools and fabrication methods, is presented for the design of generic laminated composite-based morphing structures.

Broader Impact: Morphing structures can effectively contribute to the improved fuel economy in automobiles through reductions in aerodynamic drag and vehicle weight. The multifunctional composites, demonstrated using relatively inexpensive

materials, are suitable for mass-market products. The composite framework enables applications in the fields of morphing aircraft and automobiles, soft robotics, and biomimetics.

This is dedicated to my family.

Acknowledgments

The work presented in this dissertation has been possible through guidance and support from a number of people. I would like to thank Prof. Marcelo Dapino, Prof. Rebecca Dupaix, Prof. Ryan Harne, and Prof. Haijun Su for serving on my Ph.D. committee. My Ph.D. journey has been an enriching and gratifying experience thanks to my advisor Prof. Marcelo Dapino. His guidance has been invaluable on all fronts ranging from developing research ideas to honing my communication and presentation skills. I thank Prof. Dapino for providing me with opportunities to present at conferences and for appointing me as a graduate fellow of the Smart Vehicle Concepts Center (SVC), a National Science Foundation Industry-University Cooperative Research Center.

I am fortunate to have worked with Dr. Leon Headings throughout my Ph.D. research. His creative ideas and critical feedback in our brainstorming sessions and his attention-to-detail in our papers have been of great help, especially early on in my research. I would like to thank the SVC members for their regular feedback and motivation. Special thanks to Mr. Tom Greetham and Dr. Ryan Hahnen for their support. I thank Toyota Technical Center (Ann Arbor, MI) for initiating my research project, especially Dr. Umesh Gandhi, Mr. Ryohei Tsuruta, Mr. Kazuhiko Mochida, and Mr. Eiji Itakura (Toyota Motor Corp., Japan). The mentorship of Prof. Rajendra Singh (OSU) has been vital in all aspects of my life as a graduate researcher.

I would like to thank all the MAE staff for supporting me throughout my graduate program. Special thanks to SVC staff Tommie Blackledge, graduate advisors Janeen Sands and Nick Breckenridge, machine shop staff Chad Bivens, Walter Green, Kevin Wolf, and Aaron Orsborn, and administrative staff Charles Slonaker, Ralph Orr, and Ann Sanders.

It has been a pleasure to work with my colleagues at the Smart Materials and Structures Lab. These highly-motivated individuals have fostered a work culture that is ideal for sharing each other's ideas and providing feedback. I would like to thank my seniors Dr. Jungkyu Park, Dr. Sushma Santapuri, Dr. Hafez Tari, Dr. Justin Scheidler, Dr. Adam Hehr, Dr. Zhangxian Deng, Dr. Sheng Dong, and Dr. John Larson. Other students I have worked with are too many to list here but I would like to mention Bryant Gingerich, Matthew Scheidt, Yitong Zhou, Tianyang Han, Gowtham Venkatraman, Hongqi Guo, Sai Vemula, Arun Ramanathan, Sean Chilelli, Ismail Nas, Brad Losey, Chase Young, and Alex Avila.

This research would not have been possible without the support from my friends and family. I would like to particularly thank Anshuman Pandey and Vinay Singh Chauhan for their constant support and camaraderie. I thank my friends Kirti Mishra, Kaushik Krishna, Rahul Taduri, Shashank Nagavarapu, Ayush Garg, Srivatsava Krishnan, Bharat Hegde, Venkat KV, Yeswanth Pottimurthy, and Apeksha Dave. I am very grateful to my parents, in-laws, and grandparents for their unconditional love and encouragement throughout my academic pursuit. Lastly, I would like to thank my wife and best friend, Ranjani. She has patiently endured all my research-related talk and has been my daily source for motivation. I thank her for pushing me to do my best and always being there for me.

Vita

March 6, 1989 Born - Hyderabad, India

May, 2011 B.S. Mechanical Engineering,
National Institute of Technology Kar-
nataka,
Surathkal, India

2014–2018 Graduate Fellow - NSF IUCRC Smart
Vehicle Concepts Center,
Graduate Research Associate - Smart
Materials and Structures Lab,
The Ohio State University

Publications

V.S.C. Chillara, L.M. Headings, and M.J. Dapino “Self-folding laminated composites for smart origami structures.” *Proceedings of ASME Conference on Smart Materials, Adaptive Structures and Intelligent Systems*, Colorado Springs, Colorado, 8968, September 2015.

V.S.C. Chillara, L.M. Headings, and M.J. Dapino “Multifunctional laminated composites with intrinsic pressure actuation and prestress for morphing structures.” *Composite Structures*, 157, 265-274, 2016.

V.S.C. Chillara and M.J. Dapino “Mechanically-prestressed bistable composite laminates with weakly-coupled equilibrium shapes.” *Composites Part B: Engineering*, 111, 251-260, 2017.

V.S.C. Chillara and M.J. Dapino “Bistable morphing composites with selectively pre-stressed laminae.” *SPIE Smart Structures and Materials + Nondestructive Evaluation and Health Monitoring*, Portland, Oregon, 10165, March 2017.

V.S.C. Chillara and M.J. Dapino “Stability considerations and actuation requirements in bistable laminated composites.” *Composite Structures*, 184, 1062-1070, 2018.

V.S.C. Chillara and M.J. Dapino “Shape memory alloy-actuated bistable composites for morphing structures.” *SPIE Smart Structures and Materials + Nondestructive Evaluation and Health Monitoring*, Denver, Colorado, 10596, March 2018.

V.S.C. Chillara, L.M. Headings, R. Tsuruta, E. Itakura, U. Gandhi, and M.J. Dapino “Shape memory alloy-actuated prestressed composites with application to morphing automotive fender skirts.” *In preparation*.

V.S.C. Chillara and M.J. Dapino “Stress-biased laminated composites for smooth folds in origami structures.” *In preparation*.

Fields of Study

Major Field: Mechanical Engineering

Studies in:

Engineering Mechanics
Smart Materials and Structures

Table of Contents

	Page
Abstract	ii
Dedication	v
Acknowledgments	vi
Vita	viii
List of Figures	xiv
List of Tables	xx
1 Background	1
1.1 Morphing structures	1
1.1.1 Automotive applications	2
1.1.2 Aerospace applications	2
1.1.3 Integration of morphing structures	3
1.2 Laminated composites as morphing structures	5
1.2.1 Stretchable composites	7
1.2.2 Flexible composites	9
1.2.3 Foldable composites	11
1.2.4 Composite actuation	14
1.3 Analytical modeling	17
1.4 Research questions	18
1.5 Dissertation outline	21
2 Multifunctional Laminated Composites	23
2.1 Composite description	24
2.2 Research approach	26
2.3 Fabrication of mechanically-prestressed composites	27
2.3.1 Elastomeric matrix composites	27
2.3.2 Composite lamination	30
2.4 Analytical modeling framework	32
2.4.1 Strain model	33
2.4.2 Nonlinear response of an EMC	35
2.4.3 Potential Energy Function	37
2.4.4 Computation of composite shape	38

2.5	Model validation	38
3	Laminated Composites with Intrinsic Pressure Actuation and Prestress	41
3.1	Introduction	42
3.2	Fluidic Prestressed Composite	43
3.2.1	Description of laminae	44
3.2.2	Laminate configurations	45
3.3	Analytical Model	46
3.3.1	Strain energy of the composite	46
3.3.2	Work done by applied fluid pressure	49
3.3.3	Computation of composite shape	50
3.4	Model-Based Study of Composite Response	50
3.4.1	Configuration study	50
3.4.2	Parametric study	53
3.5	Composite Fabrication	56
3.5.1	Fluidic layer	57
3.5.2	Laminated composite	59
3.6	Model Validation	60
4	Mechanically-Prestressed Bistable Composites with Weakly Coupled Equilibrium Shapes	64
4.1	Introduction	65
4.2	Analytical Model	66
4.2.1	Laminate strain formulation	67
4.2.2	Computation of stable laminate shapes	69
4.3	Laminate Fabrication	71
4.4	Measurement of laminate geometry	73
4.5	Results and Discussion	74
4.6	Parametric Study	79
4.6.1	Effect of EMC width	79
4.6.2	Effect of core modulus and thickness	80
4.6.3	Effect of laminate size	80
4.7	Response of the laminate to shape transition	83
5	Shape Memory Alloy-Actuated Bistable Composites	85
5.1	Introduction	86
5.2	Analytical Model	87
5.2.1	Composite shape computation as a function of actuation force	88
5.2.2	1-D model of an SMA actuator	90
5.2.3	Composite actuation using SMA wires	92

5.3	Results and Discussion	93
5.4	Demonstration of an SMA-actuated bistable composite	98
6	Stability Considerations and Actuation Requirements of Bistable Composites	103
6.1	Introduction	104
6.2	Analytical model	105
6.2.1	Non-dimensional composite displacements	106
6.2.2	Strain model	107
6.2.3	Strain energy computation	108
6.2.4	Work done by external forces	109
6.2.5	Computation of composite shape	112
6.3	Experiments	112
6.4	Results and discussion	117
6.5	Sensitivity study	124
7	Stress-Biased Laminated Composites for Smooth Folds in Origami Structures	127
7.1	Introduction	128
7.2	Composite fabrication	129
7.2.1	EMCs	130
7.2.2	Folds	130
7.2.3	Measurement of a 90° EMC's moduli	132
7.3	Analytical model	133
7.3.1	Composite strains	134
7.3.2	Strain Energy Function	135
7.3.3	Computation of fold angle	137
7.4	Results and Discussion	138
7.4.1	Folded shapes and model validation	139
7.4.2	Effect of crease width	141
7.4.3	Effect of crease modulus and thickness	142
7.4.4	Effect of EMC Orientation	146
8	System-Scale Implementation: Morphing Fender Skirts	149
8.1	Introduction	150
8.2	Morphing structure configuration	150
8.2.1	Fender skirt	151
8.2.2	Laminated composite	155
8.3	Analytical model of an active composite rib	156
8.3.1	Strain energy computation	157
8.3.2	Work done by an external force	159
8.3.3	Composite displacements and shape computation	161

8.3.4	Actuation using SMA wire	162
8.4	Composite rib design	165
8.4.1	Fender skirt geometry	165
8.4.2	Passive composite	165
8.4.3	SMA actuation	167
8.5	Case study: fender skirt	170
8.5.1	Fabrication	170
8.5.2	Demonstration	174
9	Contributions and Future Work	177
9.1	Summary of findings	177
9.2	Primary contributions	180
9.3	Related contributions	182
9.4	Future work	184
	Bibliography	187

List of Figures

Figure	Page
1.1 (a) Estimated contributions to the drag coefficient of a passenger car (data from Barnard [1]) and (b) potential for drag reduction through the use of morphing structures. The color-code used for morphing solutions in (b) correlates to the corresponding source of aerodynamic drag in (a).	3
1.2 (a) Morphing fender on the BMW Next 100 Years concept [2], (b) boat-tail extension on the Mercedes Benz Intelligent Aerodynamic Automobile concept [3] (bottom), and (c) inflatable front spoiler on a Porsche 911 Turbo S [4], and (d) active flaps for engine thermal management on a Ferrari 458 Speciale [5].	4
1.3 Concepts for morphing aircraft based on: (a) airfoil camber adjustment [6, 7], (b) wing span morphing [8], (c) variable wing sweep [9], and (d) span-wise bending (left) and wing-twist (right) [10].	5
1.4 Research areas for morphing structures.	7
1.5 (a) Configuration of stretchable EMCs in a morphing airfoil [11] and (b) zero-Poisson's ratio EMC coupled with a support structure to achieve span morphing in an aircraft wing [8].	8
1.6 EMC strip partially reinforced with fibers along its width.	9
1.7 (a) The stable shapes of an asymmetric 0°/90° FRP laminate [12] and (b) the stable shapes of a prestressed buckled FRP laminate [13].	10
1.8 (a) Self-folding laminated composites with creases activated by (a) shape memory alloys [14], (b) shape memory polymers [15], and (c) magneto-active elastomers [16].	12
1.9 Laminated composites actuated by: (a) piezoelectric macro-fiber composites [17], (b) piezoelectric composites in one direction and shape memory alloy wires in the other [18], (c) shape memory alloy springs [19], and (d) pneumatic pressure [20].	15

2.1	Types of laminae in a multifunctional composite. A constraining layer is flexible but not stretchable (e.g., metal sheet); the prestressed layer is capable of large strain and is laminated in a stretched condition (e.g, fiber-reinforced elastomer); an adaptive layer has a controllable stress state (e.g., smart materials and pressurized fluid channels). The adaptive layer is shown in the figure as a fluidic layer.	24
2.2	(a) Flexure, (b) stretching, and (c) folding in a prestressed composite.	25
2.3	(a) Bistability in a prestressed composite and (b) morphing of the composite through the activation of a fluidic (adaptive) layer.	26
2.4	Research flowchart.	28
2.5	Fabrication process for an elastomeric matrix composite.	29
2.6	Stress-strain curve for a 90° EMC constructed as described in section 5.1, obtained from a uniaxial tensile test.	30
2.7	Schematic diagram showing the various layers of a prestressed composite.	31
2.8	a) Setup for curing the prestressed composite, (b) final composite beam sample with a prestrain of 0.6 in the 90° EMC, and (c) final composite beam sample with a prestrain of 0.8 in the 90° EMC.	32
2.9	Geometry for the laminated composite model.	33
2.10	Curvature of the composite as a function of prestrain in the 90° EMC.	39
3.1	(a) Geometry of a fluidic prestressed composite in the unactuated state, (b) limiting actuated shape of the composite when the fluid channels are pressurized.	42
3.2	Moments induced on a composite in configuration 1 due to pressurization of the fluidic layer.	43
3.3	(a) Participating laminae and (b) possible laminate configurations of a fluidic prestressed composite.	44
3.4	Geometry for a beam model of a fluidic prestressed composite illustrated in configuration 1. The bottom face of the fluidic layer is reinforced with unidirectional fibers oriented along the Y direction.	47
3.5	Dimensions of the laminae of a fluidic prestressed composite: (a) fluidic layer, (b) constraining layer, and (c) prestressed 90° EMC.	51
3.6	Modeled curvature vs. actuation pressure of a fluidic prestressed composite in configuration 1.	52
3.7	Modeled curvature vs. actuation pressure of a fluidic prestressed composite in configuration 2.	53
3.8	Modeled curvature vs. actuation pressure of a fluidic prestressed composite in configuration 3.	54
3.9	Response of a fluidic prestressed composite on the non-dimensional width (ϕ) for $\chi = 0.6$ and $\psi = 0.4$	55
3.10	Response of a fluidic prestressed composite on the non-dimensional thickness (χ) for $\phi = 0.4$ and $\psi = 0.4$	56

3.11	Response of a fluidic prestressed composite on the non-dimensional proximity to the interface (ψ) of the fluid channel for $\phi = 0.4$ and $\chi = 0.6$	57
3.12	(a) Setup to mold the body of the fluidic layer, (b) layup of silicone rubber to create the body, (c) setup for the end cap, (d) silicone rubber poured to create the end cap, (e) fully cured fluidic layer, (f) fiber-reinforcement of the bottom face.	58
3.13	(a) Setup for the lamination of a fluidic prestressed composite, (b) trimmed laminated composite, (c) unactuated and (d) limiting actuated shapes of the composite.	59
3.14	(a) Experimental setup to measure the quasi-static response of a fluidic prestressed composite, (b) composite equipped with reflective markers, (c) spatial coordinates of the reflective markers measured by a motion capture system.	61
3.15	Plot of the curvature of a fluidic prestressed composite (sandwiched 90° EMC configuration) as a function of actuation pressure for different prestrains in the 90° EMC.	62
4.1	(a) Configuration of a mechanically-prestressed bistable laminate, (b) curved laminate due to a deformed 90° EMC, and (c) curved laminate due to a deformed 0° EMC.	66
4.2	Schematic representation of a matrix-prestressed bistable laminate.	67
4.3	(a) A spring-steel core bonded to a prestressed EMC in the 90° orientation, (b) pressure applied to the bonded region for curing, (c) laminate with a single curvature obtained upon removal of the EMC from the grips, (d) curved sample bonded to an EMC in the 0° orientation, (e) pressure applied to the bonded region after flattening the sample, (f) resulting bistable laminate with the ends of the EMCs wrapped around and bonded to the core.	71
4.4	Stable shapes of a fabricated sample of a mechanically-prestressed bistable laminate.	72
4.5	(a) Reflective markers bonded to the laminate sample for shape measurement, (b) setup showing the motion capture system used to record the equilibrium shapes of the laminate.	74
4.6	Stable cylindrical shape of a mechanically-prestressed bistable laminate with curvature about the X axis.	75
4.7	Stable cylindrical shape of a mechanically-prestressed bistable laminate with curvature about the Y axis.	76
4.8	Equilibrium curvatures of a mechanically-prestressed bistable laminate as a function of prestrain in the 90° and 0° EMCs.	78
4.9	Influence of the width of an EMC relative to core width on the stable-equilibrium curvatures of the laminate. $\epsilon_{90} = \epsilon_0 = 0.6$	79

4.10	Stable-equilibrium curvatures of the laminate as a function of core modulus and thickness. $\epsilon_{90} = 0.8$ and $\epsilon_0 = 0.5$	81
4.11	Effect of laminate size on bistability; (a)-(b) influence of core modulus on the critical characteristic length for bistability.	82
4.12	Measured dynamic response of a mechanically-prestressed bistable laminate during a transition from one stable shape to another.	83
5.1	(a) Configuration and (b) stable shapes of an SMA-actuated mechanically-prestressed bistable composite.	86
5.2	Stress-strain behavior of a shape memory alloy.	87
5.3	(a) Stress-strain behavior of a shape memory alloy, (b) operating modes of SMAs in a bistable laminate.	88
5.4	Actuation force applied on the composite by a shape memory alloy wire.	89
5.5	Phase transformation diagram of a typical 1-D shape memory alloy.	91
5.6	Force generated by an SMA as a function of composite curvature.	94
5.7	Effect of (a) temperature and (b) Martensitic volume fraction of a 90° SMA on composite curvature.	95
5.8	Effect of diameter of the 90° SMA on composite curvature.	96
5.9	Post snap-through evolution of volume fraction of the 0° SMA as a function of composite curvature.	97
5.10	(a) Stable shapes of a passive bistable composite sample and (b) room temperature (25°C) response of the 90° and 0° SMA wire actuators.	99
5.11	Setup for a shape memory alloy-actuated bistable composite.	100
5.12	Snap-through transition in an SMA-actuated bistable composite.	101
5.13	Complete shape transition profile for a shape memory alloy-actuated bistable composite.	102
6.1	Stable shapes of a mechanically-prestressed laminated composite.	105
6.2	Schematic representation of a mechanically-prestressed bistable laminate.	107
6.3	Four cases for external forces applied on a bistable composite to effect snap-through into the second stable shape. The first three cases shown in (a) through (c) are point-wise forces whereas case four shown in (d) is a uniformly distributed force.	110
6.4	Experimental setup to record shape transition in a bistable composite.	114
6.5	Fabricated samples of a mechanically-prestressed bistable laminate.	115
6.6	Measured out-of-plane displacements of \overline{AD} and \overline{BC} , as a function of (a) time and (b) actuation force, in a composite with $\epsilon_0 = \epsilon_{90} = 0.8$	116
6.7	Shape of a composite with $\epsilon_0 = \epsilon_{90} = 0.8$ in (a) the unactuated first stable state, (b) intermediate stable state during snap-through, and (c) second stable state post snap-through.	117
6.8	Stable shapes of the composite as a function of prestrain ratio ϵ_r for $\epsilon_{90} = 1$	119

6.9	Effect of aspect ratio AR on the stable shapes of the composite as a function of (a) ϵ_0 while $\epsilon_{90} = 0.6$ and (b) ϵ_{90} while $\epsilon_0 = 0.6$	120
6.10	Work done by an axial force R_h on a composite with $\epsilon_{90} = \epsilon_0$	121
6.11	Work done by an in-plane actuation force R_p as a function of (a) ϵ_0 where $m = 0$ and $\epsilon_{90} = \epsilon_0$, and (b) m where $\epsilon_0 = \epsilon_{90} = 0.6$	122
6.12	Work done by a transverse force R_v as function of ϵ_0 where $\epsilon_{90} = \epsilon_0$	123
6.13	Sensitivity of the composite's performance to (a) core modulus and (b) core thickness.	124
7.1	(a) Stress-biased folded composites with (a) a soft crease and (b) a notched crease. The figures in the inset show composite shape in the absence of EMC prestress. (c) Demonstration of folding in a stress-biased composite with non-parallel creases.	129
7.2	A fabricated stress-biased folded composite shown in: (a) top and (b) front views; (c) unfolded shape; and (d) folded shape.	131
7.3	(a) A 90° EMC and creases cut out of 0.762 mm thick steel shim; (b) steel shims laminated to a prestressed 90° EMC; (c) curing of the laminate under applied pressure; (d) composite shape after removal of prestress; (e) curved creases obtained from trimming the composite in (d).	132
7.4	Stress-strain curve recorded from a fiber pull-out test conducted on an EMC comprising silicone rubber reinforced with unidirectional carbon fibers.	133
7.5	Schematic of a stress-biased composite for modeling.	135
7.6	Schematic of a composite illustrating fold angle at the vertex of a crease.	137
7.7	Comparison of shapes of a pure crease and a crease with faces.	140
7.8	Out-of-plane deflection of the straight edges of a crease fabricated without the included faces. The data presented corresponds to $\epsilon_{90} = 0.4$	141
7.9	Comparison of shapes of a crease with flat and curved faces.	142
7.10	Fold angle as a function of crease width ratio shown for crease thickness and modulus of 0.003" and 200 GPa respectively.	143
7.11	Fold angle as a function of crease modulus and width at a constant thickness of 0.003". The modulus range for shape memory alloys is illustrated as an example for the selection of materials with controllable modulus.	144
7.12	Fold sharpness as a function of crease width and thickness, shown for a crease modulus of 2 GPa.	145
7.13	Fold angle as a function of prestrain angle for various values of transverse (fiber-direction) modulus of an EMC.	147
7.14	Fold angle as a function of prestrain angle and crease width.	148
8.1	(a) Retracted shape and (b) deployed shape of a morphing fender skirt (shown in yellow).	151

8.2	(a) Unactuated dome and (b) actuated flat shapes of a morphing fender skirt. The flexible segment in (b) is shown with transparency to highlight the details on the inner face; skin is not shown.	152
8.3	Design elements for the integration of a morphing fender skirt.	153
8.4	Approximate fender dimensions and motion limits of the left wheel of a compact passenger car.	154
8.5	Schematic representation of a prestressed composite rib with a linearly varying tapered planform in the (a) isometric view and (b) YZ plane.	155
8.6	Schematic representation of a prestressed composite with an arbitrary planform shape that can be described using explicit continuous functions.	157
8.7	Configuration of (a) in-plane force (\vec{F}) and (b) uniformly distributed vertical force (\vec{P}) on a curved plate that represents the prestressed laminated composite rib.	160
8.8	(a) Constitutive response and (b) phase transformation of a typical 1-D shape memory alloy. C_M and C_A are the stress-temperature coefficients in the Martensite and Austenite phases, respectively.	162
8.9	Influence of EMC prestrain ϵ_{90} on the out-of-plane displacement (w_0) at $(L_x, 0)$ on the composite rib.	166
8.10	Effect of panel modulus and thickness on the out-of-plane displacement w_0 . Isometric lines correspond to w_0 in mm at $(L_x, 0)$	167
8.11	Out-of-plane displacement at $(L_x, 0)$ as a function of a vertical uniformly distributed force P	168
8.12	Plots to calculate the (a) force and (b) stroke required to flatten the composite.	169
8.13	(a) Actuation temperature (T) and (b) Martensite volume fraction (ξ) of an SMA wire post actuation, as a function of its diameter D	170
8.14	Fabrication procedure for a half-scale fender skirt demonstrator. (a) Ribs cut out of a sector of Nylon sheet; (b) a 90° EMC stretched and held between a pair of grips; (c) lamination of the Nylon panel, vinyl foam core, and EMC under pressure; (d) shape of the rib after lamination; (e) assembly of the ribs and a 3D printed rigid structure; (f) linkage of the outer ends of the ribs using a compliant copper rim; (g) elements of the latch mechanism on the back of the rigid structure; (h) fender skirt assembled on a wooden frame; (i) stretchable Spandex skin installed on the fender skirt.	172
8.15	Actuation sequence for the demonstration of a morphing fender skirt.	173
8.16	(a) Unactuated domed shape and (b) actuated flat shapes of a half-scale morphing fender skirt demonstrator.	174
8.17	(a) Experimental setup to record the morphing of a fender skirt and (b) out-of-plane displacement of the rigid segment in the fender skirt demonstrator; thin and thick lines indicate the structure's flattening and retraction, respectively.	175

List of Tables

Table	Page
1.1 Survey of morphing laminated composites with embedded actuators.	6
2.1 Design details of the fabricated 90° EMC.	29
2.2 Design parameters for composite beam samples fabricated with a vinyl foam core.	31
3.1 Limits of integration for the computation of strain energy of the linear elastic layers of the composite.	48
3.2 Measured material properties of the laminae of a fluidic prestressed composite.	51
4.1 Limits of integration for the computation of the total potential energy of a mechanically-prestressed bistable laminate.	70
4.2 Material properties of the laminae for modeling and fabrication.	75
4.3 Dimensions of the laminae for modeling and fabrication	77
5.1 Measured material properties of NiTi-6 shape memory alloy wire.	94
6.1 Limits of integration for the computation of the total potential energy of a mechanically-prestressed bistable laminate.	109
6.2 Size of the displacement polynomials and strain energy integrand.	113
7.1 Polynomial coefficients of a nonlinear stress function of an EMC with zero in-plane Poisson’s ratio, obtained from a uniaxial tensile test [21].	136
7.2 Geometric and material properties of the laminae for modeling.	139
7.3 Conditions imposed on displacement polynomials for the modeling of folds at a crease with orthogonal EMC prestrain.	139
7.4 Conditions imposed on displacement polynomials for the modeling of folds at a crease with orthogonal EMC prestrain.	146

8.1	Polynomial coefficients of a nonlinear stress function of a 90° EMC made of carbon fiber-reinforced silicone, obtained from a uniaxial tensile test [21].	159
8.2	Geometric parameters for the modeled composite rib. ω is unitless. All other parameters are expressed in mm.	164
8.3	Material properties and thicknesses of the laminae for modeling and fabrication.	164
8.4	Measured material properties of a NiTi-6 shape memory alloy wire. .	168

Chapter 1

Background

1.1 Morphing structures

Morphing structures, defined as body panels that are capable of a gradual autonomous shape transformation, have gained importance in the automotive and aerospace industries since they address the need to adapt the vehicle's shape for optimal performance over a broad range of operating conditions. In automobiles, for example, aerodynamic performance is critical at high speeds whereas other factors such as ground clearance and aesthetics are a priority at low speeds. Aerodynamic drag is defined as the force that resists vehicle motion in air. A 10% reduction in drag leads to a 2% improvement in fuel economy. However, a 10% increase in vehicle weight results in a 6.5% penalty on fuel economy [22]. In aircraft, real-time morphing of wing geometry enables the optimization of aerodynamics for maximal fuel efficiency over a range of flight conditions; the use of discrete control surfaces adds weight penalty on performance. Therefore, morphing elements should be lightweight structures that are capable of withstanding aerodynamic loads while allowing significant shape changes [23]. Further, morphing components should consume minimal energy from a compact actuation source.

1.1.1 Automotive applications

The coefficient of drag (C_D) is a measure of aerodynamic drag on a body. In automobiles, reduction in C_D leads to improved fuel economy at high speed due to reduced engine load. The NHTSA standard requires an improvement in fuel economy of 13 mpg between 2015 and 2025 across all passenger vehicle segments¹. To meet this requirement, the automotive industry has worked to reduce the drag coefficient of an average new sedan from 0.32 to 0.25 (22%). The demand for higher energy efficiency in transportation is expected to increase in the future [22]. The factors contributing to aerodynamic drag are illustrated in Figure 1.1(a). Several geometric modifications to the exterior body of a vehicle have been proposed for drag reduction [24]. Implementing geometric changes as a rigid feature in the body is not practical at times due to limitations in other design areas such as vehicle weight, aesthetics, and regulatory compliance. Morphing structures enable multifunctional ability in body panels with a scope for weight reduction and improved aesthetics. The active-geometry solutions that are shown to have the most impact on aerodynamic performance are summarized in Figure 1.1(b). A few examples of morphing vehicle concepts are illustrated in Figure 1.2.

1.1.2 Aerospace applications

Rigid wings in an aircraft are designed for optimal fuel efficiency in specific operating conditions such as cruising at high altitude. Morphing the geometry of the wing is an attractive approach to optimize fuel efficiency over the entire range of flight. Wing geometry can be modified through stretching, flexure or a combination of both. Geometric parameters that can be tailored to achieve a morphing wing include span,

¹Statistics from the National Highway Traffic Safety Administration are based on a 2010 nominal baseline vehicle with gasoline engine, port fuel injection, fixed valve timing, 4-speed automatic transmission, and with $C_D = 0.32$. The estimated average fuel economy for 2015 is 41.5 mpg.

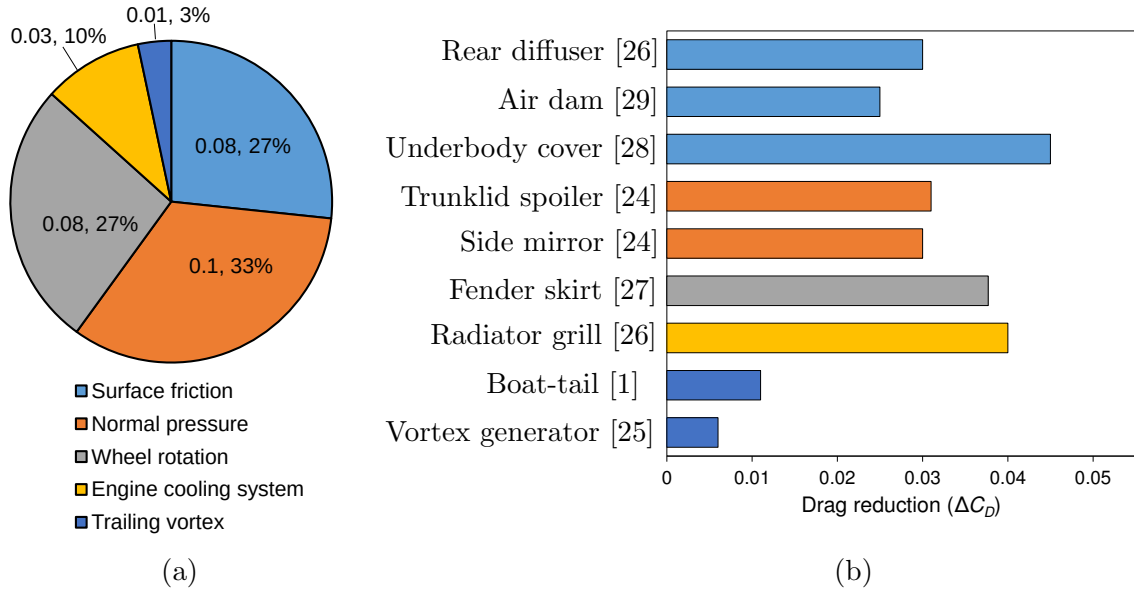


Figure 1.1: (a) Estimated contributions to the drag coefficient of a passenger car (data from Barnard [1]) and (b) potential for drag reduction through the use of morphing structures. The color-code used for morphing solutions in (b) correlates to the corresponding source of aerodynamic drag in (a).

sweep, airfoil camber, wing twist, and span-wise bending. Barbarino et al. [30] conducted an extensive review of morphing solutions for aircraft. The effectiveness of morphing each of the geometric parameters depends on the type of aircraft (commercial, military, etc.) and its specifications such as flight range, speed, agility, and payload. Morphing concepts demonstrating the important geometric modifications that benefit aircraft performance are shown in Figure 1.3.

1.1.3 Integration of morphing structures

The development of a morphing structure is an interdisciplinary process that includes research on kinematics, materials, actuation, and fabrication techniques (Figure 1.4). The kinematics of the morphing elements in a structure should be tailored to achieve a given deployed shape. Morphing elements include rigid and compliant links that provide geometric constraints and structural integrity. The mechanics of a morphing



(a) Morphing fender



(b) Boat-tail extension



(c) Active front spoiler



(d) Active flaps for engine thermal management

Figure 1.2: (a) Morphing fender on the BMW Next 100 Years concept [2], (b) boat-tail extension on the Mercedes Benz Intelligent Aerodynamic Automobile concept [3] (bottom), and (c) inflatable front spoiler on a Porsche 911 Turbo S [4], and (d) active flaps for engine thermal management on a Ferrari 458 Speciale [5].

element (e.g., stretching, bending) is coupled with its actuation mode (e.g., moment or in-plane force) and the structure's kinematics. Embedding the actuator in the morphing element enables compact and lightweight structures. Smart materials such as piezoelectrics, shape memory materials, and active polymers are candidates for embedded actuators. Actuator material selection and its configuration in the structure depend on the desired range of deformation. Novel fabrication techniques are required to realize morphing capabilities using various active and passive laminae. Functions such as multi-mode deformation, embedded actuation, and structural integrity can

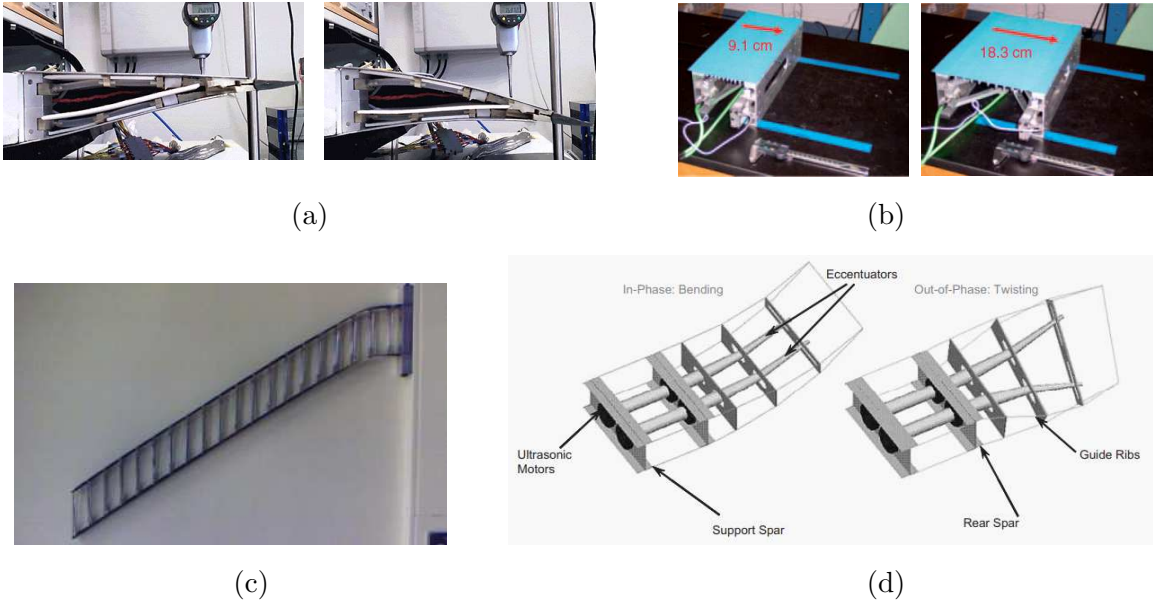


Figure 1.3: Concepts for morphing aircraft based on: (a) airfoil camber adjustment [6, 7], (b) wing span morphing [8], (c) variable wing sweep [9], and (d) span-wise bending (left) and wing-twist (right) [10].

be achieved simultaneously in a single structure using a laminated composite framework. Passive and active materials can be configured as laminae with varying degree of scale and complexity in laminated composites.

1.2 Laminated composites as morphing structures

Laminated composites have been extensively employed in the design of morphing structures. Laminae material selection is a function of the desired morphing mode. Anisotropic laminae are commonly used to tailor the composite's stiffness and hence deform it to a given shape. Laminated composites with active laminae (embedded actuation) developed for various morphing applications are summarized in Table 1.1. Designs relevant to this work are discussed in the following subsections:

Table 1.1: Survey of morphing laminated composites with embedded actuators.

Mechanics	Morphing composite	Salient feature	Actuation
Stretch	Fiber-reinforced elastomer [8, 11]; honeycomb with elastomeric infill [31]; elastomeric sheets with sandwiched: corrugated panel [32]; honeycomb [33]	Tailored stiffness	Passive
	Flexible fluidic matrix composite [34, 35]; pneumatic artificial muscle [36]	Controllable strain and stiffness [34]	Pressurized fluid
	Macro-fiber piezoceramic composite [37]	Controllable strain	Piezoelectric lamina
	Pure SMP [38]; SMP-reinforced elastomer [39]; shape memory polymer-alloy composite [40]	Shape fixity and recoverable strain	SMA [40]
Flexure	Thermally-prestressed FRP laminates with: sandwiched metallic core [41, 42]; fiber-prestress [13, 43]; initial curvature [44]	Curvature due to residual stress and tailored stiffness	Passive; SMA wires [45–47], thermal loading [44, 48]
	Fluidic muscles in a flexible medium [35, 49]; composite with intrinsic fluid channels [20, 50]; pressure-actuated cellular structure [51, 52]	Controllable curvature and stiffness [34]	Pressurized fluid
	Fiber-reinforced SMP [53]	Shape fixity and recoverable strain	SMP, external force
Fold	Bistable reeled composite [54, 55], deployable FRP boom hinge [56]	Tailored stiffness	Passive
	Fluid-filled Origami sheet [57] SMP hinge [15, 58]; active elastomer based on: embedded SMA wires[59]; dielectric and magneto-active behavior [16]	Controllable fold Active creases, self-folding	Pressurized fluid Variable modulus materials such as SMA, SMP, magnetorheological foam

SMP - shape memory polymer;
SMA - shape memory alloy;
FRP - fiber reinforced polymer

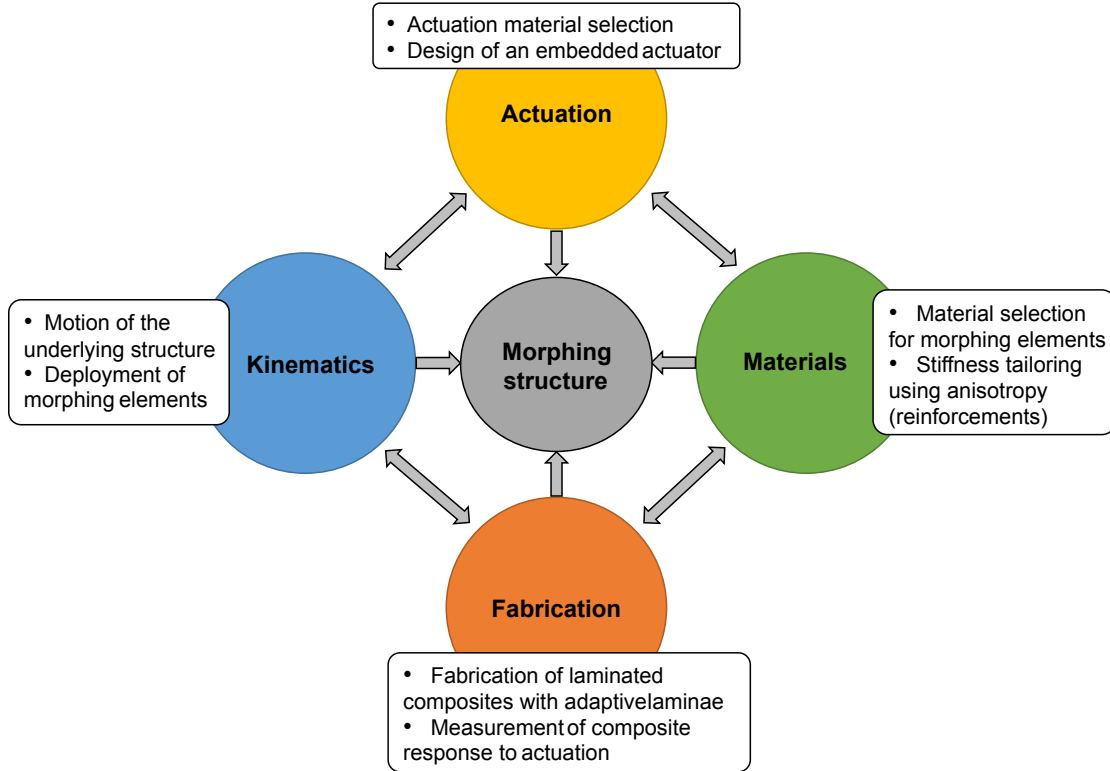


Figure 1.4: Research areas for morphing structures.

1.2.1 Stretchable composites

Stretchable materials are suitable for structures that undergo a change in surface area. Elastomers can serve as stretchable materials because of their high strain capability ($>100\%$). However, elastomers also exhibit a high Poisson's ratio (~ 0.5). Anisotropic stiffness can be incorporated into an elastomer through fiber-reinforcement; such elastomers are also known as elastomeric matrix composites (EMC) [8]. An EMC with unidirectional fibers in the transverse direction (90°) has been proposed as a flexible-skin panel in one dimension for the span morphing of an aircraft wing [8, 11] (Figure 1.5). Cylindrical pneumatic actuators that have EMC walls can perform unidirectional actuation when pressurized [60]. In these actuators, tailored stiffness

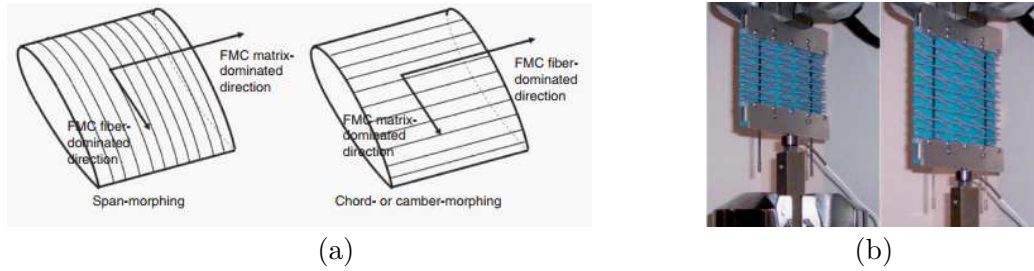


Figure 1.5: (a) Configuration of stretchable EMCs in a morphing airfoil [11] and (b) zero-Poisson's ratio EMC coupled with a support structure to achieve span morphing in an aircraft wing [8].

is achieved using the appropriate fiber-orientation. Murugan et al. [61] presented methods to optimize fiber distribution in an EMC to maximize the in-plane strain and out-of-plane stiffness.

Elastomeric matrix composites

An EMC is a fiber-reinforced elastomer whose material properties are influenced by the orientation and volume fraction of the embedded fibers. A 90° EMC strip has fibers oriented along its width (90°), making it stiff in-plane in this direction and stretchable in the orthogonal direction. Large strain (up to 100%) can be applied to a 90° EMC along the length while maintaining near-zero in-plane Poisson's ratio, provided the modulus of the fiber is much higher than that of the elastomer. Figure 1.6 illustrates the near-zero Poisson's ratio achieved by reinforcing the elastomer with fibers along the width. In contrast, the purely elastomeric region has high Poisson's ratio. Silicone rubber (poly-dimethylsiloxane) and polyurethanes are commonly used elastomeric materials since they offer good workability in the uncured state. The fabrication process for an EMC is described in Chapter 2.

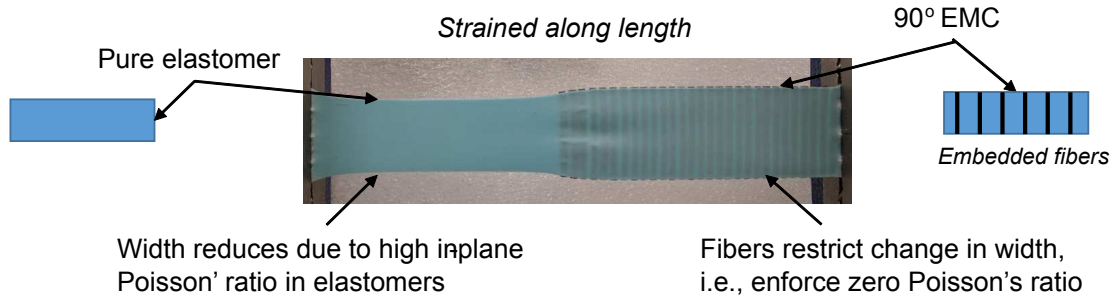


Figure 1.6: EMC strip partially reinforced with fibers along its width.

1.2.2 Flexible composites

Imparting residual stress is an attractive approach to create curvature in a passive laminated composite since it is an intrinsic feature and requires no external loads. Curvature in a fiber-reinforced polymeric (FRP) composite can be created by imparting residual stress in the matrix through high temperature curing [12, 41]. Initially-curved composites with a mechanically-prestressed matrix can serve as morphing elements when installed in a structure [62]. The anisotropy in FRP composites can be tailored using an asymmetric lay-up of fiber layers such that the composite exhibits multiple stable shapes at room temperature. The magnitude and orientation of the curvatures are influenced by the dimensions of the composite and the material properties of its laminae.

Bistability

Multistable composite laminates are candidates for morphing structures because they exhibit multiple stable shapes and require actuation only for shape transition. The basic requirement in the design of a multistable laminate is to incorporate residual stress into the structure such that multiple minima in strain energy are possible. The

methods available for inducing multistability in a panel can be classified into two categories, *viz.*, mechanical and thermal.

Residual stress can be mechanically induced in isotropic panels using plastic deformation techniques like plastic forming [63], and creating dimples [64] and corrugations [65]. Forcing an initial curvature in a stress-free plate or beam by designing the appropriate boundary conditions results in pseudo-bistable structures [44, 66]. Designs with mechanically-induced multistability are compatible with isotropic panels, but the resting shape is sensitive to the actuation force applied.

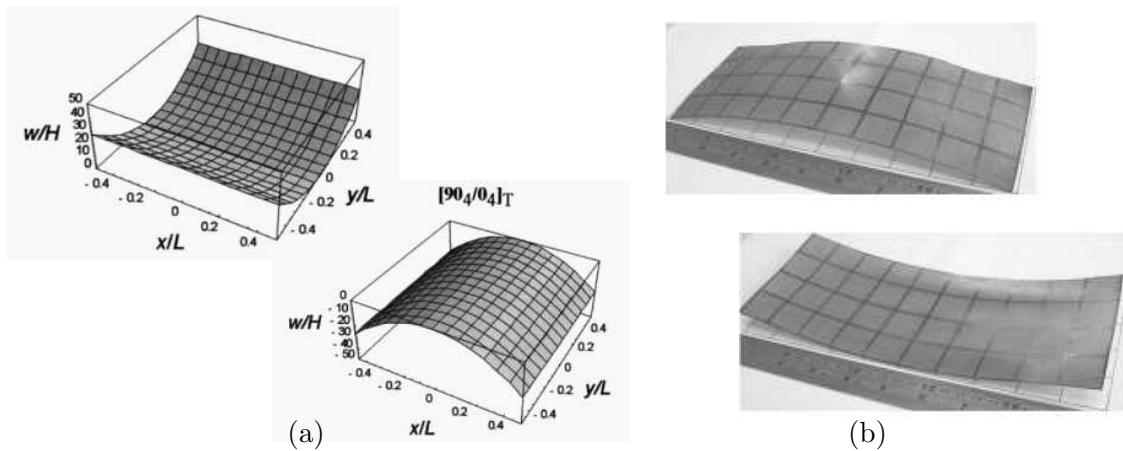


Figure 1.7: (a) The stable shapes of an asymmetric $0^\circ/90^\circ$ FRP laminate [12] and (b) the stable shapes of a prestressed buckled FRP laminate [13].

The most extensively studied multistable behavior involves asymmetric fiber-reinforced polymeric (FRP) laminates which are cured in a pre-impregnated form at high temperature and pressure. This processing ensures geometric precision and optimal strength [67]. Cooling the cured laminates to room temperature results in an intrinsic residual stress induced by a mismatch between the thermal contraction of the matrix and fiber. At room temperature, asymmetric FRP laminates can exhibit

two stable shapes that are curved in opposite directions [12] as shown in Figure 1.7(a). The magnitude of curvature is primarily influenced by the curing temperature and its direction is governed by the orientation of fiber layers [68–70]. The stable shapes of an asymmetric FRP laminate can be augmented by sandwiching an isotropic core [43]. Daynes et al. [13] selectively applied mechanical prestress to fiber layers to create a buckled region in the laminate in order to achieve symmetric curvatures (Figure 1.7(b)). Li et al. [42] developed hybrid symmetric laminates without the need for a buckled region by including two symmetric metallic layers whose thermal expansion coefficient is much higher than that of the fibers and the matrix. In laminates with thermally induced bistability, the presence of a continuous matrix material results in fully coupled shapes at room temperature, leaving little scope for tailoring individual shapes. By virtue of the thermo-mechanical process involved in fabricating FRP laminates, they are sensitive to operating temperature and humidity [71]. Application of matrix prestress in specific laminae allows combination with a wide variety of other laminae to create multifunctional composites.

1.2.3 Foldable composites

Origami-folding techniques allow large changes in surface area and as such, they could be a very efficient solution for morphing [72–75]. Origami design, involving the calculation of crease pattern and folding sequence, is well understood in surfaces with zero thickness [76]. However, implementation of these folding principles in morphing panels with finite thickness adds functional challenges related to limiting fold angle [77], structural integrity, and self-folding ability [78]. Materials tailored for a specific function, when laminated in certain configurations, exhibit synergistic multifunctional features that enable the seamless integration of folds in a structure.

In laminated composites with finite thickness, folding is typically realized as localized flexure about a crease line. A crease has finite width and its stiffness is typically much lower than that of its rigid adjacent faces; flexural stiffness of the crease is a function of its modulus and thickness. Other approaches for creating creases include the use of surrogate mechanisms such as compliant joints [79]. Boncheva et al. [80] developed foldable structures for self-assembly using corrugated elastomeric layers that are prestressed into a flat shape and laminated with metal layers in the region spanned by the faces of a fold. Actuation of an origami structure, i.e., folding and deployment, can be achieved either through the application of forces on the boundary or through the action of springs and actuators installed across the creases. Zirbel et al. [81] presented several methods for the deployment of an origami solar array, including the use of torsional springs, cables, and bistable strips in the structure.

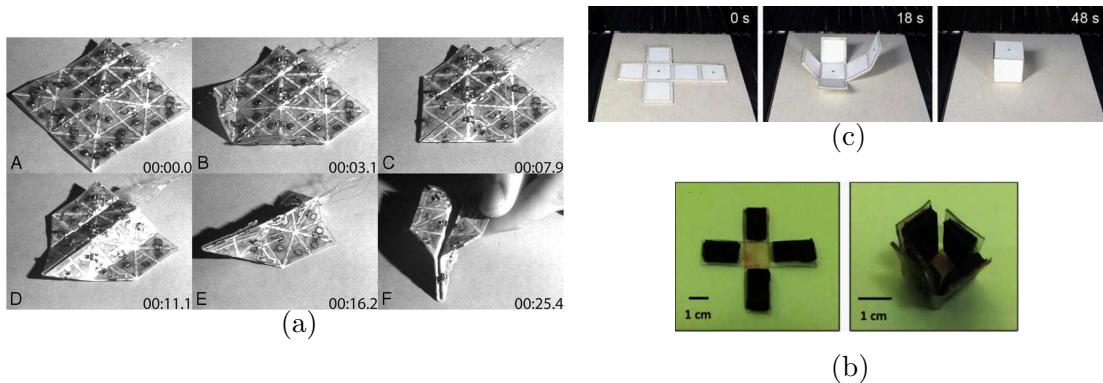


Figure 1.8: (a) Self-folding laminated composites with creases activated by (a) shape memory alloys [14], (b) shape memory polymers [15], and (c) magneto-active elastomers [16].

In laminated composites with no mechanical hinges, programming creases for self-folding is an attractive approach. One approach to self-folding is to apply a graded input to a homogenous active material to create local strain, thereby creating

a fold. Another approach involves a combination of passive materials and strain-generating smart materials in a unimorph or bimorph configuration to create creases. A multi-layer approach has added benefits due to the potential for incorporating additional functions in the composite. Shape memory alloys (SMA) and polymers (SMP) have been successfully employed as active laminae for folding sheets with pre-defined creases. Hawkes et al. [14] developed self-folding sheets using a network of bending actuators across pre-defined creases (Figure 1.8(a)). Peraza-Hernandez et al.[59] developed reprogrammable self-folding structures using shape memory alloy mesh/film as the actuator. The SMA across the crease is locally heated, thereby bending the faces towards each other to create a fold. While SMA-based designs enable two-way folding and reprogrammable crease formation, the stiffness of the hinge is limited by the bending stiffness of the SMA film.

Felton et al. [15] combined layers of SMP with pre-creased paper to form a bimorph actuator (Figure 1.8(b)). The SMP, when activated locally using resistive circuits, shrinks to create a fold through flexure. The folded shapes can be rigidized by cooling the SMP below its glass transition temperature. Ahmed et al. [16] demonstrated self-folding using dielectric and magneto-active elastomers that respond to electric and magnetic fields respectively (Figure 1.8(c)). von Lockette et al. [82] demonstrated a magnetic field-activated folding composite. The folding approaches mentioned thus far rely on the active material's configuration in the composite structure for crease formation. In this scenario, improving the functionality of the passive structure by means of an intrinsic restoring force can have some added benefits: an equilibrium geometry with a prescribed fold angle can be realized; higher global stiffness can be achieved for morphing applications; one-way actuation may be sufficient; and actuation power requirements can be minimized.

One of the major challenges that limit the maximum achievable fold angle in fiber-reinforced composites is the failure of fibers under large flexural deformation. Micromechanics studies have shown that under large flexure, in a stiff matrix such as epoxy, fibers break due to the shear stress applied by the matrix [83]. In a soft hyperelastic matrix, however, the low shear stress allows fibers to buckle out-of-plane without breaking [84, 85]. During folding, fiber buckling in a soft matrix occurs in laminae that are under compressive stress. Fiber buckling and failure in folded composites can be overcome by including pre-stretched laminae such that the innermost laminae in the fold are in tension.

1.2.4 Composite actuation

Embedded actuation is preferred for morphing panels due to the possibilities for reducing weight, size, and complexity. In most cases, the actuation material is either inserted into channels created in a passive composite [47] or is an active layer(s) in a laminated composite [37]. Passive composites can also be actuated through thermal loading [44, 48]. However, this method is mostly restricted to thermally-cured FRP laminates. Ideally, an actuation material embedded in a morphing composite should have a high power output per unit volume and operate the composite in a frequency range consistent with the structural dynamics.

Piezoelectric materials can generate an adequate amount of force [86] but require stroke amplification to achieve large deflection while maintaining system rigidity and frequency response. Schultz et al. [17] demonstrated actuation using electrically-activated piezoceramic (macro-fiber composites) laminae that are curved to conform to one of the stable shapes of a bistable composite (Figure 1.9(a)). While piezoelectric actuators enable a rapid snap-through to the second shape, they are ineffective for snap-back to the first shape due to their low strain capability (0.1 %). Kim et al.

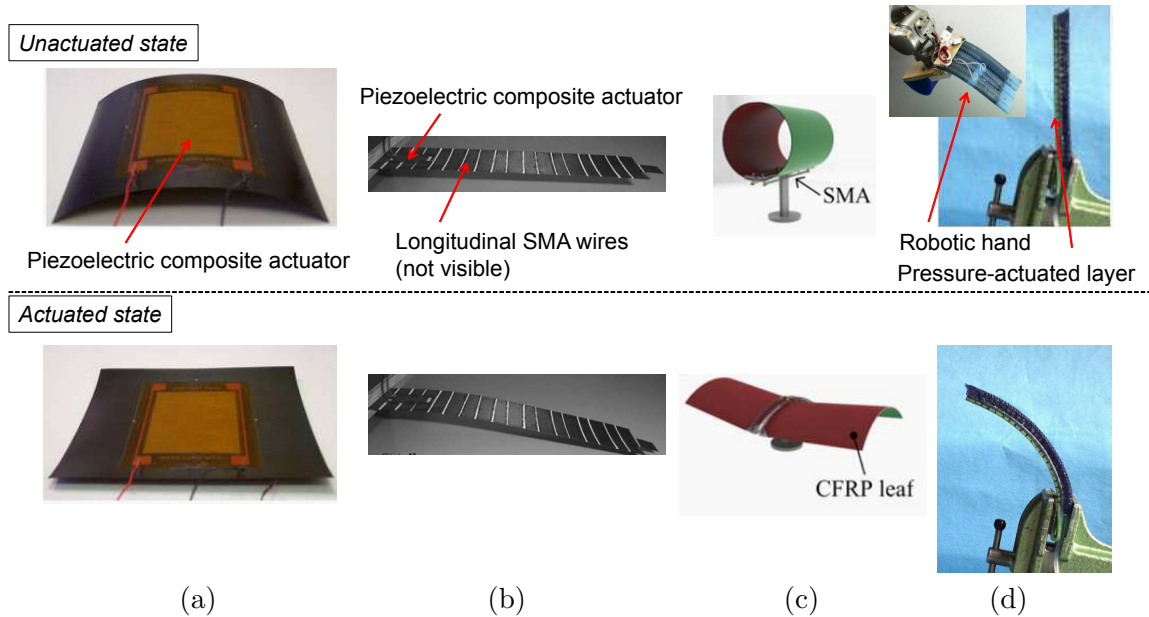


Figure 1.9: Laminated composites actuated by: (a) piezoelectric macro-fiber composites [17], (b) piezoelectric composites in one direction and shape memory alloy wires in the other [18], (c) shape memory alloy springs [19], and (d) pneumatic pressure [20].

[18] combined low strain piezoelectric laminae and high strain shape memory alloy wire (6 %) to achieve rapid snap-through and relatively slow snap-back respectively (Figure 1.9(b)).

Shape memory alloys can provide sufficient force and stroke although their application is often limited by their low operating frequency limit of about a few Hz. Continuous shape control is a challenge in the case of shape memory materials. However, in morphing structures that do not rely on the actuator’s frequency response, such as bistable composites, shape memory alloys are an attractive option for actuation. In bistable composites, the transition or snap-through between shapes occurs in milliseconds once the composite is nearly flattened by the actuator. Dano and Hyer [45] presented an analytical model for the actuation of bistable FRP laminates using SMAs. They modeled SMA wire in a tendon (straight) configuration and validated

the simulated shape transition using experiments. However, SMA actuation is more feasible for practical applications when used in a laminar configuration. Simoneau et al. [47] and Lacasse et al. [87] developed an FE model for laminated composites that are actuated using embedded SMAs; the relationship between the composites material and geometric properties, and actuation effort was studied for a monostable composite with one-way actuation. Kim et al. [19] developed a bio-inspired bistable robot actuated by SMA springs (Figure 1.9(c)). Prototypes of SMA-actuated bistable composites were designed and fabricated by Hufenbach et al. [46, 88]; SMA wires were installed so as to follow the curvature of the composite.

Hydraulic and pneumatic actuators can produce large force and stroke in the frequency range of the structure, but with a weight penalty. Lightweight and compact solutions for harnessing fluid power are offered by smart material-based miniature electrohydraulic actuators [89] that amplify the small stroke of materials with high frequency bandwidth such as piezoelectrics and magnetostrictives through fluid flow rectification. Fluid-based actuation systems are of interest in fields like soft robotics, bio-inspired structures, and morphing structures. Linear actuators such as pressurized artificial muscles are often used to create robotic mechanisms that can bend or fold [90, 91]. Flexible pneumatic bending actuators have been proposed by Deimel and Brock [20] for a soft-robotic hand that can grip objects (Figure 1.9(d)). Marchese et al. [50] developed a compliant structure with embedded fluid channels that is capable of replicating fish-like motion. Philen et al. [34, 60] and Feng et al. [49] developed variable-stiffness skins with embedded fluidic muscles that can be used for morphing aircraft wings. The basic design principle in these fluidic actuators is that linear actuation is achieved by restricting radial expansion through fiber-reinforcement while bending is achieved by bonding a constraining layer to a linear actuator.

1.3 Analytical modeling

The equilibrium shapes of an asymmetric bistable composite were modeled analytically by Hyer [92] using strain energy minimization. The composite was modeled as a laminated plate based on a Lagrangian strain formulation and classical laminate theory. Energy minimization was carried out using the Rayleigh-Ritz method and the resulting nonlinear equations were solved for the displacements of the composite. The energy-based analytical approach was further developed by Hamamoto and Hyer [93], and Dano and Hyer [94, 95]. Schlecht and Schulte [69] presented a comprehensive finite element study that was in agreement with Hyer’s analytical model. In all the analytical studies hitherto conducted, the in-plane strains and the out-of-plane displacement were approximated by quadratic polynomials containing only the terms with even power. Quadratic approximations hold for the calculation of stable shapes of the composite. However, features related to shape bifurcation such as snap-through loads [96] and geometric limits for bistability [97] cannot be accurately described using a second order strain model. Cantera et al. [98] presented a modified approach to simulate snap-through loads involving a second order strain model that includes non-uniform curvatures and uniform through-thickness normal strain. Pirrera et al. [99] showed that shape bifurcation effects can be modeled accurately using seventh order polynomials for displacements in the strain model. With ninth order displacement polynomials or higher, one can simulate the intermediate stages of snap-through but at the expense of computational cost. Lamacchia et al. [48] presented a computationally efficient semi-analytical high-order model that features decoupled stretching and bending contributions via a semi-inverse formulation of the constitutive equations. The choice of the displacement functions is influenced by the mode of deformation and the material and geometric properties of the composite’s laminae.

1.4 Research questions

The aim of this research is to develop a framework for multifunctional laminated composites that enable multiple modes of deformation such as stretching, flexure, and folding within a given morphing structure. The key research questions are as follows:

- **Is there a general laminated-composite framework for morphing structures? (chapter 2):** Adaptive laminated composites address morphing structure requirements such as low weight, compactness, and system-level compatibility. Existing morphing composites can undergo stretching, flexure, and folding but tend to lack mechanisms to achieve all these shape changes within the same structure. Further, there is need for a generic n -layered composite that enables multifunctionality through the combination of active and passive laminae.
- **Are there methods to incorporate local and global residual stress in select laminae? (chapter 2):** Functionality in existing curved composites is limited due to globally-applied residual stress. In thermally-cured bistable FRP laminates, for example, the two stable curvatures are a function of curing temperature. The performance of these composites is adversely affected by variations in operating temperature and humidity. Replacing thermal stress with mechanical stress provides the possibility to individually tailor the two stable shapes. Mechanically-prestressed composites fabricated at room temperature could exhibit hygrothermal invariance over a broad range of operating temperatures.
- **Can a prestressed layer be configured such that the resulting composite has a single dominant (cylindrical) curvature? (chapter 2):** The use of fiber-reinforced elastomers in existing morphing composite designs

is restricted to stretchable skins. The large anisotropic strain capability of these elastomers could be utilized for the application of mechanical prestress in laminated composites. An elastomer reinforced with unidirectional fibers exhibits zero in-plane Poisson's ratio when stretched in a direction orthogonal to the fiber orientation. Cylindrical composites could be designed by laminating such pre-stretched elastomers. The magnitude and direction of curvature can be tailored using the corresponding magnitude and orientation of the applied prestrain.

- **Are there mathematical models that describe the mechanics of stress-biased multifunctional composites? (chapters 2 - 7):** The inclusion of selectively-prestrained laminae yields a novel class of curved composite that has an irreversible non-zero stress state. The large strain applied to generate prestress is associated with geometric and material nonlinearities in the lamina's constitutive behavior. Further, a composite undergoing large deflection should be modeled using geometric nonlinearities in its strain model. Therefore, mathematical modeling is required to study the interaction between prestressed laminae and initially-stress-free passive and smart laminae.
- **How do the laminate stacking sequences compare with respect to the performance of a general multifunctional composite? (chapter 3):** The stacking sequence of the constraining, prestressed, and adaptive laminae is expected to influence the composite's response to actuation. For modeling purpose, an adaptive layer is considered to be a material with built-in pressurizable fluid channels. Intrinsic pressure actuation offers potential for generating high force and stroke. However, embedded configurations based on existing fluidic actuators are difficult to model and fabricate. Molding the fluid channels

into a reinforced flexible lamina rather than embedding them as individually-reinforced fluidic muscles in a flexible medium would result in a simpler model and fabrication process.

- **Can bistability be designed using prestress in selective laminae? (chapter 4, 5):** Containment of residual stress in select laminae opens the possibility to develop mechanically-prestressed bistable composites. Such composites, fabricated at room temperature, could address the drawbacks of thermally-cured bistable FRP laminates; the drawbacks are hygrothermal variations and the dependence of both shapes on the residual stress input, i.e., curing temperature. The functionality of bistable composites can be improved by dedicating a source of residual stress to each stable shape. In a composite with weakly coupled shapes, the design of each actuator is influenced only by residual stress associated with one curved shape.
- **What are the limits of bistability in mechanically-prestressed bistable composites? What are the actuation requirements associated with these composites? (chapter 6):** Residual stress generated through two sources of mechanical prestrain yields a domain of bistability that is different from that resulting from a single source (e.g., temperature in thermally-cured laminates). Therefore, a study exploring the limits of design parameters, such as the ratio of prestrains and the composite's aspect ratio, is required to determine the composite's bistability regime. High-order strain models are required to accurately model shape bifurcation phenomena such as bistability loss and snap-through actuation. Despite the availability of a wide variety of actuator designs, the relative performance of various actuation modes such as axial, transverse, and in-plane loading is not well understood. Also, actuation energy

is one performance metric for a bistable composite among others such as out-of-plane deformation (unactuated) and stiffness. Therefore, a sensitivity study of the composite's performance metrics is needed to guide material selection and geometric design.

- **How can folds be created in laminated composites? (chapter 7):** Folding in laminated composites is influenced by the thickness and material properties of the laminae. Challenges in tight folds such as buckling of the inner laminae and self-interference at the crease can be addressed by developing a curvature-based crease involving prestressed laminae; the vertex of the fold is at its center of curvature. Modeling the discontinuity in modulus or thickness between a crease and its adjacent faces may require a piece-wise approach in which each material domain is modeled as an individual composite with appropriate constraints. Through modeling, the limits of fold angle, as a function of composite size and material properties, can be determined.

1.5 Dissertation outline

The research questions outlined in the previous section are addressed in the following chapters. In Chapter 2, a multifunctional laminated composite framework is introduced and its modeling approach is described. For development purposes, prestressed laminated composites with intrinsic pressure-actuation are modeled and fabricated (Chapter 3). The interaction between active and passive laminae is discussed through a configuration study. Chapter 4 presents a mechanically-prestressed bistable composite that has weakly-coupled stable shapes. The composite is characterized using an experimentally-validated analytical model. A shape memory alloy-based push-pull actuation system is developed for bistable composite actuation (Chapter 5). Stability considerations and actuation requirements of mechanically-prestressed

bistable composites are studied in Chapter 6. The development of stress-biased composites for origami folding is discussed in Chapter 7. The modeling framework and experimental methods developed in Chapters 2 through 7 are implemented in an automotive application in Chapter 8. Through design, manufacturing, and testing, a lightweight, self-supported, and self-actuated morphing fender skirt prototype is developed. Shape memory alloy wires are embedded in a radially-configured prestressed composite ribbed structure to achieve morphing between flat and domed shapes. Key contributions, along with recommendations for future work, are summarized in Chapter 9.

Chapter 2

Multifunctional Laminated Composites

Overview

This chapter introduces a framework for multifunctional laminated composites. Elastomeric matrix composites (EMC) with zero-Poisson's ratio are presented as laminae that can be prestressed to create curvature in a composite structure. An analytical laminated-plate model, based on strain energy minimization, is presented to calculate composite curvature. The model includes material and geometric nonlinearities associated with large deformation in the composite and high strain in elastomers. A fabrication method for the incorporation of mechanical prestress is presented. Passive beam samples are fabricated to demonstrate stress-biased composites and to validate the model. The model presented in this chapter serves as a foundation for composite modeling in the chapters that follow.

2.1 Composite description

The laminae in the proposed n -layered composite are classified as constraining, prestressed, and adaptive (Figure 2.1). Each layer serves a specific purpose to enable the tailoring of shape and function of a morphing structure.

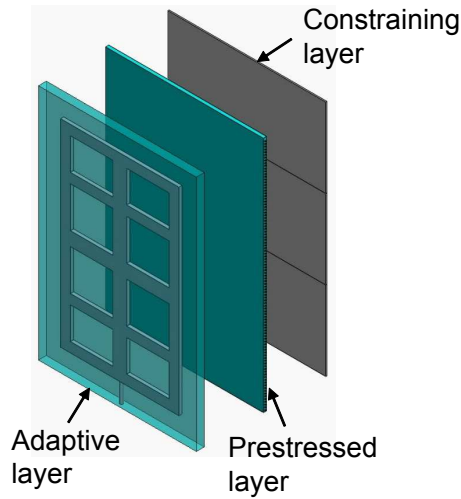


Figure 2.1: Types of laminae in a multifunctional composite. A constraining layer is flexible but not stretchable (e.g., metal sheet); the prestressed layer is capable of large strain and is laminated in a stretched condition (e.g., fiber-reinforced elastomer); an adaptive layer has a controllable stress state (e.g., smart materials and pressurized fluid channels). The adaptive layer is shown in the figure as a fluidic layer.

A constraining layer is flexible but not stretchable. It is typically a passive material that is very thin and has a high in-plane modulus relative to the other laminae. This layer augments the composite's out-of-plane deformation while suppressing in-plane strain. The constraining layer can be tailored to provide structural integrity in one direction and enable morphing in a different direction. Candidate materials include isotropic materials such as metals and various plastics, and anisotropic materials such as fiber-reinforced flexible composites. Pre-existing passive structures, such as body

panels in an automobile, can function as the constraining layer within a laminated composite framework.

A mechanically-prestressed layer is a source for internal restoring force in a laminated composite. When a prestressed layer and a constraining stress-free layer are laminated together, the resulting composite has a curved shape (2.2(a)). The prestress imbued in the composite is irreversible, thereby creating a spring-like composite that returns to its curved stable shape upon the release of applied forces. Further, prestress serves to eliminate undesired kinks and cracks in curved composites. In this work, the prestressed layer is developed using the elastomeric matrix composites introduced in Chapter 1. The prestressed and constraining layers can be configured to enable the composite to stretch, bend, and fold within the same material domain (Figure 2.2).

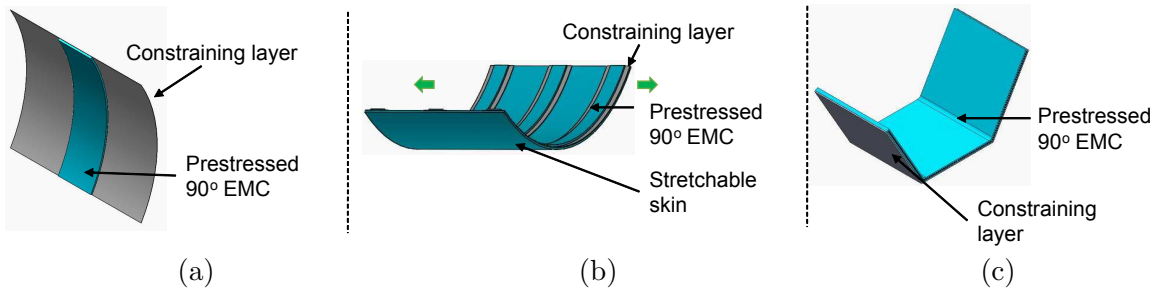


Figure 2.2: (a) Flexure, (b) stretching, and (c) folding in a prestressed composite.

An adaptive layer is capable of a controllable localized change in its stress-state; candidates for an adaptive layer are active materials like piezoelectrics, shape memory alloys, shape memory polymers, paraffin wax, magnetorheological foam, etc., or a passive material with an embedded active element like a pressurized fluid channel. Composite shape is controlled by modulating the properties of the adaptive layer.

The laminae presented thus far can be configured to achieve multiple functions such as structural integrity, built-in bistability, and built-in actuation (Figure 2.3). The stacking sequence of the laminae and domain boundary for each lamina are dictated by the composite's performance parameters such as actuation energy, stiffness, and morphing range.

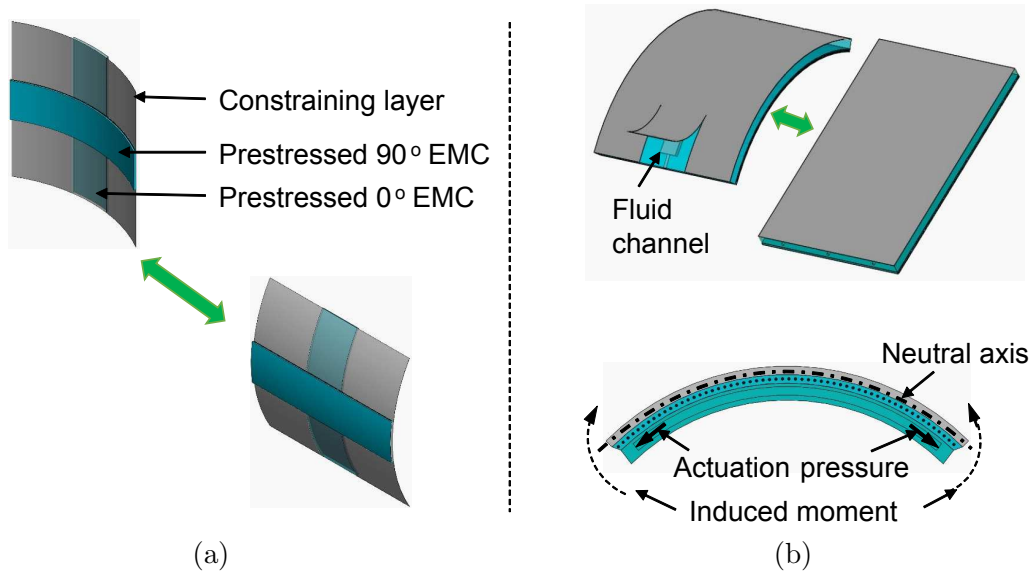


Figure 2.3: (a) Bistability in a prestressed composite and (b) morphing of the composite through the activation of a fluidic (adaptive) layer.

2.2 Research approach

In this work, a curved composite with an irreversible non-zero stress state resulting from the inclusion of selectively-prestressed laminae is presented for the first time. This new class of composite is characterized using computational modeling and experiments. Figure 2.4 summarizes the research approach. An analytical modeling framework is developed as a design tool for generic morphing structures based on

laminated composites. A variety of features including prestress, embedded actuation, bistability, and smart material integration are characterized using the analytical model. Fabrication methods are presented for these multifunctional composites and coupon-scale samples are built and tested to validate the model. The composite designs and computational tools developed at the coupon scale are applied towards an integrated design of a morphing fender skirt for an automobile. Laboratory demonstrators at the coupon and structural level indicate that the composite is suitable for mass-market products as it can be manufactured using inexpensive, commercially available materials and relatively simple processes. The broader impact of this research extends to applications in the fields of morphing aircraft [30, 86], soft robotics [100], and biomimetics [50].

2.3 Fabrication of mechanically-prestressed composites

The concept of stress-induced curvature is a building block in the design of the proposed laminated composites. Methods for the fabrication of prestressed curved composites are introduced in this section.

2.3.1 Elastomeric matrix composites

Based on the procedure described by Murray et al. [11] and Bubert et al. [8], a 90° EMC is fabricated by sandwiching two layers of unidirectional carbon fibers between two pre-cured silicone rubber sheets. Figure 2.5 shows the various stages in the fabrication process. Freshly mixed liquid silicone rubber, applied to the fibers and silicone rubber skins, cures to form an EMC with design specifications listed in Table 2.1. Rhodorsil 340/CA 45 mold making silicone rubber of durometer grade 45 (shore A) is used as the elastomeric matrix. The same rubber composition is used in the fabrication of all elastomeric elements in the multifunctional composites developed

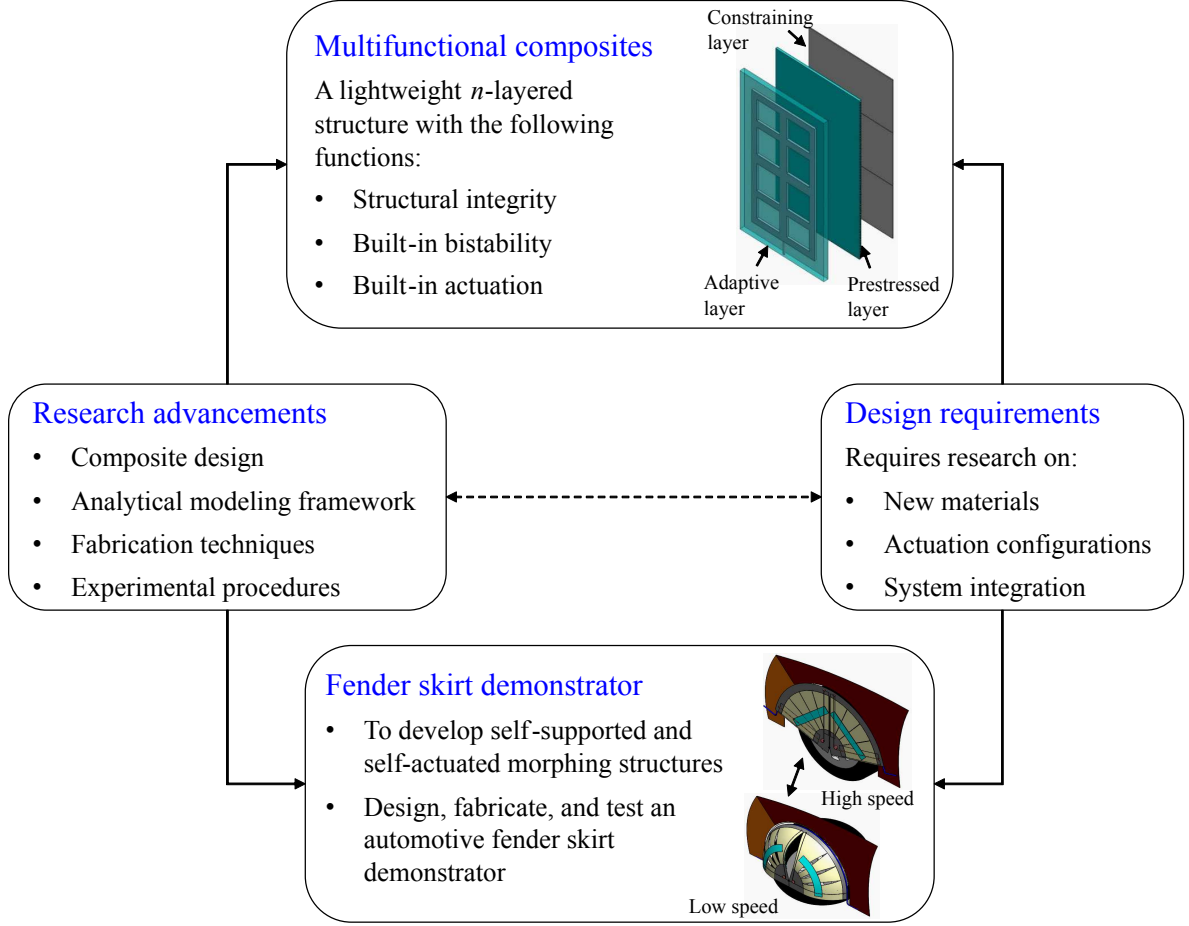


Figure 2.4: Research flowchart.

in this work. Unidirectional carbon fibers are prepared by removing transverse fibers from woven carbon fabric (Fiberglast Developments Corp., 3.1 kg/m^2). Through this process, discrete, closely spaced bundles of unidirectional fibers are obtained. The resulting EMC has zero in-plane Poisson's ratio.

Using the rule of mixtures, the longitudinal (E_L) and transverse (E_T) modulus of a fiber-reinforced composite can be calculated as:

$$E_L = E_f \nu_f + E_m(1 - \nu_f), \quad E_T = \frac{1}{\frac{\nu_f}{E_f} + \frac{1 - \nu_f}{E_m}}. \quad (2.1)$$

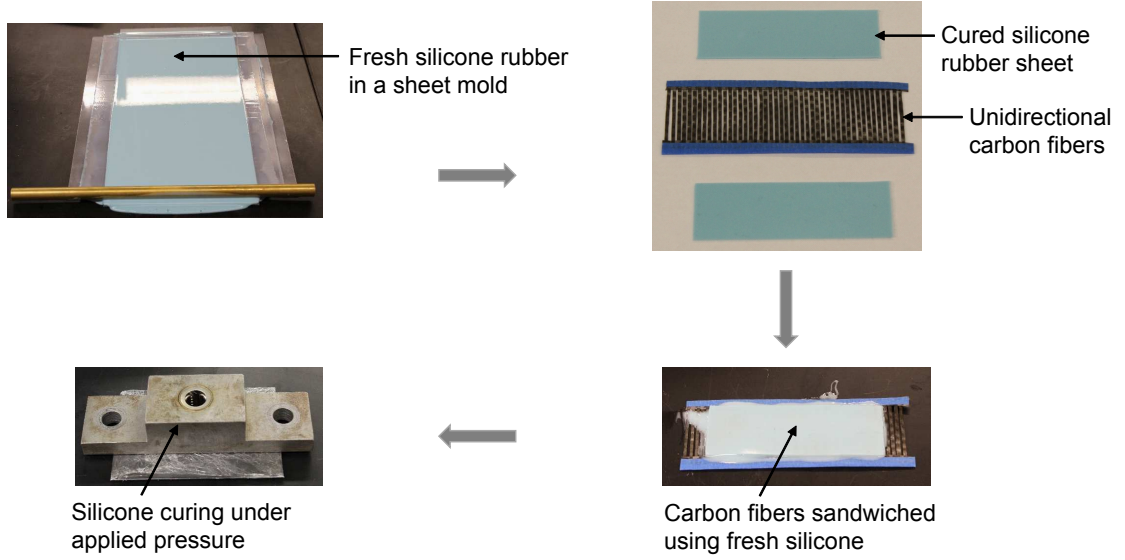


Figure 2.5: Fabrication process for an elastomeric matrix composite.

Table 2.1: Design details of the fabricated 90° EMC.

Material	Density (kg/m ³)	Volume fraction	Thickness (mm)
Silicone sheet	1340	0.83	0.76 (× 2)
Carbon fibers	53.53	0.17	0.50
Total	1113	1	2.02

For a fiber modulus of 200 GPa and an average matrix modulus of 1.2 MPa (up to 110% strain), the values of E_L and E_T are calculated to be 34 GPa and 1.45 MPa, respectively. A tensile test was conducted on the 90° EMC up to 110% strain with the response shown in Figure 2.6. It was found that the measured average transverse elastic modulus of 1.5 MPa agrees well with CLPT predictions in the tested strain range.

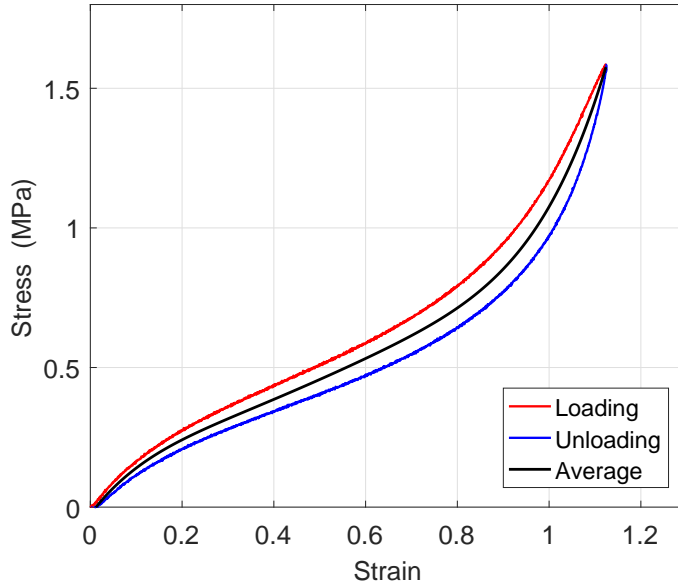


Figure 2.6: Stress-strain curve for a 90° EMC constructed as described in section 5.1, obtained from a uniaxial tensile test.

2.3.2 Composite lamination

Composite samples were fabricated with vinyl foam as a passive core material to demonstrate the use of prestress in the 90° EMC to produce curvature in the composite [101]. The selected vinyl foam is an isotropic material that is brittle in nature. However, its flexibility is improved when bonded to a 0° EMC. Figure 2.7 shows a schematic of the composite’s laminae.

The 90° EMC is stretched to a given strain and held between a pair of grips (Fig. 2.8(a)). The three layers are bonded to each other in the configuration shown in Fig. 2.7 using a silicone adhesive (DAP Auto-Marine 100% RTV silicone sealant) and the bond is allowed to cure at room temperature for 24 hours. Silicone-based adhesives are flexible and compatible with the chosen elastomeric skins and foam layer. After removal from the grips, the resulting composite beam comes to rest in a curved shape

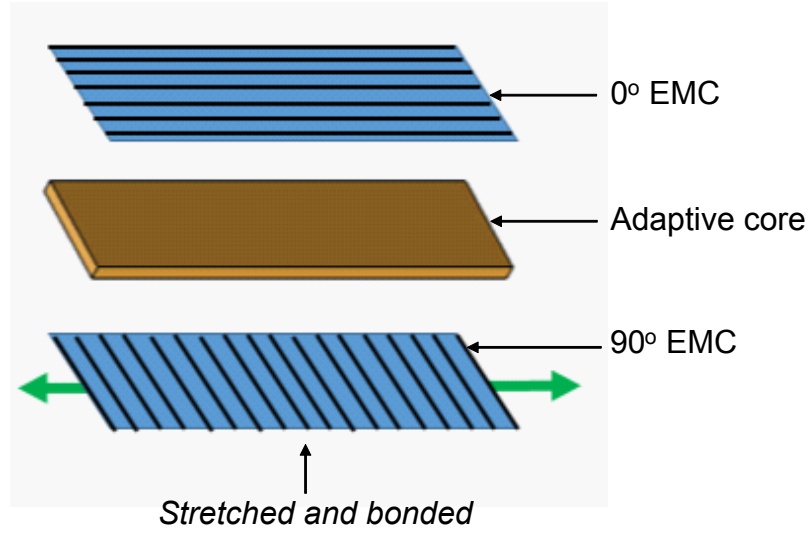
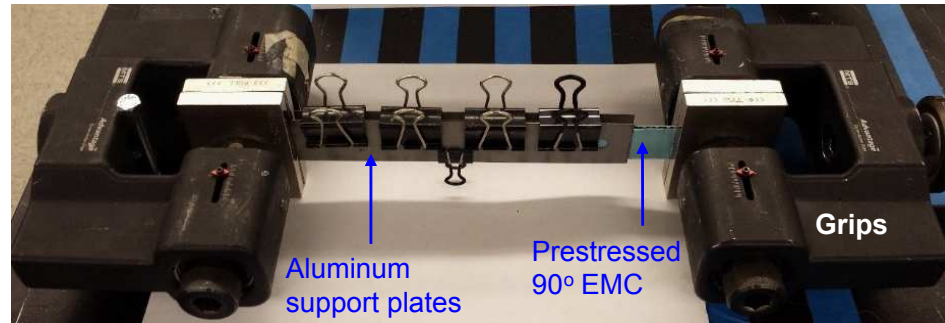


Figure 2.7: Schematic diagram showing the various layers of a prestressed composite.

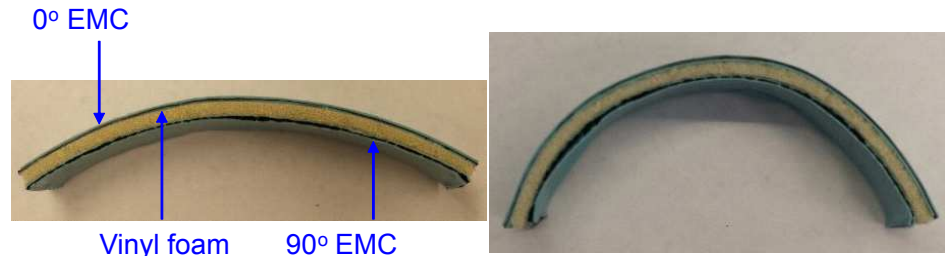
that is a function of the prestress imparted to the 90° EMC before bonding. The dimensions of the fabricated beam samples in Fig. 2.8(b) and Fig. 2.8(c) are $152.4 \times 25.4 \times 7.24$ (mm).

Table 2.2: Design parameters for composite beam samples fabricated with a vinyl foam core.

Parameter	90° EMC	Core	0° EMC	Composite
Density (kg/m^3)	1113	48	1113	646
Volume fraction	0.28	0.44	0.28	1
Thickness (mm)	2.02	3.175	2.02	7.215
E_x (MPa)	Nonlinear	30	170	-
E_y (MPa)	170	30	1.5	-
ν_{xy}	0	0.33	0	-
ν_{yx}	0	0.33	0	-



(a)



(b)

(c)

Figure 2.8: a) Setup for curing the prestressed composite, (b) final composite beam sample with a prestrain of 0.6 in the 90° EMC, and (c) final composite beam sample with a prestrain of 0.8 in the 90° EMC.

2.4 Analytical modeling framework

In this work, a mechanically-prestressed curved composite is modeled as a laminated plate. The large out-of-plane deflection of the composite is described using a Lagrangian strain formulation in conjunction with classical laminate theory. Composite strains or displacements are initially defined as unknown polynomial functions. The composite's strain energy is then computed and subsequently minimized to obtain a set of nonlinear equations that are a function of the coefficients of the displacement polynomials. These nonlinear equations are solved using the Rayleigh-Ritz method to calculate the shape of the composite.

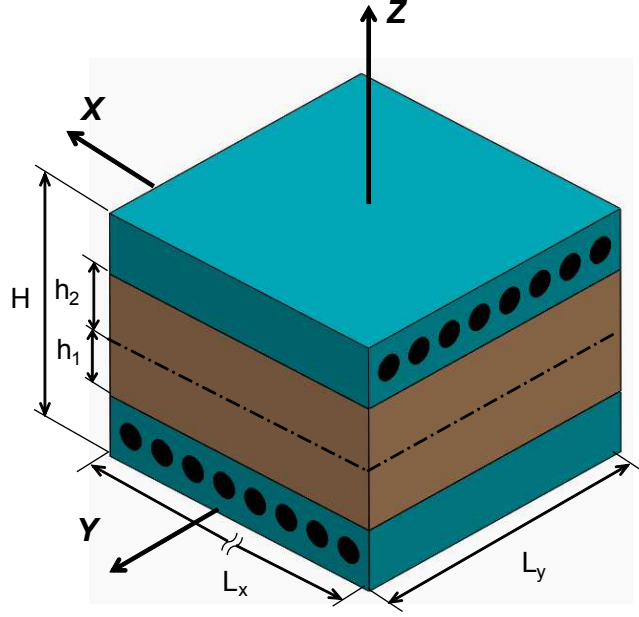


Figure 2.9: Geometry for the laminated composite model.

2.4.1 Strain model

Strain of the composite's mid-plane is described using unknown polynomial functions whose degree depends on the equilibrium shape. For example, in composites with thermally induced bistability where curvatures about two axes and out-of-plane twist are possible, third degree complete polynomials in x and y are used to describe axial strains (Hyer [92], Dano and Hyer [95]). The prestressed composite beam under consideration is expected to have a single curvature and hence simpler strain functions can be used (Figure 3.4). Longitudinal strain of the beam is described by a second-degree polynomial in x whereas lateral strain is described by a constant. A second degree polynomial in x is used to describe the out-of-plane displacement. Since the 90° EMC layer has a near-zero in-plane Poisson's ratio, curvature about the X axis is negligible. Further, it is assumed that the Poisson's ratio difference between layers has no effect on the curvature about the X axis. The stable shape is expected to

be curved about the Y axis. Per the assumptions of classical laminate plate theory, transverse shear (XZ , YZ) and transverse normal (ZZ) stresses are neglected. Based on von Karman's hypothesis [102], strains for composite materials with geometric nonlinearities, as applicable to this problem, are:

$$\epsilon_x = \frac{\partial u}{\partial x} + \frac{1}{2} \left(\frac{\partial w}{\partial x} \right)^2, \quad (2.2)$$

$$\epsilon_y = \frac{\partial v}{\partial y}, \quad (2.3)$$

$$\gamma_{xy} = \frac{\partial u}{\partial y} + \frac{\partial v}{\partial x} + \frac{\partial w}{\partial x} \frac{\partial w}{\partial y}. \quad (2.4)$$

Displacements u , v , and w of any point in the composite are written in terms of mid-plane displacements u_0 , v_0 , and w_0 in the X , Y , and Z directions, respectively, as:

$$u(x, y, z) = u_0(x) - z \frac{\partial w_0}{\partial x}, \quad (2.5)$$

$$v(x, y, z) = v_0(y), \quad (2.6)$$

$$w(x, y, z) = w_0(x). \quad (2.7)$$

Substitution of (2.5) - (2.7) into (2.2) - (2.4) yields the strain of an arbitrary plane z of the composite:

$$\epsilon_x = \frac{\partial u_0}{\partial x} + \frac{1}{2} \left(\frac{\partial w_0}{\partial x} \right)^2 - z \left(\frac{\partial^2 w_0}{\partial x^2} \right), \quad (2.8)$$

$$\epsilon_y = \frac{\partial v_0}{\partial y}, \quad (2.9)$$

$$\gamma_{xy} = \frac{\partial u_0}{\partial y} + \frac{\partial v_0}{\partial x} + \frac{\partial w}{\partial x} \frac{\partial w}{\partial y} - z \left(\frac{\partial^2 w_0}{\partial y \partial x} \right). \quad (2.10)$$

The expression for strain of an arbitrary plane z in the composite beam has the structure:

$$\epsilon_x = \epsilon_x^0 + z \kappa_x^0, \quad \epsilon_y = \epsilon_y^0, \quad \gamma_{xy} = \gamma_{xy}^0 + z \kappa_{xy}^0, \quad (2.11)$$

where ϵ_x^0 and ϵ_y^0 are the in-plane axial strains, γ_{xy}^0 is the in-plane shear strain, and κ_x^0 and κ_{xy}^0 are the curvature and twist, respectively, of the mid-plane. From (2.8) and (2.11), it can be seen that κ_x^0 is the second derivative of the displacement function w with respect to x . Assuming κ_x^0 to be constant throughout the mid-plane, a second degree polynomial in x is sufficient to approximate the mid-plane displacement w_0 in the Z direction:

$$w_0(x) = \frac{1}{2}ax^2, \quad (2.12)$$

where $-a$ represents the curvature (κ_x^0) about the Y axis [92, 95]. Strains in the X and Y directions are described using second and zero degree polynomials, respectively, as:

$$\epsilon_x^0 = c_0 + c_1x + c_2x^2 \quad \text{and} \quad \epsilon_y^0 = d_0. \quad (2.13)$$

By inspection of (2.10), γ_{xy} is zero because the polynomial functions that describe u, v , and w are independent of y, x , and y respectively. For small in-plane strains, the material behavior in the host structure can be considered to be linear. The 90° EMC, however, must be treated as a nonlinear hyperelastic layer to account for large prestrain.

2.4.2 Nonlinear response of an EMC

The response of a 90° EMC includes a 1-D geometric nonlinearity due to large axial strain and material nonlinearity due to hyperelastic behavior of the EMC. The focus in this model is the incorporation of the nonlinear mechanical behavior of an elastomer-like layer into the mechanics of a laminated composite that can be modeled using conventional laminate theories.

Peel and Jensen [103] developed a nonlinear model to describe the mechanics of fiber-reinforced elastomers. A similar method is employed to model the uniaxial response of a 90° EMC. The expression for strain of a single 90° EMC subject to a

large strain along X is written as:

$$e_x^{(90)} = \frac{\partial u}{\partial x} + \frac{1}{2} \left(\frac{\partial u}{\partial x} \right)^2, \quad (2.14)$$

where $e_x^{(90)}$ is the measured nonlinear strain and u is the constant axial displacement of the EMC under a tensile test. Since the Lagrangian strain formulation presented in (2.8) has a linear axial strain term, the nonlinear strain of the 90° EMC must be expressed in terms of linear strain so that it can be modeled as a layer in the composite. The expression for the corresponding linear axial strain is:

$$\varepsilon_x^{(90)} = \frac{\partial u}{\partial x}. \quad (2.15)$$

The nonlinear strain $e_x^{(90)}$ is expressed as a quadratic function of $\varepsilon_x^{(90)}$ by substituting (2.15) in (2.14). Solving for $\varepsilon_x^{(90)}$ and discarding the negative root (non-physical solution), one obtains $\varepsilon_x^{(90)}$ as:

$$\varepsilon_x^{(90)} = -1 + \sqrt{1 + 2e_x^{(90)}}. \quad (2.16)$$

Based on linear strain, stress is calculated incrementally as:

$$\sigma_x^{(90)}{}_i = \sigma_x^{(90)}{}_{i-1} + E_i(\varepsilon_x^{(90)}{}_i - \varepsilon_x^{(90)}{}_{i-1}), \quad (2.17)$$

where E_i is the point-wise modulus of a 90° EMC (local slope of its stress-strain curve). Peel and Jensen obtained the stress function by fitting experimental data to traditional hyperelastic models [103]. For computational efficiency, the stress function is described by a polynomial.. Since the prestressed EMC is subject to loading and unloading when the composite undergoes morphing, the average stress from the hysteretic stress-strain curve is considered as the nonlinear stress function of the 90° EMC (Figure 2.6). By the method of least squares, the reduced stress function is

described using a quartic polynomial as:

$$\sigma_x^{(90)} = -0.698\varepsilon_x^{(90)4} + 2.29\varepsilon_x^{(90)3} - 2.306\varepsilon_x^{(90)2} + 1.598\varepsilon_x^{(90)} \quad [\text{MPa}]. \quad (2.18)$$

For a 90° EMC, a polynomial stress function is preferred to traditional rubber models like the Ogden model [104] for the sake of computational efficiency. The stress function of an EMC depends on design parameters such as fiber volume fraction and orientation [61].

2.4.3 Potential Energy Function

The total potential energy (U_T) of the system can be expressed as the sum of strain energy in the host structure and residual strain energy $U^{(90)}$ in the 90° EMC. Neglecting the contribution of the silicone adhesive to the strain energy of the system, one obtains,

$$\begin{aligned} U_T = & \int_{-L_x/2}^{L_x/2} \int_{-L_y/2}^{L_y/2} \left\{ \int_{h_2}^{H/2} \left(\frac{1}{2}Q_{xx}^{(0)}\varepsilon_x^2 + Q_{xy}^{(0)}\varepsilon_x\varepsilon_y + \frac{1}{2}Q_{yy}^{(0)}\varepsilon_y^2 \right) dz \right. \\ & + \int_{-h_1}^{h_2} \left(\frac{1}{2}Q_{xx}^{(c)}\varepsilon_x^2 + Q_{xy}^{(c)}\varepsilon_x\varepsilon_y + \frac{1}{2}Q_{yy}^{(c)}\varepsilon_y^2 \right) dz \\ & \left. + \int_{-H/2}^{-h_1} U^{(90)} dz \right\} dy dx, \end{aligned} \quad (2.19)$$

where $\{Q_{xx}^{(0)}, Q_{xy}^{(0)}, \text{ and } Q_{yy}^{(0)}\}$ and $\{Q_{xx}^{(c)}, Q_{xy}^{(c)}, \text{ and } Q_{yy}^{(c)}\}$ are the plane stress-reduced stiffness parameters [102] for the 0° EMC and the core layer, respectively,

$$Q_{xx} = \frac{E_x}{1 - \nu_{xy}\nu_{yx}}, \quad Q_{xy} = \frac{\nu_{xy}E_y}{1 - \nu_{xy}\nu_{yx}}, \quad Q_{yy} = \frac{E_y}{1 - \nu_{xy}\nu_{yx}}, \quad (2.20)$$

where E and ν are the elastic modulus and Poisson's ratio of the layers of the host structure. $U^{(90)}$ is the nonlinear instantaneous strain energy term based on the area

under a nonlinear averaged stress-strain curve for the 90° EMC, which is calculated by integrating stress with respect to strain. The resulting strain energy in the prestressed 90° EMC as a function of strain of the composite and layer prestress (ϵ_0), is of the form:

$$U^{(90)} = f(\epsilon_0 - \epsilon_x, \epsilon_y). \quad (2.21)$$

2.4.4 Computation of composite shape

The equilibrium shape of the morphing composite is determined using the principle of virtual work. Exact differentials of the strain energy and work terms formed with respect to the unknown constants of strain polynomials are written as:

$$\sum_k \frac{\partial(U - W)}{\partial k} \delta k = 0, \quad k = \{a, c_0, c_1, c_2, d_0\}. \quad (2.22)$$

The partial derivatives of the strain energy and work terms are computed symbolically to obtain five nonlinear algebraic equations. These equations are solved numerically using the Newton-Raphson technique.

2.5 Model validation

The material parameters used in this model are obtained from tests carried out on the fabricated samples, as listed in Table 2.2. The longitudinal modulus (E_x) for the 0° EMC calculated using (2.1) cannot be used with this model since the fiber and the matrix do not undergo the same amount of in-plane strain. Since the modulus of silicone is much lower than that of carbon fiber, most of the in-plane strain in the 0° EMC occurs in the silicone matrix. The limiting value of stress in the 0° EMC is the shear strength of the fiber-matrix bond, which is used as the effective E_1 in the model. This E_x is measured in a uniaxial tensile test where a specimen is mounted in clamping grips and stretched until the fibers slip within the matrix. The average

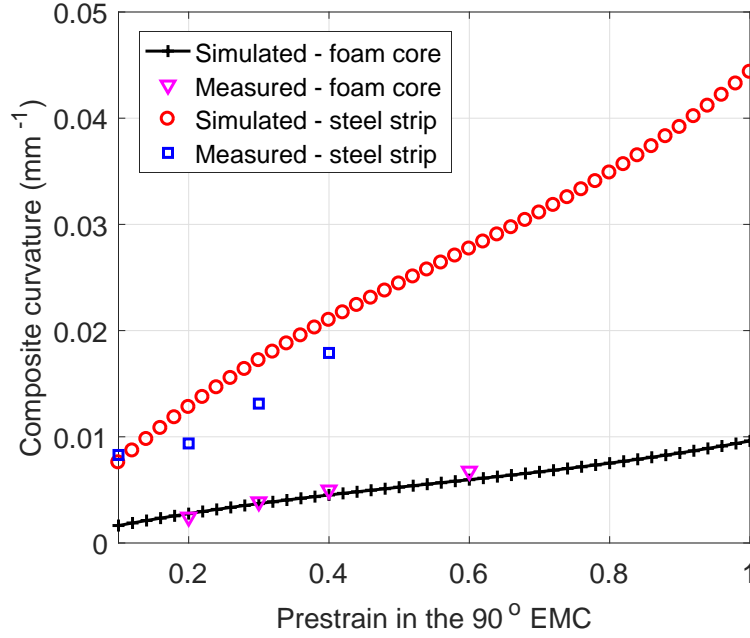


Figure 2.10: Curvature of the composite as a function of prestrain in the 90° EMC.

measured shear strength between the fibers and the matrix in the 0° EMC is 170 MPa. Curvature (κ) of the fabricated samples is assumed to be constant and is calculated using the measured values of sagitta (s) and chord length ($2L$) as:

$$\kappa = \frac{2s}{L^2 + s^2} \quad (2.23)$$

To validate the model, additional composite beam samples with a different layer configuration were fabricated. The 0° EMC is eliminated and a steel strip (4130 alloy) with a thickness of 0.127 mm and a modulus of 200 GPa is bonded to the prestressed 90° EMC. In this case, a prestrain of 0.4 in the 90° EMC results in an approximately semicircular equilibrium shape. Measured curvatures of composite samples fabricated with various values of prestrain correlate well with the simulations (Fig. 3.15).

The following chapters describe the development of various functions in a prestressed composite. Innovations in modeling and fabrication are presented relative to the methods presented in this chapter.

Chapter 3

Laminated Composites with Intrinsic Pressure Actuation and Prestress

Overview

This chapter presents a multifunctional laminated composite that exhibits a curved geometry due to intrinsic mechanical prestress and a change in curvature when fluid (liquid or gas) contained in one of its laminae is pressurized. The composite can be driven to any desired shape up to a flat limiting shape through modulation of pressure in its fluidic layer. An analytical model is developed to characterize the quasi-static response of such a composite to the applied fluid pressure for various laminate stacking sequences. A parametric study is also conducted to study the effects of the dimensions of the fluid channel and its spatial location. Composite beams are fabricated in the laminate configuration that requires the least actuation effort for a given change in curvature. Pneumatic pressure is applied to the composite in an open-loop setup and its response is measured using a motion capture system. The simulated response of the composite is in agreement with the measured response.

3.1 Introduction

This chapter presents a fluidic prestressed composite (FPC) in which fluid power is used to morph its shape from a curved to a flat geometry (Figure 3.1). Intermediate curvatures are obtained through the modulation of pressure of the contained fluid. A prestressed elastomeric layer, a fluidic layer, and a constraining layer constitute this composite. While the equilibrium shape of the proposed fluidic composite is created through the application of mechanical prestress to an elastomeric layer (Figure 3.1(a)), morphing action is accomplished through pressurization of the fluidic layer of the composite (Figure 3.1(b)).

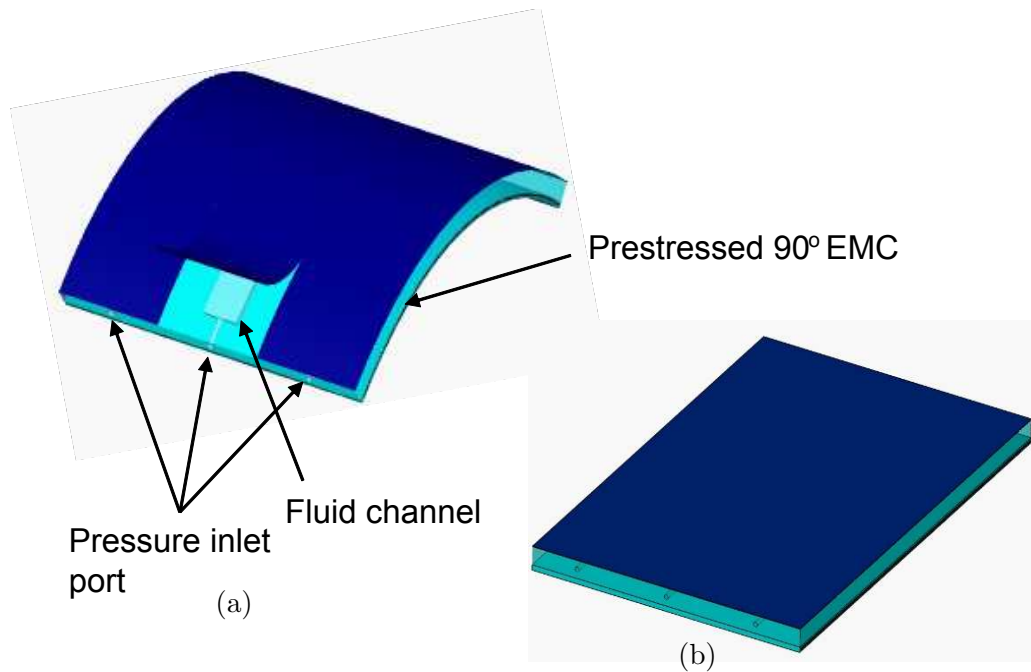


Figure 3.1: (a) Geometry of a fluidic prestressed composite in the unactuated state, (b) limiting actuated shape of the composite when the fluid channels are pressurized.

A fluidic prestressed composite is capable of controlled shape transition from a cylindrical shell to a flat plate through simultaneous actuation of parallel fluid channels that are embedded along the curve. The actuation mechanism is shown in Figure 3.2. The fluid channels are molded into a reinforced flexible lamina instead of being embedded as individually-reinforced fluidic muscles in a flexible medium as in [35, 60], and hence simplify the fabrication process. Further, molded fluid channels can have a non-cylindrical shape, leading to lower composite thickness for a given actuation effort. Complex curvatures in an FPC are possible through a vascular network of fluid channels. Through the design of individual channel dimensions, the maximum force exerted along the fluid path and hence the localized curvature can be regulated. Multiple pressure sources enable sequential actuation of various regions of the composite.

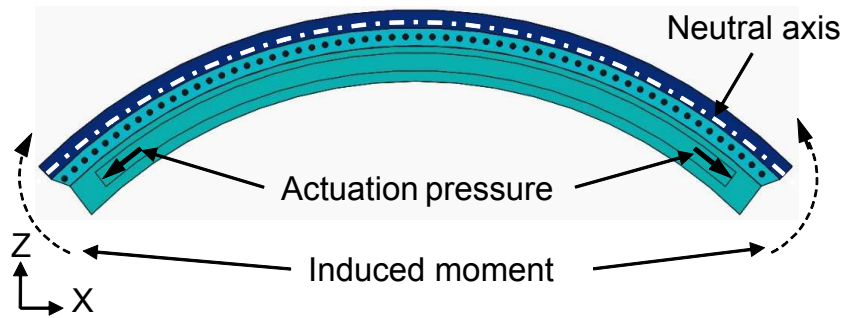


Figure 3.2: Moments induced on a composite in configuration 1 due to pressurization of the fluidic layer.

3.2 Fluidic Prestressed Composite

The laminae of a fluidic prestressed composite viz., prestressed elastomeric layer, fluidic layer, and constraining layer, are described in this section. Also, the possible

laminate configurations, each resulting in a unique response of the composite, are introduced.

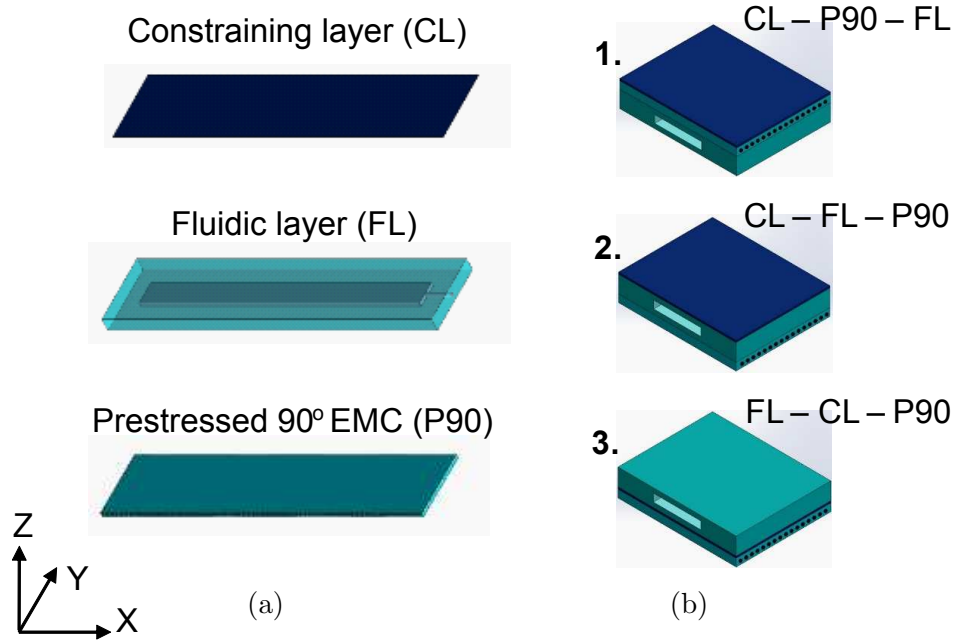


Figure 3.3: (a) Participating laminae and (b) possible laminate configurations of a fluidic prestressed composite.

3.2.1 Description of laminae

A fluidic layer consists of fluid channels molded into a continuous flexible medium (Figure 3.3(a)). Stiffness of the fluidic layer must be tailored such that the fluid channel expands only along its length when the composite is pressurized. For a channel with a rectangular cross-section, strain in the Y direction is negligible due to the constraint offered by the adjacent laminae, whereas strain in the Z direction is finite and is mitigated through reinforcement of the unbonded face of the fluidic layer with unidirectional fibers in the Y direction. The function of the constraining layer

is to translate the effect of internal forces acting along its length into curvature about the Y axis (Figure 3.2). A constraining layer can also be built into the fluidic layer through suitable fiber-reinforcement to create bending actuators for soft robotics and biomimetics applications [105]. A 90° EMC, discussed in Chapter 2, serves as the prestressed layer. The EMC has fibers oriented along the Y axis (90°), making it stiff in this direction and stretchable in the orthogonal direction (Figure 3.3(a)).

3.2.2 Laminate configurations

The laminae of a fluidic prestressed composite can be arranged in three unique configurations (Figure 3.3(b)). In configuration 1, a prestressed 90° EMC is sandwiched between a constraining layer and a fluidic layer. The equilibrium shape of the composite in the unactuated state is such that the fluidic layer is in compression. Sandwiching a fluidic layer between a constraining layer and a prestressed 90° EMC as in configuration 2 also results in a curved composite where the fluidic layer is in a compressed state. In both of these arrangements, the effect of actuation is to elongate the fluidic layer, thereby flattening the composite. The actuation effort for a given change in curvature of the composite is different between these two configurations (discussed in section 4). In configuration 3, a constraining layer is located between a fluidic layer and a prestressed 90° EMC, with the fluidic layer on the convex side of the composite at equilibrium. Pressurization of the fluid channel results in further bending of the composite. This configuration can also be realized without an EMC to generate curvature in an initially flat composite. To calculate the quasi-static curvature of an FPC, an analytical model is presented in the following section. While the proposed model is applicable to all three laminate configurations, configuration 1 is chosen for the purpose of presentation.

3.3 Analytical Model

Morphing of a fluidic prestressed composite is achieved with minimal actuation effort when the fluid channels are aligned with the direction of EMC prestrain. The simplest unit that describes this condition is a beam in which prestrain in the 90° EMC is applied in the X direction and the fluid channel is oriented along the X axis. (Figure 3.4). An FPC beam is expected to have a single equilibrium curvature in the unactuated state about the Y axis. Curvature about X is negligible since the EMC has no prestress in the Y direction (zero Poisson's ratio). Pressurization of the fluid channel does not affect the direction of composite curvature. The mechanics of an FPC beam are modeled analytically to study the influence of prestress in the 90° EMC and pressure in the fluid channel on its curvature. A nonlinear Lagrangian strain formulation is used in conjunction with classical laminate plate theory to quantify the strain energy of the composite. The strain model and the EMC's material response have been presented in Chapter 2. The fluidic and constraining layers are linearly elastic due to the relatively low in-plane strain associated with curvature in the composite. However, the 90° EMC has a nonlinear elastic behavior due to the large in-plane strain applied to it to create a prestressed condition. Actuation of the composite is modeled as the work done on the composite by the working fluid. A Rayleigh-Ritz method is employed to minimize the net energy of the composite and hence calculate the strain and curvature at quasi-static equilibrium.

3.3.1 Strain energy of the composite

The total potential energy (U) of the system can be expressed as the sum of the strain energy of the initially-stress-free host structure comprising of the fluidic ($U_{(FL)}$) and constraining layers ($U_{(CL)}$), and the residual strain energy ($U_{(P90)}$) of the 90° EMC

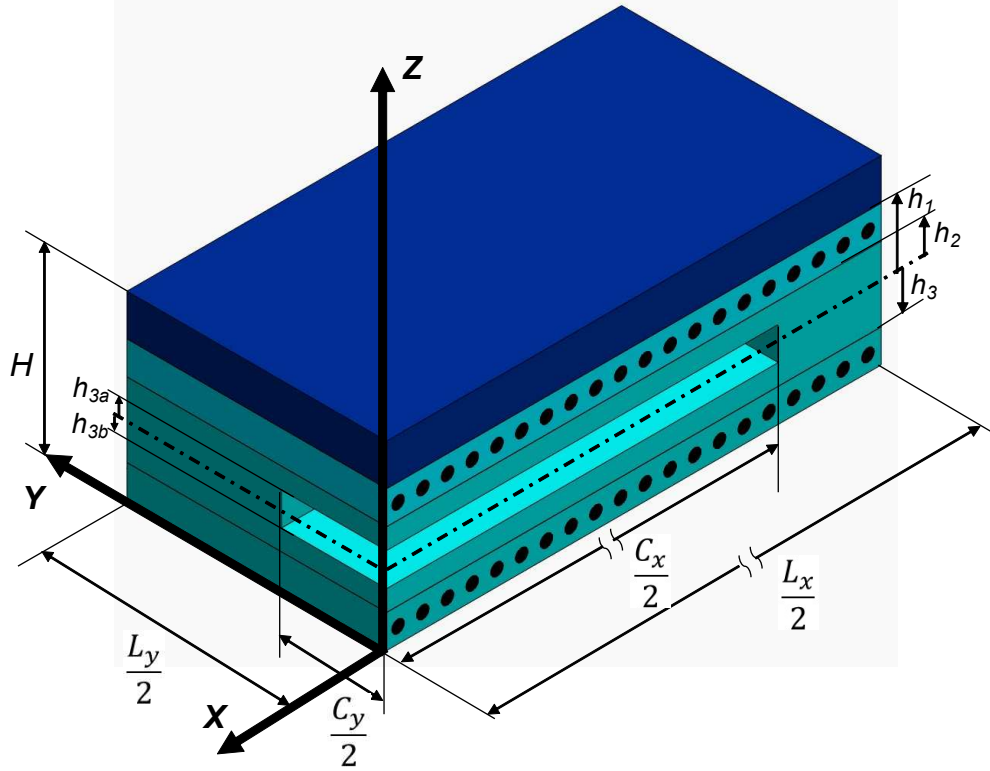


Figure 3.4: Geometry for a beam model of a fluidic prestressed composite illustrated in configuration 1. The bottom face of the fluidic layer is reinforced with unidirectional fibers oriented along the Y direction.

as:

$$U = U_{(CL)} + U_{(FL)} + U_{(P90)}. \quad (3.1)$$

In practice, the bottom face of the fluidic layer in cases 1 and 3 (Figure 3.3(b)) is reinforced with fibers in the 90° orientation to mitigate expansion in the thickness direction. In case 2, the face of the fluidic layer that is bonded to the prestressed EMC is reinforced with 90° fibers. This step is equivalent to the addition of a stress-free 90° EMC to the fluidic layer. The contribution of strain energy of the laminate adhesive to the total strain energy is assumed to be negligible. The total strain energy of the

linear elastic layers can be written as:

$$U_{(CL)} + U_{(FL)} = \int_{x_l}^{x_u} \int_{y_l}^{y_u} \int_{z_l}^{z_u} \left(\frac{1}{2} Q_{11} \epsilon_x^2 + Q_{12} \epsilon_x \epsilon_y + \frac{1}{2} Q_{22} \epsilon_y^2 \right) dz dy dx, \quad (3.2)$$

where $\{Q_{11}, Q_{12}, \text{ and } Q_{22}\}$ are the plane stress-reduced stiffness parameters [102] defined as:

$$Q_{11} = \frac{E_1}{1 - \nu_{12}\nu_{21}}, \quad Q_{12} = \frac{\nu_{12}E_2}{1 - \nu_{12}\nu_{21}}, \quad Q_{22} = \frac{E_2}{1 - \nu_{12}\nu_{21}}, \quad (3.3)$$

and E and ν are the elastic modulus and Poisson's ratio, respectively. The limits of integration that must be applied for each layer in the host structure are listed in Table 3.1.

Table 3.1: Limits of integration for the computation of strain energy of the linear elastic layers of the composite.

Coordinate	Constraining layer	Prestressed 90° EMC	Fluidic layer	Fluid channel	90° fiber-reinforcement in fluidic layer
x	$(-L_x/2, L_x/2)$	$(-L_x/2, L_x/2)$	$(-L_x/2, L_x/2)$	$(-C_x/2, C_x/2)$	$(-L_x/2, L_x/2)$
y	$(-L_y/2, L_y/2)$	$(-L_y/2, L_y/2)$	$(-L_y/2, L_y/2)$	$(-C_y/2, C_y/2)$	$(-L_y/2, L_y/2)$
z	$(h_1, H/2)$	(h_2, h_1)	$(-h_3, h_2)$	$(-h_{3b}, h_{3a})$	$(-H/2, -h_3)$
Strain energy	$U_{(CL)}$	$U_{(P90)}$	$U_{(layer)}$	$U_{(channel)}$	$U_{(reinforcement)}$
			$U_{(FL)} = U_{(layer)} - U_{(channel)} + U_{(reinforcement)}$		

The strain energy of a prestressed 90° EMC is expressed as:

$$U_{(P90)} = \int_{x_l}^{x_u} \int_{y_l}^{y_u} \int_{z_l}^{z_u} \left(U_{(P90)}^x + \frac{1}{2} Q_{22} \epsilon_y^2 \right) dz dy dx \quad (3.4)$$

where $U_{(P90)}^x$ is the strain energy in the X direction, calculated as the area under a nonlinear averaged stress-strain curve obtained from a uniaxial tensile test (Figure 2.6). The resulting strain energy in the prestressed 90° EMC as a function of strain

of the composite and layer prestress (ϵ_0), is of the form:

$$U_{(P90)} = f(\epsilon_0 - \epsilon_x, \epsilon_y). \quad (3.5)$$

3.3.2 Work done by applied fluid pressure

Pressurization of a working fluid in the fluidic layer results in actuation of the composite. The work done by a fluid on the composite can be expressed as a product of the operating pressure and the change in volume of the fluid channel due to the applied pressure. While the initial volume (V_i) of the fluid channel corresponds to the volume at static equilibrium, the final volume (V_f) is a function of the unknown strain functions in x and y . Since the constant initial volume vanishes in the energy minimization step, it is not a critical element in the computation of composite geometry. However, it is required in the calculation of actuation power. In this model, it is assumed that volume change occurs in-plane; thickness of the composite remains constant. Assuming that the working fluid is an ideal gas operating in adiabatic conditions, work done on the composite [106] by pneumatic actuation can be expressed as:

$$W = \frac{P_i V_i - P_f V_f}{\gamma - 1}, \quad (3.6)$$

where $\gamma = 1.4$ is the adiabatic coefficient of air. The volume (V_f) of the fluid channel in the actuated state can be expressed in terms of the unknown strain polynomials as:

$$V_f = \int_V (1 + \epsilon_x)(1 + \epsilon_y) dV, \quad (3.7)$$

$$= \int_V (1 + c_0 + c_1 x + c_2 x^2 + a z)(1 + d_0) dV. \quad (3.8)$$

3.3.3 Computation of composite shape

The equilibrium shape of the morphing composite is determined using the principle of virtual work. Exact differentials of the strain energy and work terms formed with respect to the unknown constants of strain polynomials are written as:

$$\sum_k \frac{\partial(U - W)}{\partial k} \delta k = 0, \quad k = \{a, c_0, c_1, c_2, d_0\}. \quad (3.9)$$

The partial derivatives of the strain energy and work terms are computed symbolically to obtain five nonlinear algebraic equations. These equations are solved numerically using the Newton-Raphson technique (or similar). The model presented thus far provides a means to design the curvature of an FPC in its unactuated state and the required actuation pressure range to obtain a flat limiting shape. The following section is a study of the response of an FPC in each of its laminate configurations.

3.4 Model-Based Study of Composite Response

The effect of laminate stacking sequence on the quasi-static response of an FPC is investigated using the analytical model. The three layer arrangements in Figure 3.3(b) are considered with the dimensions shown in Figure 3.5 and the material properties listed in Table 3.2. The configuration that results in the least actuation effort for a given change in curvature is identified. The influence of design parameters such as the size and location of the fluid channel on composite response is examined through a parametric study.

3.4.1 Configuration study

Figures 3.6 - 3.8 show the magnitude of curvature ($|\kappa_x^0|$) of an FPC in each of the possible laminate configurations calculated as a function of actuation pressure for

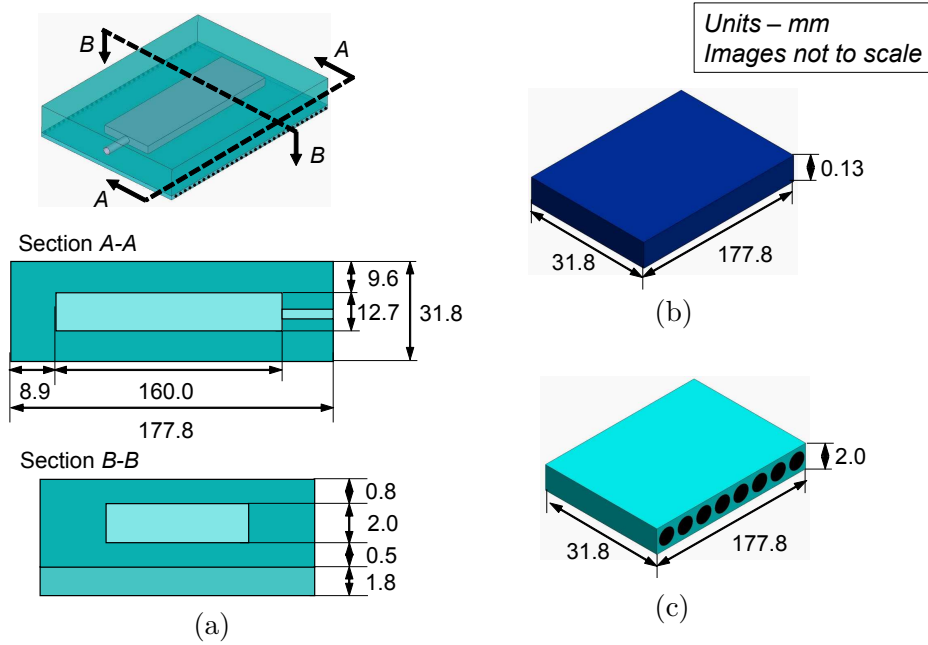


Figure 3.5: Dimensions of the laminae of a fluidic prestressed composite: (a) fluidic layer, (b) constraining layer, and (c) prestressed 90° EMC.

Table 3.2: Measured material properties of the laminae of a fluidic prestressed composite.

Lamina	E_x (MPa)	E_y (MPa)	ν_x	ν_y
Constraining layer (1095 spring steel)	200,000	200,000	0.28	0.28
Fluidic layer - pure elastomer	1.2	1.2	0.48	0.48
Fluidic layer - reinforced elastomer	1.5	170	0	0
Prestressed 90° EMC	Nonlinear	170	0	0

EMC prestrain ranging from 0.3 to 0.6. In all cases, a higher EMC prestrain yields a higher composite curvature about the Y axis for a given actuation pressure. In the unactuated state, curvature is the least in case 1 and is maximum in case 2 for a given EMC prestrain. A direct coupling between a constraining layer and an EMC enables the EMC's strain energy to be manifest primarily as a deflection (w_0) in the composite in the Z direction; the in-plane component ($\partial u/\partial x$ in (2.2)) of ϵ_x in the constraining layer is negligible. Curvature is lowest in case 1 since a part of the

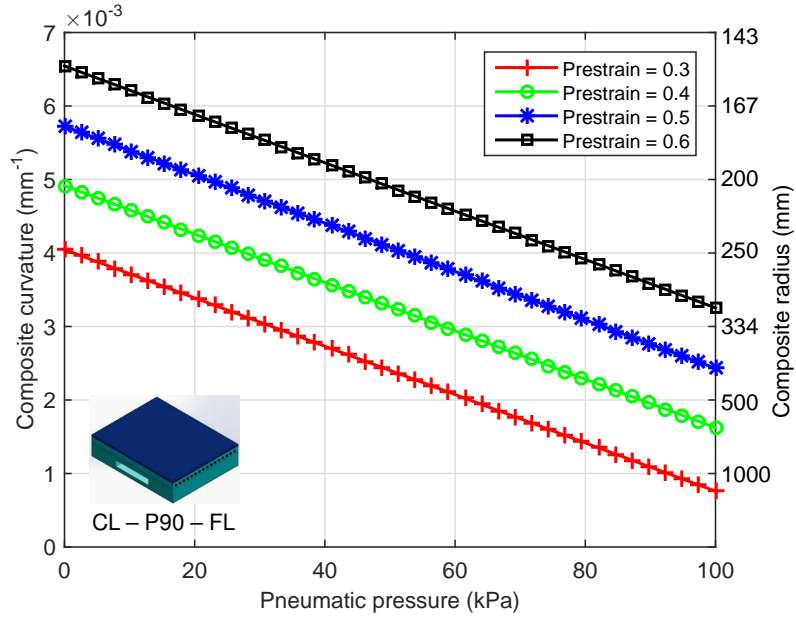


Figure 3.6: Modeled curvature vs. actuation pressure of a fluidic prestressed composite in configuration 1.

EMC's strain energy is lost to in-plane compression of the fluidic layer. Curvature in case 3 is higher than in case 1 since the mechanics of the constraining layer are minimally affected by the fluidic layer bonded to it. In case 2, composite deflection is augmented by the in-plane compressive strain ($\partial u/\partial x$) in the sandwiched fluidic layer, resulting in the highest curvature among the three cases.

Pressurization of the fluid channel results in a reduction in composite curvature in cases 1 and 2. Recognizing that the curvature corresponding to a flat shape is zero, it is apparent that the actuation pressure required to nearly flatten the composite is lower in case 1. The difference in response is attributed to the larger in-plane compressive strain in the fluidic layer in case 2. In case 3, actuation of the composite leads to an increase in its curvature. Deflection of the composite in the Z direction is accompanied by an in-plane tensile strain in the fluidic layer.

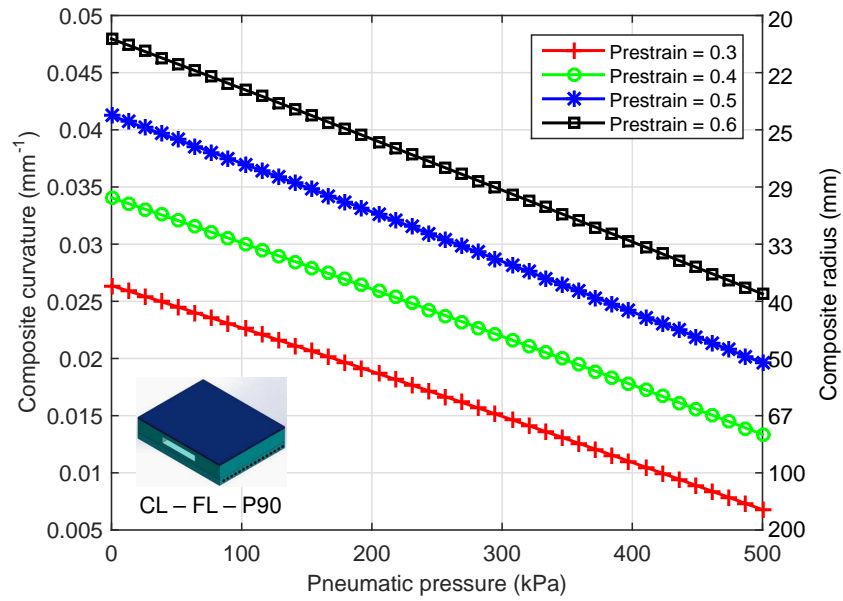


Figure 3.7: Modeled curvature vs. actuation pressure of a fluidic prestressed composite in configuration 2.

For minimal actuation effort at a given EMC prestrain, an FPC must have a higher curvature in the unactuated state with a laminate arrangement as in case 1 and must be actuated to produce a lower curvature. At lower values of EMC prestrain, the actuation pressure required to flatten the composite is lower. However, the trade-off in lowering the EMC prestrain is a loss in morphing ability.

3.4.2 Parametric study

The parameters influencing actuation effort such as thickness, width, and location of the fluid channel are examined in this section. An FPC with laminae arranged as shown in case 1 (Figure 3.3(b)) is used in this study. Prestrain in the 90° EMC is maintained constant at 0.5.

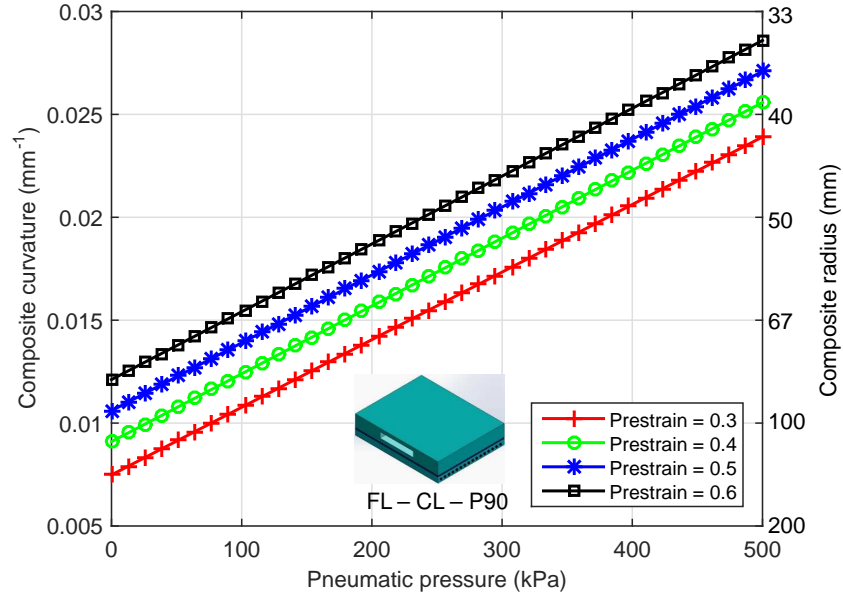


Figure 3.8: Modeled curvature vs. actuation pressure of a fluidic prestressed composite in configuration 3.

The relevant design parameters are defined as:

$$\phi = \frac{C_y}{L_y}, \quad \chi = \frac{h_{3a} + h_{3b}}{h_2 + h_3}, \quad \text{and} \quad \psi = \frac{h_2 - h_{3a}}{h_{3a} + h_{3b}}, \quad (3.10)$$

where ϕ , χ , and ψ are the non-dimensional width, thickness, and proximity (to the fluidic layer-EMC interface) of the fluid channel.

The response of an FPC for various values of ϕ is plotted in Figure 3.9. The values of χ and ψ are maintained at 0.6 and 0.4 respectively. Based on simulations conducted in an actuation pressure range of 0-50 kPa, it is observed that the magnitude of the slope of the response curve increases with an increase in ϕ . This phenomenon is a consequence of the increase in cross-sectional area of the fluid channel and hence the available force along the channel for a given actuation pressure. The increase in curvature in the unactuated state at higher ϕ is due to a reduction of material in the fluidic layer.

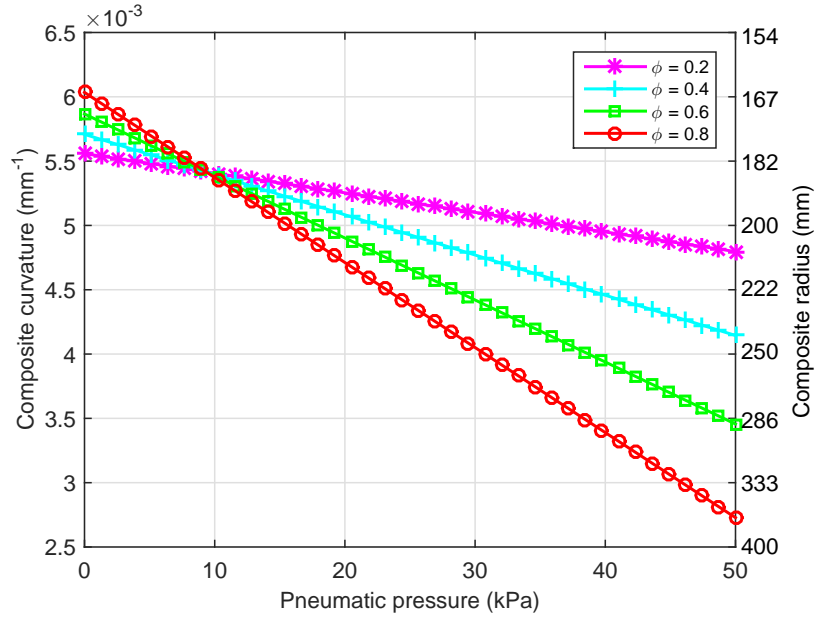


Figure 3.9: Response of a fluidic prestressed composite on the non-dimensional width (ϕ) for $\chi = 0.6$ and $\psi = 0.4$.

The effect of the non-dimensional fluid channel thickness (χ) on composite response is studied at a constant value of ϕ and ψ of 0.4 (Figure 3.10). An increase in χ enables a reduction in the actuation pressure needed to obtain a given curvature, while increasing the curvature in the unactuated state. Such behavior is explained in the same manner as done in the study on ϕ . The overall effect of increasing ϕ or χ is an enhanced morphing envelope at a lower actuation pressure.

The dimensions of the fluid channel cross-section are maintained constant ($\phi = 0.4, \chi = 0.6$) and the effect of its proximity to the prestressed EMC (ψ) is simulated (Figure 3.11). The physical equivalent of lowering ψ is a shift in the fluidic layer material towards the bottom face. The effect of this material shift is an increase in compressive stress in the fluidic layer and hence a decrease in composite curvature at a given pressure. Therefore, a decrease in the value of ψ leads to an increase in the slope (magnitude) of the response curve.

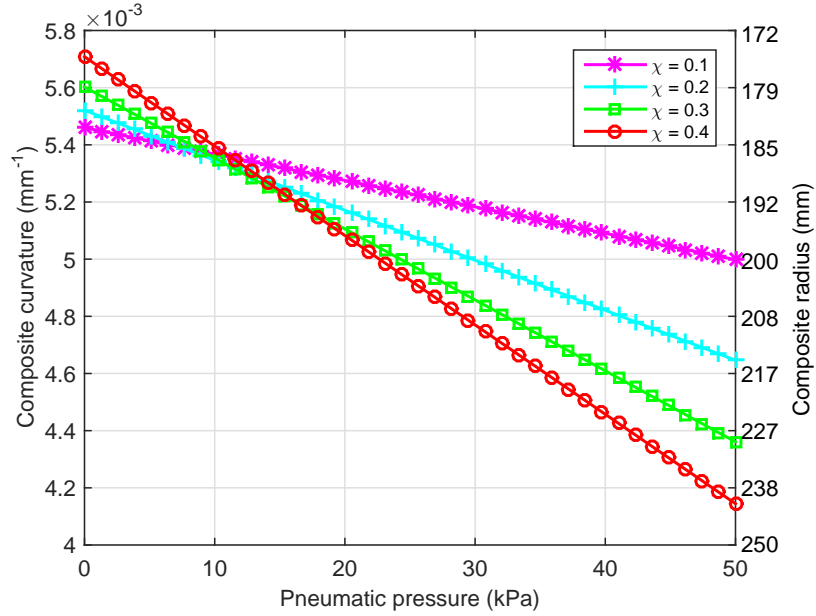


Figure 3.10: Response of a fluidic prestressed composite on the non-dimensional thickness (χ) for $\phi = 0.4$ and $\psi = 0.4$.

Theoretically, the maximum morphing ability in an FPC for a given actuation pressure range is obtained for $\phi \rightarrow 1$, $\chi \rightarrow 1$, and $\psi \rightarrow 0$. To restrict the strain of the fluid channel in Y and Z directions, the suggested practical limits for ϕ , χ , and ψ are 0.6, 0.5, and 0 respectively.

The response of an FPC in various laminate configurations and its dependence on some of the design parameters has been examined using the analytical model presented in section 3.3. A fabrication procedure for a fluidic prestressed composite is prescribed in the following section.

3.5 Composite Fabrication

Composite beam samples of an FPC in configuration 1 are fabricated to demonstrate its operation and to validate the analytical model [21]. The chosen configuration

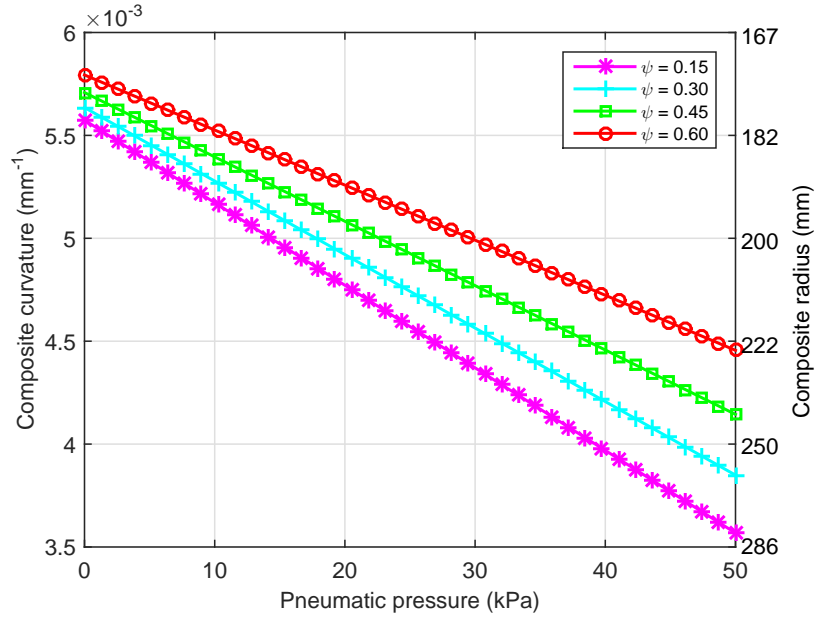


Figure 3.11: Response of a fluidic prestressed composite on the non-dimensional proximity to the interface (ψ) of the fluid channel for $\phi = 0.4$ and $\chi = 0.6$.

requires the least actuation effort among the three configurations. Dimensions and material properties of the laminae are the same as listed in Figure 3.5 and Table 3.2. The fabrication steps and material response of a 90° EMC have been described in Chapter 2. The fabrication procedure used for the fluidic layer and the composite are discussed in the following subsections.

3.5.1 Fluidic layer

The first step in the fabrication is to build molds for the fluidic layer and the fluid channel. The mold for the fluidic layer is 3D-printed whereas a steel strip is used as a mold for the fluid channel. A release agent (Pattern Release 202, National Engineering Products Inc.) is used on both molds to facilitate the removal of the cured sample. A pre-cured silicone rubber skin is sized to fit the mold for the fluidic layer and then laid out on it. The steel strip is positioned on this rubber skin (Figure 3.12(a)) and

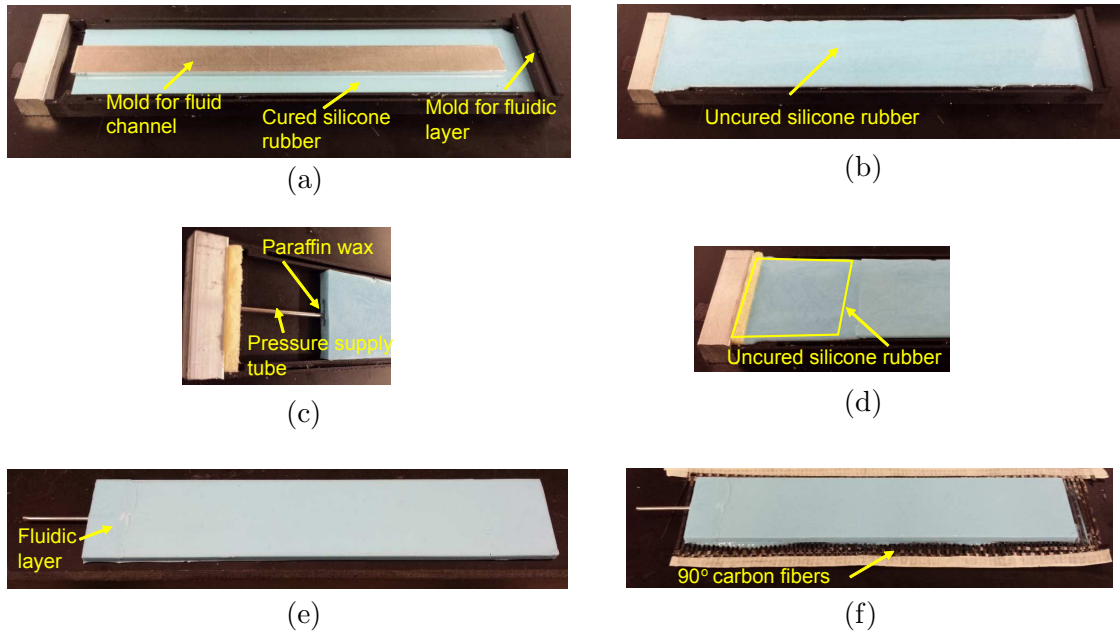


Figure 3.12: (a) Setup to mold the body of the fluidic layer, (b) layup of silicone rubber to create the body, (c) setup for the end cap, (d) silicone rubber poured to create the end cap, (e) fully cured fluidic layer, (f) fiber-reinforcement of the bottom face.

freshly mixed degassed silicone rubber is poured into the mold to create one part of the fluidic layer (Figure 3.12(b)). Upon curing, the steel strip is removed from the elastomer and the resulting void is filled with paraffin wax. Marchese et al. [100] proposed lost wax casting as a fabrication technique for soft fluidic actuators. A steel tube of diameter 1.78 mm (0.07”) is used as a pressure supply line and is positioned in the mold as shown in Figure 3.12(c). The steel tube is locked in position in the composite by smearing its outer surface with a flexible silicone adhesive that cures along with the silicone rubber surrounding it. The outlet in the elastomer is then sealed by pouring silicone rubber around the steel tube (Figure 3.12(d)). Curing of the elastomer completes the fabrication of the fluidic layer (Figure 3.12(e)). Finally, the bottom surface of the fluidic layer in the XY plane is reinforced with carbon

fibers in the Y direction. Fibers wetted with liquid silicone are sandwiched between the bottom face and a pre-cured silicone rubber skin (Figure 3.12(f)).

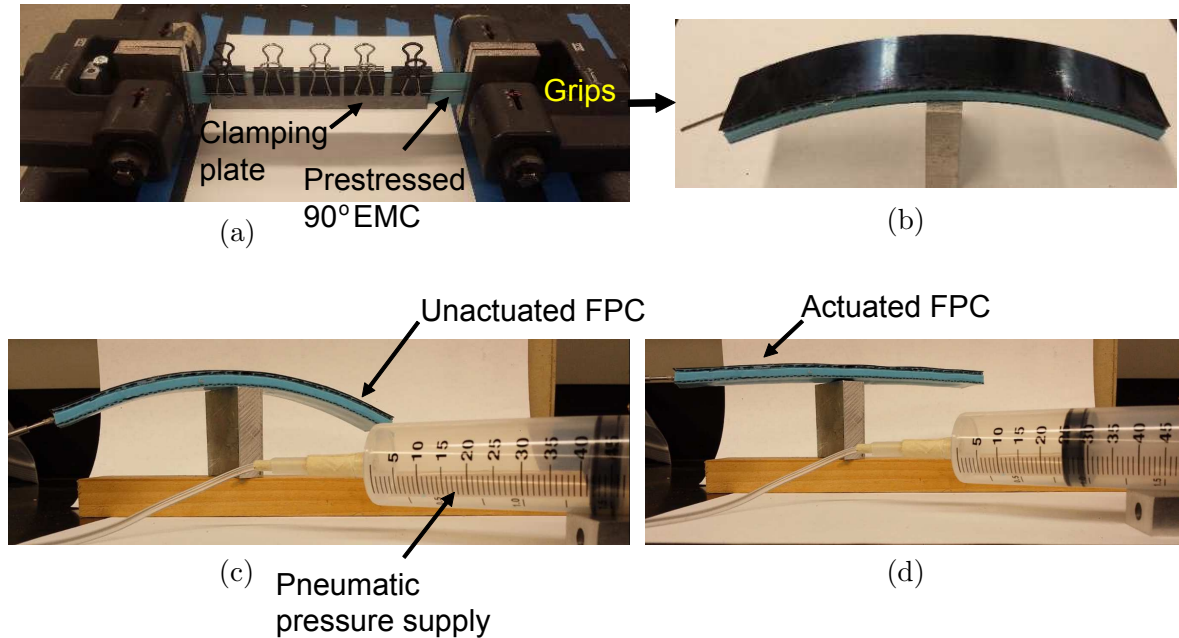


Figure 3.13: (a) Setup for the lamination of a fluidic prestressed composite, (b) trimmed laminated composite, (c) unactuated and (d) limiting actuated shapes of the composite.

3.5.2 Laminated composite

The fabricated 90° EMC layer is held at its ends by grips and prestrained to the desired value. Separately, the fluidic layer and a 1095 spring steel strip that is used as the constraining layer are bonded on either face of the prestressed EMC using a flexible silicone adhesive (DAP Auto-Marine 100% RTV silicone sealant) and allowed to cure at room temperature for 24 hours (Figure 3.13(a)). Upon removal from the grips, a fluidic prestressed composite is obtained. At this stage, the composite has a curved shape but the curvature is less than expected due to the restriction offered

by the wax (high modulus) in the fluid channel. Finally, the wax (melting point - 57°C) is melted out through the pressure supply line by placing the composite in an oven at 60°C . The resulting composite has a curved shape at equilibrium and can be pressurized to obtain a change in curvature (Figure 3.13(b)). The composite is actuated pneumatically using a disposable medical syringe to achieve a morphing function. The unactuated and actuated shapes of the fabricated FPC beam are shown in Figures 3.13(c) and 3.13(d), respectively. It has been observed that the prestressed 90° EMC can peel off from the spring steel strip over an extended period of time. This is probably caused by a high shear stress at the interface created due to a large difference in the elastic moduli of these two layers. In such a case, the roughness of the bonding surfaces influences bond strength. To improve the durability of the bond, a thin layer of paint primer is sprayed onto the metal surface.

3.6 Model Validation

The shape of an FPC beam fabricated in configuration 1 is measured as a function of pneumatic pressure in a quasi-static condition. The experimental setup for this measurement is shown in Figure 3.14(a). The composite is pressurized pneumatically using a plastic medical syringe with a diameter of 28 mm (1.1") and a stroke of 101.6 mm (4"). The syringe is rigidly mounted on a base and the position of its piston is set using a threaded rod. The applied pneumatic pressure is measured using a pressure gauge of range 0 - 103.5 kPa (0 - 15 psi) that is linked to the syringe using a saddle valve. Reflective markers placed on the concave face of the composite (Figure 3.14(b)) are tracked using an OptiTrack motion capture system consisting of four cameras that have a resolution of 1.3 megapixels. The composite is mounted on a fixture using thin double-sided tape such that shape change can occur without any restriction while its center remains stationary. Movement of the center does not affect

measurement accuracy since only the relative position of markers is required. The coordinates of the markers are then fit to a circle using the method of least squares to calculate the curvature of the composite (Figure 3.14(c)).

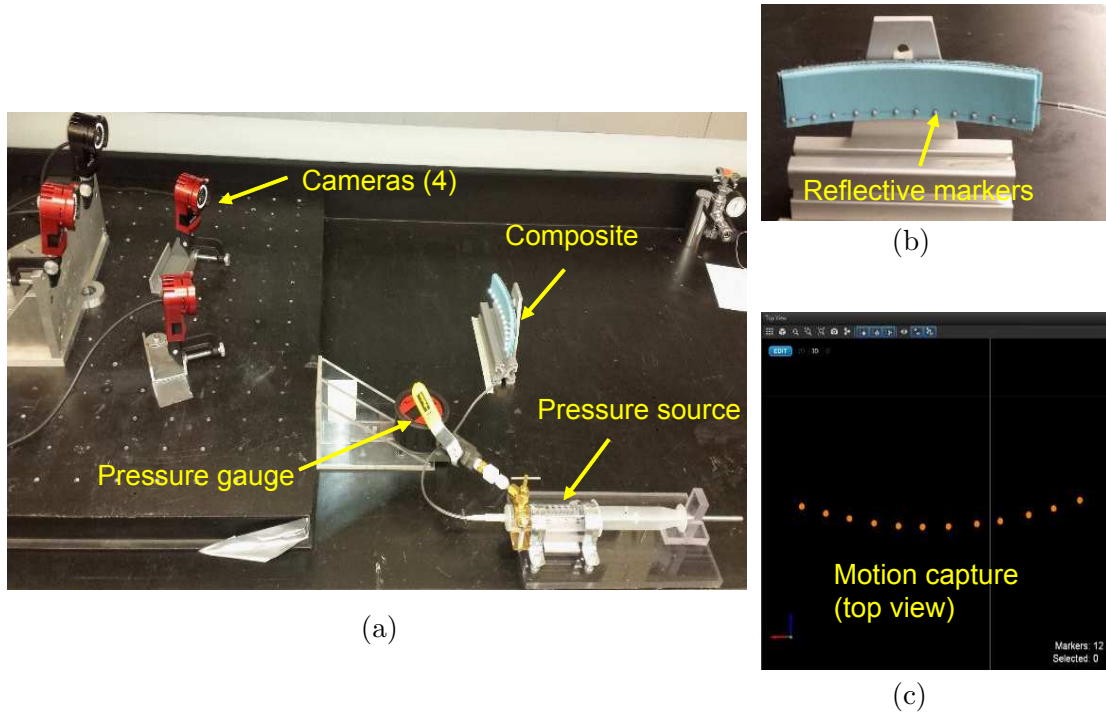


Figure 3.14: (a) Experimental setup to measure the quasi-static response of a fluidic prestressed composite, (b) composite equipped with reflective markers, (c) spatial coordinates of the reflective markers measured by a motion capture system.

The curvatures of three composite beam samples fabricated with prestrains of 0.25, 0.5, and 0.6 in the 90° EMC, are measured at discrete values of pneumatic pressure (Figure 3.15). The maximum applied pressure is restricted to 82.7 kPa (12 psi) due to the limited sealing capability of the plastic syringe, but is sufficient to nearly flatten the composites. It is observed that the measured quasi-static response of an FPC matches fairly well with the simulated response. In the unactuated state (0 kPa), the error in curvature is 0.30%, 4.00%, and 2.04% for EMC prestrains of

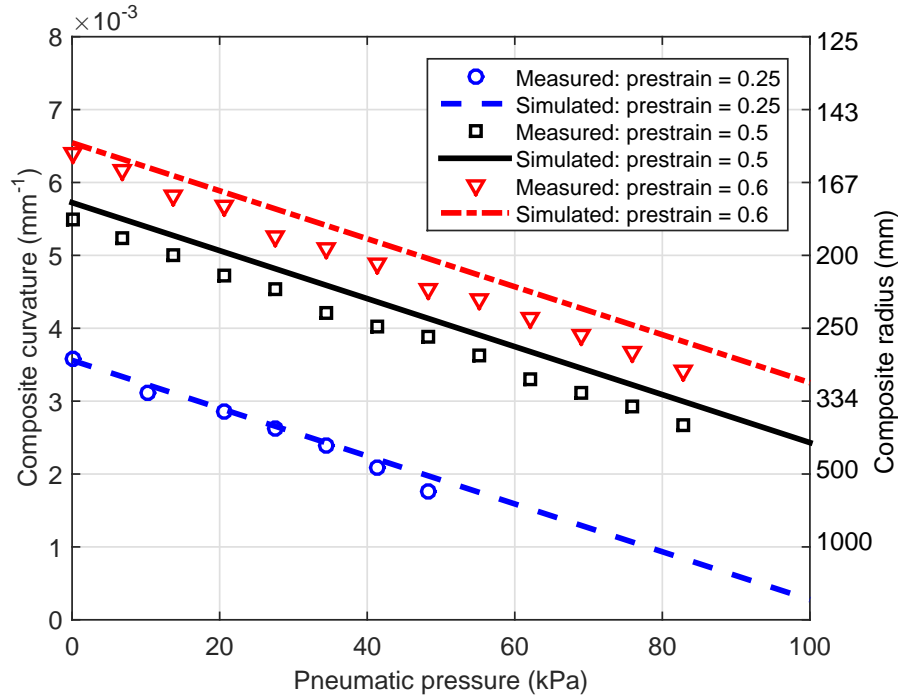


Figure 3.15: Plot of the curvature of a fluidic prestressed composite (sandwiched 90° EMC configuration) as a function of actuation pressure for different prestrains in the 90° EMC.

0.25, 0.5, and 0.6 respectively. This bias may be attributed to dimensional variability in the fabricated samples. At 82.7 kPa, the maximum error in samples with 0.5 and 0.6 prestrain is 6.66% and 8.20% respectively. In the sample with 0.25 prestrain, the maximum error is 10.2% at 48.2 kPa; the composite attains a nearly flat shape at 34.5 kPa where the error is 1.93%. The error in the nearly-flat shape is higher due to the bulging of the bottom face of the fluidic layer. The bulge is a result of the fluid channel cross-section tending towards a circle at higher pressure and is equivalent to a localized increase in composite thickness. As per the parametric study in section 4.2, an increase in fluid channel thickness (χ) yields an increase in the slope of the response curve. Since the model assumes a plane-stress condition, curvature is over-predicted in the simulated response. Bulging may be minimized by lining the inner

walls of the fluid channel with an inextensible material such that it expands only in the longitudinal direction.

A design for a fluidic prestressed composite that has a curved equilibrium geometry in the unactuated state and exhibits a controllable change in shape when actuated, is presented for the first time. An analytical model developed under a plane-stress assumption incorporates the nonlinear behavior of elastomeric layers and simulates the quasi-static response of an FPC accurately at low operating pressures. The laminate configuration of an FPC that requires the least actuation effort is identified and the effects of parameters influencing actuation are examined through a model-based study. A method for fabricating an FPC and measuring its response is presented. The simulated response of the composite is in agreement with the measured response. Durability of FPCs is an area for further investigation and optimization. When used in conjunction with a compact pressure source, fluidic prestressed composites have the potential to serve as lightweight morphing structures that can exhibit drastic, controllable changes in shape.

Chapter 4

Mechanically-Prestressed Bistable Composites with Weakly Coupled Equilibrium Shapes

Overview

This chapter presents a novel asymmetric bistable laminate that is fabricated at room temperature and whose stable shapes are analogous to those of a thermally cured fiber-reinforced polymeric composite. The laminate is composed of a stress-free isotropic core layer sandwiched between two asymmetric, mechanically-prestressed, anisotropic elastomeric layers. Its stable shapes can be independently tuned by varying the prestress in each elastomeric layer. The mechanics of the laminate are studied using an analytical laminated-plate model. The effects of core modulus, core thickness, elastomer-core width ratio, and laminate size are examined through a parametric study. Laminate samples are fabricated in the $90^\circ/\text{core}/0^\circ$ configuration for model validation. The simulated stable shapes of the laminate are in agreement with the measured shapes.

4.1 Introduction

This chapter presents a room temperature-cured asymmetric bistable laminate with stable shapes that are analogous to those of an asymmetric FRP laminate (Figure 4.1). The laminate consists of a stress-free isotropic core sandwiched between two mechanically-prestressed elastomeric matrix composites (EMCs). EMCs are fiber-reinforced elastomeric layers that are intrinsically anisotropic in nature. In the proposed laminate, they are thin elastomeric strips reinforced with fibers oriented along the width in order to achieve near-zero in-plane Poisson's ratio [8]. Cylindrical curvature can be created in an isotropic plate by bonding it to an EMC that is mechanically-prestressed in the matrix-dominated direction (Chapter 2). The resulting geometry is such that the prestressed EMC is on the concave face. Two prestressed EMC strips are aligned with fibers in the 90° and 0° orientations and are bonded on opposite faces of the core to form a bistable laminate (Figure 4.1(a)). The stable cylindrical shapes in this configuration have curvatures that are 90° apart (Figures 4.1(b) and 4.1(c)).

When the modulus of the core is much higher (10^3 times) than the modulus of an EMC in the prestressed direction, a weakly-coupled condition is possible, where the stable cylindrical shapes are independent of the prestress in the EMC on the convex face. This condition exists when the relative angle between two transversely-reinforced EMCs is 90° . Only the EMC on the concave face is associated with curvature since the orthogonal EMC (on the convex face) has near-zero in-plane Poisson's ratio. Therefore, it is possible to tune each shape independently during laminate fabrication by varying the prestress in the corresponding EMC. The magnitude of each curvature depends on the modulus and thickness of the core, and the width of each EMC. The width of an EMC is restricted to a fraction of the core width since the

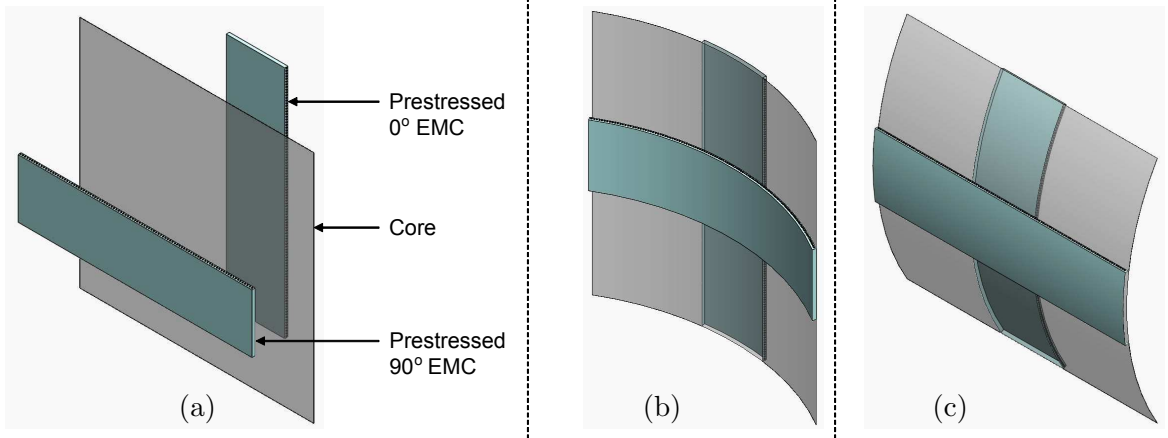


Figure 4.1: (a) Configuration of a mechanically-prestressed bistable laminate, (b) curved laminate due to a deformed 90° EMC, and (c) curved laminate due to a deformed 0° EMC.

fibers in the EMCs can have a modulus comparable to that of the core and therefore restrict curvature in the laminate.

Varying the relative angle between the two EMCs results in complex laminate shapes consisting of twist and curvature. The proposed bistable laminate design offers opportunities for the control of motion and vibration of a continuous surface through the incorporation of localized bistability. Also, the prestressed EMCs serve as damping elements that suppress vibrations persisting after snap-through from one shape to another. Mechanically-prestressed bistable laminates are fabricated at room temperature and their performance is expected to be insensitive to temperature and humidity variations.

4.2 Analytical Model

The equilibrium shapes of an asymmetric mechanically-prestressed bistable laminate can be calculated analytically by minimizing its total potential energy to obtain the coefficients of the assumed strain and displacement functions (Figure 4.2). The beam

model presented in Chapter 2 is extended to a laminated plate model with two sources of residual stress. The strain formulation for a composite plate is presented in the following subsection.

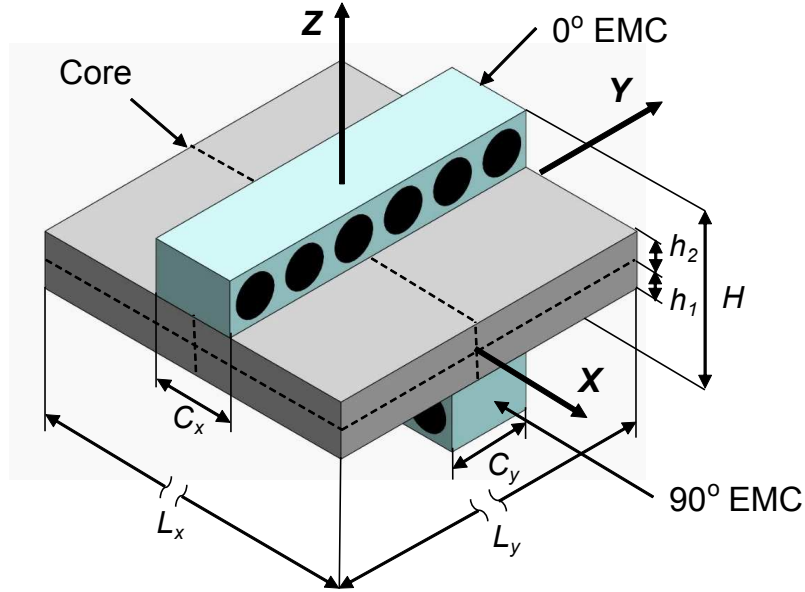


Figure 4.2: Schematic representation of a matrix-prestressed bistable laminate.

4.2.1 Laminate strain formulation

Strains for composite materials with geometric nonlinearities, as applicable to this problem, are written in accordance with von Karman's hypothesis [102] as:

$$\epsilon_x = \frac{\partial u}{\partial x} + \frac{1}{2} \left(\frac{\partial w}{\partial x} \right)^2, \quad (4.1)$$

$$\gamma_{xy} = \frac{\partial u}{\partial y} + \frac{\partial v}{\partial x} + \frac{\partial w}{\partial x} \frac{\partial w}{\partial y}, \quad (4.2)$$

$$\epsilon_y = \frac{\partial v}{\partial y} + \frac{1}{2} \left(\frac{\partial w}{\partial y} \right)^2. \quad (4.3)$$

Displacements u , v , and w of any point in the composite in the X , Y , and Z directions, respectively, are related to the displacements u_0 , v_0 , and w_0 of the geometric mid-planes (Figure 4.2) as:

$$u(x, y, z) = u_0(x) - z \frac{\partial w_0}{\partial x}, \quad (4.4)$$

$$v(x, y, z) = v_0(y) - z \frac{\partial w_0}{\partial y}, \quad (4.5)$$

$$w(x, y, z) = w_0(x, y). \quad (4.6)$$

Strain of an arbitrary plane z of the composite is obtained by substituting (4.4) - (4.6) into (4.1) - (4.3):

$$\epsilon_x = \frac{\partial u_0}{\partial x} + \frac{1}{2} \left(\frac{\partial w_0}{\partial x} \right)^2 - z \left(\frac{\partial^2 w_0}{\partial x^2} \right), \quad (4.7)$$

$$\gamma_{xy} = \frac{\partial u_0}{\partial y} + \frac{\partial v_0}{\partial x} + \frac{\partial w_0}{\partial x} \frac{\partial w_0}{\partial y} - 2z \left(\frac{\partial^2 w_0}{\partial y \partial x} \right), \quad (4.8)$$

$$\epsilon_y = \frac{\partial v_0}{\partial y} + \frac{1}{2} \left(\frac{\partial w_0}{\partial y} \right)^2 - z \left(\frac{\partial^2 w_0}{\partial y^2} \right), \quad (4.9)$$

leading to the relations:

$$\epsilon_x = \epsilon_x^0 + z\kappa_x^0, \quad \gamma_{xy} = \gamma_{xy}^0 + z\kappa_{xy}^0, \quad \epsilon_y = \epsilon_y^0 + z\kappa_y^0, \quad (4.10)$$

where ϵ_x^0 and ϵ_y^0 are the in-plane axial strains, γ_{xy}^0 is the in-plane shear strain, and κ_x^0 , κ_y^0 , and κ_{xy}^0 are the curvatures and twist, respectively, of the geometric mid-plane.

The displacement function w_0 in the Z direction is approximated as:

$$w_0(x) = \frac{1}{2}(ax^2 + bxy + cy^2), \quad (4.11)$$

such that

$$\kappa_x^0 = -\frac{\partial^2 w_0}{\partial x^2} \triangleq -a, \quad \kappa_{xy}^0 = -2\frac{\partial^2 w_0}{\partial y \partial x} \triangleq -b, \quad \kappa_y^0 = -\frac{\partial^2 w_0}{\partial y^2} \triangleq -c. \quad (4.12)$$

In-plane strains are approximated by quadratic polynomials in x and y such that the coefficients of terms with an odd degree are zero [92]:

$$\epsilon_x^0 = c_{00} + c_{20}x^2 + c_{11}xy + c_{02}y^2, \quad (4.13)$$

$$\epsilon_y^0 = d_{00} + d_{20}x^2 + d_{11}xy + d_{02}y^2. \quad (4.14)$$

Displacements u_0 and v_0 , required for the calculation of shear strain, are obtained through integration of (4.1) and (4.3) as:

$$u_0(x, y) = c_{00}x + f_1y + \frac{1}{2}(c_{11} - \frac{ab}{2})x^2y + (c_{02} - \frac{b^2}{8})xy^2 + \frac{1}{3}(c_{20} - \frac{a^2}{2})x^3 + \frac{1}{3}f_3y^3, \quad (4.15)$$

$$v_0(x, y) = f_1x + d_{00}y + \frac{1}{2}(d_{11} - \frac{cb}{2})xy^2 + (d_{20} - \frac{b^2}{8})x^2y + \frac{1}{3}(d_{02} - \frac{c^2}{2})y^3 + \frac{1}{3}f_2x^3. \quad (4.16)$$

Substitution of (4.11), (4.15), and (4.16) in (4.8) yields an expression for shear strain in the composite.

4.2.2 Computation of stable laminate shapes

The potential energy of the system (U_T) can be expressed as a function of the geometric and material properties of the laminae, total strains of the laminate, and prestrain in the EMCs as:

$$U_T = \int_V \left(U_1 + Q_{12}\epsilon_x\epsilon_y + U_2 + \frac{1}{2}Q_{16}\gamma_{xy}\epsilon_x + \frac{1}{2}Q_{26}\gamma_{xy}\epsilon_y + \frac{1}{2}Q_{66}\gamma_{xy}^2 \right) dV, \quad (4.17)$$

where $\{Q_{ij}\{i, j = 1, 2, 6\}\}$ are the plane stress-reduced stiffness parameters [102], and $U_1 = 0.5(Q_{11}\epsilon_x^2)$, $U_2 = 0.5(Q_{22}\epsilon_y^2)$ are the strain energies in the linearly strained directions in a lamina. Energies U_1 and U_2 are computed as the integral of σ_x and σ_y

for a 90° and 0° EMC respectively. This gives, for the two EMCs:

$$U_1^{(90)} = f(\epsilon_{90} - \epsilon_x), \quad U_2^{(0)} = f(\epsilon_0 - \epsilon_y) \quad (4.18)$$

where ϵ_{90} and ϵ_0 are the prestrains in the 90° and the 0° EMCs respectively. The limits of integration for the computation of strain energy are listed in Table 4.1.

Table 4.1: Limits of integration for the computation of the total potential energy of a mechanically-prestressed bistable laminate.

Lamina	x	y	z
90° EMC	$(-L_x/2, L_x/2)$	$(-C_y/2, C_y/2)$	$(-H/2, -h_1)$
Core	$(-L_x/2, L_x/2)$	$(-L_y/2, L_y/2)$	$(-h_1, h_2)$
0° EMC	$(-C_x/2, C_x/2)$	$(-L_y/2, L_y/2)$	$(h_2, H/2)$

The equilibrium shapes of the laminate are obtained by minimizing U_T using the following variational approach:

$$\delta U_T = \sum_{i=1}^{14} \frac{\partial U_T}{\partial c_i} = 0, \quad (4.19)$$

where,

$$c_i = \{a, b, c, c_{00}, c_{20}, c_{11}, c_{02}, d_{00}, d_{20}, d_{11}, d_{02}, f_1, f_2, f_3\}. \quad (4.20)$$

The fourteen equations resulting from (4.19) are solved simultaneously to calculate the strains and the out-of-plane displacement of the laminate. The expressions for U_T and δU_T are evaluated in symbolic form using MAPLE. The Newton-Raphson approach is employed to numerically approximate the equilibrium shapes of the laminate. Due to the sensitivity of the nonlinear solver to initial conditions, the initial estimates for the simulation are chosen based on the measured shapes of one fabricated sample. To obtain solutions corresponding to the stable shapes, a constraint on the Jacobian of

the system of equations is included in the model. The Jacobian matrix is computed with respect to the variables listed in (4.20) and is required to be positive definite in order to have a stable solution.

4.3 Laminate Fabrication

A fabrication procedure for a mechanically-prestressed bistable laminate is presented in this section. Samples with different values of EMC prestrain are fabricated in a 90° EMC/spring steel/ 0° EMC configuration [107]. The dimensions of the fabricated EMCs are $152.4 \times 38.1 \times 2$ mm and the volume fraction of the fibers is 0.17.

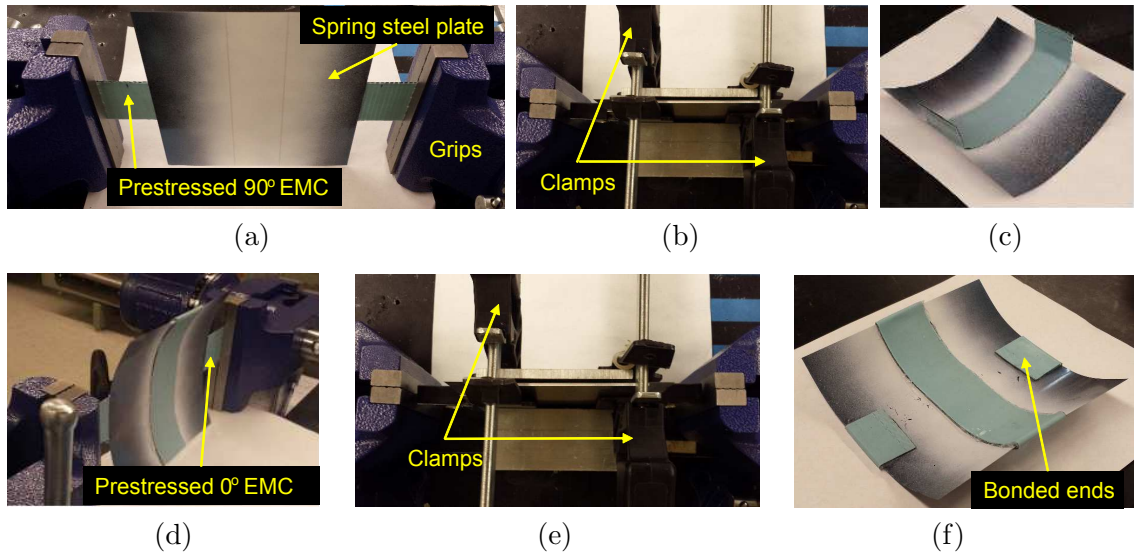


Figure 4.3: (a) A spring-steel core bonded to a prestressed EMC in the 90° orientation, (b) pressure applied to the bonded region for curing, (c) laminate with a single curvature obtained upon removal of the EMC from the grips, (d) curved sample bonded to an EMC in the 0° orientation, (e) pressure applied to the bonded region after flattening the sample, (f) resulting bistable laminate with the ends of the EMCs wrapped around and bonded to the core.

The core layer is a sheet of spring steel of dimensions $152.4 \times 152.4 \times 0.127$ mm. A paint primer (Rust-Oleum) is sprayed on the sheet to create a rough surface

for bonding the EMC to steel. One of the fabricated EMCs is stretched using a pair of grips and is then bonded to the steel sheet such that the fiber orientation in the laminate is 90° (Figure 4.3(a)). The sample is allowed to cure for 24 hours during which pressure is applied to the bonded region (Figure 4.3(b)). The resulting laminate has a cylindrical shape at equilibrium (Figure 4.3(c)). This laminate is then bonded to a prestrained EMC such that the fibers are in a 0° orientation (Figure 4.3(d)). The sample is flattened using two thick plates and is held down using clamps for curing (Figure 4.3(e)). Flattening the sample ensures minimal in-plane strain in the steel sheet when the 0° EMC is bonded to it. Fabrication trials revealed that debonding can occur during handling at the EMC-core interface at the edges of the laminate. This phenomenon is attributed to a sharp transition in stress state from the prestressed region in the EMC to the stress-free region in the core. Debonding can be prevented by curling and bonding the dangling ends of the EMC onto the opposite face of the sheet (Figure 4.3(f)).

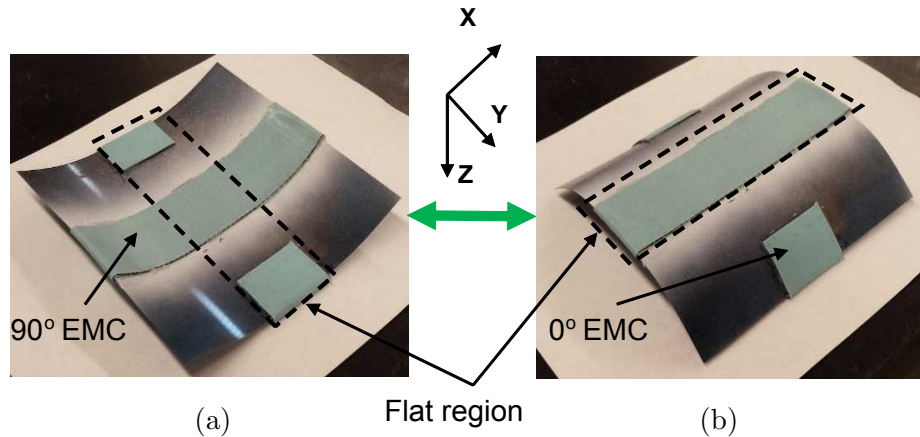


Figure 4.4: Stable shapes of a fabricated sample of a mechanically-prestressed bistable laminate.

The fabricated bistable laminate sample has two stable shapes as shown in Figure 4.4. Curvature in the laminate due to the 90° EMC (Figure 4.3(c)) is found to remain unaltered after bonding the 0° EMC to it (Figure 4.4(a)). However, the region spanning the width of the 0° EMC has a flattened appearance. This is due to the presence of two layers with very high modulus, viz., the carbon fibers in the EMC and the steel core in this region. Transition between the stable shapes is achieved by applying a moment at the ends of the composite about the axis of initial curvature.

4.4 Measurement of laminate geometry

The cylindrical stable shapes of the laminate are recorded using a 3D image capture technique. The process involves the reconstruction of a surface by mapping the coordinates of markers physically attached to the surface [108]. The image of the surface is captured using multiple cameras and the coordinates of the markers are obtained by triangulating the marker locations captured by each camera. The shapes of the fabricated laminate are measured using an OptiTrack (NaturalPoint Inc.) motion capture system that maps the coordinates of 49 hemispherical reflective markers. Each marker has a diameter of 3 mm and is bonded to the sample in a 7×7 grid (Figure 4.5(a)). The horizontal and vertical distances between markers is 25.4 mm (1 inch). Four still cameras with a resolution of 1.3 megapixels and a maximum recording speed of 120 frames per second are arranged as shown in Figure 4.5(b). Using the Motive (NaturalPoint Inc.) software, it is ensured that each marker is seen at least by 3 cameras. The cameras are calibrated to an accuracy of 0.03 mm in a capture volume of $305 \times 305 \times 305$ mm by waving a wand that contains three spherical reflective markers located inline at a fixed relative distance. A coordinate system is defined using a right angle measure that is equipped with spherical reflective markers at its ends. Two axes are obtained from these markers while the third axis is calculated as

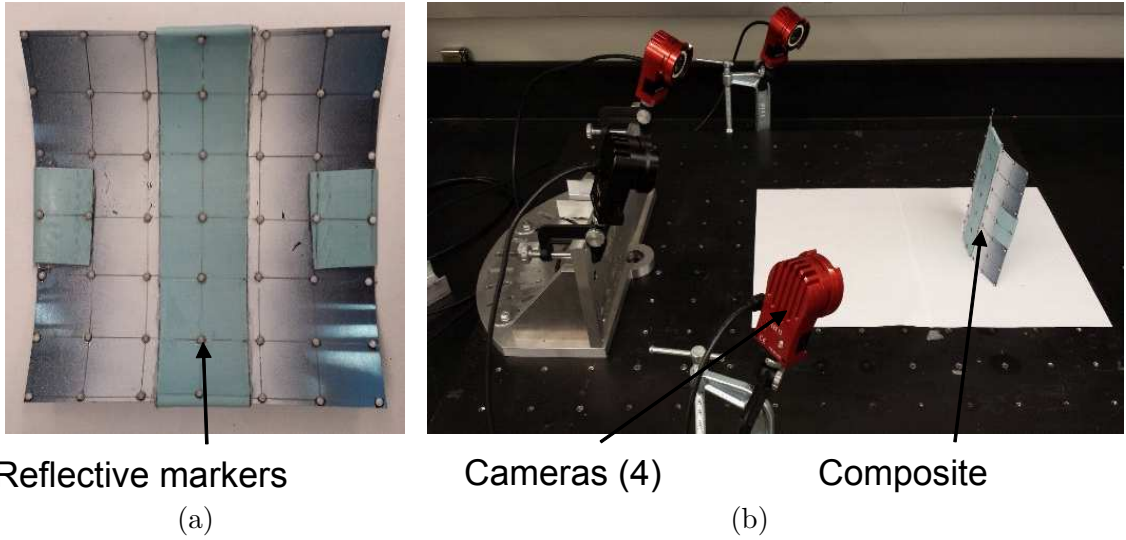


Figure 4.5: (a) Reflective markers bonded to the laminate sample for shape measurement, (b) setup showing the motion capture system used to record the equilibrium shapes of the laminate.

their cross product. The laminate sample is then placed in the capture volume in each of its stable shapes and the coordinates of each marker are obtained. The recorded marker coordinates are normalized and are fit using a quartic-quadratic polynomial to reconstruct each cylindrical shape of the laminate. While a quadratic-linear polynomial is sufficient to describe a cylindrical shape, a quartic-quadratic polynomial is required to capture the flat region in the laminate enforced by the EMC on the convex face. The reconstructed stable shapes of the laminate are plotted in Figures 4.6 and 4.7.

4.5 Results and Discussion

The simulations conducted using the model presented in section 4.2 yield three equilibrium shapes for a mechanically-prestressed bistable laminate. Two of these shapes are stable and have a cylindrical geometry while one shape is unstable and has a

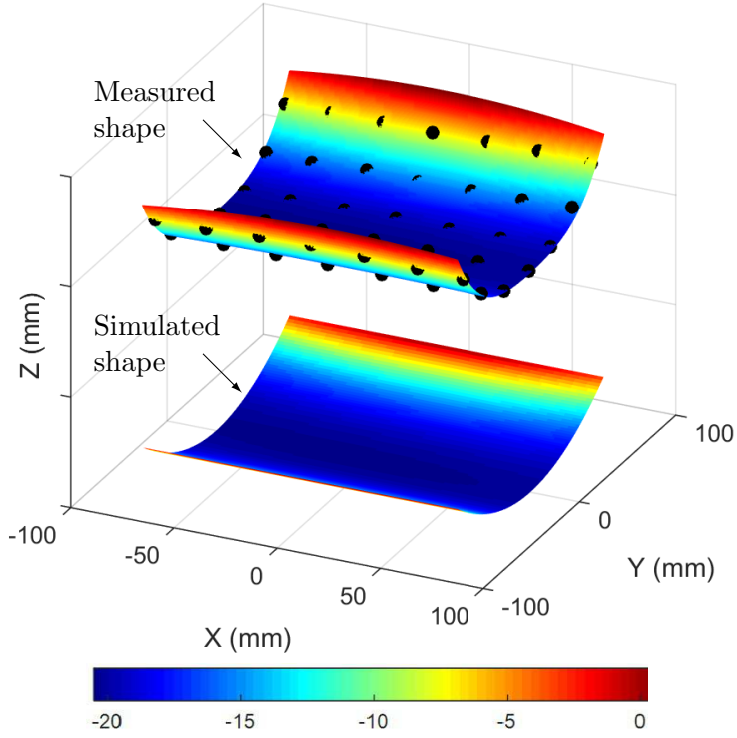


Figure 4.6: Stable cylindrical shape of a mechanically-prestressed bistable laminate with curvature about the X axis.

saddle geometry. The simulated shapes are as expected since the fabricated laminate exhibits only two cylindrical shapes.

Table 4.2: Material properties of the laminae for modeling and fabrication.

Lamina	E_1 (MPa)	E_2 (MPa)	G_{12} (MPa)	ν_{12}	ν_{21}
90° EMC	Nonlinear	0.4	1.2	0	0
Core layer	200,000	200,000	78,125	0.28	0.28
0° EMC	0.4	Nonlinear	1.2	0	0

The material properties and dimensions of the laminae used in the simulation are listed in Tables 4.2 and 4.3 respectively. The in-plane shear modulus (G_{12}) for a 90°

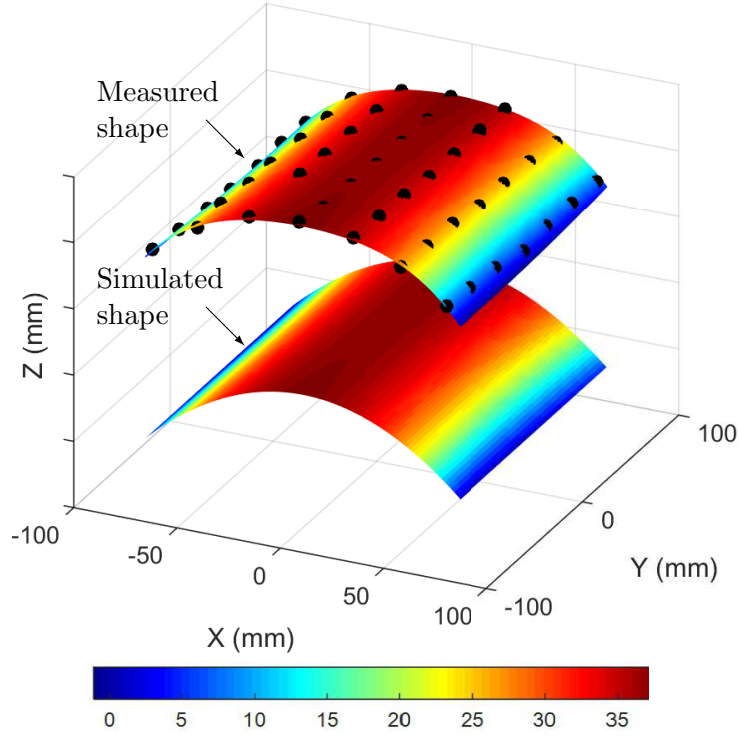


Figure 4.7: Stable cylindrical shape of a mechanically-prestressed bistable laminate with curvature about the Y axis.

and a 0° EMC is assumed to be 0.8 times its linear elastic modulus in the matrix-dominated direction [11]; G_{12} for an EMC is a constant since no twist is expected in the stable shapes of a laminate in a $90^\circ/\text{core}/0^\circ$ configuration. Poisson's ratios ν_{12} and ν_{21} for an EMC are assumed to be zero due to the high ratio of transverse (40.8 GPa) to longitudinal (1.5 MPa) modulus in the linear regime.

Simulations conducted with a transverse EMC modulus of 40.8 GPa result in very small curvatures on the order of 10^{-5} mm^{-1} . These calculations are consistent with the flat regions shown in Figure 4.4(b). However, global curvature is calculated by using the same curvature for both flat and curved regions. The assumption of constant curvature is implemented by setting the transverse EMC modulus to 0.4 MPa. This assumption is justified because the modified modulus value corresponds

Table 4.3: Dimensions of the laminae for modeling and fabrication

Lamina	Length (mm)	Width (mm)	Thickness (mm)
90° EMC	152.4	38.1	2.032
Core	152.4	152.4	0.127
0° EMC	38.1	152.4	2.032

to shear in the purely-elastomeric sub-layer that is located between the core and the fiber-reinforced elastomeric layer in the EMC; the restriction offered by the fibers in the EMC is nullified.

For a prestrain of 0.6 in each of the EMCs, the stable shapes calculated with the updated EMC modulus are compared with the corresponding measured shapes (Figures 4.6 and 4.7). The principal curvatures κ_x^0 and κ_y^0 of the fabricated sample are calculated using the method of least squares as -0.0093 mm^{-1} and 0.0057 mm^{-1} respectively. It is observed that $|\kappa_x^0|$ is greater than $|\kappa_y^0|$; the cause is a residual in-plane strain in the core when it is flattened out for bonding with the 0° EMC (Figure 4.3(e)). However, the average of $\{|\kappa_x^0|, |\kappa_y^0|\}$ of 0.0071 mm^{-1} closely matches the simulated $\{|\kappa_x^0| \text{ and } |\kappa_y^0|\}$ of 0.0076 mm^{-1} .

The stable cylindrical shapes of a laminate in the 90° EMC/core/0° EMC configuration are simulated as a function of the EMC prestrains ϵ_{90} and ϵ_0 (Figure 4.8). The associated principal curvatures κ_x^0 and κ_y^0 have a nonlinear dependence on ϵ_{90} and ϵ_0 respectively. The nonlinear variation bears resemblance to the hyperelastic response of an EMC (Figure 2.6). Curvatures κ_x^0 and κ_y^0 are respectively independent of ϵ_0 and ϵ_{90} . Since the EMCs are prestressed by applying a corresponding strain, a weakly-coupled condition exists such that each curvature is independent of the prestress in the EMC on the convex face. This condition is valid only if the prestressed EMCs are orthogonally oriented on an isotropic core; there is no twist in the laminate.

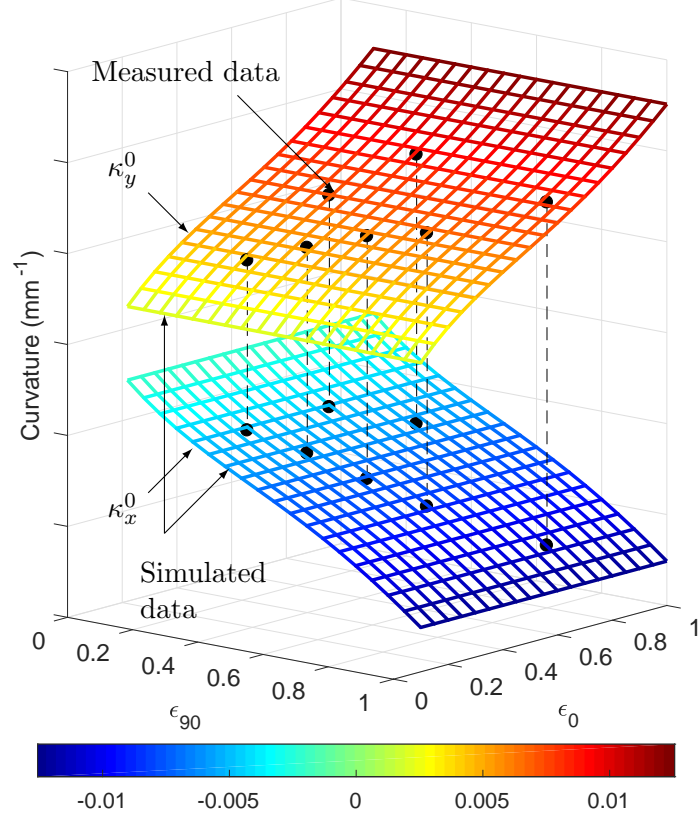


Figure 4.8: Equilibrium curvatures of a mechanically-prestressed bistable laminate as a function of prestrain in the 90° and 0° EMCs.

Seven laminate samples with prestrain values $(\epsilon_{90}, \epsilon_0)$ of $(0.3, 0.3)$, $(0.4, 0.4)$, $(0.5, 0.5)$, $(0.6, 0.6)$, $(0.8, 0.8)$, $(0.3, 0.6)$, and $(0.4, 0.8)$ are fabricated and their curvatures are measured (Figure 4.8). The simulated curvatures of the laminate are in agreement with the measured curvatures. The weakly-coupled condition is validated by the fact that κ_y^0 is equal in samples with equal ϵ_0 but unequal ϵ_{90} . The bias between $|\kappa_x^0|$ and $|\kappa_y^0|$ induced in the fabrication process is found to be constant in all samples. Accuracy of the designed shapes can be improved through simultaneous lamination but at the expense of increased complexity of the fabrication setup.

4.6 Parametric Study

A study on the effect of design parameters such as core modulus, core thickness, and size on laminate shapes is presented in this section. It is shown that besides EMC prestrain, laminate shapes can be tailored using the ratio of EMC width to core width. Material and geometric properties listed in Tables 4.2 and 4.3 are used in the analyses unless mentioned otherwise.

4.6.1 Effect of EMC width

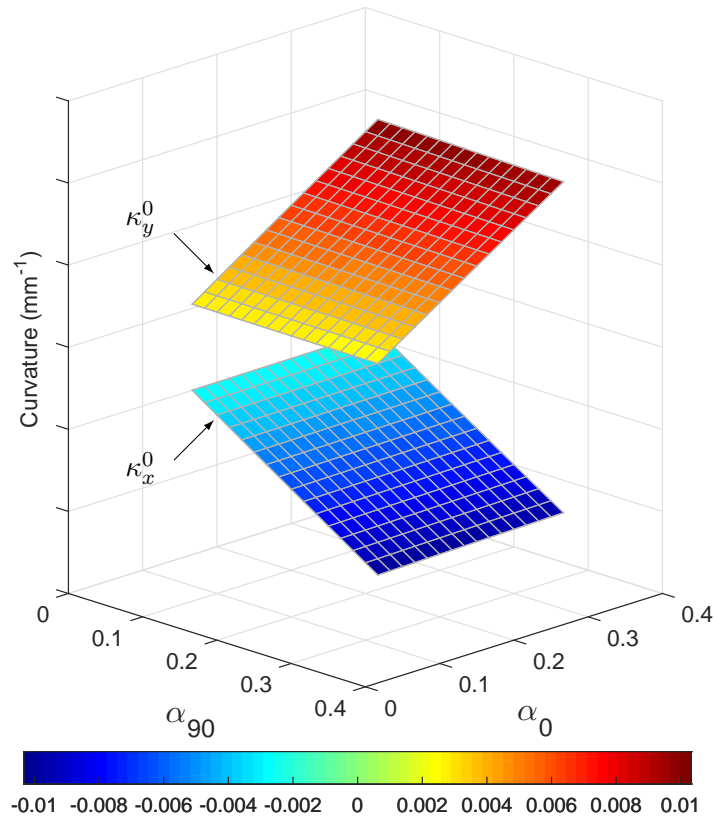


Figure 4.9: Influence of the width of an EMC relative to core width on the stable-equilibrium curvatures of the laminate. $\epsilon_{90} = \epsilon_0 = 0.6$.

A change in the width of an EMC in the laminate is associated with a change in the magnitude of prestress developed in it and hence affects laminate geometry. The non-dimensional widths of the EMCs relative to the core dimensions are defined as:

$$\alpha_{90} = \frac{C_y}{L_y}, \quad \alpha_0 = \frac{C_x}{L_x}. \quad (4.21)$$

The stable curvatures for α_{90} and α_0 ranging from 0.08 to 0.33 are plotted in Figure 4.9. Prestrains ϵ_{90} and ϵ_0 are maintained constant at 0.6. It is seen that κ_x^0 and κ_y^0 are a linear function of α_{90} and α_0 respectively. Such a trend can be attributed to a linear relationship between the width and the cross-sectional area, and hence the prestress, of an EMC. Further, κ_x^0 and κ_y^0 are independent of α_0 and α_{90} respectively, indicating the weak coupling between the EMCs.

4.6.2 Effect of core modulus and thickness

The modulus (E) and thickness ($t = h_2 - h_1$) of the isotropic core affect the two stable shapes of the laminate. Curvatures κ_x^0 and κ_y^0 are calculated for $\epsilon_{90} = 0.8$ and $\epsilon_0 = 0.5$ over a range of core modulus and thickness. Figure 4.10 is a plot of the isometric lines of $-1/|\kappa_x^0|$ and $-1/|\kappa_y^0|$. For a given t , $|\kappa_x^0|$ and $|\kappa_y^0|$ decrease with an increase in E . Further, $|\kappa_x^0|$ and $|\kappa_y^0|$ decrease with an increase in t for a fixed E . Figure 4.10 serves as a tool for the selection of the thickness of the chosen core material to obtain a given set of laminate curvatures. For example, a core material of modulus 60 GPa must be 0.185 mm thick such that the stable shapes of the laminate have radii of curvature ($|1/\kappa_x^0|$ and $|1/\kappa_y^0|$) of 100 mm and 150 mm.

4.6.3 Effect of laminate size

In thermally-cured thin unsymmetric laminates, bistability is observed beyond a particular laminate size [92]. To examine a relevant feature, the bistability of a

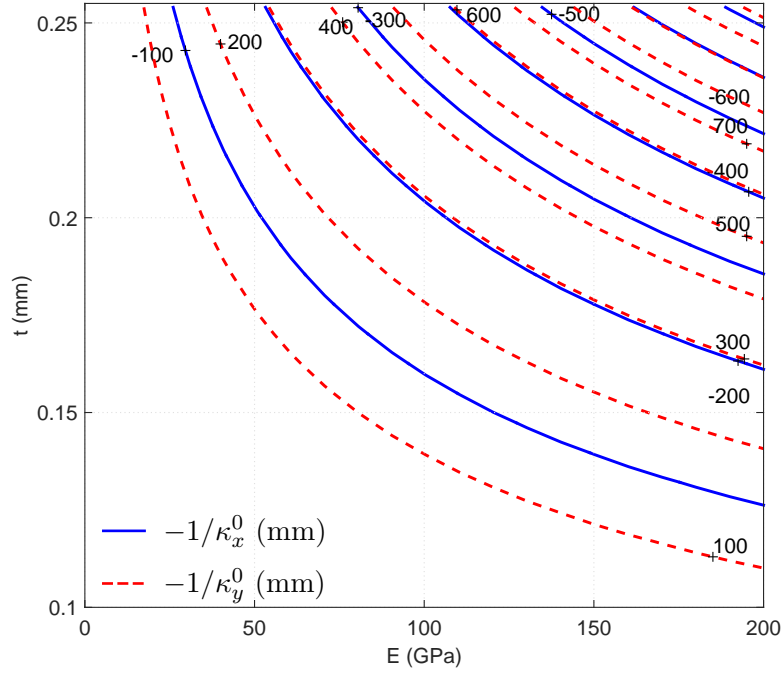


Figure 4.10: Stable-equilibrium curvatures of the laminate as a function of core modulus and thickness. $\epsilon_{90} = 0.8$ and $\epsilon_0 = 0.5$.

mechanically-prestressed square laminate is simulated for characteristic length L ($= L_x = L_y$) ranging from 25.4 mm to 228.6 mm. EMC prestrains ϵ_{90} and ϵ_0 are held constant at 0.6. Figure 4.11 shows the variation of κ_x^0 and κ_y^0 with L . It is seen that the laminate has a single stable shape up to a bifurcation length (L_b) beyond which it has two stable shapes. The solid and dotted lines represent the major and minor curvatures respectively, for a given stable shape. Each shape beyond L_b is non-cylindrical up to a critical characteristic length (L_c). Given that the core layer is a generic isotropic material, the effect of laminate size on bistability is studied for various values of core modulus (E) and thickness (t).

Figure 4.11(a) shows shape bifurcation plots for E ranging from 20 - 60 MPa and $t = 3$ mm. For a given t , L_b and L_c increase with an increase in core modulus. Beyond

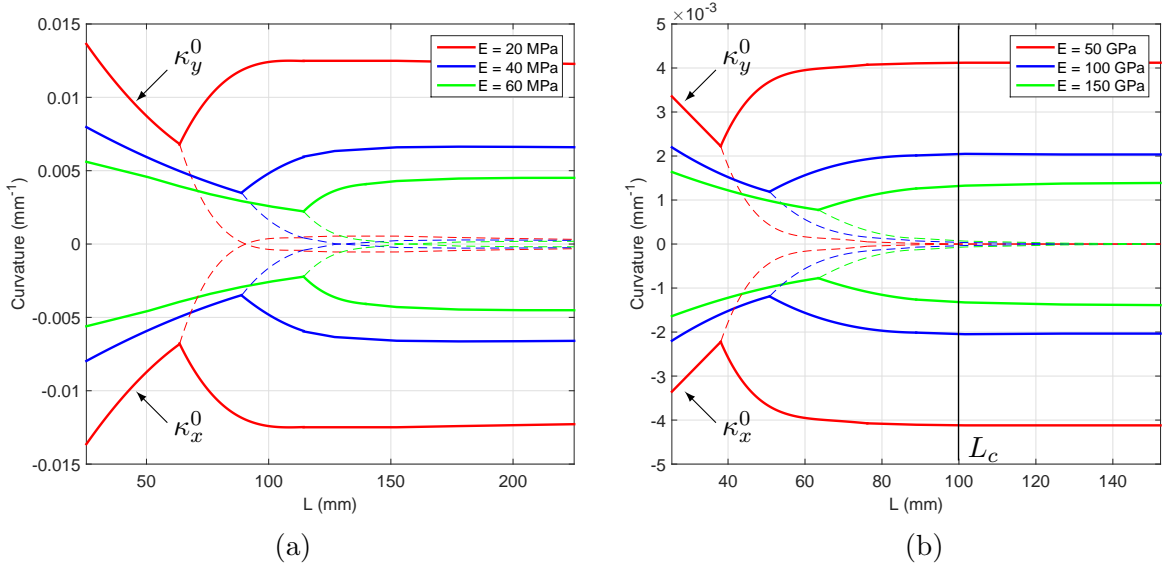


Figure 4.11: Effect of laminate size on bistability; (a)-(b) influence of core modulus on the critical characteristic length for bistability.

L_c , κ_x^0 and κ_y^0 have the same sign for each stable shape. For E ranging from 50 - 100 GPa at $t = 0.254$ mm (Figure 4.11(b)), L_b is higher for higher E whereas L_c is independent of E . In this case, κ_x^0 and κ_y^0 have opposite signs beyond L_c .

From Figure 4.11, it is apparent that bifurcation length is a function of core modulus and thickness, and hence a function of the strain energy density of the core. With higher strain energy density, the bifurcation length of a laminate in a single shape (saddle) is higher. The critical characteristic length for cylindrical stable shapes is constant when the core modulus is on the order of 10 GPa or higher. For a core whose modulus is higher than that of an elastomer (EMC) by at least four orders of magnitude, the in-plane component of strain is negligible compared to its out-of-plane deflection component ((4.1) - (4.3)). L_c is a result of the geometric nonlinearity associated with large out-of-plane deflection, and is constant in value beyond a particular core modulus. Although third-order polynomials are sufficient

to describe the scaling effect in square laminates, higher order polynomials would be required to explain the loss in bistability in laminates with high aspect ratio [99].

4.7 Response of the laminate to shape transition

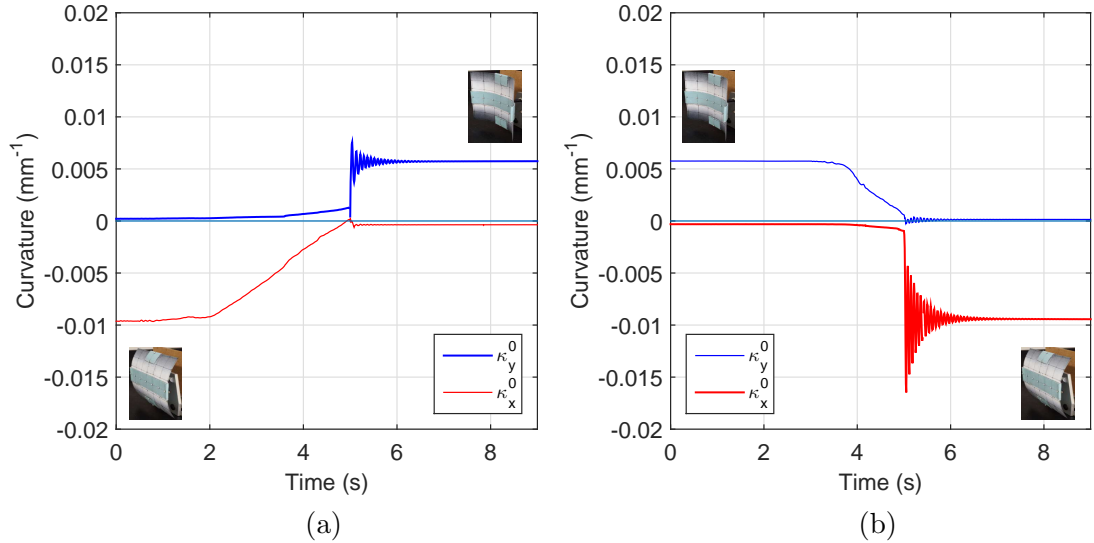


Figure 4.12: Measured dynamic response of a mechanically-prestressed bistable laminate during a transition from one stable shape to another.

This section is a report on the measured dynamic response of a matrix-prestressed bistable laminate during snap-through from one cylindrical shape to another. The motion capture camera setup described in Section 3.3 is used in this experiment. The tested sample is the same as the one shown in Figure 4.5(a). The sample is glued to the head of a thin bolt at its center to create a free boundary at the ends. The composite is initially curved about the Y axis and a moment is manually applied to it about its horizontal axis to snap into the shape with curvature about the X axis (Figure 4.12(a)). The laminate is then snapped back into its initial curvature and its response is recorded (Figure 4.12(b)). Ideally, the measured snap-through responses

must be identical. However, the equilibrium curvatures of the fabricated sample are unequal (0.0057 and 0.0093 mm^{-1}) and hence the measured responses are unequal. The vibratory amplitude is higher in the case where the laminate is snapped into the larger of the two curvatures. The frequencies corresponding to vibrations post the transitions shown in Figures 4.12(a) and 4.12(b) are measured to be 20 and 35 Hz respectively.

A room temperature-cured unsymmetric bistable laminate with tunable equilibrium shapes is proposed and demonstrated for the first time. A method for the fabrication of mechanically-prestressed bistable laminates is presented. An analytical model that includes the material and geometric nonlinearities of the laminae is developed to describe the mechanics of the composite. The simulated shapes of the laminate are in agreement with the measured shapes. The prescribed design methodology can be extended to develop bistable laminates with arbitrary EMC orientations. Mechanically-prestressed bistable laminates offer possibilities for the design of adaptive structures for motion and vibration control through the incorporation of localized bistability in existing structures.

Chapter 5

Shape Memory Alloy-Actuated Bistable Composites

Overview

This chapter presents an active bistable composite that comprises a core that is sandwiched between two prestressed fiber-reinforced elastomers and is actuated by shape memory alloy wires. The composite's shapes are modeled analytically using the strain energy model in conjunction with a 1-D constitutive model of a shape memory alloy (SMA). A sensitivity study is conducted that shows the effects of prestress and SMA properties on composite curvature and serves as a guide for the design of active bistable composites. The composite is demonstrated using NiTi shape memory wire actuators in push-pull configuration; activation of one wire resets the second wire as the composite morphs. The set of shape memory actuators not only actuate the composite in both directions, but also act as dampers that enable vibration-free shape transition.

5.1 Introduction

Shape memory alloys (SMA) are candidates for morphing applications that require lightweight actuators with large stroke (up to 6%). The mechanically-prestressed bistable composites presented in Chapter 4 can be actuated using SMAs in an embedded configuration. This chapter presents modeling and experiments to guide the design of SMA actuators for bistable composites.

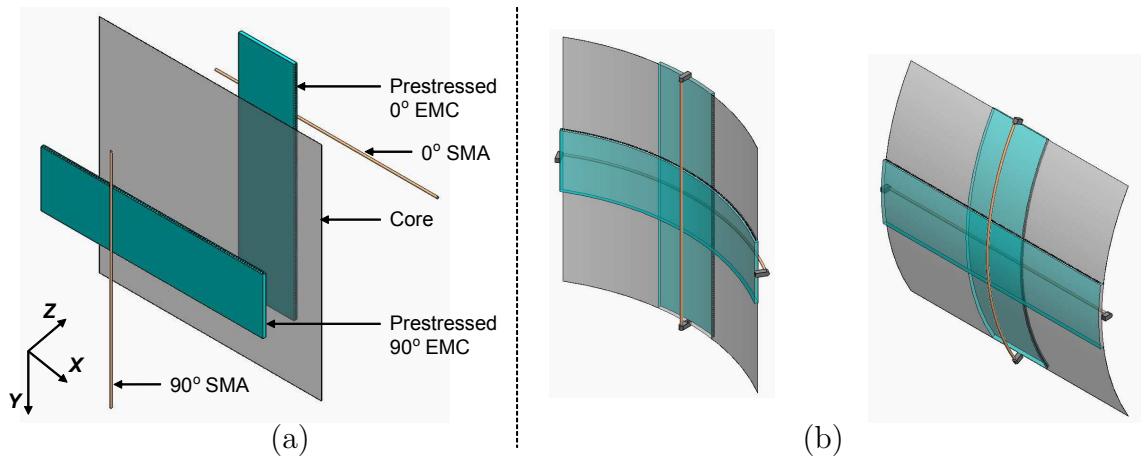


Figure 5.1: (a) Configuration and (b) stable shapes of an SMA-actuated mechanically-prestressed bistable composite.

The proposed composite is actuated using SMA wires that are assembled in the 90° and 0° orientations as shown in Figure 5.1. The high plastic strain in an SMA that is used for actuation is the result of a transformation between the high-temperature Austenite and low-temperature Martensite phases. Below Martensite temperature, the SMA transforms from twinned to detwinned Martensite when stress is applied (Figure 5.2). Heating the detwinned SMA beyond the Austenite start temperature converts the SMA to Austenite. Upon cooling, the Austenitic SMA returns to the twinned Martensite phase. In a composite that is curved about the Y axis, the 0° and

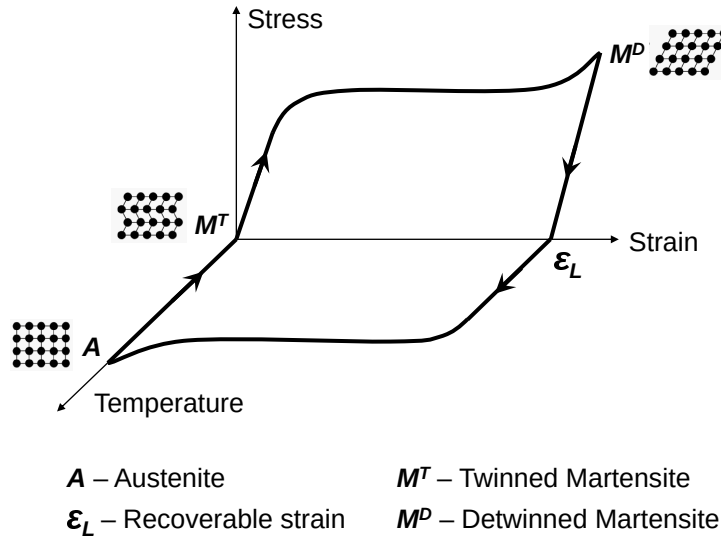


Figure 5.2: Stress-strain behavior of a shape memory alloy.

90° Martensitic SMAs are installed in the detwinned and twinned states respectively. Heating the detwinned 0° SMA to Austenite leads to a decrease in curvature about the Y axis followed by snap-through to the curvature about X axis. Post snap-through, the 90° SMA undergoes detwinning as the composite attains equilibrium. For snap-back, the 90° SMA is heated to its Austenitic phase and the 0° SMA gets detwinned as a consequence of shape transition. The phase diagram for both SMAs, associated with the morphing of the bistable composite, is shown in Figure 5.3.

5.2 Analytical Model

The strain energy function (U_T) for a passive bistable composite is described using the methodology shown in section 4.2 of Chapter 4.

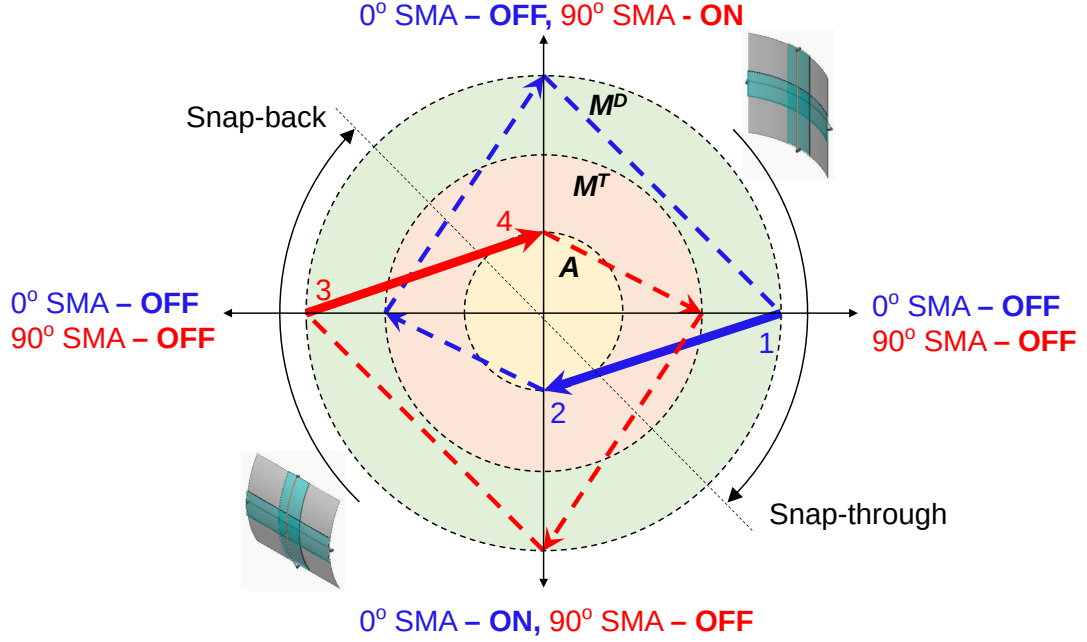


Figure 5.3: (a) Stress-strain behavior of a shape memory alloy, (b) operating modes of SMAs in a bistable laminate.

5.2.1 Composite shape computation as a function of actuation force

The actuation force generated by an SMA wire is modeled as a pair of forces (F_p) acting along the wire and tangential to the composite's mid-plane with an offset of m in the Z direction (Figure 5.4). Each force F_p is defined in terms of the unit position vector (\hat{r}_p) of force application as:

$$\vec{F}_p = -F_p \cdot \frac{\partial \hat{r}_p}{\partial x}, \quad (5.1)$$

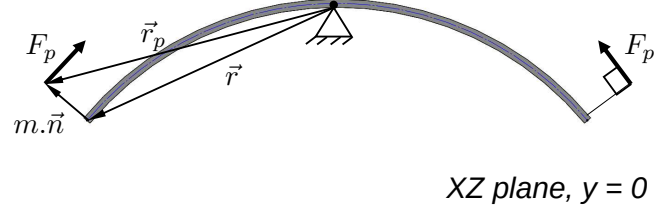


Figure 5.4: Actuation force applied on the composite by a shape memory alloy wire.

where \vec{r}_p is the sum of the position vector (\vec{r}) on the geometric mid-plane and the normal (\hat{n}) of magnitude m at \vec{r} :

$$\vec{r}_p = \vec{r} + m.\hat{n}, \quad (5.2)$$

$$= \vec{r} + m. \frac{\left(\frac{\partial \vec{r}}{\partial x} \times \frac{\partial \vec{r}}{\partial y} \right)}{\left| \frac{\partial \vec{r}}{\partial x} \times \frac{\partial \vec{r}}{\partial y} \right|}, \quad \text{where} \quad \vec{r} = \left((x + u_0)\hat{i} + (y + v_0)\hat{j} + w_0\hat{k} \right). \quad (5.3)$$

The virtual work W_p done by the pair of actuation forces, in a 0° SMA for example, can be written as:

$$\delta W_p = \vec{F}_p \cdot \delta \vec{r}_p|_{\{-\frac{L_x}{2}, 0\}} + \vec{F}_p \cdot \delta \vec{r}_p|_{\{\frac{L_x}{2}, 0\}}, \quad (5.4)$$

where \vec{r}_p is a function of composite displacements that are described in (4.15), (4.16), and (4.11). When one SMA is activated to morph the composite from one cylindrical shape to another, it is assumed that no work is done on the inactive SMA until the onset of snap-through.

The equilibrium curvatures of the composite are calculated as a function of the applied actuation force F_p using a variational approach:

$$\delta(U_T - W_p) = \sum_{i=1}^{14} \frac{\partial(U_T - W_p)}{\partial c_i} = 0, \quad (5.5)$$

where $c_i = \{a, b, c, c_{00}, c_{20}, c_{11}, c_{02}, d_{00}, d_{20}, d_{11}, d_{02}, f_1, f_2, f_3\}$. The nonlinear algebraic equations resulting from (8.12) are solved for c_i using the Newton-Raphson method.

The resulting set of equilibrium curvatures correspond to a stable shape when the

Jacobian of the system of equations is a positive definite matrix. The stable shapes of the composite are related to the thermal actuation input to the SMA by treating F_p as an internal force.

5.2.2 1-D model of an SMA actuator

The pair of forces F_p correspond to mechanical stress associated with the recoverable plastic strain of a shape memory alloy. This plastic strain is a result of the phase transformation between high-symmetry Austenite and low-symmetry Martensite. Tanaka et al. [109] modeled the constitutive behavior of an SMA in 1-D using thermodynamic relations; the kinetic law, describing the volume fraction of Martensite, was derived to be an exponential function. Liang and Rogers [110] modeled the phase transformation using a cosine function. Brinson [111] presented a cosine-based kinetic law that describes the Martensitic volume fraction as a sum of stress-induced and temperature-induced components. 1-D models can also be obtained by simplifying 3D constitutive models such as those presented by Boyd and Lagoudas [112], and Ivshin and Pence [113]. Based on the fact that accuracy is not adversely affected by the choice of the model [114], the Brinson [111] model is chosen to describe the mechanics of an SMA in the proposed bistable composite.

The one-dimensional constitutive law for a shape memory alloy can be written as:

$$\sigma - \sigma_0 = E(\xi)(\epsilon - \epsilon_0) + \Theta(T - T_0) + \Omega(\xi)(\xi - \xi_0) \quad (5.6)$$

where ϵ , T , and ξ are the strain, temperature, and Martensite volume fraction of the material. E , Θ , and Ω are the Young's modulus, stress-temperature coefficient, and phase transformation coefficient. E and Ω are calculated in terms of ξ using the rule

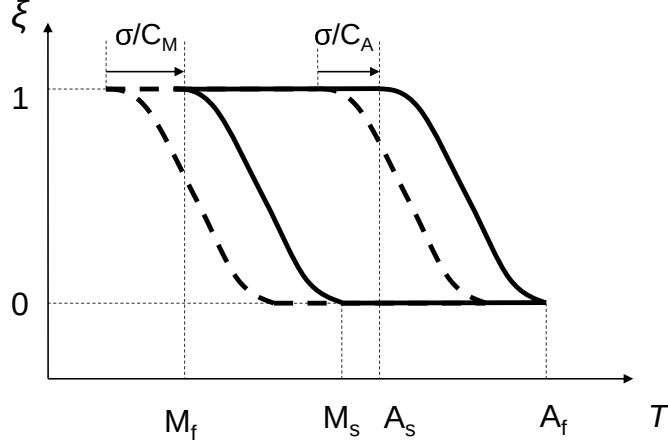


Figure 5.5: Phase transformation diagram of a typical 1-D shape memory alloy.

of mixtures as:

$$E(\xi) = E_A + \xi(E_M - E_A), \quad \Theta(\xi) = \alpha_A + \xi(\alpha_M - \alpha_A), \quad (5.7)$$

where α_M and α_A are the coefficients of thermal expansion in the Martensite and Austenite phases respectively. Further, $\Omega = -\epsilon_L E(\xi)$, where ϵ_L is the measured maximum recovery strain.

The kinetics of phase transformation of the SMA is influenced by stress and temperature and is described using a cosine function (Figure 5.5). For transformation from Martensite to Austenite, when $C_A(T - A_f) < \sigma < C_A(T - A_s)$:

$$\xi = \frac{\xi_0}{2} \left\{ \cos \left(\frac{\pi}{A_s - A_f} \left(T - A_s - \frac{\sigma}{C_A} \right) \right) + 1 \right\}, \quad (5.8)$$

where C_A is the stress-temperature coefficient for the Austenite phase, and A_s and A_f are the Austenite start and finish temperatures respectively. For transformation from Austenite to Martensite, when $T > M_s$ and $\sigma_s^{cr} + C_M(T - M_s) < \sigma < \sigma_f^{cr} + C_M(T - M_s)$:

$$\xi = \frac{1 - \xi_0}{2} \cos \left\{ \frac{\pi}{\sigma_s^{cr} - \sigma_f^{cr}} (\sigma - \sigma_f^{cr} - C_M(T - M_s)) \right\} + \frac{1 + \xi_0}{2}. \quad (5.9)$$

where C_M is the stress-temperature coefficient for the Martensite phase, M_s is Martensite start temperature, and σ_s^{cr} and σ_f^{cr} are the critical stresses corresponding to the start and finish of phase transformation.

5.2.3 Composite actuation using SMA wires

Two-way actuation of a 90° EMC/core/ 0° EMC bistable composite is achieved by activating SMAs oriented in the $90^\circ/0^\circ$ configuration (Figure 5.1); the said SMA orientation is chosen for minimal actuation effort. Upon actuation (contraction) of the 0° SMA, the composite snaps from curvature κ_{x0} to κ_{y0} . The snap-through phenomenon initiates a stress-induced transformation in the 90° SMA, beyond a critical stress, from twinned to detwinned Martensite (elongation). Activating the 90° SMA results in snap-back followed by the elongation of the 0° SMA back to its initial length.

Installation of SMA wires in a laminar configuration allows their strain to be defined in terms of composite strain by substituting z with m in (4.10). The length of a 0° SMA that is installed on a curved composite in the detwinned Martensite phase, is written in terms of Austenitic length (L_A) and equilibrium shape ($\epsilon_{x0}^{(s)}, \kappa_{x0}^{(s)}$) as $L_A(1 + \epsilon_L) = L_x(1 + \epsilon_{x0}^{(s)} + m\kappa_{x0}^{(s)})$. The length (L_i) of the 0° SMA at an intermediate shape during actuation is given by $L_i = L_x(1 + \epsilon_{x0}^{(i)} + m\kappa_{x0}^{(i)})$. The actuation strain of the 0° SMA, defined as $(L_i - L_A)/L_A$, is calculated to be:

$$\epsilon = \frac{(1 + \epsilon_{x0}^{(i)} + m\kappa_{x0}^{(i)})(1 + \epsilon_L)}{(1 + \epsilon_{x0}^{(s)} + m\kappa_{x0}^{(s)})} - 1. \quad (5.10)$$

The stroke ϵ , computed for F_p ranging from zero (equilibrium) to snap-through load, is substituted in (8.13) to calculate the corresponding temperature range for the actuation of the 0° SMA. Stress σ is computed as $F_p/(\pi D^2)$, where D is the diameter of the SMA wire.

Post snap-through, the 90° SMA is under tension with reaction forces F_p acting at $(0, -L_y/2)$ and $(0, L_y/2)$. The magnitude of F_p is unknown and is calculated for increments of curvature by simultaneously solving the constitutive law under isothermal conditions:

$$\sigma = E(\xi)((\epsilon_y + m\kappa_y) - \epsilon_L\xi), \quad (5.11)$$

and the kinetic law for phase transformation given by (8.16). The value of ξ of the 90° SMA at static equilibrium would then be used as ξ_0 in its actuation step (snap-back).

5.3 Results and Discussion

Simulations conducted on the passive composite with material properties and dimensions of the laminae as listed in Table 4.2. The stable shapes are cylindrical, orthogonal, and are defined by constant curvatures κ_{x0} and κ_{y0} (Figure 4.8). The curvatures are equal in magnitude when ϵ_{90} and ϵ_0 are equal. Therefore, the magnitude of actuation force required to achieve snap-through is unique for a given prestrain in the EMC on the concave face.

The effect of the pair of actuation forces F_p on curvature is shown in Figure 5.6 for various values of ϵ_{90} ; ϵ_0 is maintained constant at 0.6. The actuation force required for snap-through is higher for higher values of ϵ_{90} . Further, it is apparent that the slope of $|\kappa_{x0}|$ vs. F_p decreases with a decrease in $|\kappa_{x0}|$. This reduction in slope can be explained by the fact that as curvature decreases, the actuation force does more work in recovering the in-plane strain as compared to the work it does in reducing the out-of-plane deflection. In all cases of ϵ_{90} , the composite snaps into the same κ_y that corresponds to $\epsilon = 0.6$. While the assumption of constant curvature yields accurate results in the calculation of stable shapes, it is insufficient for an accurate description of actuation loads during shape transition. Higher order strain models [99, 115] are more reliable for the study of actuation loads and are presented in Chapter 6.

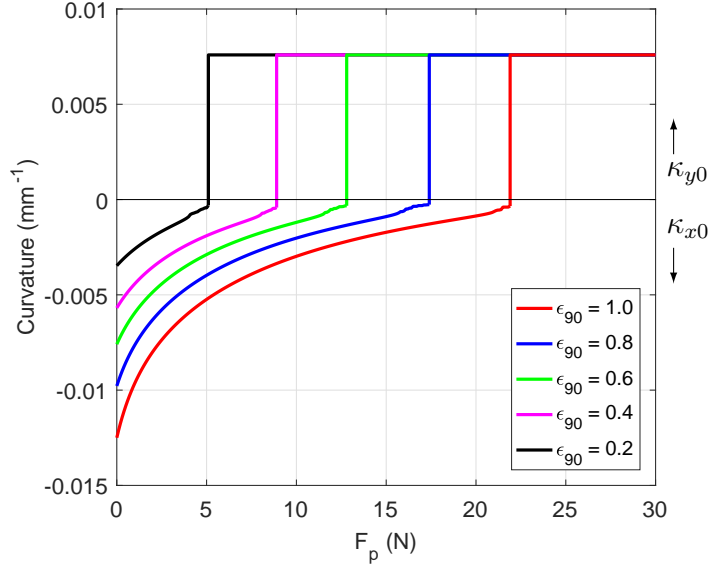


Figure 5.6: Force generated by an SMA as a function of composite curvature.

Table 5.1: Measured material properties of NiTi-6 shape memory alloy wire.

E_M (GPa)	E_A (GPa)	C_M (MPa/° C)	C_A (MPa/° C)	σ_s^{cr} (MPa)	σ_f^{cr} (MPa)
20	40	6.3	7.5	10	120
A_s (° C)	A_f (° C)	M_s (° C)	M_f (° C)	ϵ_L	
48	62	23	7	0.045	

The actuation force F_p , corresponding to various values of κ_{x0} , is applied as stress on the 0° SMA. The properties of both the SMAs used for simulation correspond those of a nickel-titanium alloy called Nitinol-6 (manufactured by Fort Wayne Metals, Inc.). The material properties of Nitinol-6 were obtained by conducting isothermal tensile tests and differential scanning calorimetry on a wire of diameter 0.584 mm (Table 5.1). To cover a range of possible results, the diameter D and maximum recoverable strain ϵ_L of the NiTi-6 SMA are chosen to be 0.889 mm and 0.08 respectively.

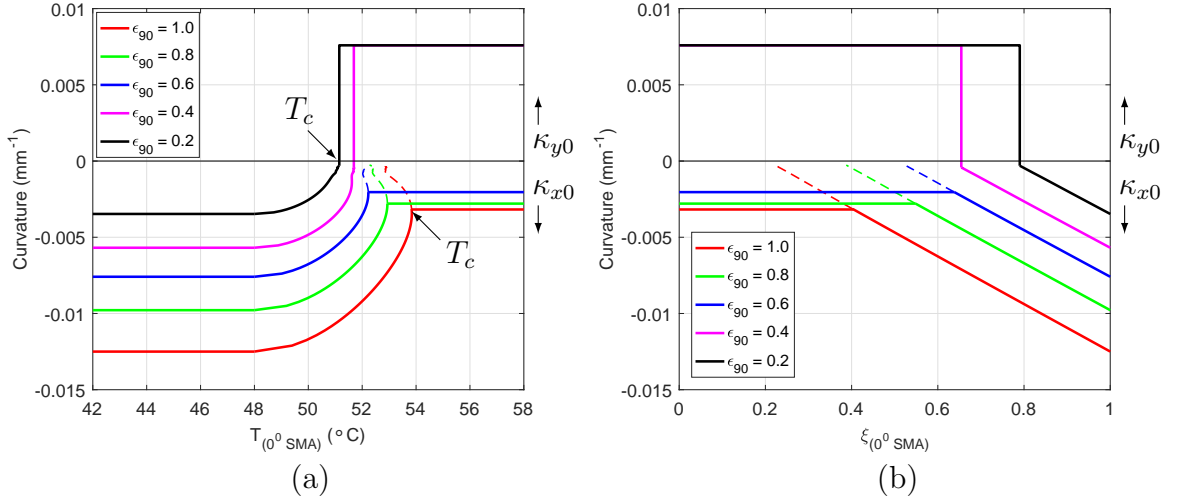


Figure 5.7: Effect of (a) temperature and (b) Martensitic volume fraction of a 90° SMA on composite curvature.

The quasistatic curvature of the composite is shown as a function of the temperature of the 0° SMA in Figure 5.7(a). The 0° SMA is assumed to be located at a distance $m = 2.54$ mm from the geometric mid-plane. The composite is initially curved about the Y axis and is at room temperature ($t_0 = 25^\circ \text{C}$). Heating the SMA does not result in a change in κ_{x0} until the temperature reaches the Austenite start temperature (A_s). Beyond A_s , κ_{x0} decreases with an increase in T up to a critical temperature T_c . For small ϵ_{90} , T_c represents the temperature at which snap-through occurs (e.g., black solid line in Figure 5.7(a)). Actuation temperature T_c increases with an increase in ϵ_{90} . Higher EMC prestrain results in larger curvatures, and therefore greater actuation stroke from the SMA.

For high ϵ_{90} , T_c is a point of inflection that indicates the minimum curvature to which the composite can be morphed; heating beyond T_c has no effect on κ_{x0} even though the recoverable strain of the SMA is sufficient for snap-through. The existence of a point of inflection κ_{x0} can be attributed to the effect of stress on the phase transformation of the SMA (Figure 5.5). Stress in the SMA increases exponentially with

decrease in curvature (Figure 5.6) and causes reversal of the SMA's transformation from Martensite to Austenite (see eq. (8.15)). At the point of inflection, the stress generated due to temperature change is equal to the applied stress due to reaction forces. It is mathematically possible to achieve further decrease in curvature by reducing temperature but such a solution would be non-physical (e.g., dotted red line in Figure 5.7(a)). Decrease in temperature brings the composite back to its initial curvature κ_{x0} (e.g., solid red line). The variation of ξ with respect to κ_{x0} is seen to be linear (Figure 5.7(b)). Phase change in the SMA is higher for higher values of EMC prestrain.

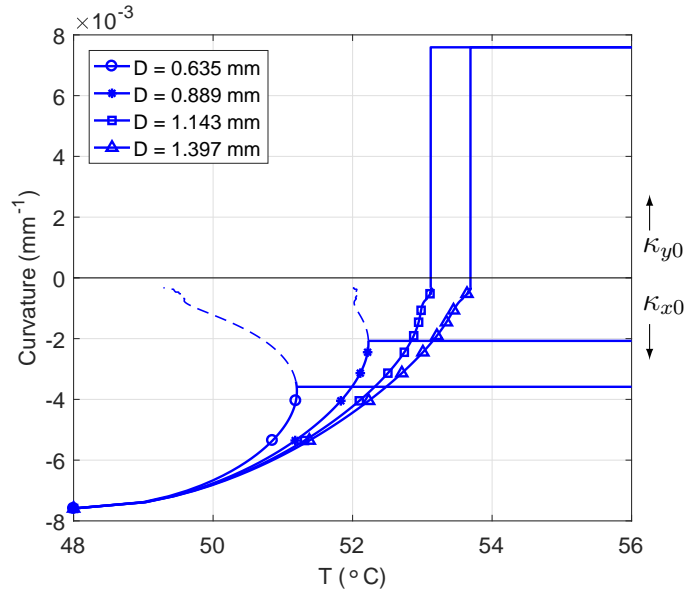


Figure 5.8: Effect of diameter of the 90° SMA on composite curvature.

To further examine the existence of a point of inflection T_c , we studied the effect of SMA wire diameter on the composite's curvature (Figure 5.8). For large values of

D such as 1.143 mm and 1.397 mm, κ_{x0} reduces monotonically with temperature, indicating that the diameter of the wire is sufficient to achieve snap-through. Reducing wire diameter below a particular value results in an inflection in the $\kappa_{x0} - T$ curve. Reduction in D leads to an amplification of stress ($F_p/(\pi D^2)$) in the wire for a given value of F_p . By simulating curvature for a range of diameter values, one can identify the minimum cross-section of the SMA in order to operate with minimal actuation energy.

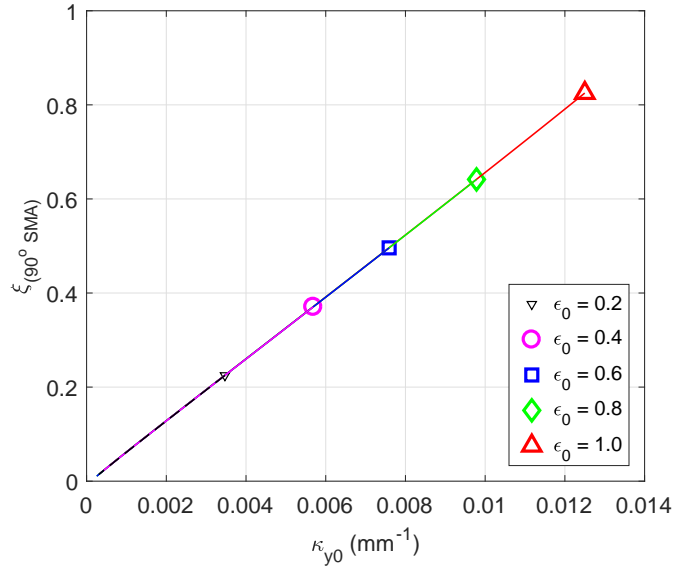


Figure 5.9: Post snap-through evolution of volume fraction of the 0° SMA as a function of composite curvature.

Immediately after snap-through, the 90° SMA is under tension whereas the 0° SMA is in a stress-free state when deactivated. The 90° SMA undergoes an isothermal phase transformation under the applied stress from snap-through load F_p (see eq. (5.11)). The evolution of Martensitic volume fraction, simulated for a 90° SMA of diameter 0.584 mm, is shown as a function of κ_{y0} in Figure 5.9. Phase change occurs

only if the stress in the SMA immediately after snap-through lies within $\sigma_s^{cr}, \sigma_f^{cr}$; for $\epsilon_0 = 0.2$, phase transformation, shown with a dotted line, does not occur since the critical stress (22.6 MPa) is greater than the maximum stress (19.4 MPa). The initial value of ξ is non zero due to the difference between T and M_s . The change in ξ , associated with plastic strain, is higher in composites with larger prestrain ϵ_0 . Complete transformation to Martensite ($\xi = 1$) occurs when ϵ_L is equal to the in-plane equilibrium strain of the composite at the SMA's location; in the case where $\epsilon_0 = 1$, ξ is less than 1 since the in-plane strain at equilibrium (0.063) is less than ϵ_L (0.08). If ϵ_L is less than the in-plane equilibrium strain, then the composite reaches a new equilibrium shape defined by ϵ_L (not shown in Figure 5.9).

5.4 Demonstration of an SMA-actuated bistable composite

In-plane actuation has been shown to be relatively energy efficient when the actuator is mounted on the convex face. This mode of actuation is made practically viable by smart materials. In this section, in-plane actuation is demonstrated using shape memory alloy wires in the configuration shown in Figure 5.1 [116].

A square composite sample is fabricated with areal dimensions as shown in Table 4.2. A 3.2 mm thick vinyl foam layer is added between the EMC and the spring steel core. The foam layer is brittle and its modulus is measured to be 25 MPa. However, when bonded to the steel core, it is flexible and serves to reduce the interlaminar shear between the EMC and the core. Figure 5.10(a) shows the stable shapes of the fabricated composite. The value of prestrain applied to both EMCs is 0.35. The maximum out-of-plane displacement, when the composite is curved about the X and Y axes, is measured to be 15 mm and 14 mm respectively; assuming constant curvature, the corresponding curvatures are 0.0051 mm^{-1} and 0.0048 mm^{-1} respectively. NiTi-6 SMA wires of 0.58 mm diameter (Fort Wayne Metals Inc.), with measured

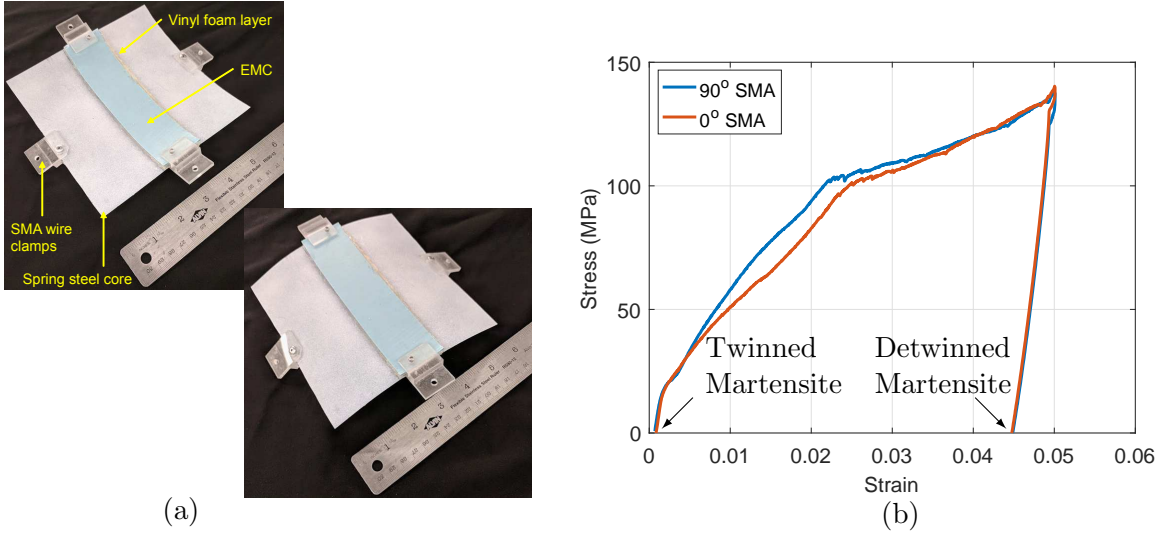


Figure 5.10: (a) Stable shapes of a passive bistable composite sample and (b) room temperature (25°C) response of the 90° and 0° SMA wire actuators.

material properties as listed in Table 5.1, are installed on the composite at a distance of 5.3 mm from the geometric mid-plane. The stress-strain response of the trained SMA wires at room temperature is shown in Figure 5.10(b). Each SMA wire is held at its ends using polycarbonate clamps and its in-plane motion is constrained using plastic bridges as shown in Figure 5.11. On a composite curved about the X axis, the 90° and 0° SMAs are installed in the detwinned Martensite and twinned Martensite phases respectively. Each wire is powered by a DC supply rated at 10 A (30 V).

The SMA wires are actuated by supplying a constant current. In the first step, only the 90° SMA is heated until the composite snaps from its curvature about X to curvature about Y . Composite shape is recorded at 100 frames per second using a motion capture system with reflective markers installed at points A , B , C , and D as marked in Figure 5.11. Out-of-plane displacement is reported as the average of w_A , w_B , w_C , and w_D . The influence of the 0° SMA on the post snap-through response of the composite is plotted in Figure 5.12. The dotted lines indicate the composite's

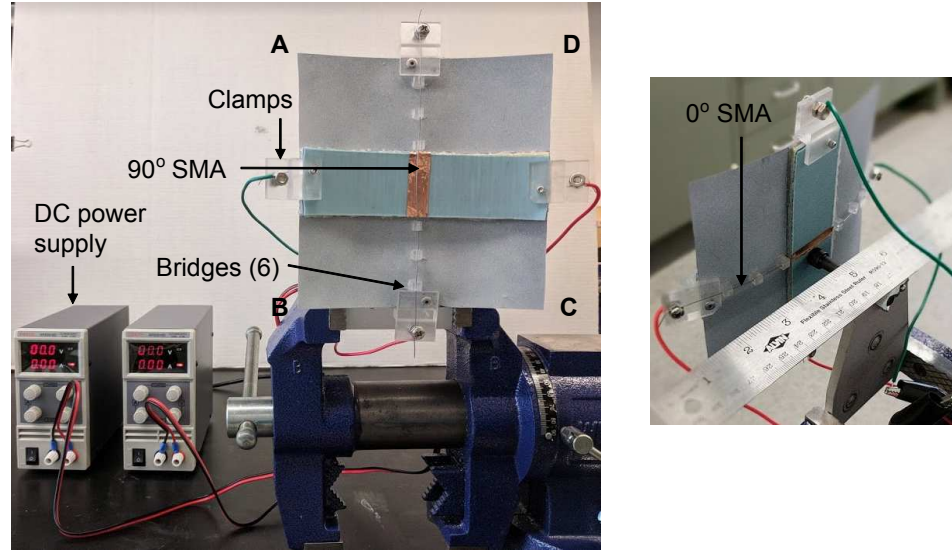


Figure 5.11: Setup for a shape memory alloy-actuated bistable composite.

response in the absence of the 0° SMA. It is observed that the time required for shape transition is higher in the presence of the 0° SMA. This SMA dampens the post snap-through vibrations to yield a second stable shape. Therefore, the demonstrated SMA actuators not only provide two-way actuation, but also to enable an almost vibration-free shape transition in the composite. Further, the resulting curvature is smaller in the presence of the 0° SMA since a fraction of the composite's strain energy is spent in detwinning the SMA. The loss in curvature is minimal when the SMA is designed to undergo complete transformation from twinned to detwinned Martensite. Lastly, it is seen that shape transition occurs in two distinct stages. Such a response is expected because a non-uniform contraction of the 0° SMA, due to sliding friction in the bridges, can result in partial snap-through.

Figure 5.13 shows snap-through and snap-back to demonstrate the complete operation of the composite. The response is plotted for three values of constant current. The time taken for complete snap-through is 8.4s, 5.5s, and 3s for an applied current

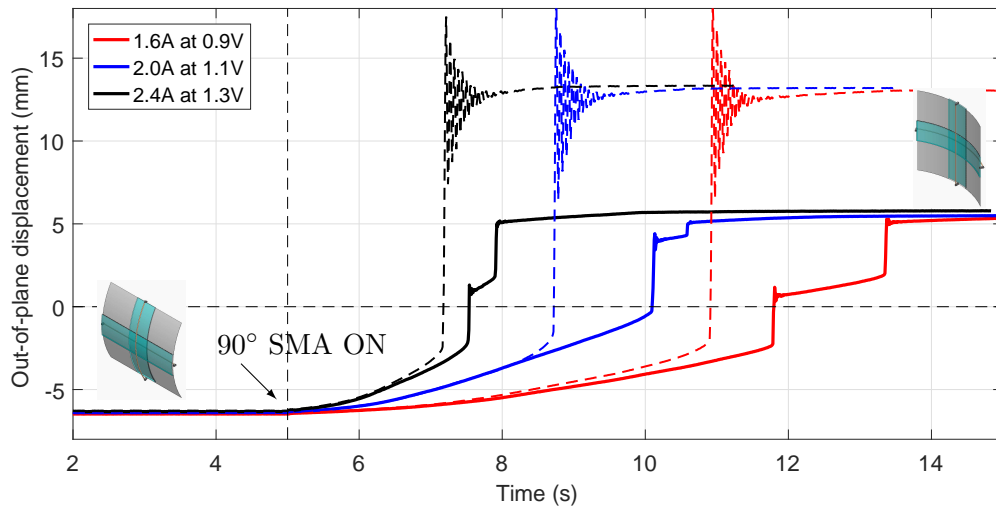


Figure 5.12: Snap-through transition in an SMA-actuated bistable composite.

(power) of 1.6 A (1.44 W), 2 A (2.2 W), and 2.4 A (3.12 W) respectively. The corresponding times for snap-back are measured to be 6.4s, 3.5s, and 2.5s respectively. Partial snap-through can be minimized or eliminated by maximizing the power applied to the SMA and by minimizing friction.

In mechanically-prestressed bistable composites with a 90° EMC/core/ 0° EMC configuration, the stable shapes are weakly coupled and can be tailored independently using EMC prestrain. This weak coupling enables one to design embedded actuators that can be sequentially activated to achieve shape adaptation. The strain energy-based model of a bistable laminated composite is combined with a 1-D constitutive model of an SMA to study the relationship between EMC prestrain and SMA parameters and thereby guide actuator design. Actuation using shape memory alloys is demonstrated at the coupon scale. The demonstrator shows that SMA actuators also serve as dampers to enable a vibration-free shape transition in bistable composites.

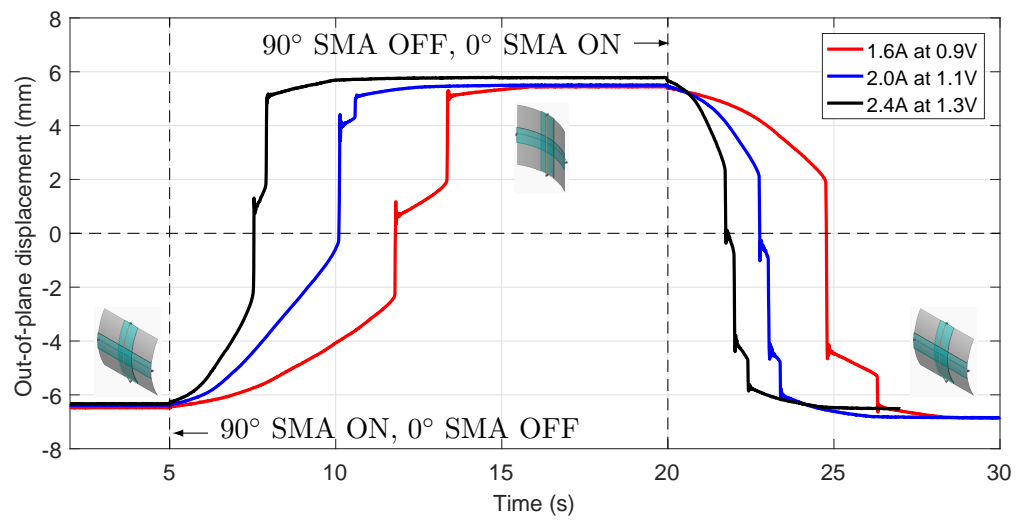


Figure 5.13: Complete shape transition profile for a shape memory alloy-actuated bistable composite.

Chapter 6

Stability Considerations and Actuation Requirements of Bistable Composites

Overview

This chapter investigates the domain of bistability and actuation requirements of bistable laminated composites. An analytical model is constructed as follows: point-wise displacements and areal dimensions are scaled; strain energy and actuation work are computed using high-order displacement polynomials; and net energy is minimized to calculate stable shapes as a function of actuation force. Shape transition is shown to be a multi-stage phenomenon through an experimental procedure involving friction-free tensile tests and 3D motion capture. The simulated actuation energies agree with measurements within 12%. Square laminates are shown to be bistable only when the ratios of laminae prestrains are greater than 0.2. It is shown that in-plane forcing requires 100 times more energy than an equivalent moment. A parametric study reveals that the composites performance parameters are more sensitive to the cores thickness than its modulus; the sensitivity of actuation energy is minimal relative to that of deformation and stiffness.

6.1 Introduction

Laminating two mechanically-prestressed layers on either side of a stress-free core results in a bistable composite (Chapter 4). When the prestressed laminae are orthogonal to each other, the equilibrium cylindrical shapes are said to be weakly coupled; each shape is influenced only by one prestressed lamina but not both (Figure 6.1). Residual stress generated through two sources of mechanical prestrain yields a domain of bistability that is different from that resulting from a single source (e.g., temperature in thermally-cured laminates). Therefore, a study exploring the the limits of design parameters, such as prestrain ratio and aspect ratio, is required to determine the composite’s bistability regime.

This chapter presents a high-order analytical strain model to systematically explore the design space of bistable composites that have two sources of residual stress. The analysis is presented through the example of a mechanically-prestressed bistable composite. The stable shapes of a rectangular composite are simulated for limiting ratios of prestrain and side length to determine the domain of bistability. A case study comparing the composite’s response to various actuation modes such as axial, transverse, and in-plane loading is presented. Tensile tests are conducted on fabricated composite samples and snap-through is recorded using a 3D motion capture system. The work associated with the measured force-deflection curves is compared with the simulated actuation work in the axial loading case. Finally, a sensitivity study is conducted to explain the effect of design parameters of the composite on its performance metrics, *viz.*, range of deformation, stiffness to operational load, and actuation energy.

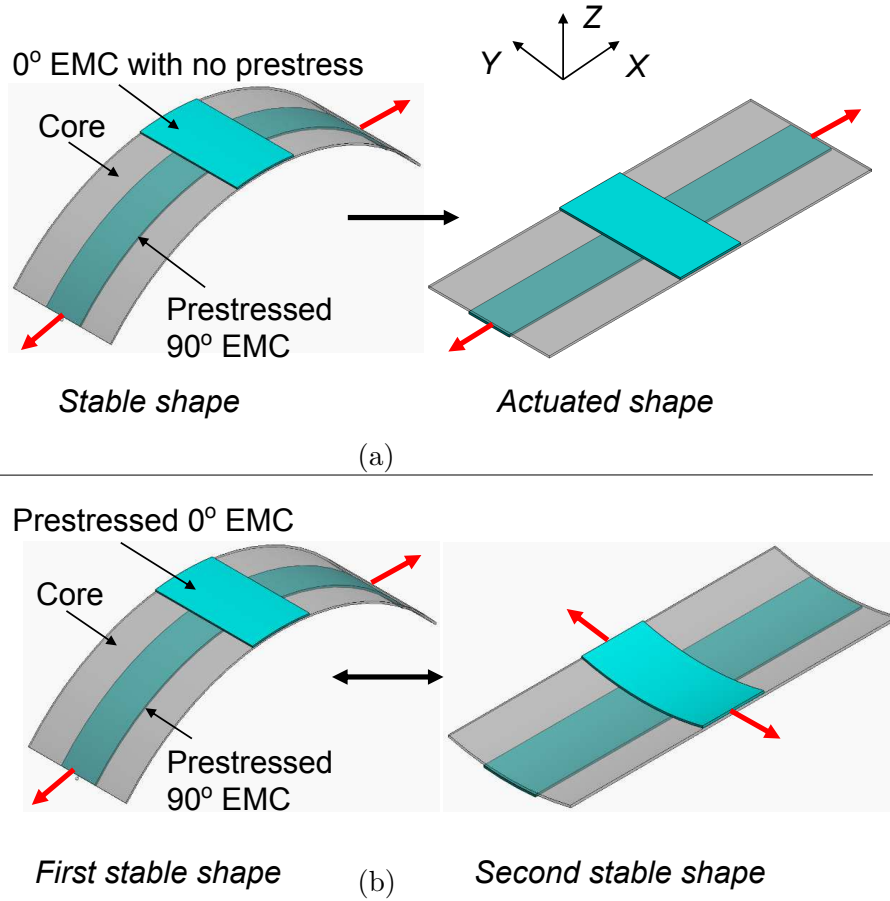


Figure 6.1: Stable shapes of a mechanically-prestressed laminated composite.

6.2 Analytical model

In this work, a mechanically-prestressed bistable composite is modeled as a laminated plate as described in Chapter 4. Cubic polynomials for displacement are sufficient to accurately simulate the stable shapes of the composite. However, an accurate description of shape bifurcation phenomenon requires the use of higher order polynomials [99]. The iterative solution of nonlinear equations involving high-order displacement polynomials has been shown to be numerically ill-conditioned [117]. For purposes of numerical conditioning, composite displacements in the current model are written in non-dimensional form.

6.2.1 Non-dimensional composite displacements

The method for scaling used here was first presented by Stein [118]. It was implemented by Diaconu and Weaver [119] in the analysis of postbuckled orthotropic laminates, and by Pirrera et al. [99] in the high-order modeling of bistable laminates. The nondimensional displacements $(\tilde{u}_0, \tilde{v}_0, \tilde{w}_0)$ at an arbitrary point on the composite's geometric mid-plane are expressed in terms of its true displacements (u_0, v_0, w_0) in the (X, Y, Z) directions as:

$$\tilde{u}_0 = \frac{u_0}{U_0}, \quad \tilde{v}_0 = \frac{v_0}{V_0}, \quad \tilde{w}_0 = \frac{w_0}{W_0}, \quad (6.1)$$

where, U_0, V_0 , and W_0 are scaling factors defined in terms of composite stiffness as:

$$U_0 = \frac{\sqrt{A_{11}^* A_{22}^* D_{11}^* D_{22}^*}}{L_x}, \quad V_0 = U_0 \frac{L_x}{L_y}, \quad W_0 = \sqrt{U_0 L_x}. \quad (6.2)$$

The terms A^* and D^* are defined as:

$$A^* = A^{-1}, \quad D^* = D - BA^{-1}B, \quad (6.3)$$

where A , B , and D are the extensional, coupled extension-bending, and bending stiffness matrices [120] of an n -layered composite expressed in terms of the plane-stress reduced stiffnesses Q_{ij} , $\{i, j = 1, 2, 6\}$ as:

$$A_{ij} = \sum_{k=1}^n Q_{ij}^{(k)} (z_{k+1} - z_k), \quad B_{ij} = \frac{1}{2} \sum_{k=1}^n Q_{ij}^{(k)} (z_{k+1}^2 - z_k^2), \quad D_{ij} = \frac{1}{3} \sum_{k=1}^n Q_{ij}^{(k)} (z_{k+1}^3 - z_k^3). \quad (6.4)$$

The x and y coordinates are scaled as follows:

$$\tilde{x} = \frac{x}{L_x}, \quad \tilde{y} = \frac{y}{L_y}. \quad (6.5)$$

The ratio of EMC width to core width is defined as per (4.21).

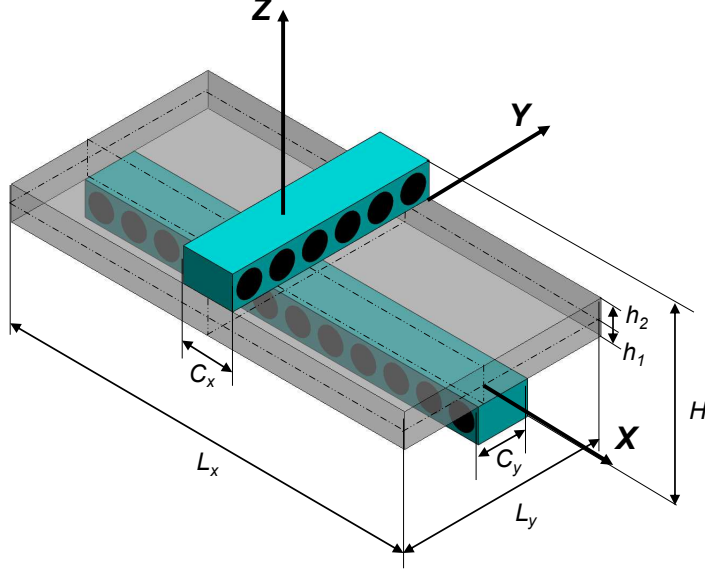


Figure 6.2: Schematic representation of a mechanically-prestressed bistable laminate.

6.2.2 Strain model

Strains of the composite (Figure 6.2), defined using a Lagrangian description as per Von Karman's hypothesis [102], are written in terms of non-dimensional displacements $(\tilde{u}, \tilde{v}, \tilde{w})$ as:

$$\epsilon_x = \frac{U_0}{L_x} \frac{\partial \tilde{u}}{\partial \tilde{x}} + \frac{1}{2} \frac{W_0^2}{L_x^2} \left(\frac{\partial \tilde{w}}{\partial \tilde{x}} \right)^2, \quad (6.6)$$

$$\gamma_{xy} = \frac{U_0}{L_y} \frac{\partial \tilde{u}}{\partial \tilde{y}} + \frac{V_0}{L_x} \frac{\partial \tilde{v}}{\partial \tilde{x}} + \frac{W_0^2}{L_x L_y} \frac{\partial \tilde{w}}{\partial \tilde{x}} \frac{\partial \tilde{w}}{\partial \tilde{y}}, \quad (6.7)$$

$$\epsilon_y = \frac{V_0}{L_y} \frac{\partial \tilde{v}}{\partial \tilde{y}} + \frac{1}{2} \frac{W_0^2}{L_y^2} \left(\frac{\partial \tilde{w}}{\partial \tilde{y}} \right)^2. \quad (6.8)$$

According to classical laminate theory, displacements of the composite can be written in terms of mid-plane displacements ($\tilde{u}_0, \tilde{v}_0, \tilde{w}_0$) as:

$$\tilde{u}(\tilde{x}, \tilde{y}, z) = U_0 \tilde{u}_0(\tilde{x}) - z \frac{W_0}{L_x} \frac{\partial \tilde{w}_0}{\partial \tilde{x}}, \quad (6.9)$$

$$\tilde{v}(\tilde{x}, \tilde{y}, z) = V_0 \tilde{v}_0(\tilde{y}) - z \frac{W_0}{L_y} \frac{\partial \tilde{w}_0}{\partial \tilde{y}}, \quad (6.10)$$

$$\tilde{w}(\tilde{x}, \tilde{y}, z) = W_0 \tilde{w}_0(\tilde{x}, \tilde{y}). \quad (6.11)$$

Equations (6.9) - (6.11) are substituted into (6.6) - (6.8) to obtain the relations for composite strain in terms of displacements of the geometric mid-plane.

Displacements of the mid-plane, described using complete polynomials of order O_p , are of the form:

$$\tilde{u}_0 = \sum_{q=0}^{O_p} \sum_{p=0}^q b_{p,q-p} \tilde{x}^p \tilde{y}^{p-q}, \quad (6.12)$$

$$\tilde{v}_0 = \sum_{q=0}^{O_p} \sum_{p=0}^q c_{p,q-p} \tilde{x}^p \tilde{y}^{p-q}, \quad (6.13)$$

$$\tilde{w}_0 = \sum_{q=0}^{O_p} \sum_{p=0}^q d_{p,q-p} \tilde{x}^p \tilde{y}^{p-q}, \quad (6.14)$$

where O_p is the chosen order of the polynomial and $b_{p,q-p}$, $c_{p,q-p}$, and $d_{p,q-p}$ are the unknown coefficients that are to be evaluated.

6.2.3 Strain energy computation

The potential energy (Φ) of the composite is expressed in terms of the material and geometric properties of the laminae as:

$$\Phi = \int_V \left(\Phi_1 + Q_{12} \epsilon_x \epsilon_y + \Phi_2 + \frac{1}{2} Q_{16} \gamma_{xy} \epsilon_x + \frac{1}{2} Q_{26} \gamma_{xy} \epsilon_y + \frac{1}{2} Q_{66} \gamma_{xy}^2 \right) dV. \quad (6.15)$$

The limits of integration are shown in Table 6.1. In this composite, the core is a linear isotropic material whereas the 90° and 0° EMCs are anisotropic materials with linear

Table 6.1: Limits of integration for the computation of the total potential energy of a mechanically-prestressed bistable laminate.

Lamina	\tilde{x}	\tilde{y}	z
90° EMC	$(-1/2, 1/2)$	$(-\alpha_{90}/2, \alpha_{90}/2)$	$(-H/2, -h_1)$
Core	$(-1/2, 1/2)$	$(-1/2, 1/2)$	$(-h_1, h_2)$
0° EMC	$(-\alpha_0/2, \alpha_0/2)$	$(-1/2, 1/2)$	$(h_2, H/2)$

strains in all directions except x and y , respectively. For linearly strained directions, Φ_1 and Φ_2 are written as per Hooke's law as $0.5(Q_{11}\epsilon_x^2)$ and $0.5(Q_{22}\epsilon_y^2)$ respectively. In the direction of prestrain, the constitutive law of an EMC is described as per (2.18). Strain energies Φ_1 and Φ_2 of the 90° and 0° EMCs respectively are computed as the integral of σ_x and σ_y based on (2.18). This gives for the two EMCs:

$$\Phi_1^{(90)} = f(\epsilon_{90} - \epsilon_x), \quad \Phi_2^{(0)} = f(\epsilon_0 - \epsilon_y). \quad (6.16)$$

It is worth noting that strains ϵ_x , ϵ_y , and γ_{xy} of the composite are expressed in terms of scaled displacements and coordinates for purposes related to numerical conditioning. On the other hand, prestrains ϵ_{90} and ϵ_0 , applied to the EMCs prior to lamination, represent the input energy content and are hence not scaled.

6.2.4 Work done by external forces

Four cases of external forces acting on the composite are studied in this work (Figure 6.3). The composite, shown in the YZ plane, is assumed to be clamped at its midpoint O and curved about the X axis in the unactuated state. Cases 1 to 3 represent actuation forces applied at points $A(0, -0.5)$ and $B(0, 0.5)$ whereas case 4 represents a uniformly distributed operational load.

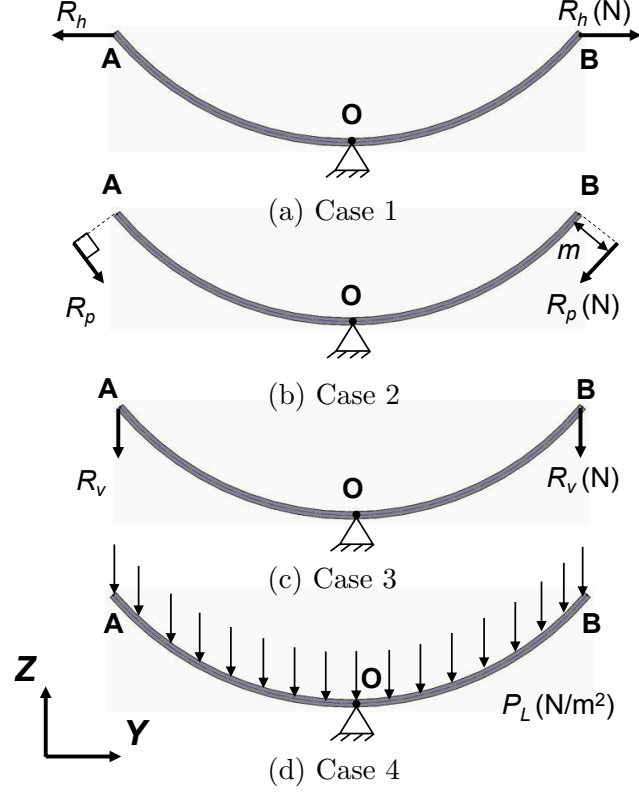


Figure 6.3: Four cases for external forces applied on a bistable composite to effect snap-through into the second stable shape. The first three cases shown in (a) through (c) are point-wise forces whereas case four shown in (d) is a uniformly distributed force.

Case 1

The composite is actuated by applying a pair of equal and opposing forces $-R_h \hat{j}$ and $R_h \hat{j}$ at A and B respectively (Figure 6.3(a)). The variational work done by \vec{R}_h is expressed as:

$$\delta W_h = -R_h V_0 \tilde{v}_0|_{\{0,-0.5\}} + R_h V_0 \tilde{v}_0|_{\{0,0.5\}} \quad (6.17)$$

Case 2

In-plane actuation is represented by a pair of forces at A and B of magnitude R_p acting in a direction tangential to the geometric mid-plane (Figure 6.3(b)). The force

\vec{R}_p , located at an offset m from the midplane, is defined as:

$$\vec{R}_{p(A)} = \frac{R_p}{L_y} \frac{\partial \vec{r}_p}{\partial \tilde{y}} \Big|_{\{0, -0.5\}}, \quad \vec{R}_{p(B)} = -\frac{R_p}{L_y} \frac{\partial \vec{r}_p}{\partial \tilde{y}} \Big|_{\{0, 0.5\}} \quad (6.18)$$

The point of application of the force \vec{r}_p is the sum of the position vector (\vec{r}) on the geometric mid-plane and the normal (\vec{n}) at \vec{r}

$$\vec{r}_p = \vec{r} + m \cdot \vec{n} \quad (6.19)$$

$$= \left((L_x \tilde{x} + U_0 \tilde{u}_0) \hat{i} + (L_y \tilde{y} + V_0 \tilde{v}_0) \hat{j} + W_0 \tilde{w}_0 \hat{k} \right) + \frac{m}{L_x L_y} \cdot \left(\frac{\partial \vec{r}}{\partial \tilde{x}} \times \frac{\partial \vec{r}}{\partial \tilde{y}} \right) \quad (6.20)$$

The variational work done by the pair of forces \vec{R}_p (Figure 6.3(c)) is written as:

$$\delta W_p = \vec{R}_{p(A)} \cdot \delta \vec{r}_p \Big|_{\{0, -0.5\}} + \vec{R}_{p(B)} \cdot \delta \vec{r}_p \Big|_{\{0, 0.5\}} \quad (6.21)$$

Case 3

The variational work done on a composite that is actuated by a transverse force $-R_v \hat{k}$ acting at A and B is written as:

$$\delta W_v = -R_v W_0 \tilde{w}_0 \Big|_{\{0, -0.5\}} - R_v W_0 \tilde{w}_0 \Big|_{\{0, 0.5\}}. \quad (6.22)$$

Case 4

The operational load acting on a composite is represented as a uniformly distributed force (P_L) acting in the $-Z$ direction (Figure 6.3(d)). The corresponding variational work is given by:

$$\delta W_l = \int_{-0.5}^{0.5} \int_{-0.5}^{0.5} P_L W_0 \tilde{w}_0 dx dy \quad (6.23)$$

The net variational work (δW) done on the composite by various actuation forces is written as:

$$\delta W = \delta W_p + \delta W_h + \delta W_v + \delta W_l \quad (6.24)$$

6.2.5 Computation of composite shape

The equilibrium shapes of the composite are obtained as a function of actuation force by minimizing the net energy using the variational Rayleigh-Ritz approach:

$$\sum_i \frac{\partial(\Phi - W)}{\partial C_i} = 0, \quad (6.25)$$

where $C_i = \{b_{p,q-p}, c_{p,q-p}, d_{p,q-p}\}$ for p ranging from 0 to q and q ranging from 0 to O_p . The expressions for U_T , W , and their partial derivatives are derived in symbolic form using MAPLE. The nonlinear equations resulting from (6.25) are solved in MATLAB using the Newton-Raphson method. Composite shape is computed for various polynomial orders of the strain model. Prior to computation, the number of terms in the complete displacement polynomials are reduced by applying the conditions of symmetry. Since the composite is clamped at the center, \tilde{u}_0 is odd in x and even in y , \tilde{v}_0 is even in x and odd in y , and \tilde{w}_0 is even in x and y and is zero at the center. The number of unknown coefficients for each polynomial order is shown in Table 6.2. The order of the strain energy integrand involving a mechanically-prestressed EMC is greater than twice that of the integrand for a thermally-cured FRP laminate with linear matrix material (Table 6.2); the order is directly proportional to the computational cost of the model. For polynomial orders 3 to 5, simulation was carried out on a standalone workstation whereas higher order polynomial models were simulated using clusters at the Ohio Supercomputer Center [121]. Computational cost can be lowered by 20% by reducing σ in (2.18) to a cubic function.

6.3 Experiments

Experimental measurement of the snap-through force of a bistable composite involves the application of a controlled force or displacement on the composite in a quasistatic

Table 6.2: Size of the displacement polynomials and strain energy integrand.

Order (n)	Reduced unknowns	Order of $d\Phi(\tilde{x}, \tilde{y})$	
		Prestressed EMC	Thermally-cured FRP
3	8	10	4
4	11	30	12
5	17	30	12
6	21	50	20
7	29	50	20
8	35	70	28
9	44	70	28

setup. To this end, Dano and Hyer [122] applied a moment at two points on the composite in a three-point bending setup. They performed a force-controlled experiment where strain was measured using bonded strain gauges. Potter et al. [115] developed a position-controlled experiment to measure the composite's displacement and the applied force simultaneously. The sample was placed on its edges on a low-friction aluminum plate and a transverse point load was applied at the center using a steel ball. A perforated plate with holes in a 11×11 grid was aligned inline with the composite. Deformation at each position increment was measured through the holes with a caliper. Experiments revealed that the snap-through phenomenon comprises multiple events. In particular, one half of the composite undergoes smooth shape transition leading to a partial snap-through following which the other half snaps-through to the second stable shape. Cantera et al. [98] employed Potter's approach but used rods to suspend the composite at its vertices for reduced friction. Tawfik et al. [123] presented an improved frictionless experimental setup in which the edges of the composite slide on an air cushion.

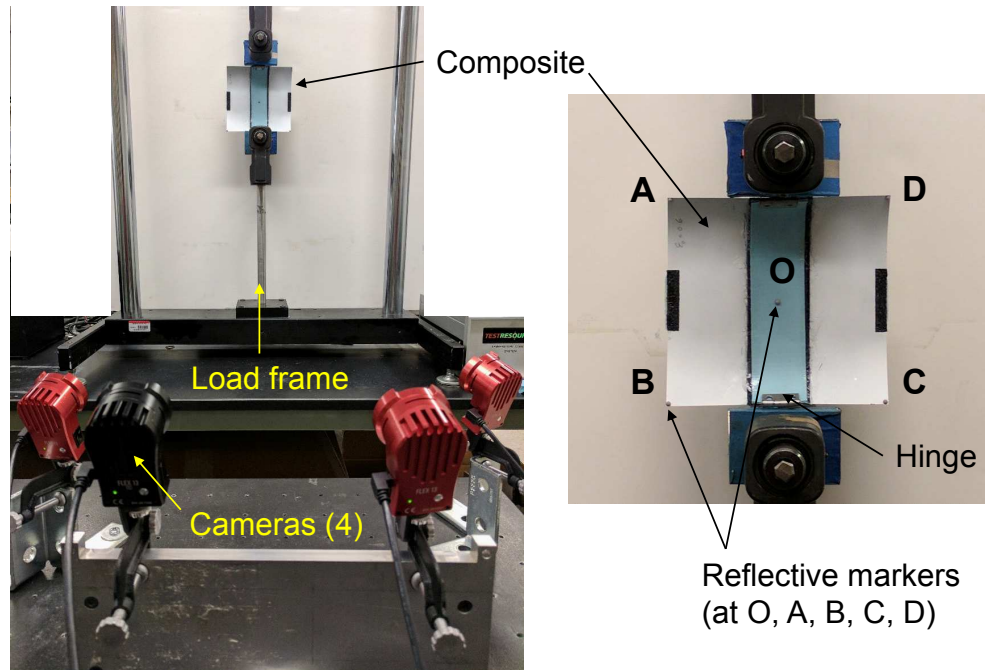


Figure 6.4: Experimental setup to record shape transition in a bistable composite.

The proposed experimental procedure involves flattening a curved composite until snap-through in a uniaxial tensile test (Figure 6.4). Given that the stable shapes of the composite are weakly coupled, it is sufficient to record actuation from the first shape to the second. The straight edges AD and BC of a cylindrical composite are held in a load frame at their midpoint using small hinges. The hinges are bonded to the EMC on the concave side and their axis of rotation is parallel to the respective straight edges. There is no sliding or rolling contact with the composite. The head of the load frame (Test Resources Inc.) moves vertically and measures the force profile using an inline 200 N load cell. The displacement of the frame head is recorded by an in-built rotary encoder. Tip displacement of the composite is separately measured by a 3D motion capture system; the frame measures displacement only up to snap-through. Betts et al. [108] used a video camera system that tracks circular markers to measure the stable shapes of a bistable laminate. In the present setup, hemispherical reflective

markers of 3 mm diameter are placed at the center (O) and the four vertices (A , B , C , D) of a square laminate. A set of four still cameras (OptiTrack, Natural Point Inc.), with a resolution of 1.3 megapixels, is used to record the position of each marker through coordinate triangulation. The cameras are mounted to have a capture volume of $1.1 \times 1.1 \times 1.1$ (m).

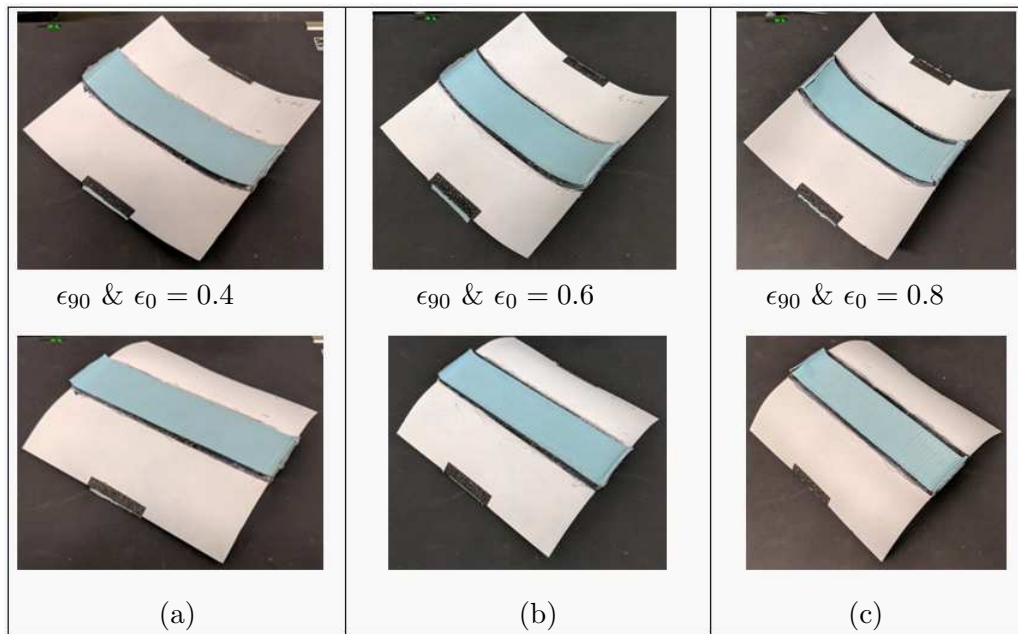


Figure 6.5: Fabricated samples of a mechanically-prestressed bistable laminate.

Square test samples are fabricated in the 90° EMC/core/ 0° EMC configurations with equal prestrain values of 0.4, 0.6, and 0.8 in both EMCs (Figure 6.5) [124]. The dimensions of the laminae are shown in Table 4.3. Prior to testing, the cameras are calibrated to an accuracy of 0.021 mm by waving a calibration wand that contains inline markers over a span of 250 mm. The coordinate system is set using markers mounted on the ends of a right angle measure. To simplify data processing, the axes (X, Y, Z) are defined such that the XY plane is aligned parallel to the plane

containing the four vertices (markers) of the composite. Quasistatic tensile tests are conducted on each sample by moving the frame head at a rate of 5 mm/min until the composite snaps into its second shape. The load frame and the motion capture system are synchronized to record displacement at 10 frames per second. Each sample is tested five times for repeatability. Measurements from the fifth test are presented in this paper.

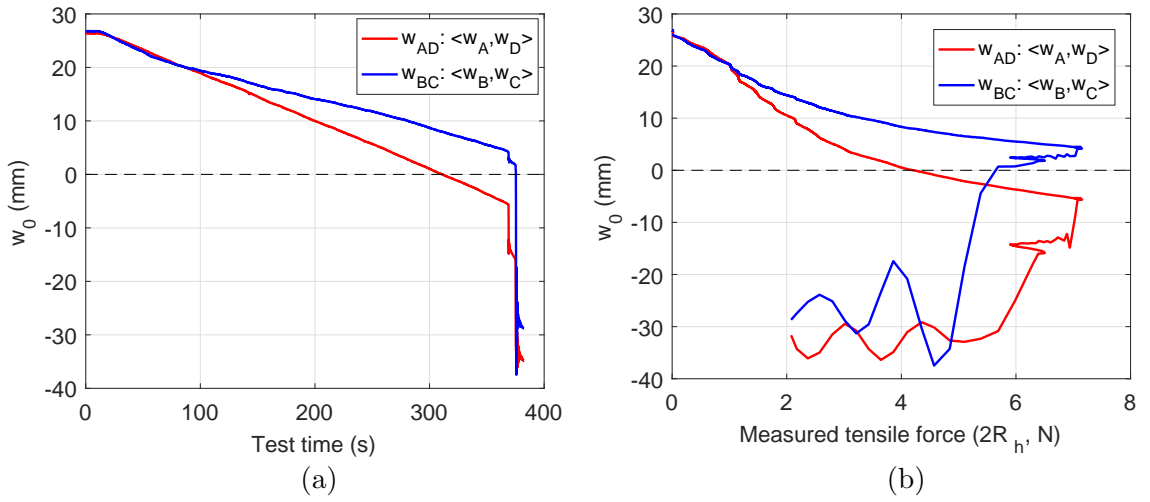


Figure 6.6: Measured out-of-plane displacements of \overline{AD} and \overline{BC} , as a function of (a) time and (b) actuation force, in a composite with $\epsilon_0 = \epsilon_{90} = 0.8$.

The out-of-plane tip deflection w_0 of the composite is calculated for each straight edge (\overline{AD} , \overline{BC}) as the average of the z displacements of its vertices. The respective deflections w_{AD} and w_{BC} of \overline{AD} and \overline{BC} evolve differently with time and actuation force as shown in Figure 6.6. At $w_{AD} = 0$, $w_{BC} > w_{AD}$ and w_{AD} is continuous (Figure 6.6(a)). In the vicinity of $w_{BC} = 0$, both w_{AD} and w_{BC} are discontinuous (Figure 6.6(b)). The sharp drop in displacement at the discontinuity, occurs in two stages. The drop in force in the first stage is partial, indicating an intermediate shape in the snap-through event (Figure 6.6(b)). Snap-shots of the shape transition

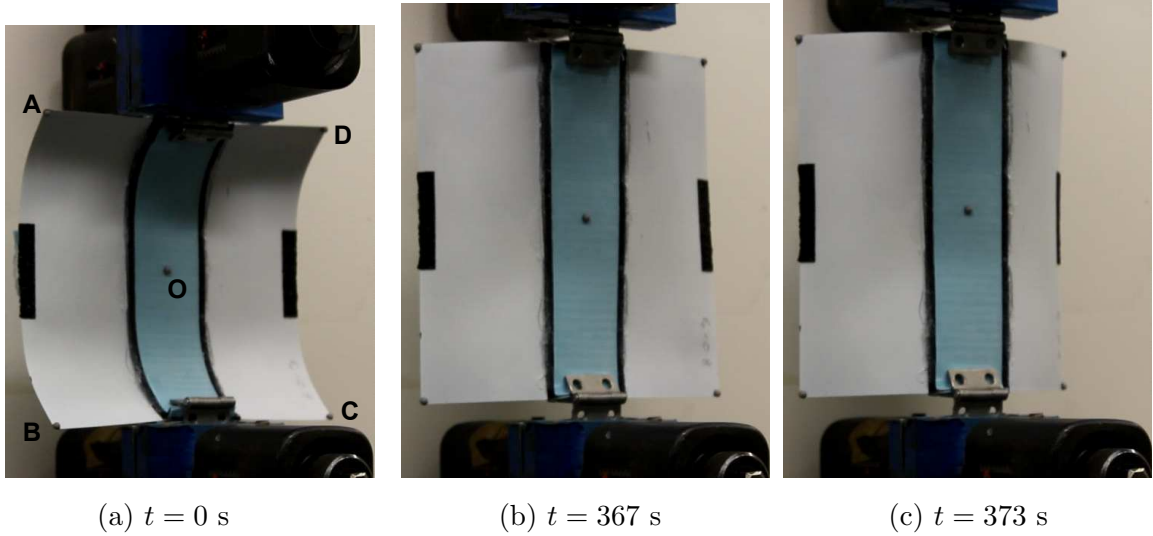


Figure 6.7: Shape of a composite with $\epsilon_0 = \epsilon_{90} = 0.8$ in (a) the unactuated first stable state, (b) intermediate stable state during snap-through, and (c) second stable state post snap-through.

of the composite are shown in Figure 6.7. Upon flattening, the composite undergoes a partial snap-through into an intermediate stable shape that has \overline{AD} in its second curved shape while \overline{BC} remains straight (Figure 6.7(b)). Flattening the composite further results in a full-snap through in which \overline{BC} snaps into the second curved shape and both edges reach equilibrium simultaneously (Figure 6.7(c)). The snap-through behavior of the tested samples is similar to those of the thermally-cured FRP laminates tested by Potter et al. [115].

6.4 Results and discussion

Results based on experiments and model-based simulations are presented in the following sequence:

- The stable shapes of a square laminate are simulated as a function of ϵ_{90} and ϵ_0 for various orders of the displacement polynomials. Subsequent results are presented using a chosen high-order polynomial.

- The effect of aspect ratio on the bistability regime of rectangular laminates is simulated as a function of ϵ_{90} and ϵ_0 .
- Work done on a square composite is computed for forces defined in cases 1 to 3. The analytical model is validated against measured data.
- Sensitivity of the composite's tip displacement (w_0), stiffness to transverse pressure (K_L), and snap-through work (W_p) done by an in-plane actuator, is analyzed for a given change in core modulus and thickness.

Simulations conducted using the analytical model presented in section 6.2 yield two stable cylindrical shapes of the composite in the unactuated state. The dimensions and measured material properties of the laminae used for both simulation and experiments are shown in Tables 4.3 and 4.2 respectively. For the calculation of the scaling factors U_0 , V_0 , and W_0 , E_1 of a 90° EMC is averaged to be 1.5 MPa over a strain range of 0 to 1. In the following analyses, the composite is considered to be initially curved about the X axis.

The tip displacement (w_0) of a stable square composite in its unactuated state is calculated as a function of prestrain ratio ϵ_r ($= \epsilon_0/\epsilon_{90}$) ranging from 0.01 to 1 while ϵ_{90} is maintained constant at 1. Figure 6.8 shows w_0 as a function of ϵ_r for various orders of the displacement polynomials; the first half of ϵ_r is emphasized to illustrate the loss in bistability at its lower extremity. Displacement w_0 , corresponding to the first shape, decreases with a decrease in ϵ_r until a critical ratio ϵ_{rc} where the shape ceases to exist. Below ϵ_{rc} , the composite has only the second cylindrical shape. Shape 2, as indicated in Figure 6.8, is influenced by ϵ_{90} and is invariant to changes in ϵ_0 when $\epsilon_r < 1$. Since the stable shapes are weakly coupled, similar results are obtained at the higher extremity of ϵ_r ; ϵ_{90} ranging from 0 to 1 at $\epsilon_0 = 1$ represents the higher extremity. Such an envelope for bistability is characteristic of laminates that have

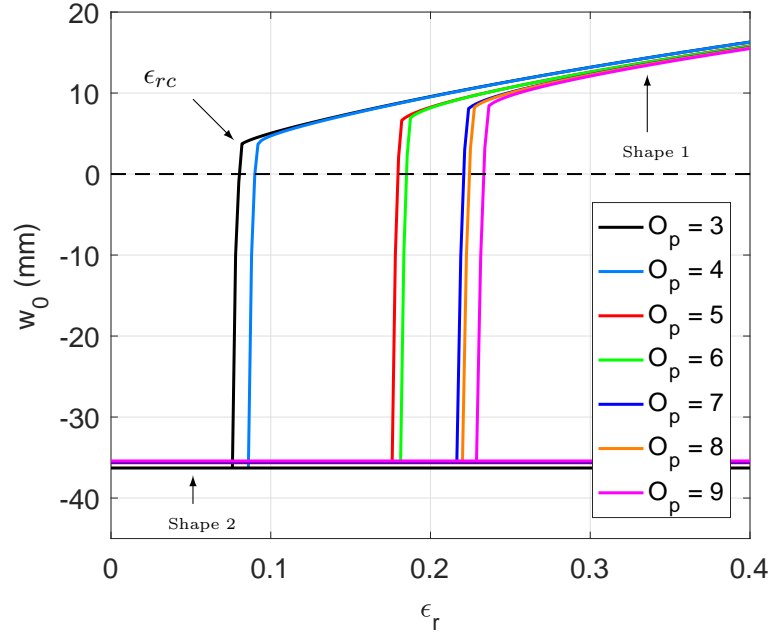


Figure 6.8: Stable shapes of the composite as a function of prestrain ratio ϵ_r for $\epsilon_{90} = 1$.

two sources of prestress. Thermally cured FRP laminates have a single source of residual stress and exhibit a saddle shape (small deformation) outside the domain of bistability.

With an increase in polynomial order from three to nine, ϵ_{rc} increases as well as converges to a particular value. Further, the displacement w_0 at ϵ_{rc} is higher in higher-order models. For $\epsilon_r > \epsilon_{rc}$, the difference in w_0 among various polynomial orders is negligible. ϵ_{rc} for each polynomial of type O_{2p} ($p > 2$) is close to that of the odd-order polynomial of type O_{2p-1} . Due to the imposed symmetry conditions on \tilde{u}_0 , \tilde{v}_0 , and \tilde{w}_0 , the additional terms in O_{2p} relative to O_{2p-1} are seen only in \tilde{w}_0 . Therefore, out-of-plane deflection w_0 has a minor effect on ϵ_{rc} whereas in-plane strain has a dominant effect. In the third, seventh, and ninth order cases, ϵ_{rc} is 0.082, 0.224, and 0.236 respectively. Given the marginal increase in model accuracy from seventh

to ninth order, seventh order displacement polynomials are chosen for further analysis in the interest of computational cost (see Table 6.2).

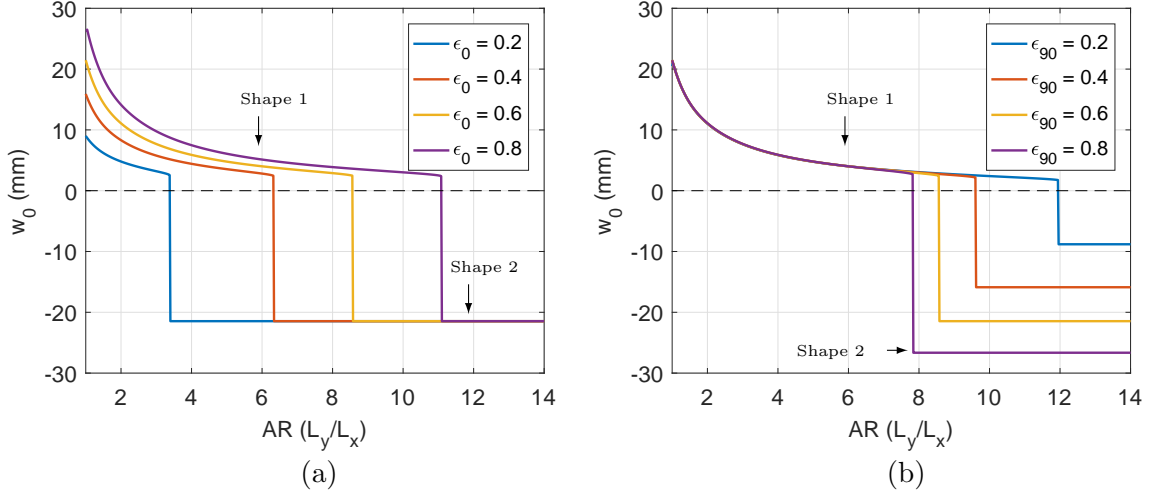


Figure 6.9: Effect of aspect ratio AR on the stable shapes of the composite as a function of (a) ϵ_0 while $\epsilon_{90} = 0.6$ and (b) ϵ_{90} while $\epsilon_0 = 0.6$.

The effect of aspect ratio AR (L_y/L_x) of a rectangular laminate is simulated at $L_x = 152.4$ mm by varying one EMC prestrain at a time. In the first case, a constant prestrain $\epsilon_{90} = 0.6$ is maintained in the EMC on the convex face (Figure 6.9 (a)). The value of AR corresponding to the loss of bistability increases with an increase in ϵ_0 . Beyond the critical value of AR , only one stable cylindrical shape exists (as in Figure 6.1(a)). When ϵ_0 is treated to be constant (at 0.6), the limiting AR increases with an increase in ϵ_{90} (Figure 6.9(b)). An increase in aspect ratio for a given width is associated with an increase in the strain energy of the core, thereby requiring higher prestrains with ϵ_r close to 1 for the existence of bistability.

Work done on the composite by external forces in cases one to three (Figure 6.3) is computed as per (6.17), (6.21), and (6.22). For comparison, W_h , W_p , and W_v are plotted as a function of tip displacement w_0 .

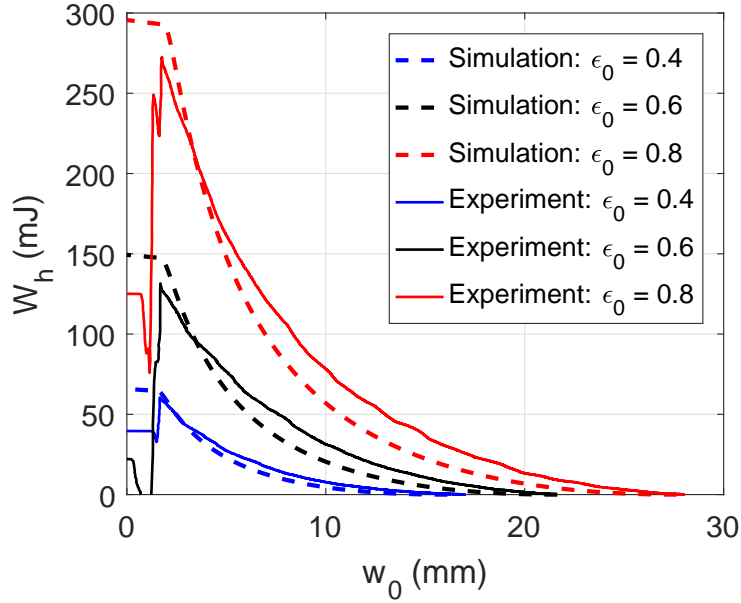


Figure 6.10: Work done by an axial force R_h on a composite with $\epsilon_{90} = \epsilon_0$.

The simulated actuation work W_h is compared with the corresponding experimentally measured values to validate the analytical model (Figure 6.10). Flattening of the composite is associated with an exponential increase in W_h up to the point of snap-through. Post snap-through, experiments indicate a small drop in W_h followed by a sharper drop before reaching a steady value as w_0 tends to zero. The existence of two energy peaks is consistent with the observation (section 6.3) that in the chosen laminate configuration, snap-through occurs in two stages. Energy peaks are not seen in the simulated curves because displacements are calculated as a function of a monotonically increasing force R_h ; at snap-through, there is a sharp drop in w_0 but not R_h . For all practical purposes, snap-through force and tip displacement profile are sufficient to design actuators for bistable composites. The simulated energy profile is in agreement with experimental data. The model over-predicts snap-through energy

by 7.7%, 12.1%, and 6.7% with respect to the measured value (higher peak) in samples with prestrains of 0.4, 0.6, and 0.8, respectively. The corresponding error in the simulated tip displacement at snap-through relative to the measured displacement (at higher peak) is 6.2%, 2.43%, and -8.8%. Higher model accuracy can be achieved by increasing the order of the displacement polynomials.

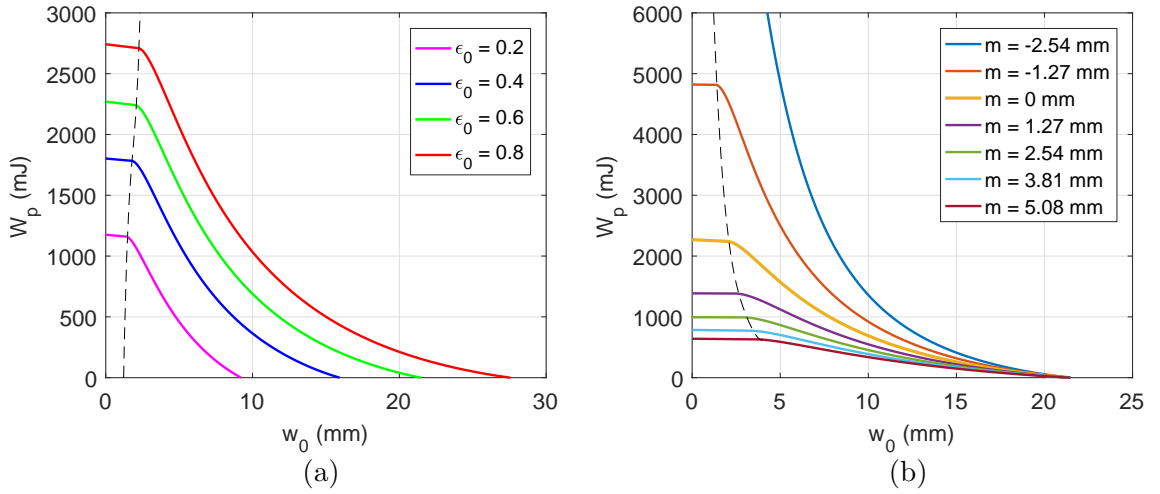


Figure 6.11: Work done by an in-plane actuation force R_p as a function of (a) ϵ_0 where $m = 0$ and $\epsilon_{90} = \epsilon_0$, and (b) m where $\epsilon_0 = \epsilon_{90} = 0.6$.

Figure 6.11(a) shows the energy profile pertaining to an in-plane force R_p applied at the geometric mid-plane ($m = 0$); prestrains ϵ_0 and ϵ_{90} are assumed to be equal. The energy required for snap-through increases with an increase in ϵ_0 . Further, snap-through is initiated at a higher displacement w_0 for higher values of ϵ_{90} . Figure 6.11(b) shows the energy profile for non-zero values of the force offset m from the geometric mid-plane at constant values of ϵ_0 and ϵ_{90} of 0.6. Increasing the offset towards the convex face of the composite ($m > 0$) results in a decrease in snap-through energy. This behavior is attributed to the associated reduction in the total displacement

recovered by a given R_p (see (6.9) - (6.11)). Moving the actuator towards the concave face results in an exponential increase in snap-through energy.

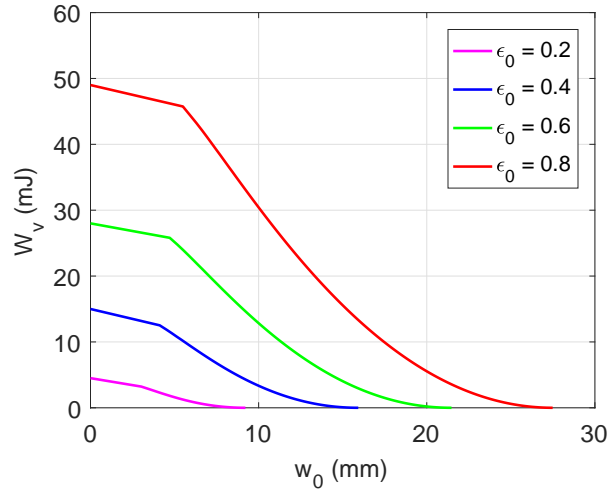


Figure 6.12: Work done by a transverse force R_v as function of ϵ_0 where $\epsilon_{90} = \epsilon_0$.

The actuation energy associated with a transverse force is simulated for various values of ϵ_0 assuming ϵ_0 and ϵ_{90} are equal (Figure 6.12). While W_v has a similar trend as W_h and W_p , it is worth noting that force R_v varies linearly with w_0 whereas R_h and R_p vary exponentially (not illustrated). A comparison of the various energy profiles of actuation forces acting at points A and B (Figure 6.3) shows that for a given actuation stroke, W_h is an order of magnitude higher than W_v and W_p is an order of magnitude higher than W_h . Therefore, the minimum and maximum energy configurations are associated with a pure moment and a pure in-plane force respectively. Also, the displacement w_0 at which snap-through occurs is highest in the case of a pure-moment and least when actuated by an in-plane force.

6.5 Sensitivity study

The parameters that quantify the composite's morphing performance are: displacement w_0 in the unactuated state; stiffness K_L to transversely-applied pressure P_L (case 4); and work W_p done by an in-plane force R_p to achieve snap-through from a stable initial shape. Figure 6.13(a) shows the effect of core modulus ranging from 100 to 200 GPa on the composite's performance parameters; thickness is maintained constant at 0.127 mm. Each parameter is normalized with respect to the lowest value in the simulated range. Increasing the modulus by 100 GPa yields a reduction in w_0 by 48.3%. On the other hand, K_L , and W_p increase by 93.3%, and 18.1% respectively. Sensitivity of the parameters to core thickness is shown in Figure 6.13(b); core modulus is assumed to be 100 GPa. Doubling the thickness of the core results in -83.8%, 520%, and -10.5% change in w_0 , K_L , and W_p respectively.

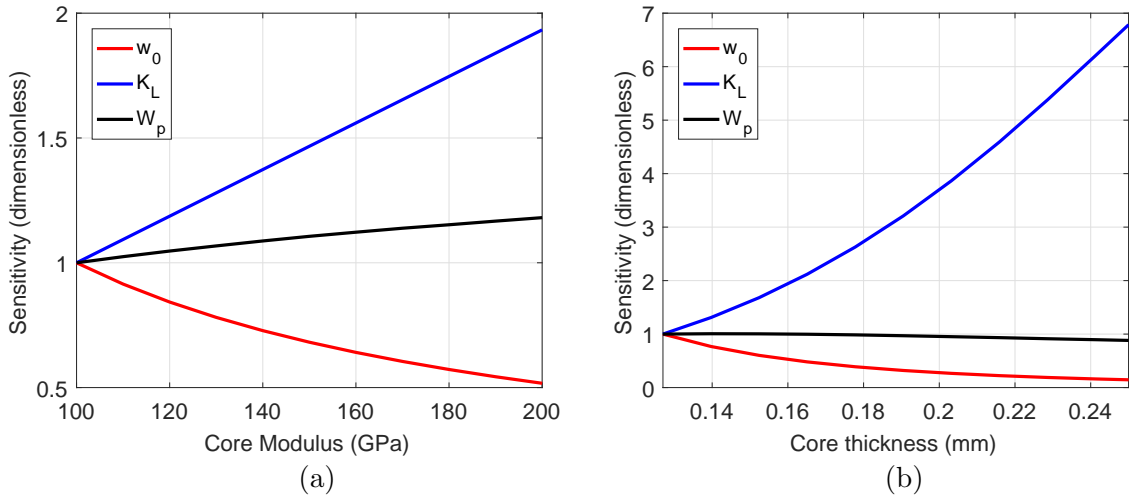


Figure 6.13: Sensitivity of the composite's performance to (a) core modulus and (b) core thickness.

An increase in core modulus or thickness translates to an increase in strain energy and hence a decrease in out-of-plane deformation for a given prestress configuration; deformation is more sensitive to thickness change. A decrease in deformation is accompanied by an increase in stiffness for any modulus or thickness. Stiffness is more sensitive to thickness than to modulus due to the cubic dependence of the stiffness matrix coefficients on thickness in (6.4). Higher actuation work is required to recover the strain energy associated with higher core modulus. Among the three performance parameters, stiffness is the most sensitive to the properties of the core whereas actuation energy is the least.

The limits of bistability of rectangular laminates with two sources of prestress are studied for the first time through this work. A novel experimental procedure, involving friction-free tensile testing and 3D motion capture, is presented to study the snap-through characteristics of mechanically-prestressed composites. Experiments show that these composites exhibit a multi-stage snap-through phenomenon akin to that seen in thermally-cured FRP laminates. A high-order strain model is developed to accurately determine the domain of bistability of the composite as a function of prestrain ratio. The aspect ratio limit for bistability can be extended by increasing prestrain in both EMCs and by maintaining the prestrain ratio close to one. A distinct feature in orthogonal-ply bistable composites with two sources of mechanical prestress is that they need not be symmetric along the thickness. Further, loss in bistability due to insufficient prestress in one EMC yields a single cylindrical shape. A comparison of various actuation modes using the experimentally-validated analytical model shows that the application of a pure moment requires the least amount of energy. In-plane actuation, which is made practically viable by smart materials, is relatively energy efficient when the actuator is mounted on the convex face of a curved composite. Among the evaluated performance parameters, out-of-plane stiffness and actuation

(in-plane) energy are respectively found to be the most and least sensitive to the properties of the core. Mechanically-prestressed composites offer possibilities for the design of active bistable elements for morphing panels.

Chapter 7

Stress-Biased Laminated Composites for Smooth Folds in Origami Structures

Overview

This chapter presents a strategy for the creation of smooth folds in flat and curved laminated composites; the approach is applicable to smart folding structures with reconfigurable creases. An analytical laminated-plate model, based on strain energy minimization, is presented to calculate fold angle as a function of laminate parameters. Folds, realized as localized curvature at a crease, are modeled using piecewise displacement polynomials. Folded composites, created by laminating prestressed fiber-reinforced elastomers with zero in-plane Poisson's ratio, are fabricated for demonstration and model validation. The simulated out-of-plane deflection of the curved creases is in agreement with measurements. Parametric studies are conducted to characterize the sensitivity of fold angle and sharpness to variations in laminate properties. Narrow creases require higher prestress for a given fold angle than wider creases. Fold sharpness can be maximized by minimizing crease width and thickness. Anisotropy in the prestressed elastomer is a tradeoff between achieving zero Poisson's ratio for unidirectional prestress and maximizing the range of crease orientations for foldability.

7.1 Introduction

A stress-biased composite comprises a creased constraining layer laminated to a prestressed layer (Figure 7.1(a)); a constraining layer is flexible but has high in-plane modulus relative to the prestressed layer. The modulus or thickness of the constraining layer in the creased region is much lower than that of the faces (Figures 7.1(a) and 7.1(b)). A prestressed layer is highly stretchable and is laminated in the stretched state across one or more creases. Figure 7.1(c) shows a demonstration of folds in a stress-biased composite; fabrication details are discussed in section 8.5.1. In origami terms, prestressed composites exhibit mountain folds at equilibrium. Valley folds can be created by laminating the prestressed layer on the opposite face of the constraining layer. Theoretically, two prestressed laminae are sufficient to completely fold the composite. This simple yet powerful approach to create folds poses several research questions related to: fold angle at a crease with rigid faces as a function of magnitude and orientation of prestress; and effect of crease width, modulus, and thickness on fold angle and sharpness. To address these research questions, an analytical laminated-plate model is developed in this work.

Mechanical prestress in folded composites provides several additional design possibilities. For example, curved faces can be created in a folded structure by extending the prestressed laminae onto the faces. This feature is particularly useful in the folding of curved shells [125, 126]. Prestress also enables bistability [107] in the faces of a fold. Origami tessellations such as Miura-Ori could serve as a constraining layer, resulting in novel metamaterial characteristics. To preserve surface area post-folding, the prestressed layer can be extended beyond the composite to serve as a stretchable skin on the morphing structure. Therefore, a mechanically-prestressed composite structure can not only serve multiple functions, but is also capable of multiple morphing modes like stretching, flexure, and folding.

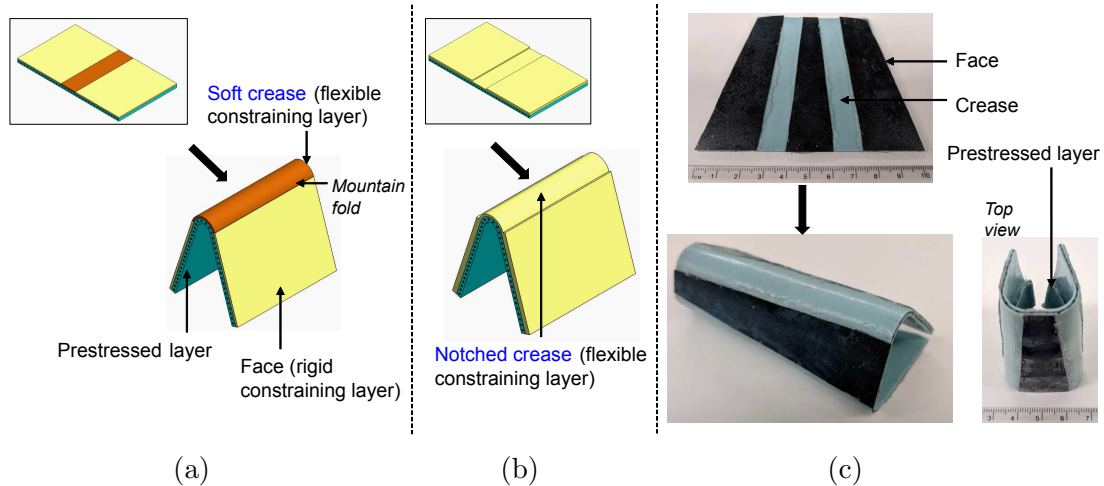


Figure 7.1: (a) Stress-biased folded composites with (a) a soft crease and (b) a notched crease. The figures in the inset show composite shape in the absence of EMC prestress. (c) Demonstration of folding in a stress-biased composite with non-parallel creases.

A method for the fabrication of a passive folded composite is presented in section 7.2. An analytical model based on laminated plate theory is developed to characterize the fold angle at a crease with relatively rigid faces (section 7.3). Composite displacements are defined using piecewise functions to accurately describe the large localized out-of-plane deflection associated with a folded crease. The simulated folded shapes with flat and curved faces are presented in section 7.4. Parametric studies are conducted to characterize the sensitivity of fold angle to the material properties and dimensions of the crease, and the magnitude and orientation of the applied prestrain.

7.2 Composite fabrication

A method for the fabrication of mechanically-prestressed folded composites is presented in this section. Creases of various widths are fabricated to demonstrate the influence of crease width on fold angle and to validate the analytical model.

7.2.1 EMCs

In this work, folded composites are created by laminating prestressed fiber-reinforced elastomers and a creased constraining layer. The elastomer comprises silicone rubber reinforced with unidirectional carbon fibers; fiber-reinforced elastomers are also referred to as elastomeric matrix composites (EMC). The EMC shown in Figure 1.6 is prestressed in the X direction. A portion of this EMC is reinforced with fibers in the Y direction. Addition of fibers in this 90° orientation yields zero in-plane Poisson's ratio whereas isotropic elastomers have a Poisson's ratio of 0.4 - 0.5. The EMCs are fabricated by sandwiching unidirectional carbon fibers between a pair of pre-cured silicone rubber sheets. The design details and the constitutive response of a 90° EMC are presented in Chapter 2.

7.2.2 Folds

Figures 7.2(a) and 7.2(b) show a composite that is folded at its crease by laminating a mechanically-prestressed layer. The constraining layer is a silicone rubber skin (durometer grade 45 A) reinforced with a single layer of woven carbon fabric. Rigid faces are created by laminating 0.127 mm thick spring steel shims to the constraining layer (Figure 7.2(b)). The faces have a square geometry with a side length of 76.2 mm. The width of the crease is 19 mm. A 90° EMC of width 38.1 mm is prestressed to 0.25 strain and is laminated over the length of the constraining layer. Fiber-reinforced composites with a soft matrix not only serve as a constraining layer, but also mitigate the shear stress between a highly-stretched elastomer and an inextensible material such as steel. The prestressed composite exhibits a fold through large deflection at the crease. The faces remain flat because the high-modulus fibers in the constraining layer and the steel backing provide sufficient stiffness to restrict out-of-plane deformation. Figures 7.2(c) and 7.2(d) show the unfolded and folded shapes respectively. In the

unactuated state, or in the absence of external forces, the composite has a folded stable shape. The interior angle between the faces is measured to be 120° .

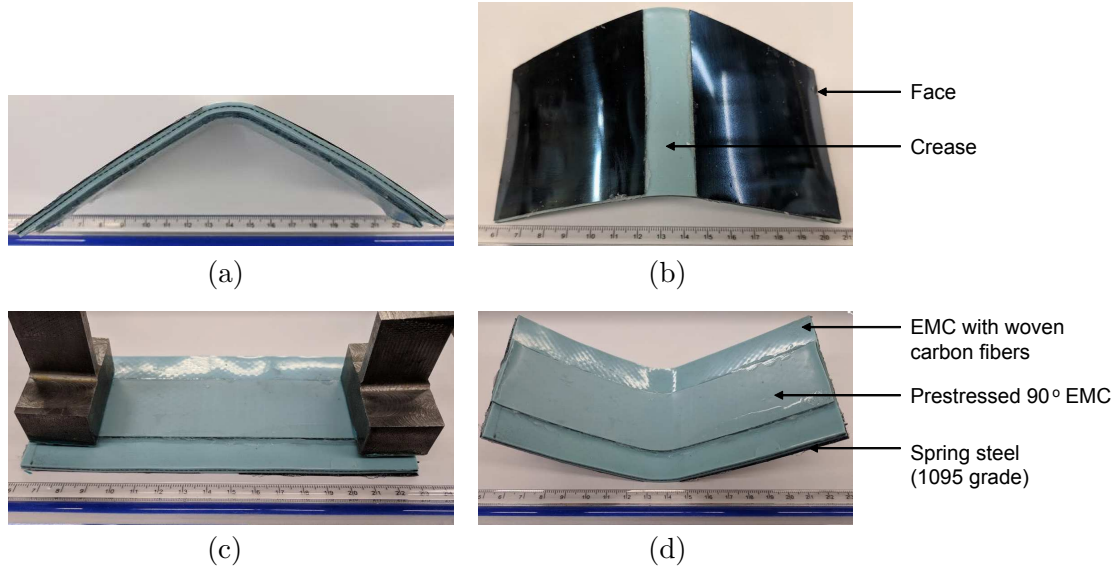


Figure 7.2: A fabricated stress-biased folded composite shown in: (a) top and (b) front views; (c) unfolded shape; and (d) folded shape.

To examine the effect of crease width, pure creases with widths ranging from 6.35 mm to 31.75 mm are laminated to a prestressed EMC as shown in Figure 7.3 (a). All creases are laminated to the same EMC to minimize variation in input prestress between samples (Figure 7.3(b)). The laminated composite, shown in Figure 7.3(c), is cured under pressure for 24 hours. The shape of the composite after removal of prestress is shown in Figure 7.3(d). By visual inspection, the out-of-plane deformation increases with an increase in crease width. Figure 7.3(d) provides an example for stretchable composites with localized curvature and folds. To eliminate end-effects in measurement, the creases are trimmed from the EMC and their curvature is measured (Figure 7.3(e)).

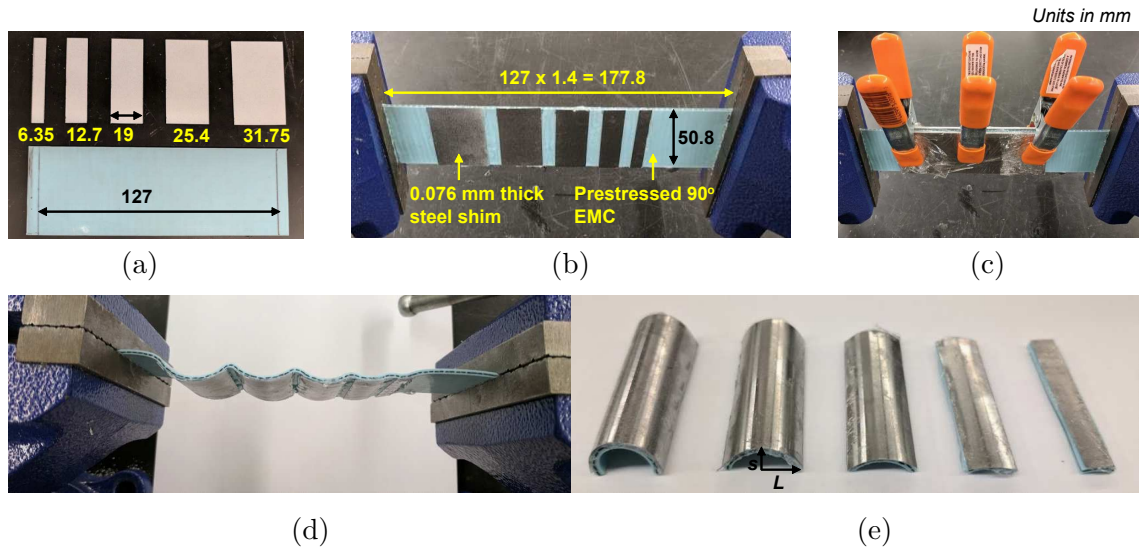


Figure 7.3: (a) A 90° EMC and creases cut out of 0.762 mm thick steel shim; (b) steel shims laminated to a prestressed 90° EMC; (c) curing of the laminate under applied pressure; (d) composite shape after removal of prestress; (e) curved creases obtained from trimming the composite in (d).

7.2.3 Measurement of a 90° EMC's moduli

A 90° EMC, shown in Figure 1.6, exhibits a nonlinear rubber-like elastic behavior in the X direction. Strain in the Y direction is relatively negligible due to the restriction offered by the fibers. Assuming that the modulus of carbon fiber and silicone rubber (assumed linear up to 0.2 strain) is 240 GPa and 1.2 MPa respectively, transverse modulus E_2 is calculated per the rule of mixtures [102] to be 40.8 GPa. However, this value of E_2 is not a good approximation for modeling large out-of-plane deflections in the EMC since the fibers are not uniformly distributed in the matrix. The elastomeric constraining layer, for example, has a similar transverse modulus E_2 as that of a 90° EMC but can undergo large deflection at the crease due to the low transverse shear modulus of the soft matrix. (Figure 7.2(d)).

For modeling based on classical laminate theory, E_2 is assumed to be the modulus corresponding to the bond strength between the fibers and the matrix. To measure this modulus, a fiber-pull-out test is conducted in a tensile testing machine. Unidirectional carbon fibers (3.1 kg/m^2 , Fiberglass developments Corp.), oriented in the direction of vertical motion of the test frame, are pulled out of silicone rubber (Rhodorsil V340-CA45). The size of the test sample is $50.8 \times 19 \times 2 \text{ mm}$. From the stress strain response, shown in Figure 7.4, the effective transverse modulus for small in-plane strain (under 4%) is calculated to be 250 MPa.

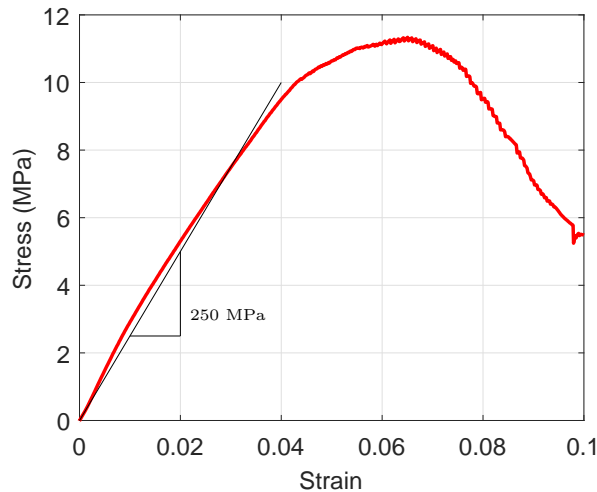


Figure 7.4: Stress-strain curve recorded from a fiber pull-out test conducted on an EMC comprising silicone rubber reinforced with unidirectional carbon fibers.

7.3 Analytical model

Schenk and Guest modeled the elastic behavior of origami structures by treating the folds as pin-joints with a finite stiffness [127]. Peraza-Hernandez et al. [128] studied the structural mechanics of creases with non-zero width. Their modeling effort

included a simplified strain energy-based numerical model that assumes zero in-plane strain and constant curvature. However, the faces adjacent to a crease act as elastic boundary conditions, thereby requiring an assumption of non-constant curvature and finite in-plane strain. Mattioni et al. [129] presented a piecewise-displacement model to calculate the shapes of bistable composites with elastic boundary conditions.

In this work, a folded composite is modeled in its most basic form as a structure that comprises two faces joined by a crease (Figure 7.5). A fold is characterized by large curvature at the crease relative to the face. Strains are modeled per classical laminate theory in conjunction with von Karman’s hypothesis [102]. Strain energy is minimized to calculate the folded shape. In curved composites, global curvature is modeled using displacement functions that can be described using polynomials [92, 107]. However, in a folded structure, the curvature of the crease is expected to be much higher than that of the faces. Description of displacements in global form yields poor accuracy and numerical ill-conditioning for the modeling of high localized curvature. Global displacement functions are also not scalable; the choice of the polynomial is sensitive to the width of the face relative to the crease. To account for localized curvature at the crease, piecewise displacement functions are used to model the deformation of the crease and the faces.

7.3.1 Composite strains

The strain formulation of the composite is as presented in Chapter 4. Prestrain in an EMC is applied in the direction orthogonal to fiber-orientation in order to maintain zero in-plane Poisson’s ratio. Fold angle is expected to be maximum and minimum when the direction of prestrain is perpendicular and parallel to the crease, respectively. Modeling the relation between fold angle and prestrain orientation provides insight into the design of multiple non-parallel folds using a single prestressed EMC.

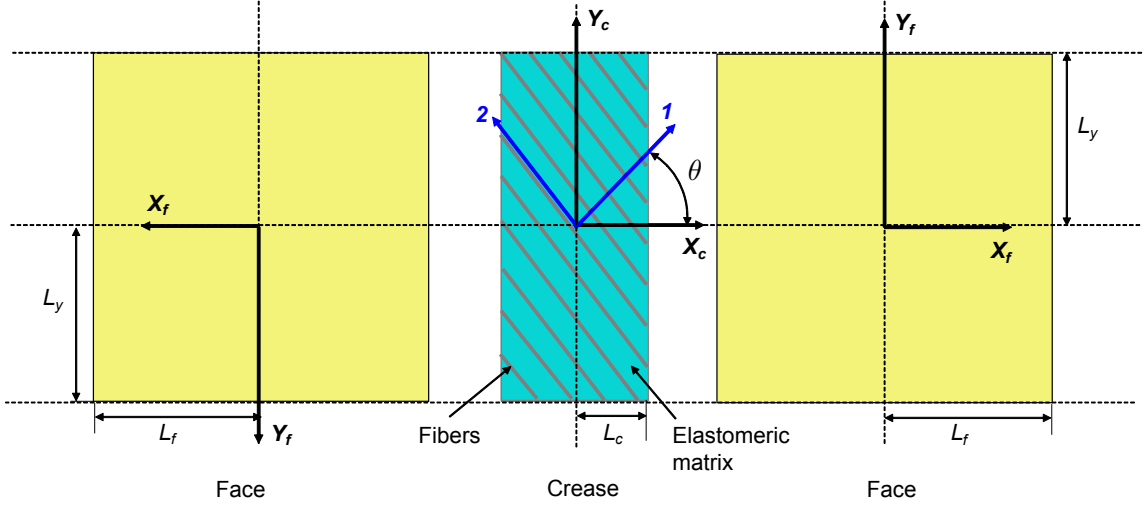


Figure 7.5: Schematic of a stress-biased composite for modeling.

Assuming a plane stress condition, strain in the material coordinates of an EMC (1-2 axes in Figure 7.5) is written in terms of composite strain as:

$$\begin{Bmatrix} \epsilon_1 \\ \epsilon_2 \\ \epsilon_6 \end{Bmatrix} = \begin{bmatrix} \cos^2 \theta & \sin^2 \theta & \sin \theta \cos \theta \\ \sin^2 \theta & \cos^2 \theta & -\sin \theta \cos \theta \\ -2 \sin \theta \cos \theta & 2 \sin \theta \cos \theta & \cos^2 \theta - \sin^2 \theta \end{bmatrix} \begin{Bmatrix} \epsilon_x \\ \epsilon_y \\ \gamma_{xy} \end{Bmatrix}, \quad (7.1)$$

where θ is the angle between the X axis and direction of the applied prestrain (1 axis).

7.3.2 Strain Energy Function

The total strain energy (Φ) can be expressed in terms of strain energy of the crease (Φ_c), faces (Φ_f), and the prestressed EMC (Φ_e) as:

$$\Phi = \Phi_c + 2\Phi_f + \Phi_e. \quad (7.2)$$

$$\Phi_c = \int_{-L_c}^{L_c} \int_{-L_y}^{L_y} \int_{h_1}^{h_2} \left(\frac{1}{2} Q_{11}^{(c)} \epsilon_x^2 + Q_{12}^{(c)} \epsilon_x \epsilon_y + \frac{1}{2} Q_{22}^{(c)} \epsilon_y^2 + \frac{1}{2} Q_{66}^{(c)} \gamma_{xy}^2 \right) dz dy dx, \quad (7.3)$$

where Q_{ij} ($i, j = 1, 2, 6$) are the plane stress-reduced stiffness parameters [102].

$$\Phi_f = \int_{-L_f}^{L_f} \int_{-L_y}^{L_y} \int_{h_1}^{H/2} \left(\frac{1}{2} Q_{11}^{(f)} \epsilon_x^2 + Q_{12}^{(f)} \epsilon_x \epsilon_y + \frac{1}{2} Q_{22}^{(f)} \epsilon_y^2 + \frac{1}{2} Q_{66}^{(f)} \gamma_{xy}^2 \right) dz dy dx. \quad (7.4)$$

The right and left faces are defined such that their strain energies are the same. The thickness of the crease and face is given by $(h_2 - h_1)$ and $(H/2 - h_1)$ respectively.

The condition $h_2 > h_1$ always holds.

$$\begin{aligned} \Phi_{90} = & \int_{-L_c}^{L_c} \int_{-L_y}^{L_y} \int_{-H/2}^{h_1} \left(\frac{p_1}{5} (\epsilon_{90} - \epsilon_1)^5 + \frac{p_2}{4} (\epsilon_{90} - \epsilon_1)^4 \right. \\ & \left. + \frac{p_3}{3} (\epsilon_{90} - \epsilon_1)^3 + \frac{p_4}{2} (\epsilon_{90} - \epsilon_1)^2 + \frac{1}{2} Q_{22}^{(90)} \epsilon_2^2 + \frac{1}{2} Q_{66}^{(90)} \gamma_6^2 \right) dz dy dx. \end{aligned} \quad (7.5)$$

Note that the areal dimensions of the EMC can be modified to model cases where the EMC extends onto the faces. The coefficients p_1 through p_4 in (8.5) correspond to a nonlinear constitutive equation of an EMC comprising silicone rubber reinforced with carbon fibers. The stress-strain curve is obtained from a uniaxial tensile test [21]. The values of the coefficients are listed in the Table 8.1.

Table 7.1: Polynomial coefficients of a nonlinear stress function of an EMC with zero in-plane Poisson's ratio, obtained from a uniaxial tensile test [21].

p_1	p_2	p_3	p_4
-0.698 x 10 ⁶	2.29 x 10 ⁶	-2.306 x 10 ⁶	1.598 x 10 ⁶

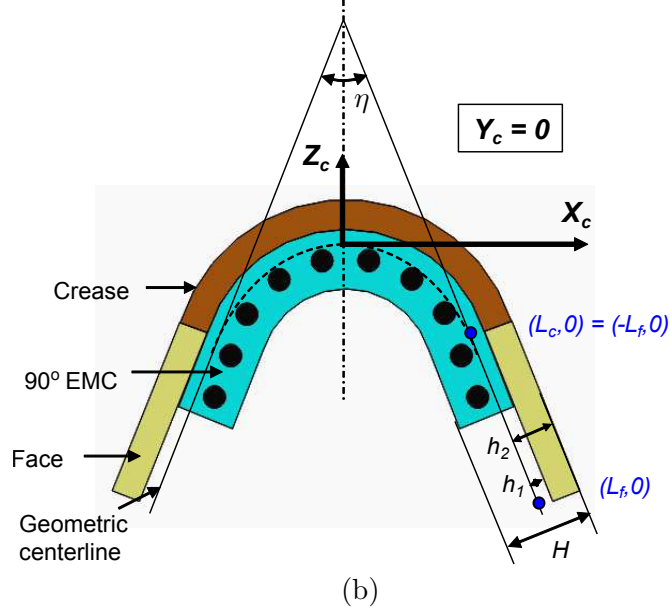


Figure 7.6: Schematic of a composite illustrating fold angle at the vertex of a crease.

7.3.3 Computation of fold angle

Mid-plane displacements of each composite section are described by polynomial functions as:

$$u_0 = \sum_{j=0}^{O_i} \sum_{i=0}^q b_{i,j-i} x^i y^{i-j}, \quad (7.6)$$

$$v_0 = \sum_{j=0}^{O_i} \sum_{i=0}^q c_{i,j-i} x^i y^{i-j}, \quad (7.7)$$

$$w_0 = \sum_{j=0}^{O_i} \sum_{i=0}^q d_{i,j-i} x^i y^{i-j}, \quad (7.8)$$

where O_i is the polynomial order that is chosen for each segment based on the expected deformed shape. b , c , and d are the sets of coefficients to be computed. The displacement polynomials specific to various cases of folding are presented in section

7.4. The geometric equality constraints that couple the crease and face are as follows:

$$u_0^{(c)}(L_c, L_y) = u_0^{(f)}(-L_f, L_y), \quad (7.9)$$

$$v_0^{(c)}(L_c, L_y) = v_0^{(f)}(-L_f, L_y), \quad (7.10)$$

$$w_0^{(c)}(L_c, L_y) = w_0^{(f)}(-L_f, L_y), \quad (7.11)$$

$$\frac{\partial w_0^{(c)}}{\partial x}(L_c, L_y) = \frac{\partial w_0^{(f)}}{\partial x}(-L_f, L_y). \quad (7.12)$$

Constraints defined in (7.9)-(7.12) are also applied between at $(-L_c, -L_y)$ on the crease and $(-L_f, L_y)$ on the left face. The constraints are simplified based on the symmetry conditions specific to an analysis (section 7.4). The total potential energy is minimized using the constrained optimization function *fmincon* in MATLAB to yield a set of nonlinear equations with the polynomial coefficients $b_{i,j-i}$, $c_{i,j-i}$, and $d_{i,j-i}$ as the independent variables. Fold angle of the crease is defined as the internal angle subtended by the faces at the vertex of the fold (Figure 7.6). The inclination of each face, curved or flat, is obtained by calculating the slope of the face from the points $(L_f, 0)$ and $(-L_f, 0)$. The fold angle (η) is defined as:

$$\eta = 2 \left(90 - \frac{\pi}{180} \left(\tan^{-1} \left(\frac{w_0|_{(L_f,0)} - w_0|_{(-L_f,0)}}{(L_f + u_0|_{(L_f,0)}) - (-L_f + u_0|_{(-L_f,0)})} \right) \right) \right). \quad (7.13)$$

7.4 Results and Discussion

Simulations are conducted on a composite with a single crease whose dimensions and material properties are listed in Table 7.2. The composite's configuration is as shown in Figure 7.5. EMC prestrain is applied in the X direction. The folded shape of the composite is expected to be symmetric about the Y axis. Deformation of the crease is expected to symmetric about the X axis. By imposing symmetry conditions, the

Table 7.2: Geometric and material properties of the laminae for modeling.

Parameter	Face (steel)	Crease (steel)	90° EMC
Length (mm)	50.8 [$2L_y$]	50.8 [$2L_y$]	50.8 [$2L_y$]
Width (mm)	63.5 [$2L_f$]	19.05 [$2L_c$]	19.05 [$2L_c$]
Thickness (mm)	0.2	0.0762	2
E_1 (MPa)	200,000	200,000	Nonlinear
E_2 (MPa)	200,000	200,000	250
G_{12} (MPa)	100,000	100,000	125
ν_{12}	0.28	0.28	0
ν_{21}	0.28	0.28	0

displacement polynomials are simplified per the relations listed in Table 7.3. For folds with flat faces, the order of the polynomials for u_0 , v_0 , and w_0 can be reduced to 1.

Table 7.3: Conditions imposed on displacement polynomials for the modeling of folds at a crease with orthogonal EMC prestrain.

Crease			Face	
	O_i	Condition	O_i	Condition
u_0	3	Odd in x , even in y , $u_0(0,0) = 0$	3	Even in y
v_0	3	Odd in y , even in x , $v_0(0,0) = 0$	3	Odd in y , $v_0(0,0) = 0$
w_0	4	Even in x and y , $w_0(0,0) = 0$	4	Even in y

7.4.1 Folded shapes and model validation

The deformation of a crease with and without the included faces is calculated for an EMC prestrain of 0.3 (Figure 7.7). In the crease with included faces, EMC prestrain is applied only at the crease. The composite is seen to deform only within the region of prestress application, i.e., at the crease, while the faces remain flat. The inclusion of faces has minimal effect on the out-of-plane deflection at the straight edges of the

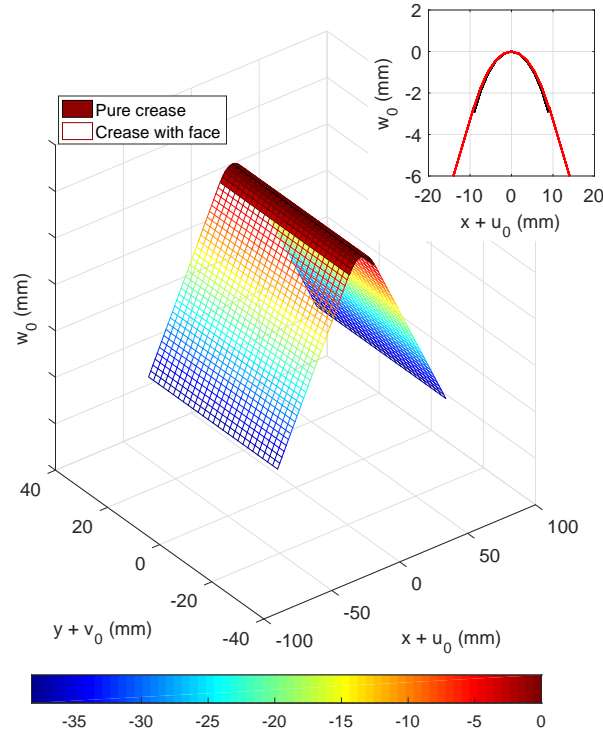


Figure 7.7: Comparison of shapes of a pure crease and a crease with faces.

crease. The small difference in deflection can be attributed to the tangency condition imposed numerically between the crease and the face (inset in Figure 7.7). This result is consistent with the observation by Mattioni et al. [129] that the inclusion of an elastic boundary on the straight edge of a cylindrically-curved plate has negligible impact on its curvature. Given the negligible difference between the shapes of a crease with and without the faces, the analytical model can be validated by comparing the simulated curved shapes of pure creases with the corresponding shapes of the fabricated composites (shown in Figure 7.3). The measured out-of-plane deflection of the fabricated curved creases is in agreement with the corresponding simulated values (Figure 7.8).

Curved faces in a folded composite are created by extending the prestressed EMC lamina to cover the faces. The simulated folded shape is plotted in Figure 7.9 with

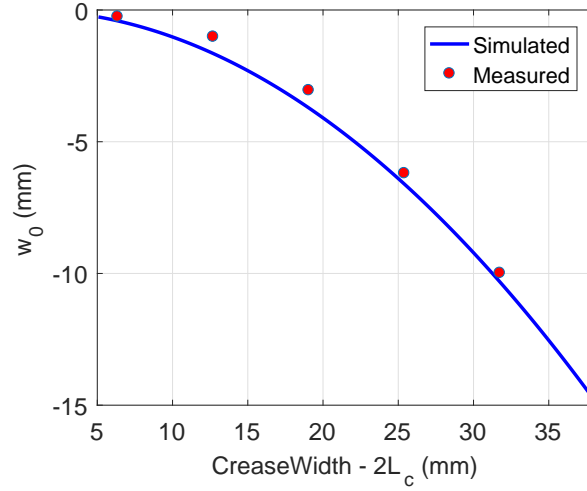


Figure 7.8: Out-of-plane deflection of the straight edges of a crease fabricated without the included faces. The data presented corresponds to $\epsilon_{90} = 0.4$.

reference to a fold with flat faces for $\epsilon_{90} = 0.3$. By visual inspection it is seen that the curves that define the crease and the face are tangential. Curvature in the faces yields higher out-of-plane displacement at the edge of the face (inset in Figure 7.9). Therefore, the composite's global curvature contributes to the design of folded shapes. Relative to a flat face, a convex global curvature in the face decreases the fold angle (tighter fold) whereas a concave curvature increases it.

7.4.2 Effect of crease width

Figure 7.10 shows the variation of fold angle as a function of crease width for various values of EMC prestrain. For a given value of ϵ_{90} , fold angle reduces with an increase in crease width. Such a response can be attributed to the choice of the nonlinear displacement polynomials. The out-of-plane deflection w_0 is an even monotonically increasing function of x . In-plane displacement u_0 also increases with an increase in x but at a lower rate than w_0 (see Table 7.3). Therefore, from (7.13), η decreases with

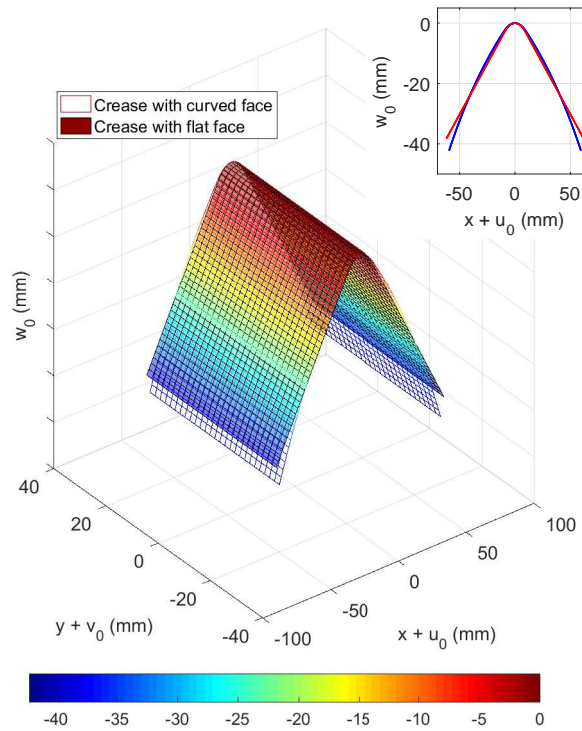


Figure 7.9: Comparison of shapes of a crease with flat and curved faces.

an increase in crease width since $\arctan(x)$ is an increasing function. Folding limit in narrow creases can be increased by applying higher prestrain to the EMC. With reduction in crease width, the sensitivity of fold angle to EMC prestrain reduces. This trend can be explained by the fact that in narrow creases, where EMC thickness is comparable to crease width, the strain energy associated with prestress manifests as high in-plane strain in the EMC. In wide creases, however, the input strain energy primarily manifests as out-of-plane deformation.

7.4.3 Effect of crease modulus and thickness

Figure 7.11 shows the variation of fold angle as a function of crease modulus and width. For a given width of the crease, fold angle reduces exponentially with linear reduction in modulus. Fold angle is more sensitive to modulus change in wide creases

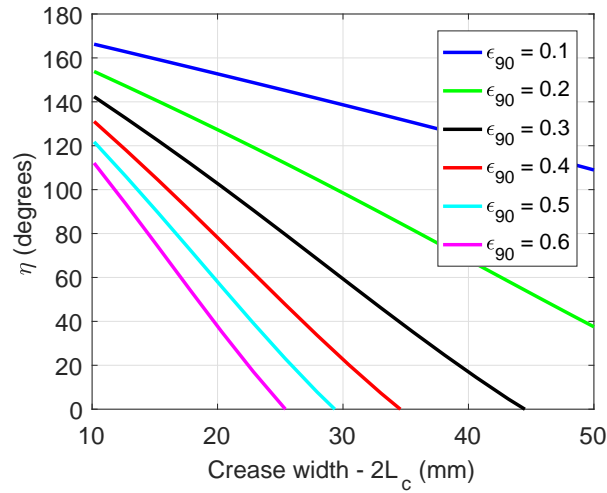


Figure 7.10: Fold angle as a function of crease width ratio shown for crease thickness and modulus of 0.003” and 200 GPa respectively.

as compared to narrow creases. Fold limit can be maximized by maximizing width and minimizing modulus. However, crease width may be limited by the required scale and resolution of folds in an origami structure. Folding can be achieved by actively softening the crease. This actuation approach can be realized using smart materials with controllable modulus such as SMAs [130] and SMPs [131], magnetorheological materials [132], and phase change materials [133]. Fold angle reduces upon softening due to the intrinsic restoring force in the prestressed EMC. For example, an SMA crease, laminated with a prestressed EMC in its twinned Martensite phase, can fold by undergoing detwinning; modulus of detwinned Martensite is about 25 GPa. The composite can be unfolded by heating the SMA to the Austenite phase (modulus of about 75 GPa). The folding range that can be achieved using SMA creases is marked using planes in Figure 7.11.

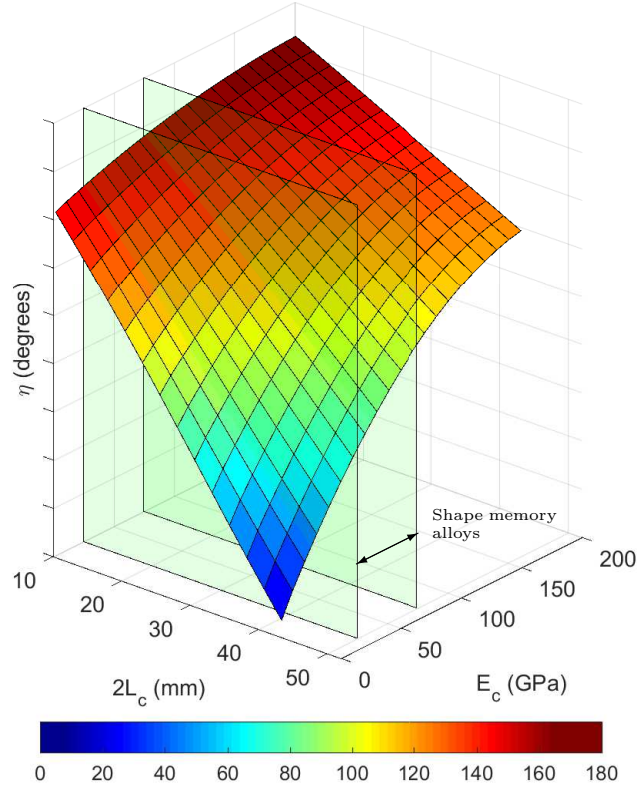


Figure 7.11: Fold angle as a function of crease modulus and width at a constant thickness of 0.003". The modulus range for shape memory alloys is illustrated as an example for the selection of materials with controllable modulus.

Fold sharpness (Ω) is defined in terms of fold angle (η), crease thickness ($t = h_2 - h_1$), and width ($2L_c$) as follows:

$$\Omega = \frac{\eta}{2L_c t}. \quad (7.14)$$

Figure 7.12 shows the variation of fold sharpness as a function of crease width and thickness, simulated for a crease modulus of 2 GPa. EMC prestrain is maintained constant at 0.3. For a given thickness, Ω reduces exponentially with an increase in crease width. At constant crease width, sharpness can be increased by reducing crease thickness up to a critical value. Below this critical t , the composite is completely folded, i.e., $\eta \rightarrow 0$. Therefore, lowering t below the critical value does not effect

Ω . Fold sharpness can be maximized by minimizing crease width and thickness. It is worth noting that the composite's thickness can also be lowered by reducing the EMC's thickness, thereby improving fold sharpness. However, a reduction in EMC thickness corresponds to a reduction in the strain energy associated with a given prestrain. Thin EMCs would require higher prestrain to generate a given fold angle as compared to thick EMCs.

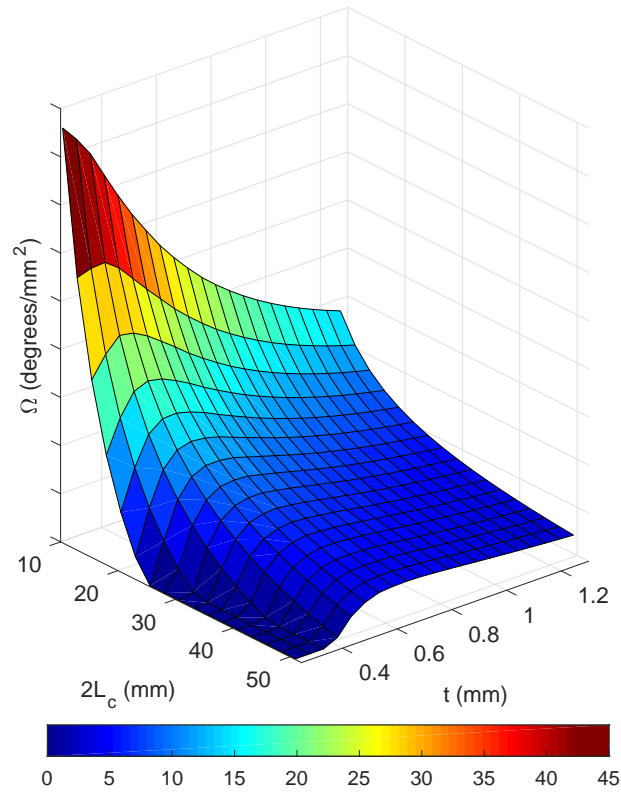


Figure 7.12: Fold sharpness as a function of crease width and thickness, shown for a crease modulus of 2 GPa.

7.4.4 Effect of EMC Orientation

The orientation of prestrain in an EMC is expected to influence fold angle. The displacement polynomials chosen for this study include twist in the crease at non-orthogonal orientations of the EMC. The conditions imposed on the polynomials are listed in Table 7.4. While the crease can twist, the faces are assumed to be inflexible; therefore, the material properties of the face do not influence the results. As a result, the edges of the crease that are parallel to the Y axis in a flat composite, remain straight when folded.

Table 7.4: Conditions imposed on displacement polynomials for the modeling of folds at a crease with orthogonal EMC prestrain.

Crease			Face	
	O_i	Condition	O_i	Condition
u_0	3	Terms with odd power, $u_0(0,0) = 0$	1	Includes xy term
v_0	3	Terms with odd power, $v_0(0,0) = 0$	1	Includes xy term
w_0	4	Terms with even power, $w_0(0,0) = 0$	1	Includes xy term

For a crease modulus, thickness, and width of 200 GPa, 0.025 mm, and 19 mm respectively, fold angle (η) is calculated as a function of prestrain angle (θ). Figure 7.13 shows η for various values of transverse modulus E_2 . Fold angle at the crease increases with an increase in θ , yielding an almost flat composite at around 45° . The range of θ for fold generation, increases with a decrease in E_2 . However, the tradeoff in reducing bond strength between the EMC's fibers and matrix is a non-negligible in-plane Poisson's ratio. For $0 < \theta < 45$, calculations of the slope $\partial w_0 / \partial y$ of the faces revealed that the twist in the composite is negligible (not illustrated). Such a response can be attributed to three factors: high planar aspect ratio of crease;

the straight-edge condition imposed on the crease; and a high crease modulus. For $\theta = 45^\circ$, a large twist was observed. This result corresponds to a pure twisting mode in a fold-free composite.

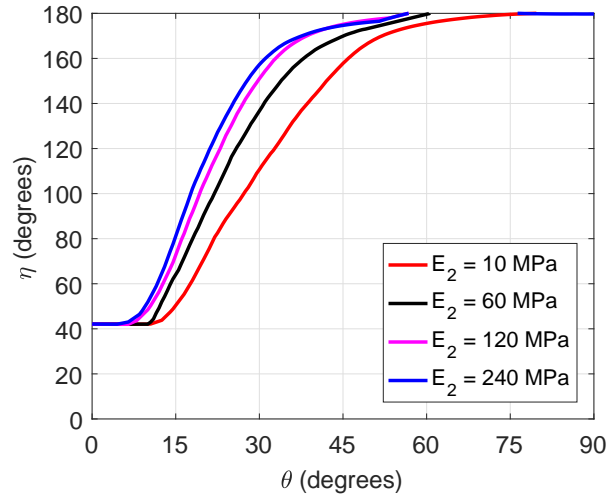


Figure 7.13: Fold angle as a function of prestrain angle for various values of transverse (fiber-direction) modulus of an EMC.

Fold angle can be maximized by orienting the EMC prestrain orthogonal to the crease. For a given fold angle, the energy deficit associated with EMC rotation can be compensated by increasing the prestrain. However, there may be practical limits on prestrain associated with the composite's durability; minimizing prestrain translates to minimal shear stress between the EMC and the constraining layer, thereby maximizing durability. Figure 7.14 shows the variation of η as a function of crease width and θ for a transverse modulus of 250 MPa. The range of prestrain orientations ($0 < \theta < 45$) that yield folds is independent of crease width. However, wider creases provide a higher range of foldability (η), as shown in previous results.

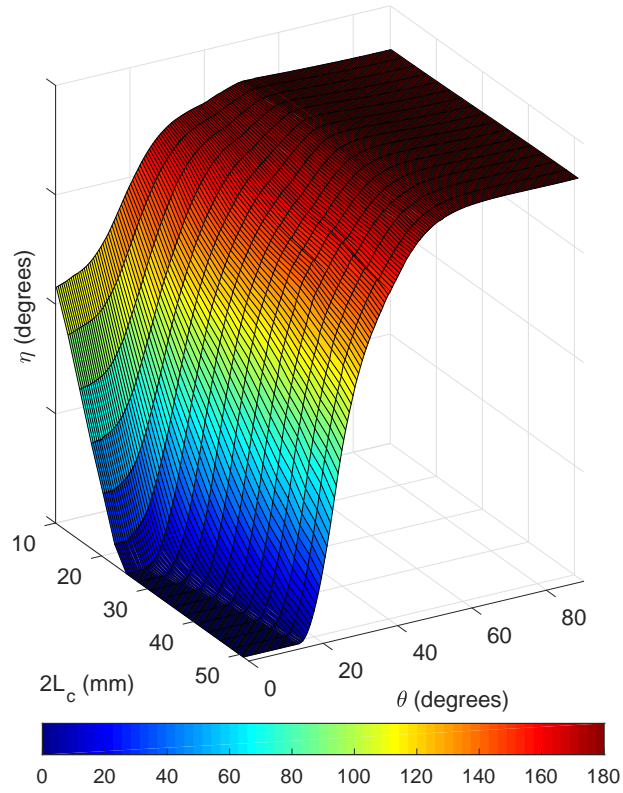


Figure 7.14: Fold angle as a function of prestrain angle and crease width.

Smooth folds can be created in pre-creased laminated composites by applying prestress to select laminae. This versatile approach not only enables localized prestress application for folding at a given crease, but also allows folding at multiple non-parallel creases using a single source of prestress. The stress-biased composites presented in this work have the potential to serve as a framework for smart origami structures with reconfigurable creases.

Chapter 8

System-Scale Implementation: Morphing Fender Skirts

Overview

This chapter presents smart laminated composites for adaptive panels. Morphing panels can be effective for drag reduction, e.g., adaptive fender skirts. Mechanical-prestress provides tailored curvature in composites without the drawbacks of thermally-induced residual stress. When driven by smart materials such as shape memory alloys (SMA), mechanically-prestressed composites can serve as building blocks for morphing structures. An analytical energy-based model is presented to calculate the curved shape of a composite as a function of force applied by an embedded actuator. Shape transition is modeled by providing the actuation force as an input to a 1-D thermomechanical constitutive model of an SMA wire. A design procedure, based on the analytical model, is presented for morphing fender skirts comprising radially-configured smart composite elements. A half-scale fender skirt for a compact passenger car is designed, fabricated, and tested. The demonstrator has a domed unactuated shape and morphs to a flat shape when actuated using SMAs. Rapid actuation is demonstrated by coupling SMAs with integrated quick-release latches; the latches reduce actuation time by 95%. The demonstrator is 62% lighter than an equivalent dome-shaped automotive steel panel.

8.1 Introduction

For design purposes, we define a fender skirt as an extension of a fender that covers the wheel, as shown in Figure 8.1(a). A fender skirt eliminates the turbulence caused by mixing of the flow stream originating from wheel rotation with the boundary layer of flow on the vehicle body [27]. Flat fender skirts that cover rear wheels have already been implemented; examples include Ford Probe (prototypes I-V, 1979-84), Honda Insight (2000), and Volkswagen XL1 (2011). For steered wheels however, dome-shaped skirts are required to avoid collision during wheel steer. The addition of a rigid dome-shaped skirt leads to increased vehicle width that could have adverse affects on aerodynamic performance and driving dynamics. To address these limitations, we present a design methodology for adaptive fender skirts that are flat at high speed for optimal aerodynamic efficiency and switch to a domed shape to accommodate steering of the wheel at low speed (Figure 8.1). Under normal operating conditions, steering angles are typically less than 5° at highway speeds (> 60 mph or 96.5 kph) whereas large steering angles are common for low speed operations such as parking maneuvers. The BMW Vision “Next 100 Years” is an example of a vehicle concept that features morphing fenders [2]. In the BMW concept, the fender is the morphing element whereas the fender skirt is rigid.

8.2 Morphing structure configuration

The configuration of an adaptive fender skirt is presented in this section to motivate the design of a morphing structure based on smart laminated composites. The types of laminae in a smart composite and their functions are also described.

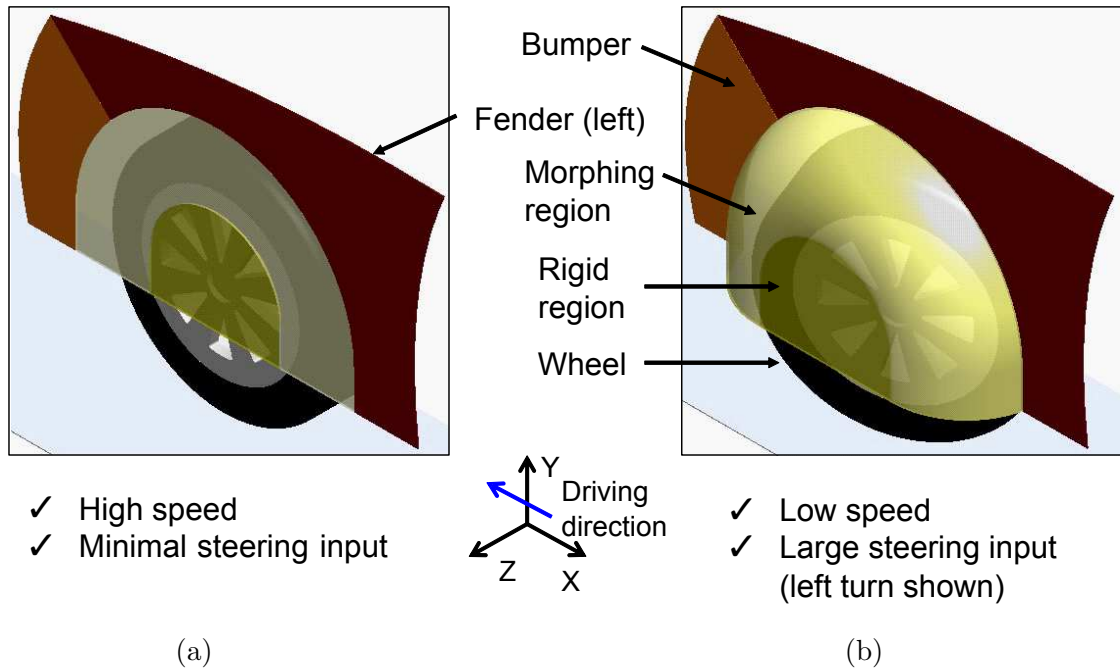


Figure 8.1: (a) Retracted shape and (b) deployed shape of a morphing fender skirt (shown in yellow).

8.2.1 Fender skirt

In this work, a fender skirt is envisioned as a dome-shaped structure that comprises curved laminated composite ribs in a radial configuration (Figure 8.2(a)). A curved rib is created by laminating a mechanically-prestressed layer to a flexible panel. In our design, prestress is applied using elastomeric matrix composites (EMCs). The EMC used is a rectangular strip with unidirectional fibers oriented in a direction perpendicular to that of the applied prestress. A material in this configuration, referred to as a 90° EMC, has zero in-plane Poisson's ratio [11]. The central portion of the dome is rigid and flat in order to: limit vehicle width; provide structural integrity; and couple the ribs for a smooth global shape transition. At the circumference of the rigid region, flexible ribs are arranged in a radial configuration. The outer edges of the flexible ribs are linked using a compliant rim with constant curvature; the rim is semicircular when the structure is in the domed shape. Each rib has a trapezoidal

planform and is actuated using a shape memory alloy wire that is installed along the axis of symmetry of the rib. The SMA wires contract when heated to morph the structure between the domed and flat shapes (Figure 8.2(b)).

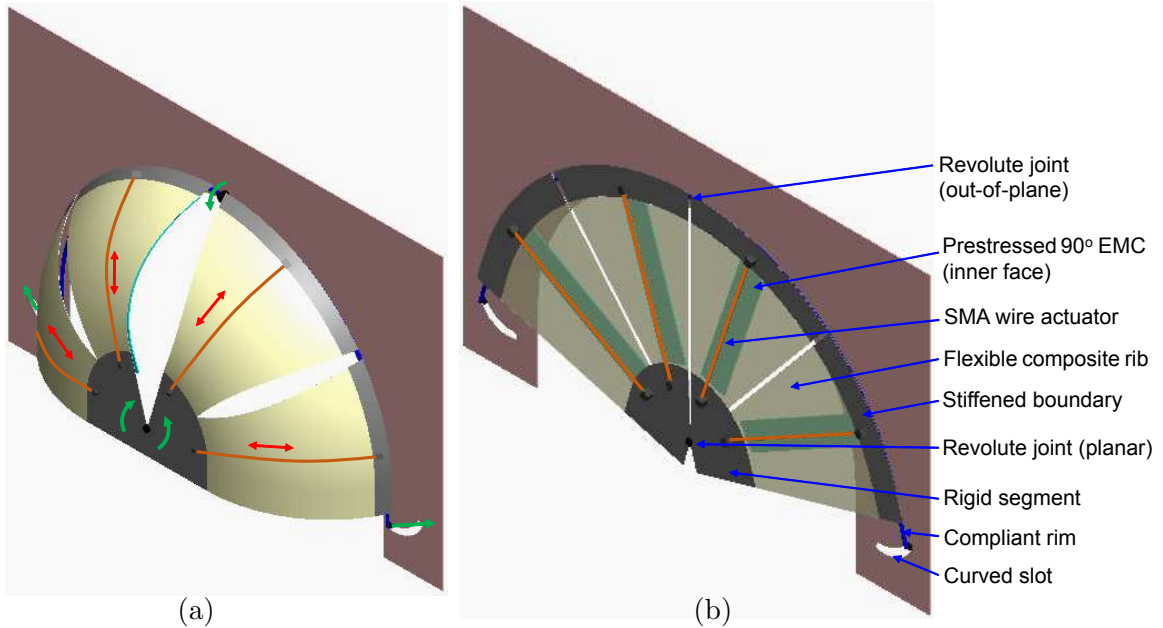


Figure 8.2: (a) Unactuated dome and (b) actuated flat shapes of a morphing fender skirt. The flexible segment in (b) is shown with transparency to highlight the details on the inner face; skin is not shown.

The mid-point of the rim is fixed whereas the rim ends slide in curvilinear slots in the fender. Morphing between domed and flat shapes is such that the total surface area is constant. As a consequence, there is localized shear strain in the panel. To relieve the shear strain, a 1-D hinge (revolute joint) is included at the geometric center of the rib sectors. Ideally, each rib is independently connected to the hinge to eliminate shear. For design simplicity, all ribs on one side (left and right) of the hinge have a common rigid segment. Each rib is designed to have a cylindrical curvature along the radial line of the fender skirt. Smoothness of the domed shape increases

with an increase in resolution of the ribs. For modeling purposes, the ribs in the structure are assumed to be identical even though their edges may be shaped to: conform to the boundaries; provide strain relief during morphing; and ensure that the structure is flush with the neighboring vehicle body panels.

Assuming that the radially-configured ribs are identical, one can model a single rib to design the global shape of the structure. The benefit of considering a single rib is that one can develop an analytical model that is computationally inexpensive when compared to a finite-element model of the entire structure. An analytical model of a rib guides planform design, material selection, and actuator design. The various design elements considered for the integration of the morphing structure are shown in Figure 8.3. The design considerations for the structure are discussed in detail in section 8.5.2.

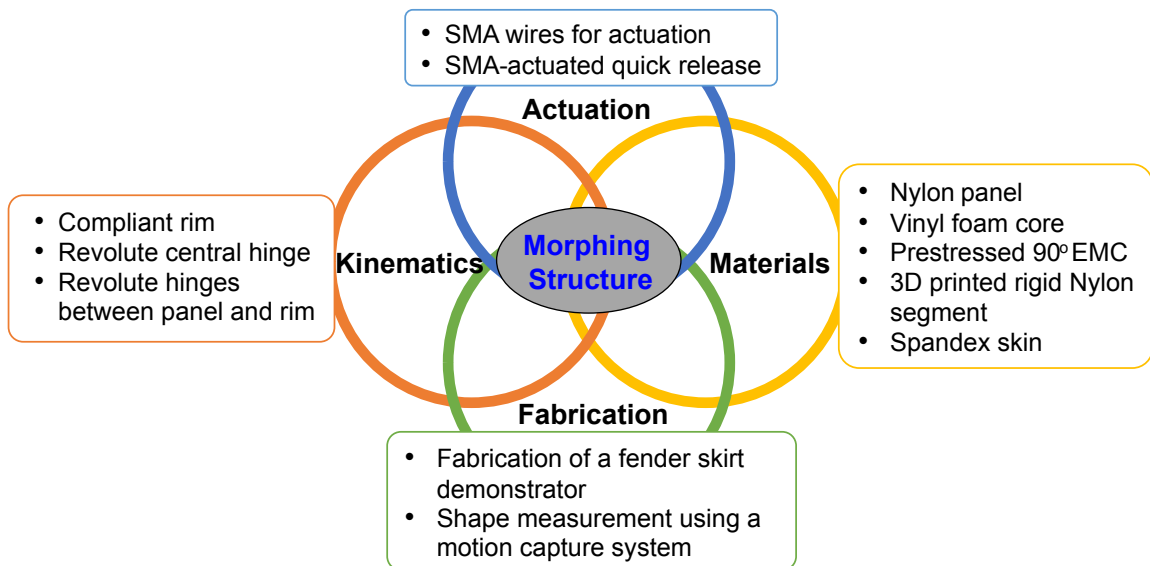


Figure 8.3: Design elements for the integration of a morphing fender skirt.

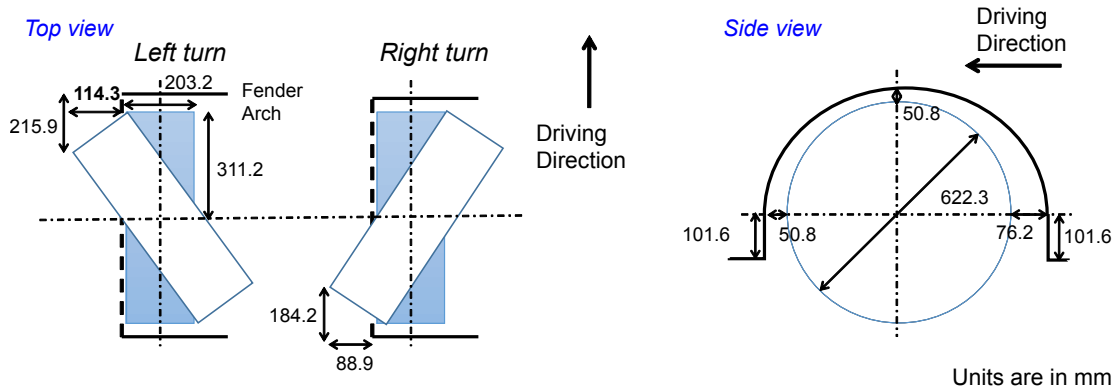


Figure 8.4: Approximate fender dimensions and motion limits of the left wheel of a compact passenger car.

For a compact passenger car with standard features, the maximum out-of-plane displacement of the wheel is measured to be 114.3 mm. The geometry of a steered wheel relative to its fender is shown in Figure 8.4. To accommodate wheel rotation with a factor of safety of 1.33, the target out-of-plane displacement for the fender skirt is set to 152.4 mm. The maximum aerodynamic pressure at 144 kph (90 mph) is assumed to be 500 Pa and 1000 Pa in the flat and domed shapes, respectively. In both shapes, the pressure acts on the inner face of the skirt. The maximum allowable deflection of the structure in any shape is 5%. The mass of the morphing structure is expected to be less than that of a typical 0.8 mm thick steel automotive body panel. The fender skirt should have minimal moving parts to ensure durability and robustness. Mechanical connections, such as sliders for in-plane motion, should be minimized to prevent environmental intrusion through dust, snow, etc., from jamming the morphing mechanism.

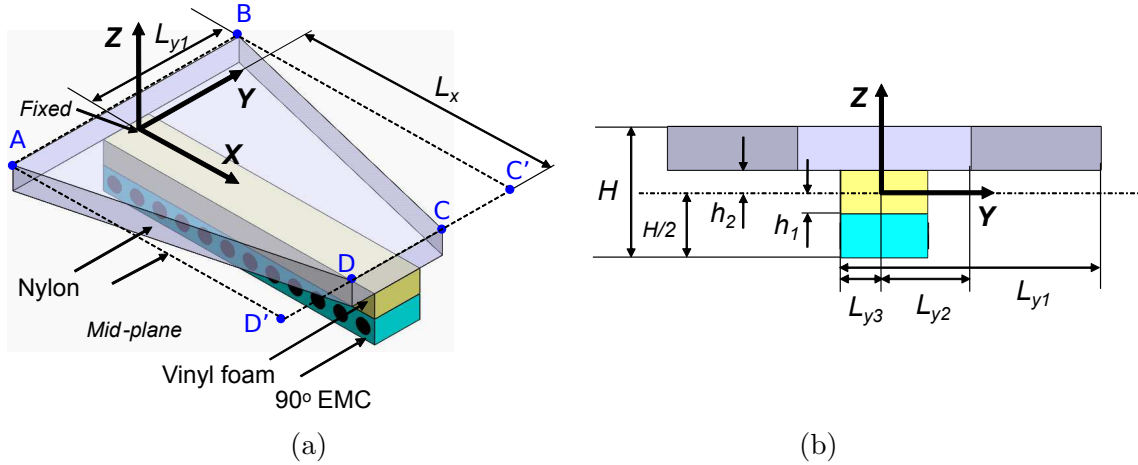


Figure 8.5: Schematic representation of a prestressed composite rib with a linearly varying tapered planform in the (a) isometric view and (b) YZ plane.

8.2.2 Laminated composite

The passive composite comprises constraining and prestressed laminae with an optional sandwiched core (Figure 8.5). A constraining layer is flexible but has high in-plane modulus relative to the prestressed layer. Candidate materials for the constraining layer include metals, plastics, and anisotropic fiber-reinforced composites. The constraining layer's shape is tailored to match the shape of an element of a morphing structure or its entirety. The prestressed layer is typically a highly-stretchable elastic material, preferably with zero in-plane Poisson's ratio; examples include anisotropic elastomers. The benefit of restricting the Poisson's ratio to zero is that the magnitude and orientation of a given cylindrical component of the composite's curved shape can be tailored using the respective magnitude and orientation of the applied prestress [107].

In this work, the constraining layer is made of Nylon plastic and the prestressed layer is a 90° EMC that is made of silicone rubber reinforced with unidirectional carbon fibers. The prestressed layer is laminated in a rectangular shape to ensure uniform distribution of prestress. Post lamination, the uniformly-prestressed layer

can be trimmed to match the shape of the constraining layer. A sandwiched core is included to increase the offset between the prestressed and constraining laminae with a goal of lowering the prestrain required to achieve a given curvature (discussed in section 8.4). The core is a flexible material with a modulus value that lies between that of the constraining and prestressed layers but is closer to that of the prestressed layer. Low-density vinyl foam is used as a sandwiched core over the area spanned by the prestressed layer.

8.3 Analytical model of an active composite rib

A composite rib is modeled based on classical laminate theory along with von Karman's hypothesis for small in-plane strains and moderate rotations. The composite's strain energy is calculated based on strains formulated using assumed displacement functions. Work done by actuation forces is computed using the variational principle. Minimization of the net energy using a Rayleigh-Ritz technique yields the displacement functions that define the shape of the composite. The strain model for a laminated plate is outlined in the Appendix.

The modeling approach presented in this section is applicable to composites with arbitrary planform shapes that can be defined using explicit continuous functions (Figure 8.6). Examples of explicit functions include $h(x, y) = k_1x + k_2y$ and $h(x, y) = k_3x^2 + k_4xy + k_5y^2$ for linear and elliptical planform shapes, respectively. Strain energy can be calculated by integrating the continuous functions over the composite's volume. For smooth, complex shapes defined using multiple shape functions, displacements would have to be modeled using high-order polynomials. Symmetry in composite shape, if present, can be considered to simplify the displacement polynomials prior to computation. Uniform distribution of stress is desired in the prestressed

layer. To create strain corresponding to uniform stress, the prestressed layer is considered to be a rectangle. The modeling approach is demonstrated for a trapezoidal composite rib with linearly varying planform (as in Figure 8.5).

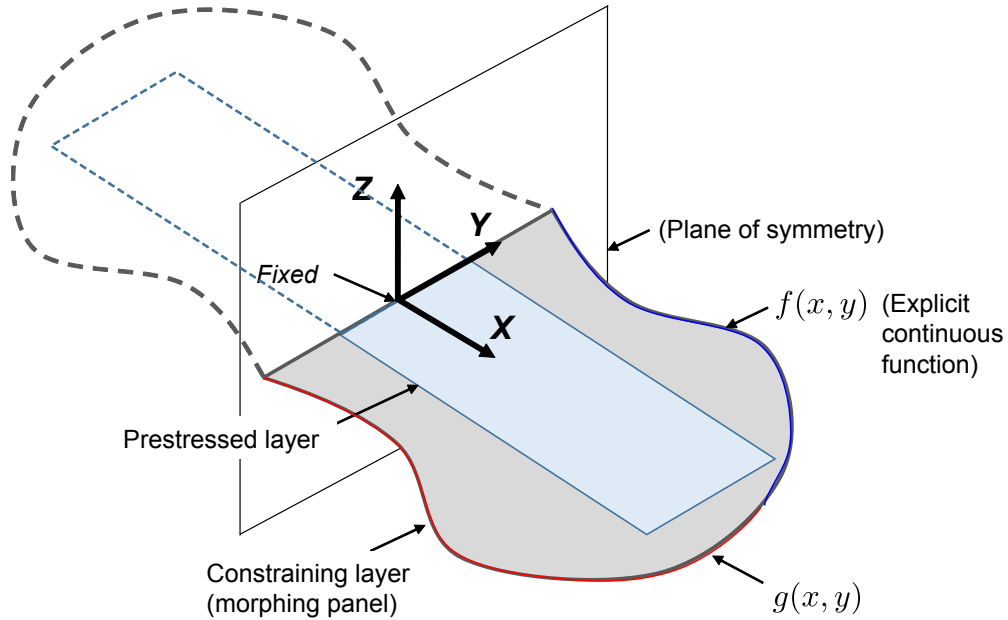


Figure 8.6: Schematic representation of a prestressed composite with an arbitrary planform shape that can be described using explicit continuous functions.

8.3.1 Strain energy computation

The geometry of a composite rib in the fender skirt is shown in Figure 8.5. The rib is clamped at the origin and is symmetric about the XZ plane; all edges except the edge containing the origin are free. The composite comprises a trapezoidal panel bonded to a rectangular 90° EMC strip. A sandwiched core is included to provide sufficient curvature at low prestrain (discussed in section 8.4); the core is assumed to be a flexible, low density foam. The areal dimensions of the core are the same as

those of the EMC. The taper in a trapezoidal panel is defined as:

$$\omega = \frac{L_{y1} - L_{y2}}{L_x}. \quad (8.1)$$

The minimum value of ω is zero, whereas the maximum value corresponds to $L_{y2} = 0$ and is a function of the aspect ratio L_{y1}/L_x .

The strain energy of the tapered panel $ABCD$, obtained by subtracting the energy in the triangular regions ADD' and BCC' from the energy in the rectangle $ABC'D'$ (Figure 8.5), is written as:

$$\begin{aligned} \Phi_p = & \left(\int_0^{L_x} \int_{-L_{y1}}^{L_{y1}} d\Phi_p \, dy \, dx \right) - \left(\int_0^{L_x} \int_{L_{y1}-\omega x}^{L_{y1}} d\Phi_p \, dy \, dx \right) \\ & - \left(\int_0^{L_x} \int_{L_{y1}}^{\omega x - L_{y1}} d\Phi_p \, dy \, dx \right). \end{aligned} \quad (8.2)$$

The integrand in (8.2) is defined as:

$$d\Phi_p = \int_{h_2}^{H/2} \left(\frac{1}{2} Q_{11}^{(p)} \epsilon_x^2 + Q_{12}^{(p)} \epsilon_x \epsilon_y + \frac{1}{2} Q_{22}^{(p)} \epsilon_y^2 + \frac{1}{2} Q_{16}^{(p)} \gamma_{xy} \epsilon_x + \frac{1}{2} Q_{26}^{(p)} \gamma_{xy} \epsilon_y + \frac{1}{2} Q_{66}^{(p)} \gamma_{xy}^2 \right) dz, \quad (8.3)$$

where Q_{ij} , $\{i, j = 1, 2, 6\}$ are the plane stress-reduced stiffnesses [102] and ϵ_x , ϵ_y , and γ_{xy} are the strains of the composite (Appendix).

The respective strain energy of the core and 90° EMC is:

$$\begin{aligned} \Phi_c = & \int_0^{L_x} \int_{-L_{y3}}^{L_{y3}} \int_{-h_1}^{h_2} \left(\frac{1}{2} Q_{11}^{(c)} \epsilon_x^2 + Q_{12}^{(c)} \epsilon_x \epsilon_y + \frac{1}{2} Q_{22}^{(c)} \epsilon_y^2 \right. \\ & \left. + \frac{1}{2} Q_{16}^{(c)} \gamma_{xy} \epsilon_x + \frac{1}{2} Q_{26}^{(c)} \gamma_{xy} \epsilon_y + \frac{1}{2} Q_{66}^{(c)} \gamma_{xy}^2 \right) dz \, dy \, dx, \end{aligned} \quad (8.4)$$

$$\begin{aligned} \Phi_{90} = & \int_0^{L_x} \int_{-L_{y3}}^{L_{y3}} \int_{-H/2}^{-h_1} \left(\frac{p_1}{5} (\epsilon_{90} - \epsilon_x)^5 + \frac{p_2}{4} (\epsilon_{90} - \epsilon_x)^4 \right. \\ & \left. + \frac{p_3}{3} (\epsilon_{90} - \epsilon_x)^3 + \frac{p_4}{2} (\epsilon_{90} - \epsilon_x)^2 + \frac{1}{2} Q_{22}^{(90)} \epsilon_y^2 + \frac{1}{2} Q_{66}^{(90)} \gamma_{xy}^2 \right) dz dy dx. \end{aligned} \quad (8.5)$$

The coefficients p_1 through p_4 are those of a quartic polynomial that describes the nonlinear stress function of a 90° EMC. These coefficients, shown in Table 8.1, are determined experimentally from a uniaxial tensile test. The large deformation model of an EMC, obtained from a measured stress-strain curve, is described per the procedure shown in [21]. The total strain energy of the system is expressed in terms of the strain energies of the constituent layers as:

$$\Phi = \Phi_p + \Phi_c + \Phi_{90}. \quad (8.6)$$

Table 8.1: Polynomial coefficients of a nonlinear stress function of a 90° EMC made of carbon fiber-reinforced silicone, obtained from a uniaxial tensile test [21].

p_1	p_2	p_3	p_4
-0.698×10^6	2.29×10^6	-2.306×10^6	1.598×10^6

8.3.2 Work done by an external force

Chillara and Dapino [134] presented an analytical approach to model in-plane SMA wire actuators using a pair of tangential point forces. Using this approach, in-plane actuation is modeled in the configuration shown in Figure 8.7(a).

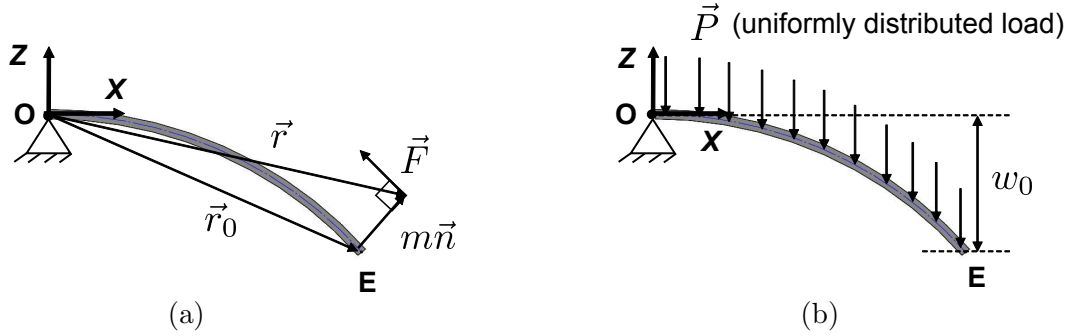


Figure 8.7: Configuration of (a) in-plane force (\vec{F}) and (b) uniformly distributed vertical force (\vec{P}) on a curved plate that represents the prestressed laminated composite rib.

The actuation force is expressed in terms of its position vector (\vec{r}) as:

$$\vec{F} = -F \frac{\partial \vec{r}}{\partial x} \bigg/ \left| \frac{\partial \vec{r}}{\partial x} \right|, \quad (8.7)$$

where \vec{r} is written in terms of the position of the point (\vec{r}_0) on the mid-plane and the normal (\vec{n}) of magnitude m at \vec{r} :

$$\vec{r} = \vec{r}_0 + m \vec{n}, \quad (8.8)$$

$$= \vec{r}_0 + m \frac{\left(\frac{\partial \vec{r}_0}{\partial x} \times \frac{\partial \vec{r}_0}{\partial y} \right)}{\left| \frac{\partial \vec{r}_0}{\partial x} \times \frac{\partial \vec{r}_0}{\partial y} \right|}, \quad \text{where} \quad \vec{r}_0 = \left((x + u_0)\mathbf{i} + (y + v_0)\mathbf{j} + w_0\mathbf{k} \right) \quad (8.9)$$

and u_0, v_0 , and w_0 are the displacements of an arbitrary point on the composite's mid-plane in the X , Y , and Z directions, respectively. Virtual work done by the actuation force is written as:

$$\delta W_F = -\vec{F} \cdot \delta \vec{r} |_{\{L_x, 0\}}, \quad (8.10)$$

For stiffness calculation, virtual work done by a uniformly distributed vertical force of magnitude P (Figure 8.7(b)) can be expressed as:

$$\delta W_P = \left(\int_0^{L_x} \int_{-L_{y1}}^{L_{y1}} P w_0 dy dx \right) - \left(\int_0^{L_x} \int_{L_{y1}-\omega x}^{L_{y1}} P w_0 dy dx \right) - \left(\int_0^{L_x} \int_{L_{y1}}^{\omega x - L_{y1}} P w_0 dy dx \right). \quad (8.11)$$

8.3.3 Composite displacements and shape computation

Displacements u_0 , v_0 , and w_0 are assumed to be polynomial functions with unknown coefficients. The composite is expected to have non-uniform curvature due to its trapezoidal planform. Therefore, w_0 is defined by a complete quartic polynomial in order to describe the variation in curvature. Since curvature is about the Y axis, the polynomial order for u_0 is considered to be higher than that of v_0 . Displacements u_0 and v_0 are assumed to have orders 5 and 3, respectively. Given that the composite is symmetric about the X axis, v_0 is assumed to be odd in y and even in x . Though the composite lies in the $x > 0$ space, its shape can be assumed to be symmetric about the X axis. This choice does not affect the solution since strain energy is computed only for $x > 0$. Therefore, u_0 is odd in x and even in y . The out-of-plane displacement w_0 is even in x and y . The resulting displacement polynomials have 14 coefficients (c_i) in total. The equilibrium shapes of the composite are obtained as a function of the external forces by minimizing the net energy using the variational Rayleigh-Ritz approach:

$$\sum_i \frac{\partial(\Phi - W_F - W_P)}{\partial c_i} = 0, \quad (8.12)$$

where i ranges from 1 to 14. The fourteen nonlinear equations are solved for the coefficients using the Newton-Raphson method.

8.3.4 Actuation using SMA wire

A shape memory alloy undergoes a large recoverable strain when the applied stress and operating temperature are above a critical minimum value; the material transforms to the Martensite phase. The strain can be recovered by heating the material to its Austenite phase. The constitutive behavior of a typical 1-D SMA (Figure 8.8(a)) can be modeled using thermodynamic relations and a kinetic law describing the material's phase. The volume fraction of Martensite is commonly described as an exponential [109] or cosine function [110] of temperature (Figure 8.8(b)). Brinson [111] developed a constitutive model for shape memory alloys where the Martensite volume fraction has temperature-induced and stress-induced components. Since the choice of the model does not adversely affect accuracy [114], the multivariant constitutive model, as formulated by Brinson, is chosen to simulate the composite's actuation.

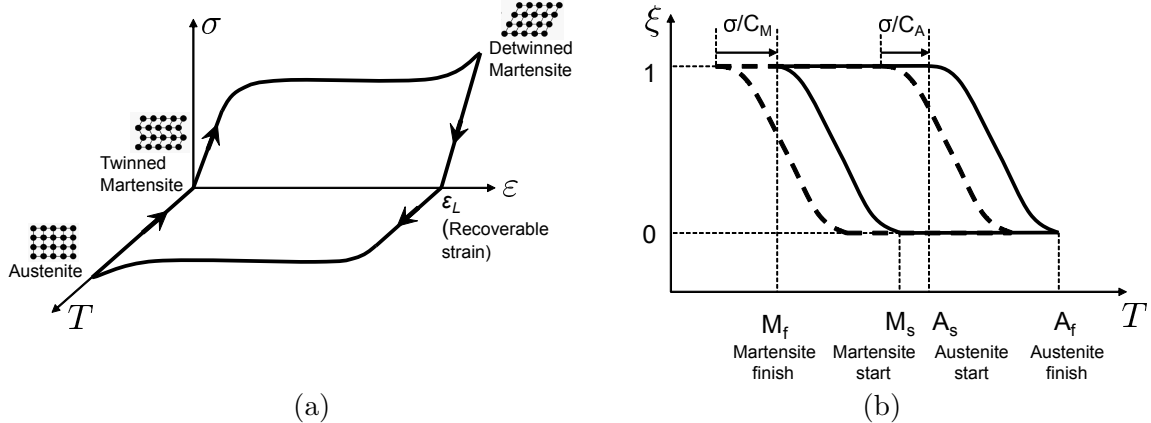


Figure 8.8: (a) Constitutive response and (b) phase transformation of a typical 1-D shape memory alloy. C_M and C_A are the stress-temperature coefficients in the Martensite and Austenite phases, respectively.

The one-dimensional constitutive law for an SMA is written as:

$$\sigma - \sigma_0 = E(\xi)(\epsilon - \epsilon_0) + \Theta(T - T_0) + \Omega(\xi)(\xi - \xi_0), \quad (8.13)$$

where ϵ , T , and ξ are the strain, temperature, and Martensite volume fraction of the material. E , Θ , and Ω are the Young's modulus, stress-temperature coefficient, and phase transformation coefficient. Using the rule of mixtures, E and Θ are expressed in terms of ξ as:

$$E(\xi) = E_A + \xi(E_M - E_A), \quad \Theta(\xi) = \alpha_A + \xi(\alpha_M - \alpha_A), \quad (8.14)$$

where α_M and α_A are the coefficients of thermal expansion in the Martensite and Austenite phases, respectively. Further, $\Omega = -\epsilon_L E(\xi)$, where ϵ_L is the maximum recoverable strain of the material.

The kinetics of phase transformation of the SMA is influenced by stress and temperature and is described using a cosine function (Figure 8.8(b)). For transformation from Martensite to Austenite, when $C_A(T - A_f) < \sigma < C_A(T - A_s)$:

$$\xi = \frac{\xi_0}{2} \left\{ \cos \left(\frac{\pi}{A_s - A_f} \left(T - A_s - \frac{\sigma}{C_A} \right) \right) + 1 \right\}, \quad (8.15)$$

where C_A is the stress-temperature coefficient for the Austenite phase, and A_s and A_f are the Austenite start and finish temperatures, respectively. For transformation from Austenite to Martensite, when $T > M_s$ and $\sigma_s^{cr} + C_M(T - M_s) < \sigma < \sigma_f^{cr} + C_M(T - M_s)$:

$$\xi = \frac{1 - \xi_0}{2} \cos \left\{ \frac{\pi}{\sigma_s^{cr} - \sigma_f^{cr}} (\sigma - \sigma_f^{cr} - C_M(T - M_s)) \right\} + \frac{1 + \xi_0}{2}, \quad (8.16)$$

where C_M is the stress-temperature coefficient for the Martensite phase, M_s is Martensite start temperature, and σ_s^{cr} and σ_f^{cr} are the critical stresses corresponding to the beginning and end of phase transformation.

The SMA wire is installed at an offset m from \overline{OE} and is clamped above points O and E , as shown in Figure 8.7(a), to ensure that it does not induce twist in the composite. The wire is installed on a curved composite in the detwinned Martensite phase. When heated, the wire contracts to the Austenite phase to flatten the

composite. Upon deactivation, the SMA becomes detwinned due to prestress in the composite. Given that the SMA is mounted at an offset m from the mid-plane, its strain can be expressed in terms of composite strain. Actuator strain (ϵ) is written in terms of wire length in the Austenite phase (L_A) and an intermediate phase (L_i) as:

$$\epsilon = \frac{(1 + \epsilon_{x0}^{(i)} + m\kappa_{x0}^{(i)})(1 + \epsilon_L)}{(1 + \epsilon_{x0}^{(s)} + m\kappa_{x0}^{(s)})} - 1. \quad (8.17)$$

Per (8.12) and (8.17), strain can be calculated for a given actuation force. The temperature of the SMA corresponding to a flat composite can be obtained from (8.13); stress (σ) is calculated as $4F/(\pi D^2)$.

Table 8.2: Geometric parameters for the modeled composite rib. ω is unitless. All other parameters are expressed in mm.

L_x	L_{y1}	L_{y2}	ω	L_{y3}	H	h_1	h_2
152.4	76.2	28.55	0.312	31.75	5.975	2.1875	-0.9875

Table 8.3: Material properties and thicknesses of the laminae for modeling and fabrication.

	Nylon panel	Vinyl foam core	Prestressed 90° EMC
Thickness (mm)	0.8	3.125	2
E_1 (MPa)	1000	30	Nonlinear
E_2 (MPa)	1000	30	1.5
G_{12} (MPa)	500	15	0.4
ν_{12}	0.28	0.33	0
ν_{21}	0.28	0.33	0

8.4 Composite rib design

8.4.1 Fender skirt geometry

The geometry of the fender skirt's domed shape is based on an envelope created around a wheel at its steering limits; the relevant dimensions of the fender and wheel are shown in Figure 8.4. The ratio of the radius of the rigid segment to that of the fender is determined through an interference study in Solidworks (Dassault Systems). To prove the concept, modeling and demonstration of the fender skirt are shown in half-scale. The values of the geometric parameters of each rib are as shown in Table 8.2. The material properties and thicknesses of the laminae used for simulation are listed in Table 8.3.

8.4.2 Passive composite

The stress in an EMC prior to lamination influences composite curvature. For a given EMC material, prestress is a function of the corresponding strain, width, and thickness. Figure 8.9(a) shows the effect of EMC prestrain ϵ_{90} on the out-of-plane displacement at $(L_x, 0)$. The nonlinear dependence of w_0 on ϵ_{90} resembles the nonlinear material response of an EMC, as previously discussed by Chillara and Dapino [107]. For a given width and thickness, ϵ_{90} is chosen so that w_0 is 60 mm; the target w_0 is obtained by subtracting the offsets due to the hinges and mounts from a required w_0 of 76 mm. EMC width and thickness are chosen based on assembly constraints. Inclusion of a vinyl foam core reduces prestrain requirements for a given out-of-plane deflection. For $w_0 = 60$ mm, ϵ_{90} reduces by 26% upon the inclusion of a foam layer. From Figure 8.9(a), the required EMC prestrain in the rib is 0.5.

For an EMC prestrain of 0.5, Figure 8.10 serves as a guide for the choice of panel material and thickness. The simulated modulus range corresponds to plastics, such

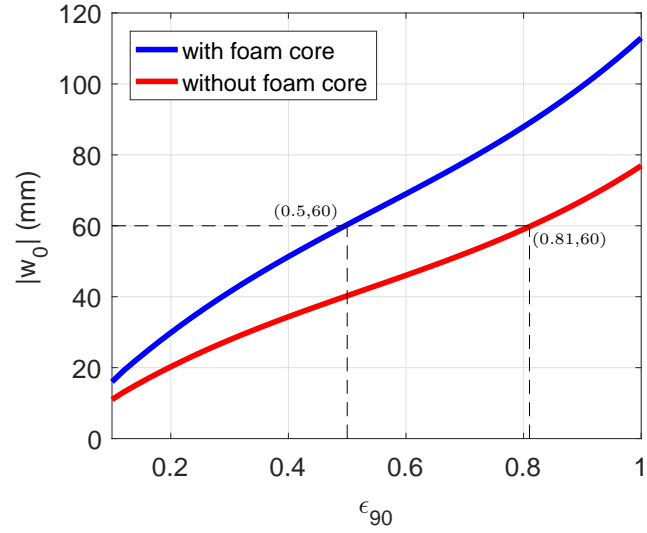


Figure 8.9: Influence of EMC prestrain ϵ_{90} on the out-of-plane displacement (w_0) at $(L_x, 0)$ on the composite rib.

as Nylon, that allow the panel's edges to conform to the skin for a smooth external appearance. Other material options include commonly used automotive materials such as aluminum and steel. For demonstration purposes, it is assumed that the panel is made of Nylon of modulus 1 GPa. For $w_0 = 60\text{mm}$, the corresponding thickness is obtained from Figure 8.10 as 0.8 mm.

Figure 8.11 shows the out-of-plane deflection w_0 at $(L_x, 0)$ as a function of a uniformly distributed vertical force P . Stiffness, defined as the product of the slope of the pressure-deflection curve (k) and panel area, is calculated to be 1.78 N/mm. It is observed that stiffness is independent of EMC prestrain. Tip deflection at -500 Pa and -1000 Pa are 2.7% and 5.4% of rib length, respectively. Therefore, for small deflections, stiffness is constant and independent of the shape of the passive composite. However, stiffness depends on the modulus and thickness of the laminae (simulation not shown). It is worth noting that the design for stiffness is based on an unconstrained edge at $x = L_x$ whereas, in the fender skirt, the edges at $x = 0$

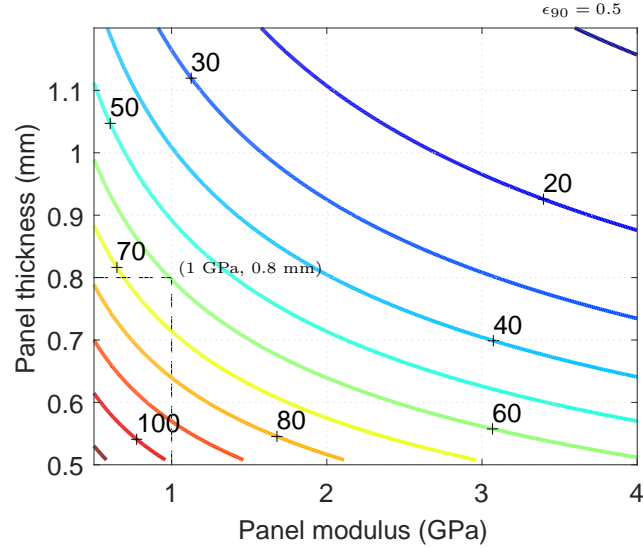


Figure 8.10: Effect of panel modulus and thickness on the out-of-plane displacement w_0 . Isometric lines correspond to w_0 in mm at $(L_x, 0)$.

and $x = L_x$ are hinged and fixed, respectively. The added boundary conditions and the structure's kinematic design are expected to augment the designed stiffness. Simulation of the structure's stiffness requires a finite element analysis that is beyond the scope of this paper.

8.4.3 SMA actuation

Figure 8.12(a) shows the deflection at $(L_x, 0)$ as a function of an in-plane actuation force F . The force that flattens the composite pertains to $w_0 = 0$. Flattening force increases with an increase in the offset m of force application from the mid-plane. Actuator stroke, calculated as the in-plane strain at $z = m$, also increases with an increase in m (Figure 8.12(b)). An offset of 6 mm is applied such that the actuator stroke matches a recoverable strain of 0.045 of the chosen NiTi #6 (Fort Wayne Metals Inc.) SMA wire. The flattening force at $m = 6$ mm is 24.8 N.

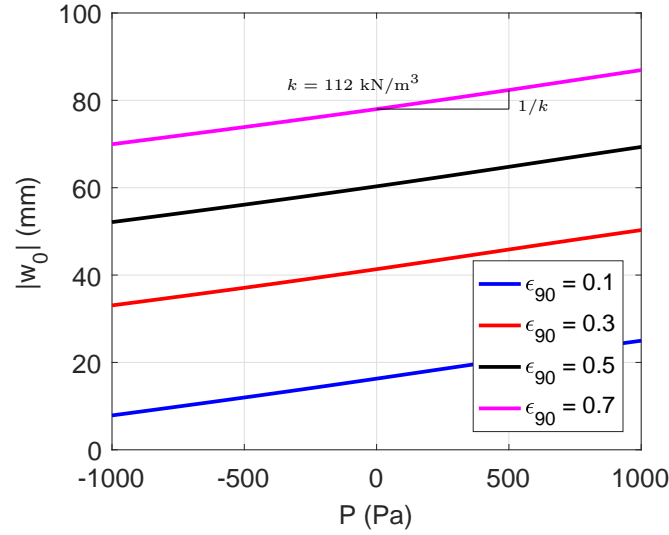


Figure 8.11: Out-of-plane displacement at $(L_x, 0)$ as a function of a vertical uniformly distributed force P .

Table 8.4: Measured material properties of a NiTi-6 shape memory alloy wire.

E_M (GPa)	E_A (GPa)	C_M (MPa/° C)	C_A (MPa/° C)	σ_s^{cr} (MPa)	σ_f^{cr} (MPa)
20	40	6.3	7.5	10	120
A_s (° C)	A_f (° C)	M_s (° C)	M_f (° C)	ϵ_L	
48	62	23	7	0.045	

For an automotive application, the selection of an SMA material is influenced by the range of operating temperatures. The Austenite start and finish temperatures should be higher than the maximum operating temperature, whereas the Martensite start and finish temperatures should be lower than the minimum operating temperature. For demonstration purposes, a NiTi #6 SMA with properties listed in Table 8.4 is considered in the design. Heating temperatures required to generate a flattening force of 24.8 N are calculated for various values of NiTi #6 wire diameter (Figure

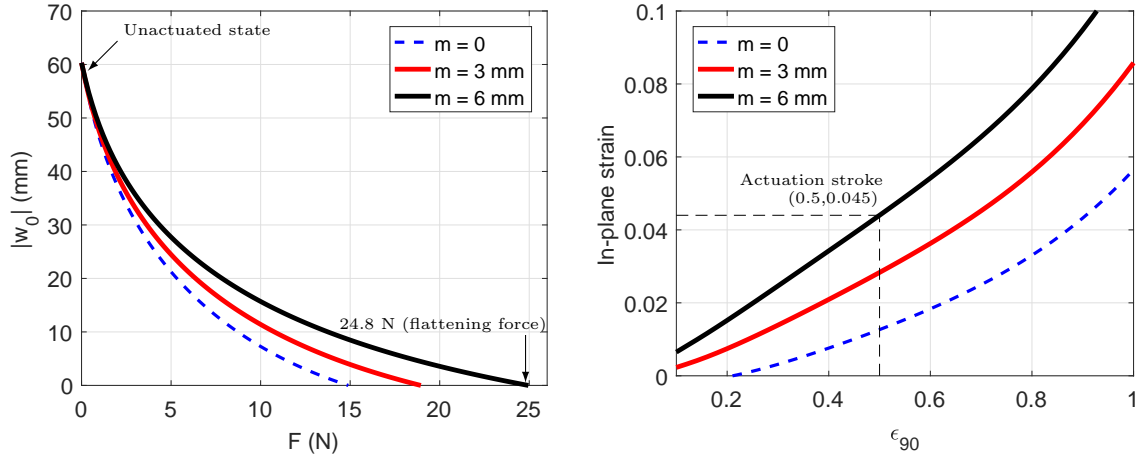


Figure 8.12: Plots to calculate the (a) force and (b) stroke required to flatten the composite.

8.13(a)). The corresponding change in Martensite volume fraction is plotted in Figure 8.13(b). In Martensite to Austenite transformation, stress retards phase change, thereby requiring higher temperatures than in the stress-free case to achieve actuation. For a given flattening force, increasing wire diameter lowers stress and hence lowers actuation temperature. As a consequence of the lowering of stress and actuation temperature, the change in Martensite volume fraction reduces with an increase in wire diameter. An SMA wire of 0.58 mm diameter is chosen for demonstration; the wire is heated to 55°C to flatten the composite. Using (8.16), it can be verified that the volume fraction changes from $\xi = 0.68$ (from Figure 8.13(b)) to $\xi = 1$ when the composite returns to the domed shape after the actuation input is switched off.

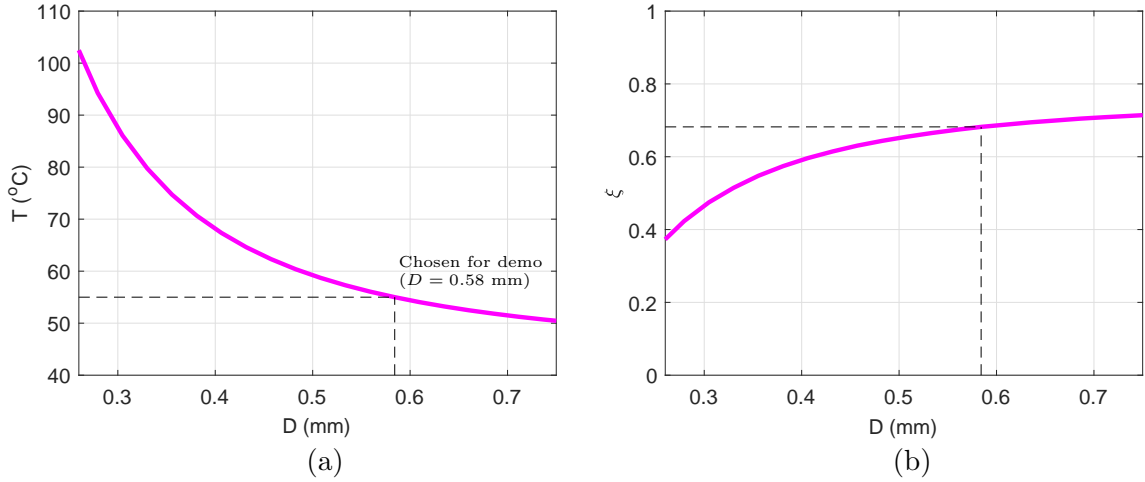


Figure 8.13: (a) Actuation temperature (T) and (b) Martensite volume fraction (ξ) of an SMA wire post actuation, as a function of its diameter D .

8.5 Case study: fender skirt

8.5.1 Fabrication

The steps involved in the fabrication of the fender skirt are illustrated in Figure 8.14. The ribs are cut out of a sector of a circular Nylon panel with an included angle of 148° and a radius of 228.6 mm. To accommodate the rigid portion (Figure 8.2(b)), a smaller sector of radius 76.2 mm is removed from the larger sector prior to rib preparation Figure 8.14(a). An EMC strip is stretched to 1.5 times its stress-free length and held between a pair of grips Figure 8.14(c). The prestressed EMC is laminated with a sandwiched vinyl foam (Divinycell, 48 kg/m^3 , Fiberglast Developments Corp.) core to each rib using a flexible adhesive (DAP automarine silicone sealant) as shown in Figure 8.14(c). Upon curing for 24 hours, a cylindrical rib is obtained (Figure 8.14(d)). The out-of-plane displacement of the rib is measured to be 63 mm. The measured displacement agrees well with the simulated value of $w_0 = 60$ mm. The prestressed EMC is oriented asymmetrically relative to the trapezoidal Nylon rib

such that the in-plane reaction forces applied by the structure are in the horizontal and vertical directions for effective flattening; prestressed laminae can be oriented symmetrically in the structure when the rib resolution is sufficiently high. As the fender skirt flattens, the vertical component of reaction force aids in rotation of the central hinge and the horizontal component forces the ends of the rim to slide outwards. Stiffeners are added to the rim-side edges of the ribs to prevent buckling at the hinges during morphing; the effect of the stiffener on the out-of-plane displacement is negligible.

The two halves of the central region are 3D-printed using Nylon and are connected by the central hinge. The curved ribs are then riveted to the rigid segment to obtain a domed shape (Figure 8.14(e)). The hinges on the ribs are linked together using a compliant rim made of copper wire. NiTi #6 SMA wires of 0.58 mm diameter are trained using cyclic stress-strain tests at a constant temperature of 80°C. The wires are then installed on 3 mm thick polycarbonate bridges that are bonded to outer face of the panel; bridges are added to maintain an offset of 6 mm from the mid-plane (Figure 8.14(f)). The wire is clamped on the outer end of the panel and is latched at the inner end. The response time of the actuator SMA, and hence the structure, is on the order of seconds. In order to quickly return from an intermediate shape to the domed shape in emergency maneuvers, a rotary latch is designed to release the active SMA (Figure 8.14(g)). The response time for retraction to the domed shape is expected to be on the order of milliseconds. Two such latches, one on each half of the rigid segment, are actuated using one SMA wire; the latch SMA is installed in the detwinned Martensite phase. The latches are also coupled by a spring that retracts them to the initial shape and returns the latch SMA to the detwinned Martensite phase.

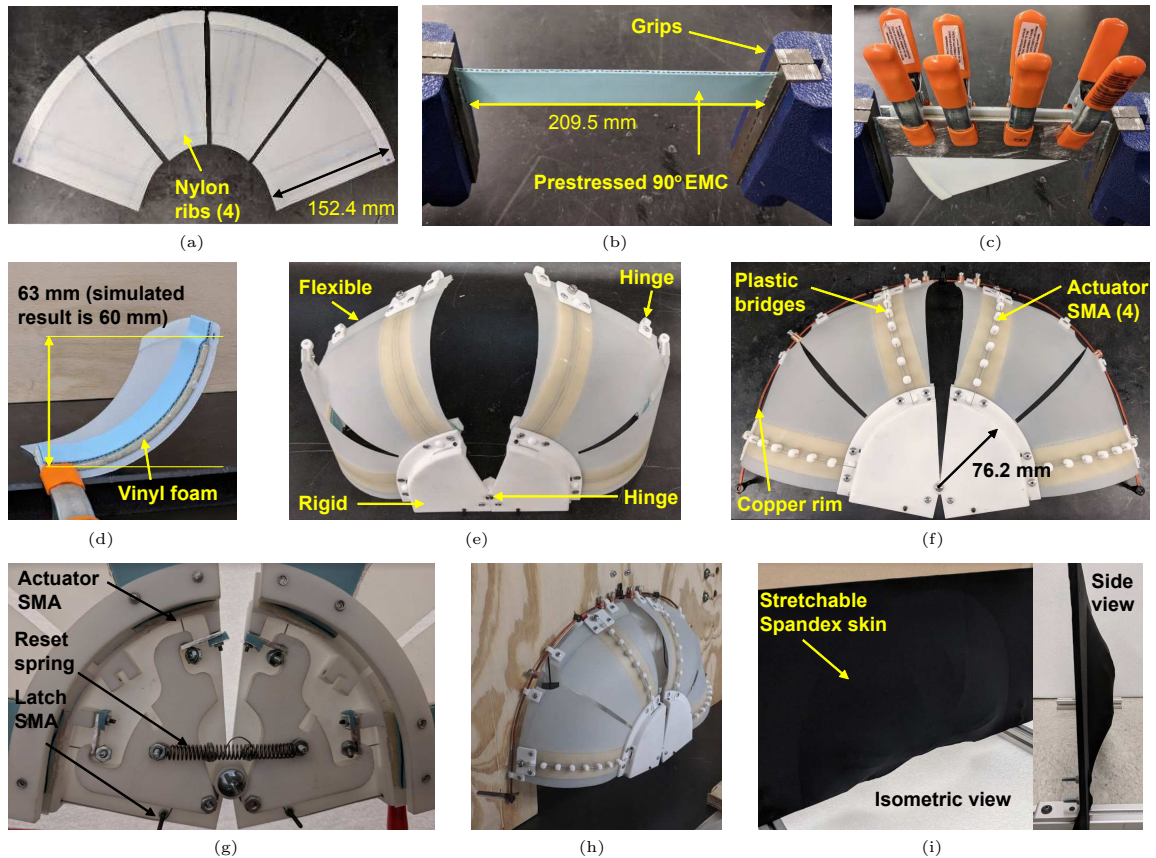


Figure 8.14: Fabrication procedure for a half-scale fender skirt demonstrator. (a) Ribs cut out of a sector of Nylon sheet; (b) a 90° EMC stretched and held between a pair of grips; (c) lamination of the Nylon panel, vinyl foam core, and EMC under pressure; (d) shape of the rib after lamination; (e) assembly of the ribs and a 3D printed rigid structure; (f) linkage of the outer ends of the ribs using a compliant copper rim; (g) elements of the latch mechanism on the back of the rigid structure; (h) fender skirt assembled on a wooden frame; (i) stretchable Spandex skin installed on the fender skirt.

The rim is connected, at two points near its center, to a wooden frame that represents the fender (Figure 8.14(h)). The fender skirt is covered by a skin that extends smoothly onto the fender (Figure 8.14(i)). The skin is made of a polyether-polyurea copolymer, commonly known as Spandex. The skin material used is easily stretchable and slides smoothly on the fender skirt. Therefore, there is no shear in the skin due to internal rotations in the fender skirt. The mass of the half-scale demonstrator, excluding electrical connections and the frame, is 355 grams. The demonstrator is 62% lighter than an equivalent automotive steel body panel of 0.8 mm thickness.

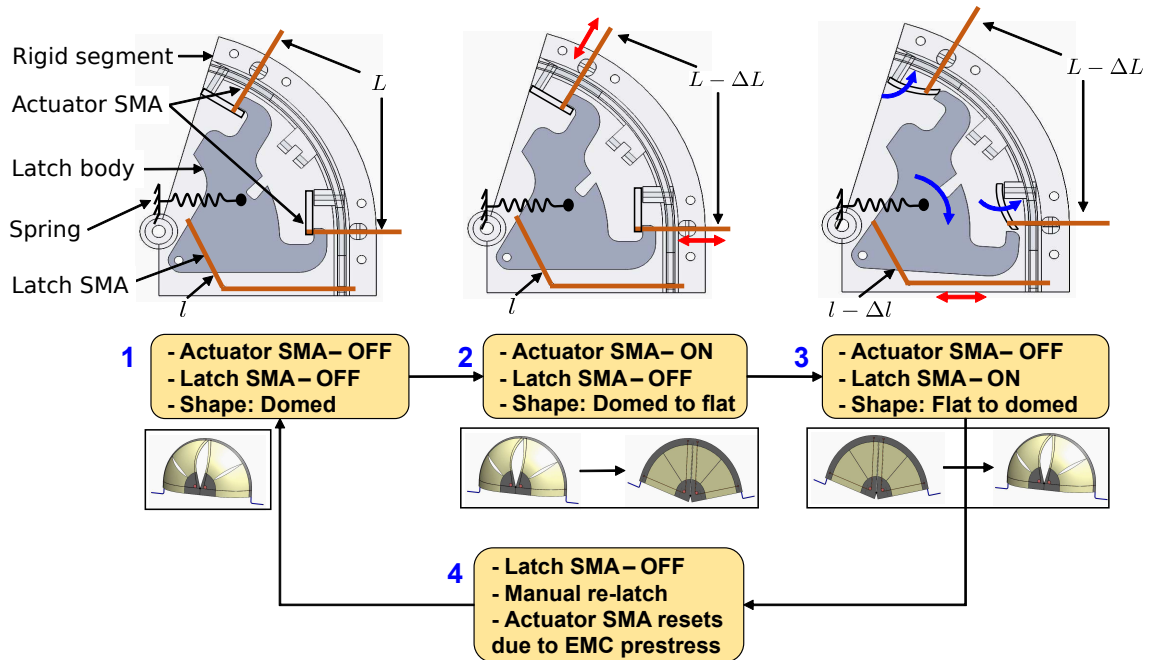


Figure 8.15: Actuation sequence for the demonstration of a morphing fender skirt.

8.5.2 Demonstration

The actuation sequence for the demonstrator is shown in Figure 8.15. The SMAs that actuate the composite and the latch are referred to as *actuator SMA* and *latch SMA*, respectively. In the unactuated state, the fender skirt is in the domed shape (stage 1). The structure is flattened by activating the actuator SMAs in the latched state (stage 2). From an intermediate shape, the structure is returned to the domed shape by activating the latch SMA (stage 3); the actuator SMA is turned off in this stage. In final stage, the latch SMA is turned off and the actuator SMAs are manually latched back for re-use. The latch SMA is stretched back to its detwinned Martensite state by the spring. Automatic system reset can be achieved by allowing the end-point of the actuator SMAs to slide in slots created in the latch body. The slots would have a curved profile to accommodate latch rotation. A manual-reset mechanism, however, is sufficient to demonstrate the complete operating cycle of a fender skirt.



Figure 8.16: (a) Unactuated domed shape and (b) actuated flat shapes of a half-scale morphing fender skirt demonstrator.

The unactuated and actuated shapes of the fender skirt are shown in Figure 8.16. The actuator SMAs on each half of the structure are electrically connected in series.

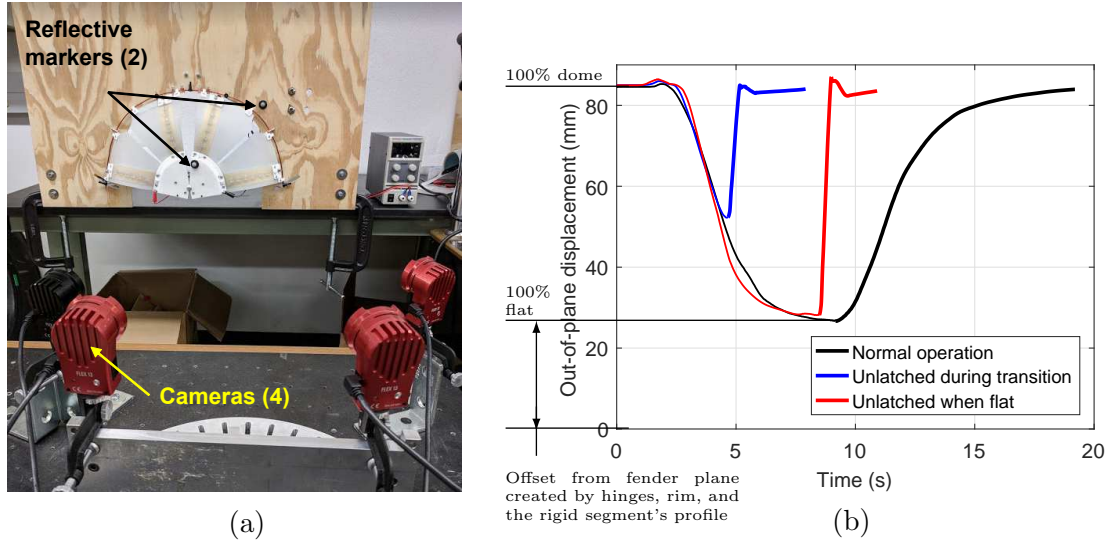


Figure 8.17: (a) Experimental setup to record the morphing of a fender skirt and (b) out-of-plane displacement of the rigid segment in the fender skirt demonstrator; thin and thick lines indicate the structure’s flattening and retraction, respectively.

The electrical branches on either half are connected in parallel. The current supplied to the set of actuator SMAs to achieve the shape in Figure 8.16(b) is 4.6 A at 2.7 V; the actuation power is 12.4 W, which corresponds to 3.1 W per SMA. The out-of-plane deformation of the fender skirt is measured using a motion capture system (Figure 8.17(a)). A reflective marker, bonded to the rigid segment, is tracked using a set of four cameras. The steps involved in shape measurement using a motion capture system are discussed in detail by Chillara et al. [107]. The coordinates of the marker relative to those of a reference marker on the frame are obtained for one morphing cycle.

Figure 8.17(b) shows the out-of-plane displacement of a fender skirt in the domed-shape for the following cases: 1. actuation to flat shape through heating and cooling of the actuator SMAs in forced air (table fan); 2. actuation to an intermediate shape in the sequence described in Figure 8.15; and 3. actuation to flat shape per the sequence in Figure 8.15. In the first case, the time taken for flattening and recovery

is 9.1 s and 10 s, respectively. However, when the actuator SMAs are unlatched, recovery time reduces to 0.5 s in cases 2 and 3. Therefore, in operating conditions involving high-steering rate, an SMA-actuated fender skirt can be designed to have a response time in the order of milliseconds.

Morphing fender skirts based on smart composites have been presented for the first time in this work. SMA-actuated prestressed curved composites are modeled analytically. The analytical model serves as a preliminary tool for shape tailoring, composite material selection, and actuator design. Comprehensive modeling of fender skirt shapes requires finite-element multiphysics simulations that account for the kinematics, aerodynamic interactions, thermo-mechanical behavior of SMAs, nonlinear material response of EMCs, and large deformation of the composites. A morphing fender skirt for a compact passenger car has been successfully demonstrated at half-scale. When coupled with a quick-release latch mechanism, SMA actuators are shown to be capable of actuation speeds on the order of milliseconds. An attractive alternative to quick-release latches would be bistability in the ribs of the fender skirt. SMA-actuated bistable composites could reduce design complexity and the overall weight of the structure. Smart material-driven prestressed composites have the potential to serve as building blocks in the development of morphing structures with complex geometries.

Chapter 9

Contributions and Future Work

9.1 Summary of findings

Morphing panels offer opportunities as adaptive surfaces in advanced aircraft and automobiles for optimal performance over a broad range of operating conditions (Chapter 1). For example, in automobiles, reduced aerodynamic drag is critical at high speed whereas minimal disruption in operation is the priority at low speed. The improved fuel economy possible through morphing panels is a tradeoff between drag reduction and added weight. Requirements such as low weight, compactness, and system-level compatibility can be addressed using adaptive laminated composites. Existing morphing composites can undergo stretching, flexure, and folding but tend to lack mechanisms to achieve all these shape changes simultaneously. To bridge this research gap, a multifunctional laminated composite is developed (Chapter 2). The composite is capable of multiple morphing modes and adaptive features such as controllable curvature, bistability, and autonomous folding. Its laminae are classified based on function as constraining, adaptive, and prestressed laminae.

The use of fiber-reinforced elastomers in existing morphing composite designs is restricted to stretchable skins. In this work, fiber-reinforced elastomers are not only considered as stretchable elements, but also as selectively-prestrained laminae to create an innovative stress-biased curved composite that has an irreversible non-zero

stress state; the curved shapes range from flat to coiled states. This approach allows one to create curved multifunctional composites by combining prestrained laminae and smart laminae that have controllable stress-states; functionality in existing curved composites is limited due to globally-applied residual stress.

The interaction between prestressed and stress-free laminae is explained using an analytical model (Chapter 2). The model is developed in a direct approach, based on strain energy minimization, to calculate composite shape for a given set of laminate parameters. The model incorporates material and geometric nonlinearities associated with highly-strained elastomers and a laminated composite with large deflection. For the development of a multifunctional composite framework, the adaptive lamina is considered to be a passive material containing fluid channels that are pressurized to achieve actuation (Chapter 3). The fluid channels are molded into a flexible elastic medium instead of embedding individual fluidic muscle actuators. This configuration is simpler to model and fabricate compared to the existing approaches for fluidic actuation; actuator work is a function of channel volume which in turn is a function of the unknown strain functions of the composite. The model compares well with experiments conducted on fabricated pressure-actuated composites at the coupon-scale, with a maximum error of $\pm 6\%$.

A matrix-prestressed bistable laminate, fabricated at room temperature, is presented as a robust alternative to thermally-cured FRP bistable laminates (Chapter 4). Besides the potential for hygrothermal invariance, the bistable laminate design enables individual tailoring of shapes using prestress in specific laminae, a feature that is lacking in FRP laminates where both shapes are affected by curing temperature. The domain of bistability is quantified for rectangular composites with two sources of residual stress. A non-dimensional high-order strain model is constructed to simulate bistability limits as a function of aspect ratio and the ratio of prestrains

(Chapter 6); cubic displacement polynomials are sufficient to calculate stable shapes whereas high-order polynomials are required to describe transitional phenomena.

Shape transition is shown to be a multi-stage phenomenon through a new experimental procedure involving friction-free tensile tests and 3D motion capture (Chapter 6). The simulated actuation energies agree with measurements within 12%. A comparison of various actuation modes such as axial, in-plane, and transverse, shows that in-plane forcing requires 100 times more energy than an equivalent moment. However, in-plane actuation, which is made viable by smart materials, is relatively energy efficient when the actuator is mounted on the convex face of a curved composite. An active bistable composite driven by in-plane SMA wires is modeled and fabricated (Chapter 5). The SMA wire actuators are installed on either face of the composite in a push-pull configuration where activation of one wire switches composite shape and simultaneously resets the phase of the antagonistic shape memory wire. The set of shape memory actuators not only actuate the composite in both directions, but also act as dampers that enable vibration-free shape transition. Parametric studies are conducted using the analytical model to describe the effects of material and geometric properties of the laminae on the composite's performance metrics such as morphing range, actuation energy, and out-of-plane stiffness.

A folding strategy using the multifunctional composite framework is presented (Chapter 7). Smart laminae with controllable modulus, when included in stress-biased composites, can be locally activated to realize autonomous folding. The analytical model developed in this work is a tool for designing folds for a given set of laminae. From model-based analysis, it is shown that narrow creases demand high input prestrain relative to wider creases. Fold sharpness can be maximized by minimizing crease width and thickness. From an input energy standpoint, folding is most effective when prestress is applied across the crease at a 90° angle. The EMC's anisotropy is

a tradeoff between achieving zero in-plane Poisson's ratio for unidirectional prestress and maximizing the range of crease orientations for foldability.

A thorough literature survey is conducted on the effect that aerodynamic treatments have on vehicle drag. A morphing fender skirt is demonstrated since it provides a good trade-off between drag reduction (0.038 points) and practical implementation. Through design, manufacturing, and testing, a lightweight, self-supported, and self-actuated morphing fender skirt is developed based on the multifunctional composites characterized at the coupon scale (Chapter 8). Shape memory alloy wires are embedded in a radially-configured prestressed composite ribbed structure to achieve morphing between flat and domed shapes. Rapid actuation is demonstrated by coupling SMAs with integrated quick-release latches; the latches reduce actuation time by 95%. The demonstrator is 62% lighter than an equivalent dome-shaped automotive steel panel.

9.2 Primary contributions

1. **Innovative stress-biased curved composites with an irreversible non-zero stress state**

Incorporation of mechanically-prestressed laminae is a unique method to imbue permanent residual stress in a material without subjecting it to plastic deformation. When paired with suitable laminae, mechanically-prestressed composites exhibit curved shapes. Such composites are candidates for morphing structures since they can be coupled with adaptive laminae comprising smart materials such as piezoelectrics, shape memory alloys, and active polymers; the stress state of adaptive laminae can be controlled to achieve a range of morphing shapes. The stress-bias serves as a built-in spring in the material, thereby limiting actuation to one direction.

2. Design framework for multifunctional laminated composites

Multifunctional morphing structures can be developed using a laminated composite framework comprising three types of laminae, viz., constraining, adaptive, and prestressed. The composite framework has potential not only to realize multiple morphing modes such as stretching, flexure, and folding, but also to achieve adaptive functions such as bistability and self-actuation.

3. Analytical models for design and characterization

The analytical model of a mechanically-prestressed composite serves as a tool for the selection of passive and adaptive laminae towards the development of morphing structures. The parametric sensitivity analyses presented guide the design of various morphing configurations and functions including flexure, folding, bistability, and smart actuation. As demonstrated, the laminated-plate model can be combined with constitutive or free energy-based smart-material models to characterize adaptive composites.

4. Fabrication methods for mechanically-prestressed composites

The method for lamination of prestressed layers is integral to the design of stress-biased morphing structures. The use of a prestressed anisotropic elastomer with zero in-plane Poisson's ratio enables tailoring of a single cylindrical shape whose axis is perpendicular to the direction of prestress. Complex curvatures can be created by superposing prestressed laminae oriented in different directions. The process presented in this work enables the lamination of prestressed material patches in pre-assembled structures (e.g., vehicle body) for localized shape tailoring.

9.3 Related contributions

1. Model-based characterization of the interaction between prestressed and adaptive laminae

Analysis of the stacking configurations of a multifunctional composite indicates that the energy requirement for actuation is minimal in the constraining/prestressed/adaptive layer configuration. In the minimal configuration, minimizing the offset between the actuator (in the adaptive layer) and the prestressed layer minimizes actuation effort.

2. Development of pressure-actuated prestressed composites

An approach for creating adaptive laminae with built-in fluid channels is presented. Fluid channels are molded into a flexible lamina that is tailored using anisotropy to deform in plane without bulging out of plane. This design is scalable in complexity; fluid channels of varying cross-sections can be configured in a vascular network for localized curvature control. The fabrication process is simpler than incorporating individually-reinforced fluidic muscles in a flexible medium. Modeling is relatively simple as the work done in actuation can be expressed as a function of composite strains.

3. Modeling and development of a new type of bistable composite

Mechanically-prestressed composites enhance the design space of existing bistable laminated composites as their residual stress is contained to specific laminae. In composites with orthogonally-prestressed laminae, the stable shapes are weakly coupled; each shape can be tailored using a specific lamina. Since the composites are fabricated at room temperature, they are potentially invariant to

changes in temperature and humidity; hygrothermal sensitivity is an inherent drawback in thermally-cured FRP laminates.

4. Modeling of the stability and actuation of bistable composites

In rectangular bistable composites with two sources of residual stress, the ratio of prestress should lie within a specific range. Outside this range, the composite has a single stable curvature. A comparison of actuation modes shows that the energy requirement for in-plane actuation is two orders of magnitude higher than that for transverse out-of-plane actuation.

5. Strategy for smooth folding of laminated composites

A method for achieving smooth folds, based on prestress applied over a crease, is presented. The complexity associated with creation of smooth folds using compliant joints and tucks can be addressed by this technique. The approach prevents buckling of inner laminae since the innermost lamina is stretched prior to lamination. The effect of material and geometric properties has been studied using an analytical model.

6. Antagonistic SMAs for actuation and damping in bistable composites

Actuation of bistable composites using SMAs in an antagonistic configuration shows that a given SMA wire acts as an actuator in the activated state and as a damper in the unactivated state. The set of SMAs enable an almost vibration-free shape transition. A modeling approach has been presented for designing SMA actuators in a push-pull configuration.

7. Design approach for morphing automotive structures

SMA-actuated prestressed composites have been modeled as elements in a morphing structure. Through the demonstration of a morphing fender skirt, a

design approach for the implementation of multifunctional composites is demonstrated. A quick-release latch mechanism is developed to operate SMA actuators with a response time in the order of milliseconds.

9.4 Future work

1. Incorporation of variable-stiffness capability in pressure-actuated prestressed composites

The working fluid in pressure-actuated composites can be trapped using valves to harness the fluid's high bulk modulus for rigidization of the composite. This feature enables the composite to morph to a given shape while providing adequate stiffness in that shape. The potential research questions are: fabrication method for embedded valves that lock a fluidic layer; and inclusion of the fluid's bulk modulus in the model for stiffness calculation.

2. Inclusion of self-sensing capability in multifunctional composites

Flexible sensors such as piezoelectric polymers (PVDF - polyvinylidene fluoride) can be included as adaptive laminae in a mechanically-prestressed composite. Piezoelectric laminae undergo a change in in-plane strain resulting from shape morphing of the composite and generate a corresponding charge. The output signal from the sensor serves as a control input that drives the actuator to achieve a given curved shape. The analytical model presented can be enhanced to account for the constitutive response of the sensor.

3. Computational modeling of a bistable morphing fender skirt

Bistable composites can replace quick-release latches for the rapid actuation of a morphing structure such as a fender skirt. Bistability can be added to an

existing body/structure by bonding prestressed layers and creating the appropriate boundary conditions. Tailoring of the stable shapes may require finite element methods for the optimization of the stiffness of the composite's core. The analytical model presented in this work guides the preliminary design of materials and geometry for a bistable morphing structure.

4. Development of self-folding composites with reconfigurable creases

Smart materials that have a controllable modulus can be activated to configure creases in a prestressed composite. Examples of variable modulus laminae include shape memory alloys, shape memory polymers, magnetorheological materials, and phase change materials such as paraffin wax. Creases can be formed in a fold-free composite by lowering the active material's modulus whereas folding is driven by the restoring force in the prestressed layer.

5. Development of an inverse model to determine composite configuration for a given set of morphing shapes

In this work, the analytical model is developed in the direct form to calculate stable shapes based on laminae properties. While the direct model is suitable for composite characterization, an inverse model is a better tool for the optimization of laminae properties for a desired curved shape. The research challenges in inverse modeling lie in the consideration of material and geometric nonlinearities associated with laminate response.

6. Dynamic characterization of mechanically-prestressed composites

An elastically-applied stress-bias may provide opportunities for tuning the dynamic response of a structure. For example, the natural frequency and damping ratio of the structure may be a function of the magnitude and direction of the

applied prestress. Mathematical modeling is required to characterize the dynamics of a stress-biased composite.

The multifunctional composite framework, analytical modeling, and fabrication methods developed in this dissertation can be applied to the above described future research objectives. Developments resulting from the suggested objectives would enable smart lightweight morphing structures that can serve a range of applications in the fields of aerospace and automotive engineering, soft robotics, and biomimetics.

Bibliography

- [1] Barnard RH. Road vehicle aerodynamic design-an introduction. Addison Wesley Longman Limited; 1996.
- [2] BMW vision Next 100 Years concept. BMW Group; 2016. [Online]. Available: <https://www.bmwgroup.com/en/next100/brandvisions.html>.
- [3] Mercedes-Benz Intelligent Aerodynamic Automobile: digital transformer. Daimler Communications, 70546 Stuttgart/Germany; 2015. [Online]. Available: <https://www.mercedes-benz.com/en/mercedes-benz/design/mercedes-benz-design/concept-cars/concept-iaa-intelligent-aerodynamic-automobile/>.
- [4] Porsche active aerodynamics (PAA). Porsche AG; 2017. [Online]. Available: <https://www.porsche.com/international/models/911/911-turbo-models/911-turbo/chassis/porsche-active-aerodynamics-paa/>.
- [5] Ferrari 458 Speciale active aerodynamics. Ferrari S.P.A; 2014. [Online]. Available: http://auto.ferrari.com/en_US/sports-cars-models/past-models/458-speciale/.
- [6] Morphing Wing Created Using Smart Materials and Actuators. Engineering 360 - IEEE GlobalSpec; 2018. [Online].

Available: <https://insights.globalspec.com/article/7578/morphing-wing-created-using-smart-materials-and-actuators>.

- [7] Jodin G, Scheller J, Rizzo KJ, Duhayon E, Rouchon JF, Braza M. Dimensionnement d'une maquette pour l'investigation du morphing électroactif hybride en soufflerie subsonique. In: 22e Congrès Français de Mécanique (CFM 2015); 2015. p. 1–13.
- [8] Bubert EA, Woods BK, K, Kothera CS, Wereley WM. Design and Fabrication of a Passive 1D Morphing Aircraft Skin. *Journal of Intelligent Material Systems and Structures*. 2010;21(17):1699–1717.
- [9] Mattioni F, Weaver PM, Potter KD, Friswell MI. The application of thermally induced multistable composites to morphing aircraft structures. In: *The 15th International Symposium on: Smart Structures and Materials & Nondestructive Evaluation and Health Monitoring*. International Society for Optics and Photonics; 2008. p. 693012–693012–11.
- [10] Kudva JN. Overview of the DARPA Smart Wing Project. *Journal of Intelligent Material Systems and Structures*. 2004;15(4):261–267.
- [11] Murray G, Gandhi F, Bakis C. Flexible matrix composite skins for one-dimensional wing morphing. *Journal of Intelligent Material Systems and Structures*. 2010;21(17):1771–1781.
- [12] Hyer MW. Some Observations on the Cured Shape of Thin Unsymmetric Laminates. *Journal of Composite Materials*. 1981;15(2):175–194.
- [13] Daynes S, Potter KD, Weaver PM. Bistable prestressed buckled laminates. *Composites Science and Technology*. 2008;68(15–16):3431–3437.

- [14] Hawkes E, An B, Benbernou NM, Tanaka H, Kim S, Demaine ED, et al. Programmable matter by folding. *Proceedings of the National Academy of Sciences*. 2010;107(28):12441–12445.
- [15] Felton SM, Tolley MT, Shin B, Onal CD, Demaine ED, Rus D, et al. Self-folding with shape memory composites. *Soft Matter*. 2013;9(32):7688–7694.
- [16] Ahmed S, Lauff C, Crivaro A, McGough K, Sheridan R, Frecker M, et al. Multi-Field Responsive Origami Structures: Preliminary Modeling and Experiments. In: *ASME 2013 International Design Engineering Technical Conferences and Computers and Information in Engineering Conference*. American Society of Mechanical Engineers; 2013. p. V06BT07A028.
- [17] Schultz MR, Hyer MW, Brett Williams R, Keats Wilkie W, Inman DJ. Snap-through of unsymmetric laminates using piezocomposite actuators. *Composites Science and Technology*. 2006;66(14):2442–2448.
- [18] Kim HA, Betts DN, Salo AIT, Bowen CR. Shape Memory Alloy-Piezoelectric Active Structures for Reversible Actuation of Bistable Composites. *American Institute of Aeronautics and Astronautics Journal*. 2010;48(6):1265–1268.
- [19] Kim SW, Koh JS, Lee JG, Ryu J, Cho M, Cho KJ. Flytrap-inspired robot using structurally integrated actuation based on bistability and a developable surface. *Bioinspiration and Biomimetics*. 2014;9(3):036004.
- [20] Deimel R, Brock O. A compliant hand based on a novel pneumatic actuator. In: *2013 IEEE International Conference on Robotics and Automation*; 2013. p. 2047–2053.

- [21] Chillara VSC, Headings LM, Dapino MJ. Multifunctional composites with intrinsic pressure actuation and prestress for morphing structures. *Composite Structures*. 2016;157:265–274.
- [22] Future U.S trends in the adoption of light-duty automotive technologies. For American Petroleum Institute, by H-D Systems, Washington DC; 2013.
- [23] Daynes S, Weaver PM. Review of Shape-Morphing Automobile Structures: Concepts and Outlook. *Proceedings of the Institution of Mechanical Engineers, Part D: Journal of Automobile Engineering*. 2013;227(11):1603–1622.
- [24] Hucho WH. *Aerodynamics of Road Vehicles: From Fluid Mechanics to Vehicle Engineering*. Elsevier Science; 2013.
- [25] Koike M, Nagayoshi T, Hamamoto N. Research on aerodynamic drag reduction by vortex generators. *Mitsubishi Motors Technical Review*. 2004;(16).
- [26] Hucho WH, Ahmed SR. *Aerodynamics of road vehicles: from fluid mechanics to vehicle engineering*. Society of Automotive Engineers; 1998.
- [27] Sunny SA. Effect of turbulence in modeling the reduction of local drag forces in a computational automotive model. *International Journal of Energy and Environment*. 2011;2(6):1079–1100.
- [28] Buchheim R, Leie B, Lückoff H. Der neue Audi 100—Ein Beispiel für konsequente aerodynamische Personenwagen-Entwicklung. *Automobiltechnische Zeitschrift*. 1983;85:419–425.
- [29] Costelli AF. Aerodynamic characteristics of the Fiat UNO car. *Society of Automotive Engineers: Technical Paper*. 1984;(840297).

- [30] Barbarino S, Bilgen O, Ajaj RM, Friswell MI, Inman DJ. A Review of Morphing Aircraft. *Journal of Intelligent Material Systems and Structures*. 2011;22(9):823–877.
- [31] Murray GJ, Gandhi F. Auxetic honeycombs with lossy polymeric infills for high damping structural materials. *Journal of Intelligent Materials Systems and Structures*. 2013;24(9):1090–1104.
- [32] Dayyani I, Khodaparast HH, Woods BKS, Friswell MI. The design of a coated composite corrugated skin for the camber morphing airfoil. *Journal of Intelligent Materials Systems and Structures*. 2015;26(13):1592–1608.
- [33] Olympio KR, Gandhi F. Flexible Skins for Morphing Aircraft Using Cellular Honeycomb Cores. *Journal of Intelligent Materials Systems and Structures*. 2010;21(17):1719–1735.
- [34] Philen M, Shan Y, Bakis C, Wang KW, Rahn C. Variable Stiffness Adaptive Structures utilizing Hydraulically Pressurized Flexible Matrix Composites with Valve Control. In: 47th AIAA/ASME/ASCE/AHS/ASC Structures, Structural Dynamics, and Materials Conference; 2006. p. 2134.
- [35] Shan Y, Philen M, Lotfi A, Li S, Bakis CE, Rahn CD, et al. Variable stiffness structures utilizing fluidic flexible matrix composites. *Journal of Intelligent Material Systems and Structures*. 2009;20(4):443–456.
- [36] Chou CP, Hannaford B. Measurement and modeling of McKibben pneumatic artificial muscles. *IEEE Transactions on Robotics and Automation*. 1996;12(1):90–102.

- [37] Bilgen O, Kochersberger KB, Inman DJ, Ohanian OJ. Novel, bidirectional, variable-camber airfoil via macro-fiber composite actuators. *Journal of Aircraft*. 2010;47(1):303–314.
- [38] Yin WL, Sun QJ, Zhang B, Liu JC, Leng JS. Seamless Morphing Wing with SMP Skin. *Advanced Materials Research*. 2008;47-50:97–100.
- [39] Chen S, Chen Y, Zhang Z, Liu Y, Leng J. Experiment and analysis of morphing skin embedded with shape memory polymer composite tube. *Journal of Intelligent Materials Systems and Structures*. 2014;25(16):2052–2059.
- [40] Song JJ, Chen Q, Naguib HE. Constitutive modeling and experimental validation of the thermo-mechanical response of a shape memory composite containing shape memory alloy fibers and shape memory polymer matrix. *Journal of Intelligent Materials Systems and Structures*. 2016;27(5):625–641.
- [41] Daynes S, Weaver P. Analysis of Unsymmetric CFRP–Metal Hybrid Laminates for Use in Adaptive Structures. *Composites Part A: Applied Science and Manufacturing*. 2010;41(11):1712–1718.
- [42] Li H, Dai F, Weaver PM, Du S. Bistable hybrid symmetric laminates. *Composite Structures*. 2014;116:782–792.
- [43] Daynes S, Diaconu CG, Potter KD, Weaver PM. Bistable prestressed symmetric laminates. *Journal of Composite Materials*. 2010;44(9):1119–1137.
- [44] Eckstein E, Pirrera A, Weaver PM. Multi-mode morphing using initially curved composite plates. *Composite Structures*. 2014;109:240–245.
- [45] Dano ML, Hyer MW. SMA-induced snap-through of unsymmetric fiber-reinforced composite laminates. *International Journal of Solids and Structures*. 2003;40(22):5949–5972.

- [46] Hufenbach W, Gude M, Kroll L. Design of multistable composites for application in adaptive structures. *Composites Science and Technology*. 2002;62(16):2201–2207.
- [47] Simoneau C, Terriault P, Lacasse S, Brailovski V. Adaptive Composite Panel with Embedded SMA Actuators: Modeling and Validation. *Mechanics Based Design of Structures and Machines*. 2014;42(2):174–192.
- [48] Lamacchia E, Eckstein E, Pirrera A, Weaver P. Morphing structures: non-linear composite shells with irregular planforms. In: 56th AIAA/ASCE/AHS/ASC Structures, Structural Dynamics, and Materials Conference; 2015. p. 0962.
- [49] Feng N, Liu L, Liu Y, Leng J. A bio-inspired, active morphing skin for camber morphing structures. *Smart Materials and Structures*. 2015;24(3):035023.
- [50] Marchese AD, Onal CD, Rus D. Autonomous soft robotic fish capable of escape maneuvers using fluidic elastomer actuators. *Soft Robotics*. 2014;1(1):75–87.
- [51] Pagitz M, Lamacchia E, Hol JMAM. Pressure-actuated cellular structures. *Bioinspiration and Biomimetics*. 2012;7(1):016007.
- [52] Pagitz M, Bold J. Shape-changing shell-like structures. *Bioinspiration and Biomimetics*. 2013;8(1):016010.
- [53] Zhang CS, Ni QQ. Bending behavior of shape memory polymer based laminates. *Composite Structures*. 2007;78(2):153–161.
- [54] Compton-Bishop QM, Daton-Lovett AJ, Curry RG. Industrial and commercial applications of bistable reeled composites. In: SPIE's 7th Annual International Symposium on Smart Structures and Materials. vol. 3991; 2000. p. 335–343.

- [55] Pellegrino S. Bistable Shell Structures. In: 46th AIAA/ASME/ASCE/AHS/ASC Structures, Structural Dynamics and Materials Conference; 2005. p. 1934.
- [56] Yee JCH, Pellegrino S. Folding of woven composite structures. *Composites Part A: Applied Science and Manufacturing*. 2005;36(2):273–278.
- [57] Li S, Wang KW. Fluidic origami: a plant-inspired adaptive structure with shape morphing and stiffness tuning. *Smart Materials and Structures*. 2015;24(10):105031.
- [58] Lan X, Liu Y, Lv H, Wang X, Leng J, Du S. Fiber Reinforced Shape-Memory Polymer Composite and its Application in a Deployable Hinge. *Smart Materials and Structures*. 2009;18(2):024002.
- [59] Peraza-Hernandez E, Hartl D, Galvan E, Malak R. Design and Optimization of a Shape Memory Alloy-Based Self-Folding Sheet. *Journal of Mechanical Design*. 2013;135(11):111007.
- [60] Philen M, Shan Y, Wang KW, Bakis C, Rahn C. Fluidic Flexible Matrix Composites for the Tailoring of Variable Stiffness Adaptive Structures. In: 48th AIAA/ASME/ASCE/AHS/ASC Structures, Structural Dynamics, and Materials Conference; 2007. p. 1703.
- [61] Murugan S, Saavedra Flores EI, Adhikari S, Friswell MI. Optimal design of variable fiber spacing composites for morphing aircraft skins. *Composite Structures*. 2012;94(5):1626–1633.
- [62] Lachenal X, Weaver PM, Daynes S. Multi-stable composite twisting structure for morphing applications. *Proceedings of the Royal Society A: Mathematical, Physical and Engineering Science*. 2012;468(2141):1230–1251.

- [63] Kebabze E, Guest SD, Pellegrino S. Bistable prestressed shell structures. *International Journal of Solids and Structures*. 2004;41(11–12):2801–2820.
- [64] Seffen KA. Mechanical memory metal: a novel material for developing morphing engineering structures. *Scripta Materialia*. 2006;55(4):411–414.
- [65] Norman AD, Seffen KA, Guest SD. Multistable corrugated shells. *Proceedings of the Royal Society of London A: Mathematical, Physical and Engineering Sciences*. 2008;464(2095):1653–1672.
- [66] Brinkmeyer A, Santer M, Pirrera A, Weaver PM. Pseudo-bistable self-actuated domes for morphing applications. *International Journal of Solids and Structures*. 2012;49(9):1077–1087.
- [67] Fernlund G, Rahman N, Courdji R, Bresslauer M, Poursartip A, Willden K, et al. Experimental and numerical study of the effect of cure cycle, tool surface, geometry, and lay-up on the dimensional fidelity of autoclave-processed composite parts. *Composites Part A: Applied Science and Manufacturing*. 2002;33(3):341–351.
- [68] Hyer MW. Calculations of the room-temperature shapes of unsymmetric laminates. *Journal of Composite Materials*. 1981;15:296–310.
- [69] Schlecht M, Schulte K. Advanced Calculation of the Room-Temperature Shapes of Unsymmetric Laminates. *Journal of Composite Materials*. 1999;33(16):1472–1490.
- [70] Lee H, Lee JG, Ryu J, Cho M. Twisted shape bi-stable structure of asymmetrically laminated CFRP composites. *Composites Part B: Engineering*. 2017;108:345–353.

- [71] Etches J, Potter K, Weaver P, Bond I. Environmental effects on thermally induced multistability in unsymmetric composite laminates. *Composites Part A: Applied Science and Manufacturing*. 2009;40(8):1240–1247.
- [72] Snyder MP, Sanders B, Eastep FE, Frank GJ. Vibration and Flutter Characteristics of a Folding Wing. *Journal of Aircraft*. 2009;46(3):791–799.
- [73] Cromvik C, Eriksson K. Airbag folding based on origami mathematics. *Origami*. 2006;4:129–139.
- [74] Felton S, Tolley M, Demaine E, Rus D, Wood R. A method for building self-folding machines. *Science*. 2014;345(6197):644–646.
- [75] Daynes S, Trask RS, Weaver PM. Bio-inspired structural bistability employing elastomeric origami for morphing applications. *Smart Materials and Structures*. 2014;23(12):125011.
- [76] Lang RJ. A Computational Algorithm for Origami Design. In: *Proceedings of the Twelfth Annual Symposium on Computational Geometry*; 1996. p. 98–105.
- [77] Zirbel SA, Lang RJ, Thomson MW, Sigel DA, Walkemeyer PE, Trease BP, et al. Accommodating Thickness in Origami-Based Deployable Arrays. *Journal of Mechanical Design*. 2013;135(11):111005.
- [78] Peraza-Hernandez EA, Hartl DJ, Malak RJ Jr, Lagoudas DC. Origami-inspired active structures: a synthesis and review. *Smart Materials and Structures*. 2014;23(9):094001.
- [79] Delimont IL, Magleby SP, Howell LL. Evaluating Compliant Hinge Geometries for Origami-Inspired Mechanisms. *Journal of Mechanisms and Robotics*. 2015;7(1):011009.

- [80] Boncheva M, Whitesides GM. Templated Self-Assembly: Formation of Folded Structures by Relaxation of Pre-stressed, Planar Tapes. *Advanced Materials*. 2005;17(5):553–557.
- [81] Zirbel SA, Trease BP, Magleby SP, Howell LL. Deployment Methods for an Origami-Inspired Rigid-Foldable Array. In: *The 42nd Aerospace Mechanism Symposium*; (NASA/CP-2014-217519); 2014. p. 189–194.
- [82] von Lockette P, Sheridan R. Folding Actuation and Locomotion of Novel Magneto-Active Elastomer (MAE) Composites. In: *ASME 2013 Conference on Smart Materials, Adaptive Structures and Intelligent Systems*; 2013. p. V001T01A020.
- [83] Berbinau P, Soutis C, Guz IA. Compressive failure of 0 unidirectional carbon-fibre-reinforced plastic (CFRP) laminates by fibre microbuckling. *Composites Science and Technology*. 1999;59(9):1451–1455.
- [84] Murphey T, Meink T, Mikulas M. Some micromechanics considerations of the folding of rigidizable composite materials. In: *19th AIAA Applied Aerodynamics Conference. Fluid Dynamics and Co-located Conferences*; 2001. p. 1418.
- [85] López Jiménez F, Pellegrino S. Folding of fiber composites with a hyperelastic matrix. *International Journal of Solids and Structures*. 2012;49(3):395–407.
- [86] Huber JE, Fleck NA, Ashby MF. The selection of mechanical actuators based on performance indices. *Proceedings of the Royal Society A*. 1997;453(1965):2185–2205.

- [87] Lacasse S, Terriault P, Simoneau C, Brailovski V. Design, manufacturing, and testing of an adaptive composite panel with embedded shape memory alloy actuators. *Journal of Intelligent Material Systems and Structures*. 2014;26(15):2055–2072.
- [88] Hufenbach W, Gude M, Czulak A. Actor-initiated snap-through of unsymmetric composites with multiple deformation states. *Journal of Materials Processing Technology*. 2006;175(1–3):225–230.
- [89] Chapman EG, Herdic SL, Keller CA, Lynch CS. Development of miniaturized piezo-hydraulic pumps. In: *Smart Structures and Materials*. International Society for Optics and Photonics; 2005. p. 299–310.
- [90] Zhang Z, Philen M. Review: Pressurized Artificial Muscles. *Journal of Intelligent Material Systems and Structures*. 2012;23(3):255–268.
- [91] Martinez RV, Fish CR, Chen X, Whitesides GM. Elastomeric Origami: Programmable Paper-Elastomer Composites as Pneumatic Actuators. *Advanced Functional Materials*. 2012;22(7):1376–1384.
- [92] Hyer MW. The Room-Temperature Shapes of Four-Layer Unsymmetric Cross-Ply Laminates. *Journal of Composite Materials*. 1982;16(4):318–340.
- [93] Hamamoto A, Hyer MW. Non-linear temperature-curvature relationships for unsymmetric graphite-epoxy laminates. *International Journal of Solids and Structures*. 1987;23(7):919–935.
- [94] Dano ML, Hyer MW. The response of unsymmetric laminates to simple applied forces. *Mechanics of Composite Materials and Structures*. 1996;3(1):65–80.

- [95] Dano ML, Hyer MW. Thermally-Induced Deformation Behavior of Unsymmetric Laminates. *International Journal of Solids and Structures*. 1998;35(17):2101–2120.
- [96] Diaconu CG, Weaver PM, Arrieta AF. Dynamic analysis of bi-stable composite plates. *Journal of Sound and Vibrations*. 2009;322(4–5):987–1004.
- [97] Gigliotti M, Wisnom MR, Potter KD. Loss of bifurcation and multiple shapes of thin [0/90] unsymmetric composite plates subject to thermal stress. *Composites Science and Technology*. 2004;64(1):109–128.
- [98] Cantera MA, Romera JM, Adarraga I, Mujika F. Modelling of [0/90] laminates subject to thermal effects considering mechanical curvature and through-the-thickness strain. *Composite Structures*. 2014;110:77–87.
- [99] Pirrera A, Avitabile D, Weaver PM. Bistable plates for morphing structures: A refined analytical approach with high-order polynomials. *International Journal of Solids and Structures*. 2010;47(25–26):3412–3425.
- [100] Marchese AD, Katzschmann RK, Rus D. A recipe for soft fluidic elastomer robots. *Soft Robotics*. 2015;2(1):7–25.
- [101] Chillara VSC, Headings LM, Dapino MJ. Self-folding laminated composites for smart origami structures. In: *ASME 2015 Conference on Smart Materials, Adaptive Structures and Intelligent Systems*; 2015. p. 8968.
- [102] Reddy JN. *Mechanics of Laminated Composite Plates - Theory and Analysis*. Boca Raton, FL: CRC Press; 1997.
- [103] Peel LD, Jensen DW. Nonlinear Modeling of Fiber-Reinforced Elastomers and the Response of a Rubber Muscle Actuator. *Papers-American Chemical Society Division of Rubber Chemistry*. 2000;(30).

- [104] Ogden RW. Large Deformation Isotropic Elasticity - On the Correlation of Theory and Experiment for Incompressible Rubberlike Solids. *Proceedings of the Royal Society of London A Mathematical and Physical Sciences*. 1972;326(1567):565–584.
- [105] Polygerinos P, Wang Z, Overvelde JTB, Galloway KC, Wood RJ, Bertoldi K, et al. Modeling of soft fiber-reinforced bending actuators. *IEEE Transactions on Robotics*. 2015;31(3):778–789.
- [106] Moran MJ, Shapiro HN. In: *Fundamentals of engineering thermodynamics*. John Wiley & Sons; 2000. p. 45–46.
- [107] Chillara VSC, Dapino MJ. Mechanically-prestressed bistable composite laminates with weakly coupled equilibrium shapes. *Composites Part B: Engineering*. 2017;111:251–260.
- [108] Betts DN, Salo AIT, Bowen CR, Kim HA. Characterisation and modelling of the cured shapes of arbitrary layup bistable composite laminates. *Composite Structures*. 2010;92(7):1694–1700.
- [109] Tanaka K, Kobayashi S, Sato Y. Thermomechanics of transformation pseudoelasticity and shape memory effect in alloys. *International Journal of Plasticity*. 1986;2(1):59–72.
- [110] Liang C, Rogers CA. One-Dimensional Thermomechanical Constitutive Relations for Shape Memory Materials. *Journal of Intelligent Material Systems and Structures*. 1990;1(2):207–234.

- [111] Brinson LC. One-dimensional constitutive behavior of shape memory alloys: thermomechanical derivation with non-constant material functions and redefined martensite internal variable. *Journal of Intelligent Material Systems and Structures*. 1993;4(2):229–242.
- [112] Boyd JG, Lagoudas DC. A thermodynamical constitutive model for shape memory materials. Part I. The monolithic shape memory alloy. *International Journal of Plasticity*. 1996;12(6):805–842.
- [113] Ivshin Y, Pence TJ. A Thermomechanical Model for a One Variant Shape Memory Material. *Journal of Intelligent Material Systems and Structures*. 1994;5(4):455–473.
- [114] Brinson LC, Huang MS. Simplifications and Comparisons of Shape Memory Alloy Constitutive Models. *Journal of Intelligent Material Systems and Structures*. 1996;7(1):108–114.
- [115] Potter K, Weaver P, Seman AA, Shah S. Phenomena in the bifurcation of unsymmetric composite plates. *Composites Part A: Applied Science and Manufacturing*. 2007;38(1):100–106.
- [116] Chillara VSC, Dapino MJ. Shape memory alloy-actuated bistable composites for morphing structures. In: *SPIE 2018 Conference on Smart Structures and Non-Destructive Evaluation*, 5 Mar., Denver, CO; 2018. p. 10596–7.
- [117] Wall WA, Gee M, Ramm E. The challenge of a three-dimensional shell formulation-the conditioning problem. In: *Proceedings of ECCM, Athens, Greece*; 2000. p. 99.

- [118] Stein M. Postbuckling of orthotropic composite plates loaded in compression. *American Institute of Aeronautics and Astronautics Journal*. 1983;21(12):1729–1735.
- [119] Diaconu CG, Weaver PM. Postbuckling of long unsymmetrically laminated composite plates under axial compression. *International Journal of Solids and Structures*. 2006;43(22–23):6978–6997.
- [120] Hyer MW. *Stress analysis of fiber-reinforced composite materials*. DEStech Publications, Inc; 2009.
- [121] Center OS. Ohio supercomputer center; 1987. <http://osc.edu/ark:/19495/f5s1ph73>.
- [122] Dano ML, Hyer MW. Snap-through of unsymmetric fiber-reinforced composite laminates. *International Journal of Solids and Structures*. 2002;39(1):175–198.
- [123] Tawfik SA, Stefan Dancila D, Armanios E. Planform effects upon the bistable response of cross-ply composite shells. *Composites Part A: Applied Science and Manufacturing*. 2011;42(7):825–833.
- [124] Chillara VSC, Dapino MJ. Stability considerations and actuation requirements in bistable laminated composites. *Composite Structures*. 2018;184:1062–1070.
- [125] Kilian M, Flöry S, Chen Z, Mitra NJ, Sheffer A, Pottmann H. Curved Folding. *ACM Transactions on Graphics*. 2008;27(3):75:1–75:9.
- [126] Dureisseix D. An Overview of Mechanisms and Patterns with Origami. *International Journal of Space Structures*. 2012;27(1):1–14.

- [127] Schenk M, Guest SD. Origami folding: A structural engineering approach. In: Origami 5: Fifth International Meeting of Origami Science, Mathematics, and Education. CRC press; 2011. p. 291–304.
- [128] Peraza Hernandez EA, Hartl DJ, Akleman E, Lagoudas DC. Modeling and analysis of origami structures with smooth folds. *Computer-Aided Design*. 2016;78:93–106.
- [129] Mattioni F, Weaver PM, Friswell MI. Multistable composite plates with piecewise variation of lay-up in the planform. *International Journal of Solids and Structures*. 2009;46(1):151–164.
- [130] Brinson LC. One-dimensional constitutive behavior of shape memory alloys: thermomechanical derivation with non-constant material functions and redefined martensite internal variable. *Journal of Intelligent Materials Systems and Structures*. 1993;4(2):229–242.
- [131] Leng J, Lan X, Liu Y, Du S. Shape-Memory Polymers and their Composites: Stimulus Methods and Applications. *Progress in Materials Science*. 2011;56(7):1077–1135.
- [132] Glaser R, Caccese V, Shahinpoor M. Development of magneto-rheological fluid composites with rigidification characteristics. *Smart Materials and Structures*. 2011;20(4):045018.
- [133] DeSain JD, Brady BB, Metzler KM, Curtiss TJ, Albright TV. Tensile Tests of Paraffin Wax for Hybrid Rocket Fuel Grains. *AIAA*. 2009;5115:1–27.
- [134] Chillara VSC, Dapino MJ. Bistable morphing composites with selectively-prestressed laminae. In: *SPIE 2017 Conference on Smart Structures and Non-Destructive Evaluation*, 25 Mar., Portland, OR; 2017. p. 10165–28.